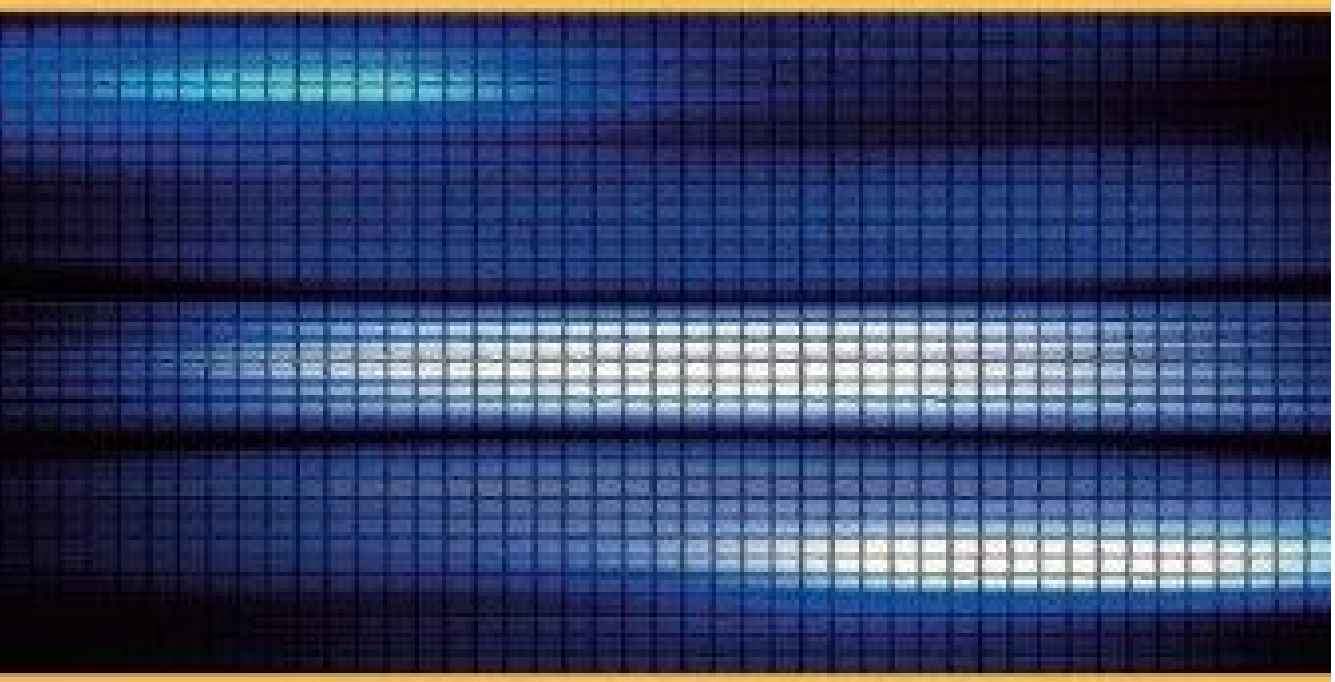

Nano Lithography

Edited by
Stefan Landis

ISTE

WILEY

Nano-Lithography

Nano-Lithography

Edited by
Stefan Landis

iSTE

WILEY

First published 2011 in Great Britain and the United States by ISTE Ltd and John Wiley & Sons, Inc.
Adapted and updated from *La nanolithographie* published 2010 in France by Hermes Science/Lavoisier
© LAVOISIER 2010

Apart from any fair dealing for the purposes of research or private study, or criticism or review, as permitted under the Copyright, Designs and Patents Act 1988, this publication may only be reproduced, stored or transmitted, in any form or by any means, with the prior permission in writing of the publishers, or in the case of reprographic reproduction in accordance with the terms and licenses issued by the CLA. Enquiries concerning reproduction outside these terms should be sent to the publishers at the undermentioned address:

ISTE Ltd
27-37 St George's Road
London SW19 4EU
UK

www.iste.co.uk

John Wiley & Sons, Inc.
111 River Street
Hoboken, NJ 07030
USA

www.wiley.com

© ISTE Ltd 2011

The rights of Stefan Landis to be identified as the author of this work have been asserted by him in accordance with the Copyright, Designs and Patents Act 1988.

Library of Congress Cataloging-in-Publication Data

Nanolithography English
Nano-lithography / edited by Stefan Landis.
p. cm.
Includes bibliographical references and index.
ISBN 978-1-84821-211-4
1. Microlithography. 2. Nanotechnology. I. Landis, Stefan. II. Title.
TK7872.M3N3613 2011
621.3815'31--dc22

2010046516

British Library Cataloguing-in-Publication Data
A CIP record for this book is available from the British Library
ISBN 978-1-84821-211-4

Printed and bound in Great Britain by CPI Antony Rowe, Chippenham and Eastbourne.

FSC
www.fsc.org
MIX
Paper from responsible sources
FSC® C013604

Table of Contents

Foreword xi
Jörge DE SOUSA NORONHA

Introduction xvii
Michel BRILLOUËT

Chapter 1. X-ray Lithography: Fundamentals and Applications 1
Massimo TORMEN, Gianluca GRENCI, Benedetta MARMIROLI and Filippo ROMANATO

1.1. Introduction. 1
1.2. The principle of X-ray lithography 5
1.2.1. The irradiation system for XRL 7
1.2.2. Properties of synchrotron radiation 9
1.2.3. High Resolution and Deep XRL 12
1.2.4. Examples of X-ray lithography beamlines 12
1.2.5. Scanner/stepper 18
1.2.6. The mask 19
1.3. The physics of X-ray lithography 25
1.3.1. How phase and intensity of X-rays are altered by interaction with matter. 25
1.3.2. X-ray lithography as a shadow printing technique 27
1.3.3. X-ray absorption in a resist and physical mechanisms involved in its exposure 30
1.3.4. Physical model of electron energy loss in resists 35
1.3.5. Diffraction effects in X-ray lithography. 40
1.3.6. Coherence of synchrotron radiation from bending magnet devices 41

1.3.7. Basic formulation of diffraction theory for a scalar field. 44
1.3.8. Rayleigh–Sommerfeld formulation of diffraction by a planar screen 47
1.3.9. An example of diffraction effects: Poisson's spot in X-ray lithography 51
1.4. Applications 55
1.4.1. Optimal photon energy range for high resolution and deep X-ray lithography 55
1.4.2. Diffraction effects on proximity lithography. 56
1.4.3. High resolution 3D nano structuring. 61
1.4.4. 3D polymer structures by combination of NanoImprint (NIL) and X-ray lithography (XRL) 64
1.4.5. Micromachining and the LIGA process. 66
1.4.9. Micro-optical element for distance measurement 77
1.5. Appendix 1 79
1.6. Bibliography 79

Chapter 2. NanoImprint Lithography 87
Stefan LANDIS

2.1. From printing to NanoImprint. 87
2.2. A few words about NanoImprint 90
2.3. The fabrication of the mold 96
2.4. Separating the mold and the resist after imprint: de-embossing 100
2.4.1. The problem 100
2.4.2. Adhesion 102
2.4.3. Adhesion and physico-chemical surface properties 103
2.4.4. Surface treatment of the mold 107
2.4.5. Treatment of the resist 114
2.4.6. Characterization of the demolding process 114
2.5. The residual layer problem in NanoImprint 118
2.5.1. The residual layer: a NanoImprint specific issue 118
2.5.2. Is the thickness of the residual layer predictable? 120
2.5.3. How can the process impact the thickness of the residual layer? 125
2.6. Residual layer thickness measurement 132
2.6.1. Macro-scale approach: coherence between film color and thickness 134
2.6.2. Microscopic approach 136

2.7. A few remarks on the mechanical behavior of molds and flow properties of the nanoimprint process 148
2.8. Conclusion 157
2.9. Bibliography 157

Chapter 3. Lithography Techniques Using Scanning Probe Microscopy 169
Vincent BOUCHIAT

3.1. Introduction. 169
3.2. Presentation of local-probe microscopes. 170
3.3. General principles of local-probe lithography techniques. 171
3.4. Classification of surface structuring techniques using local-probe microscopes 173
3.4.1. Classification according to the physical nature of the interaction 174
3.4.2. Comparison with competing advanced lithography techniques . . . 176
3.4.3. Industrial development perspectives. 177
3.5. Lithographic techniques with polymer resist mask. 179
3.5.1. Electron beam exposure of resists by scanning probe microscopes 180
3.5.2. Development of a resist dedicated to AFM nano-lithography 182
3.5.3. Lithography using mechanical indentation 184
3.6. Lithography techniques using oxidation-reduction interactions 185
3.6.1. Direct fabrication by matter deposition induced by STM microscopy 186
3.6.2. Local anodization under the AFM tip 188
3.7. “Passive” lithography techniques 198
3.7.1. Dip-pen lithography 198
3.7.2. Alignment technique by means of a mechanical masking (stencil mask) 200
3.8. Conclusions and perspectives 200
3.9. Bibliography 201

Chapter 4. Lithography and Manipulation Based on the Optical Properties of Metal Nanostructures 207
Renaud BACHELOT and Marianne CONSONNI

4.1. Introduction. 207
4.2. Surface plasmons 208
4.2.1. Definition of a volume plasmon 208

4.2.2. Delocalized surface plasmons 209
4.2.3. Localized surface plasmons 212
4.2.4. Application to lithography 216
4.3 Localized plasmon optical lithography 216
4.3.1. Near-field optical lithography by optical edge effect 217
4.3.2. Use of nanoparticle resonances 220
4.4. Delocalized surface plasmon optical lithography 222
4.4.1. Coupling between nanostructures and delocalized surface plasmons 223
4.4.2. Surface plasmon launch and interferences 224
4.5. Conclusions, discussions and perspectives 225
4.6. Bibliography 226

Chapter 5. Patterning with Self-Assembling Block Copolymers 231
Karim AISSOU, Martin KOGELSCHATZ, Claire AGRAFFEIL, Alina PASCALE and Thierry BARON

5.1. Block copolymers: a nano-lithography technique for tomorrow? 231
5.2. Controlling self-assembled block copolymer films 233
5.3. Technological applications of block copolymer films 237
5.4. Bibliography 244

Chapter 6. Metrology for Lithography 249
Johann FOUCHER and Jérôme HAZART

6.1. Introduction 249
6.2. The concept of CD in metrology 250
6.2.1. CD measurement after a lithography stage: definitions 250
6.2.2. What are the metrological needs during a lithography step? 251
6.3. Scanning electron microscopy (SEM) 254
6.3.1. SEM principle 254
6.3.2. Matter–electron interaction 258
6.3.3. From signal to quantified measurement 263
6.3.4. Provisional conclusion on scanning electron microscopy 266
6.4. 3D atomic force microscopy (AFM3D) 266
6.4.1. AFM principle 267
6.4.2. Three-dimensionnal AFM (AFM3D) special features 275
6.4.3. Provisional conclusion on AFM 3D 286
6.5. Grating optical diffractometry (or scatterometry) 286
6.5.1. Principle 287

6.5.2. Example: ellipsometry characterization of post development lithography 290
6.5.3. Pros and cons 296
6.5.4. Optical measurements analysis 297
6.5.5. Specificities of scatterometry for CD metrology 305
6.5.6. Scatterometry implementation: R&D versus production 307
6.5.7. New fields for scatterometry 310
6.6. What is the most suitable technique for lithography? 310
6.6.1. Technique correlation 313
6.6.2. Technique calibration 313
6.6.3. Process development 314
6.6.4. Evaluation of morphological damage generated by the primary electron beam from CD-SEM 314
6.7. Bibliography 316

List of Authors 321

Index 323

Foreword

"*An image is a pure creation of spirit*." (*Pierre Reverdy*)

Today, in a world of eternal representation, we are the observers of the theater of the grand image for as far as the eye can see, a theater which incessantly unfolds in the marvelous recording box that is our brain. Though we see them, the touch and even the substance of illustrations sometimes escape us completely, so much so that we can almost not differentiate between representative illusion and the physical reality of beings and things. Yet, the representation of the world in our eyes is not the same as the one that we want to transpose, to put into images. There, the reality of that which is visible is captured by our brains, which makes copies which are sometimes faithful, sometimes untrue. To produce these images we have, since the dawn of mankind, resorted to sometimes extremely complex alchemies, where invention has struggled with various materials, as a result of which we have been able to leave behind our illustrated drawings, the prints of our lives and of our societies.

For some 32,000 years man has not stopped etching, doodling, drawing, copying, painting, reproducing – for nothing, for eternity – producing millions of infinite writings and images which are the imperishable memory of his genius. How did he do it, with which materials, on what, and why? The alchemy of representation, in its great complexity, deserves to be slowed down, so that we can try to understand, for example, how today's images reach us in a kind of gigantic whirlwind, whereas 200 years ago these things were still rather sober. Or how else could we go from an image that we can look at, to an image that is difficult to see, or to one that we cannot even see with the naked eye? Whereas now we throw things away, in the past images were preciously preserved. Are the images which we try to preserve today not the same as the ones we were preserving yesterday?

Foreword written by Jörge DE SOUSA NORONHA.

It is amongst the cavemen that that which I call the *image maker* can first be outlined. Collating their visions, their dreams, their beliefs on cave walls, these first *imagicians* undoubtedly bequeathed to us the only widely known account of this period. In their wake, we will be able to better evaluate the formal evolution of the visual representation of nature and things, this inevitable invention in which we endeavor to capture the spirit through an artefact.

Man had to train long and hard to finally tame and durably transmit the images of the world which surrounded him. The techniques employed across the ages to make and convey these images, the materials, the pigments, the bindings, the instruments and the mediums, either natural, chemical or manufactured, not only conditioned the appearance of the image itself but also its durability.

Cave paintings, coins, palaces, churches, are just some of the mediums which have left us with invaluable visual evidence of more or less remote pasts, sometimes essential for putting together the history of humanity. If we consider the manufacturing and the trading of images from the beginning, and in its totality, we can distinguish two major periods: the longest, the pre-photographic; and the post-photographic, which began in the first half of the 19th Century, and which is therefore extremely recent. Admittedly, our eyes can see but they cannot take photographs. The images that they collect are transitory fragments in a "band-width", a time kept in the memory, often lost, far from any material existence, and for which any attempt at verbal transcription is on this side of reality. For other animals, sight is part of a sub-conscious effort to survive. For man, by contrast, sight is a conscious irreplaceable instrument, appreciating the outside world, which is an integral part of his own physical and mental development. For us, to see is natural. However, representing what we see calls upon a certain kind of initiation. How were the first painters of history introduced to engraving and drawing? How were they able to find or invent the tools and materials needed to succeed?

The tools, materials and shapes are the three essential ingredients needed to build and formalize the representation of the visible. Footprints on sand, for example, undoubtedly the first prints left by man, were already kinds of natural images of the body, and most probably were the root of the original idea to make images. The tool here was man's own foot, with its shape, using a soft and flexible material, a support able to keep an image. Thus, without any doubt, the earth and sand were among the first image mediums, even before other sketches came to cover other materials, and other surfaces.

The various attempts leading to the reproduction and spreading of visible images or texts, little by little, drove man to develop very clever techniques, sometimes born out of chance, or sometimes by increasingly elaborate research. The first stone engravings (from before 600 BC) precede, by a long time, the first examples of

wood engravings (c. 200 AD), or metal engravings made by a direct method, then etchings, or the invention of typographical characters, and, finally, lithography itself, which has been, from the 19th Century onwards, a practically irreplaceable means of reproduction, and remains an essential part of the book and publicity industries, even today.

The document media have also diversified and evolved incessantly since the beginning. Stone, bone or ivory, terracotta, glass, skins, leaves, wood, parchment, paper, celluloid, vinyl, are just some of the aids bequeathed to us, with greater or lesser clarity or brittleness, the precious evidence of life and the history of mankind.

In 1796, 43 years before the invention of photography, the lithographic reproduction technique was invented by Aloïs Senefelder in Germany. Developed during the first half of the 20th Century, it brought, without question, the most important graphic revolution in the worlds of text reproduction and printed images. In this respect, we can consider two very great periods in the history of print: one, the pre-lithographic period, and the other which began with lithography in all of its forms. Here, two distinct lithographic fields start to truly develop: on one side, the advanced forms of the graphics industry (and the photolithographic industry); and, on the other side, a completely innovative form of artistic expression, now freed from the technical constraints of engraving and now able to devote itself with joy to those much freer forms of graphics, with drawings made (or transferred) directly onto the lithographic support itself. These two domains participated, together, in the technical developments which led finally to the offset printing methods used overwhelmingly today and which profit from these most advanced technologies.

As far as the photographic reproduction of images was concerned, one major challenge was the faithful reproduction of half-tones. This problem was solved in 1884 by Meisenbach, the inventor of the linear screen which was quickly applied to typographical image reproduction and then successively to photo-lithography and to offset printing. This photographic support itself already contained the seeds and the "secret" of the visibility of half-tones, incorporating the smoothness of the granular nature even of photosensitive emulsions. But to print them, it was necessary to find a way of transcribing them in a printing matrix, initially in black and white, and then later in color. An interesting characteristic is that the various screens which we have just alluded to, in particular the finest or ultra-fine (higher than 80 lines/cm) or the most recent digital grids forming an ultra-fine grid of random dots, have always tried to more or less blend in, until made invisible to the naked eye. The printed images our eyes can see are actually optical illusions. Today, if we look closely at a beautiful reproduction of an engraving by Durer, or at a painting by Vélasquez, for example, it is impossible to distinguish the dots from the printing screens which they are made from. Already in the 19th Century, commercial chromolithography used clever methods to create half-tones, either with the proper matrix granulation (stones

or granulated metal), or by dots, drawn very finely with a feather, which simultaneously allowed the ranges and mixtures of the colors, of which there are some sublime examples. In the art field, it is nowadays necessary to use a microscope with a magnification of ×30 to determine the true nature of a printing technique.

Even in the first half of the 20th Century, we saw the first steps of a very new aid to knowledge. Indeed, 1936 and the publication of a founding article by Alan Turing, "On computable numbers with an application to the Entscheidungsproblem", is the true starting point of the creation of programmable computers. But it was especially from the 1980s that the use of computers was democratized and, little by little, became essential to the world of information and imagery. From then on, texts and images have been created by each and everyone, with no need to be preserved in a physical, material way, but instead held on other media which we would not have dared to even imagine 30 years earlier. The image, which is still the product of another optical illusion, while keeping its own graphic originality, from now on needs no hardware support to be visible. It has its own light, can be modified at will, engraved, printed, and sent to the entire world with the single touch of a button. The image, in this case, is created in all its subtleties of color and light, not by a material screen, but by something which replaces it virtually, a succession of dots invisible to the eye (pixels) which are now at the origin of texts and images digitally recorded on our computers.

During the second half of the 20th Century, the American Jack Kilby invented the very first printed circuit (in 1958), another artefact in the service of knowledge transmission which is at the root of modern data processing, and the mass production of electronic chips with integrated transistors began not much later. For his work and his some 60 patents, Kilby received the Nobel Prize for Physics in 2000. All these circuits are used in a more or less direct way nowadays, in information recording and image handling and storage. The big family of integrated circuits and microprocessors continues to move forward, and with them has come another new technology, microscopic photolithography, which makes new plate sensitization techniques possible and, thanks to the use of masks and light beams, the engraving of circuit supports in smaller and smaller micro-relief (such as, for example, the various chip-cards with integrated circuits, whether analog or digital).

At the beginning of the third millennium, another "image" architecture was already on the horizon, in a nanosphere with still vague contours, which curiously made us swing from a visible optical illusion towards an invisible physical reality. Indeed, from micro-photolithography to polymeric nanostructured materials by nanolithographic printing, the miniaturization of 3D engraved spaces took a giant leap forward. micro-dimensions are already virtually invisible to the naked eye; those of nano-dimensions will need a scanning electron microscope to be seen.

Lithography has thus exceeded the old domains of printed texts and of the "macro-image" with which we were more familiar, to reach other limits, in a new nano-imagery resolutely emerging from a dream world.

Ultra-miniaturized circuits, texts and images can, from now on, be conceived in infinitesimal spaces, and it may even be possible to think that millions of images, for example, could in the future easily be stored in less than one square meter of recording space.

However, we still know little about the stability and perennial nature of these digital media. How will the enormous mass of documentation recorded each day, all the images and mixed texts, be preserved? What will become of them in the coming centuries? We, who have already benefitted from many "recordings" of the past, also have a shared responsibility for the way in which we leave our imprints for future generations. From now on, we dare to hope, copying and the successive multiplication of documents will allow a kind of systematic and unlimited preservation of writings and images for the future.

Jörge DE SOUSA NORONHA

Introduction

Implications of Lithography

The microelectronic industry is remarkable for its exponential growth over recent decades. At the heart of this success is "Moore's law", a simple technical and economic assessment according to which it is always possible to integrate more and more functions into a circuit at reduced costs. This observation, made in the mid-1960s, has been transformed into a passionate obligation to fulfill its own prophecy, and has focused the efforts of an entire generation of microelectronics researchers and engineers.

Anyone talking about greater integration density is thinking about increasing our capacity to precisely define and place increasingly smaller components, building and using materials to support them. Lithography is succeeding in this arena, using increasingly sophisticated techniques, and is essential to the progress of the semiconductor industry because it allows a reduction in the size of patterns as well as an increase in the integration density of the integrated circuits at an economically acceptable cost.

The issue of dimension is considered so central to all microelectronic improvements that the industry calls each generation of the process, or each technological node, after a dimension which characterizes the technology; often, the half-pitch of the most dense interconnection is used. For a 45 nm technology for example, the minimum period of the interconnection pattern is 90 nm. Doubling the integration density of a circuit means decreasing its linear dimensions by 0.7: the nominal typical dimensions of advanced technologies follow one another at this rate, from 90 nm to 65 nm then 45 nm, 32 nm, 22 nm, etc.

Introduction written by Michel BRILLOUËT.

From a very simplistic point of view, the fabrication of integrated circuits concatenates and alternates two types of processing on the wafer (Figure I.1); either:

– a functional layer is deposited by a lithographic process. The material is localized by removing the extra material in the non-selected areas (subtractive process): this is the case, for example, for contact holes through an isolating layer; or

– a specific area is defined where a technological process is locally applied, the confinement system being removed at the end of the step (additive process): this is the case for ionic implantation or localized electro-deposition.

The efficiency of the lithographic process depends on only a few fundamental parameters:

– the capability of printing even the smallest patterns, or resolution;

– the precise alignment of each layer of a circuit;

– the capacity to obtain repeatable patterns, of a controlled geometrical shape;

– the capacity to control fabrication costs as a function of the products' typology.

A greater integration density implies that the very smallest patterns must be able to be manufactured, hence the focus on ultimate resolution for lithography techniques. Patterns of just a dozen nanometers do not surprise anyone anymore, and even atomic resolutions are now achievable, with today's more sophisticated experimental conditions.

Optical lithography remains the preferred production choice. Despite inevitably being abandoned once the physical limits of the micron, and then of the 100 nm, are crossed, it remains today the preferred technique for mass production for 32 nm, thanks to the numerous innovations of the past 20 years.

In optical lithography, a polymer layer called a photosensitive resist is deposited on a wafer. This resist is composed of a matrix which is transparent to the exposure wavelength and contains photosensitive compounds. When the image of the patterns from a mask is projected onto the wafer (and onto the photosensitive resist), the areas exposed are submitted to a photochemical reaction which, if completed correctly, enables the dissolution of the resist in those areas (in the case of positive resists), or prevents dissolution (in the case of negative resists). We can therefore obtain perfectly delimited areas for which the substrate is bare, and have areas still protected by the resist, allowing a subsequent local treatment. At the end of the process, the resist is removed from the wafer. During the fabrication of integrated circuits, this step is repeated several dozen times, hence the central role of lithography in microelectronics.

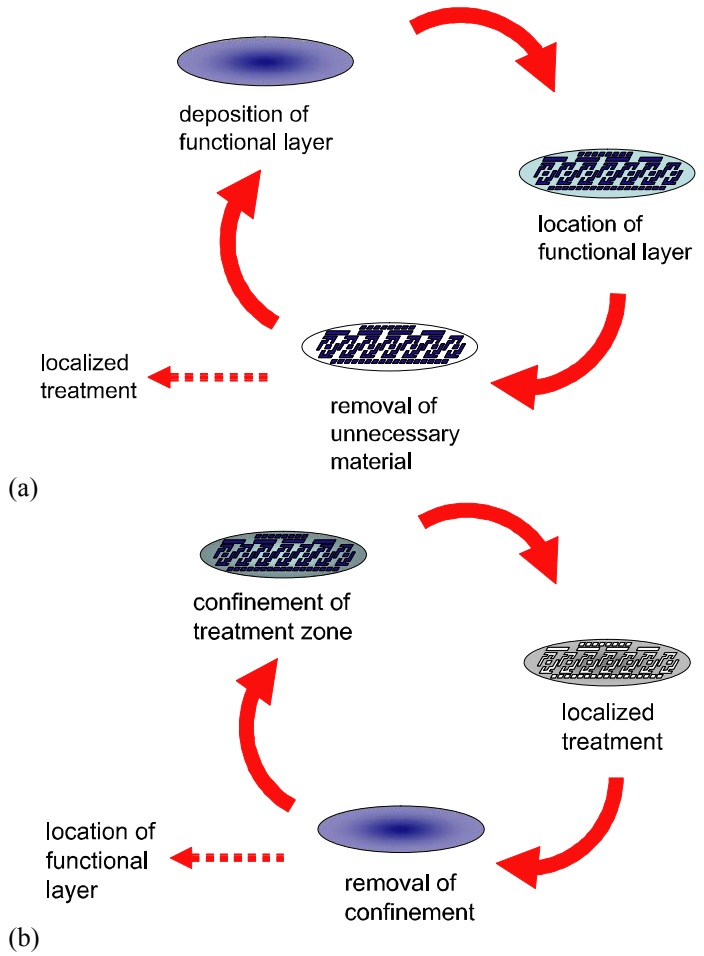

Figure I.1. *A localized process using lithography can be (a) subtractive (by locally removing non-functional material), or (b) additive (by forcing the local treatment of the wafer where it is required)*

In order to understand simply how this technique reaches its highest resolution, we can refer to the standard formula giving the resolution, R:

$$R = k_1 \times \lambda / NA$$

in which λ is the wavelength of the exposure light, NA the numerical aperture of the projection optics and k_1 a factor depending on the technological process. Each of these factors corresponds to a way of improving the image resolution.

Improvements were first made by decreasing the exposure wavelength λ. This was why, in the 1980s, the first tools started using different radiations from a mercury lamp (λ = 436 nm, called g-line radiation; 405 nm, or h-line; and then 365 nm, or i-line), usually using reduction projection optics based on quartz. Each wavelength change was accompanied by process changes that were major at the time, but which, in retrospect, could now be qualified as minor.

The first transition came in the 1990s with the use of deep ultraviolet excimer lasers, first with 248 nm (with a KrF laser) and then 193 nm (with an ArF laser), and allowed feature size resolution below the 0.1 μm limit to be reached. However, this evolution required major changes in either projection optics (use of CaF_2 in addition to quartz) or in the choice of the transparent matrix of the photosensitive resist.

The normal evolution would have moved towards F_2 lasers (λ = 157 nm) which need projection optics made mainly out of CaF_2, a material whose bi-refringence has proven to be a major obstacle: in the decade after 2000, after many years of development, industry finally concluded that it was illusory to continue down this path for mass production.

Reducing the k_1 parameter then appeared very promising. This is achieved by first improving the resist process, for example by increasing its contrast with nonlinear phenomena or by controlling the diffusion of the photosensitive compound. By optimizing illumination techniques (annular, quadripolar, etc.), it is also possible to gain resolution and process control but often by promoting certain shapes or pattern orientations.

It has been, above all, by mastering diffraction phenomena, and thus influencing the exposure light phases, that progress has been the most spectacular: it has been acknowledged that it is now possible to go beyond the Rayleigh criterion and print patterns even smaller than the exposure wavelength. From laboratory curiosities, these techniques have now become the workhorse of the microelectronics industry and are now known under the name “Resolution Enhancement Techniques”.

In a very schematic manner, and for a certain illumination and resist process, we will try to calculate what the patterns and phase-differentiated areas on a mask should be in order to achieve an image on a wafer which matches an image initially conceived by circuit designers. The reverse calculations are extremely complex and demand very powerful computers in order to obtain the result (in some cases taking up to several days, which affects the cycle time of prototypes of new circuits). In the end, the goal is to take proximity effects between close patterns (thus a combinational explosion of the calculation time) into account, by in turn taking into account the most precise possible optical models (and, as the technologies improve, it is important to not only take into account intensity and phase but also light

polarization). The resulting pattern on a mask becomes particularly complex, and the cost of a mask set for a new circuit can exceed several million dollars for the most advanced technologies, which can become a major obstacle for small production volumes.

Despite this complexity, it is increasingly difficult to find a solution for arbitrary patterns (called random logic patterns, even though this term is inappropriate). The idea arose to simplify the problem by grouping patterns with the most periodicities (and therefore easier to process) and obtain the desired design on a wafer by multiple exposures. This approach, despite its significant production costs, has become common in the most advanced technologies.

Additionally, the numerical aperture (NA) of the projection tool has been studied, even though we know that an increase of the NA can only be made to the detriment of the depth of field. Of course, NA has increased over recent years, thus decreasing the size of the exposed field. This is why print patterns were "photo-repeated" by repeating the exposure of a field a few centimeters in size over the entire wafer (the tool used is called a photo-repeater or "stepper"), then the area exposed was reduced a little more by scanning a light-slit over the exposure field (using a tool called a "scanner"). Unfortunately lithography was limited by the numerical aperture, which could not exceed 1.

Researchers then returned to their old optical knowledge: by adding a layer of liquid (with a higher index than air) between the first lens of the exposure tool and the resist, the limit could be overrun. This "immersion lithography" has not been established without difficulties. The defect density generated by this process was at first high, not to mention there being an increased complexity of the lithographic tool. The conjunction of these major difficulties encountered in 157 nm lithography and the need to decrease the dimensions made this technique viable and it is starting to be used for mass production.

The next step was to increase the refraction index of the liquid to above that of water, and that of the projection systems (the lenses) to above that of quartz. However, in the case of 157 nm, this approach is blocked by major material problems, and the future of this path beyond that of the resist-water-quartz system seems highly endangered.

Many believe that a major decrease of the exposure wavelength would significantly relax the constraints that apply to lithography. Hence there has been a unique worldwide effort to develop Extreme UltraViolet lithography (EUV) using the 13.5 nm wavelength. However, despite an enormous effort during the past two decades, this technology stays blocked by major problems of source power and industrial facilities able to produce defectless masks. Initially foreseen to be

introduced for 90 nm technologies, it has difficulties addressing 22 nm technologies. As a result, initially peripheral aspects, such as high numerical aperture optics, come back to the forefront, even though other technological problems are still unresolved for industrial manufacturing.

Complexity has considerably increased the cost of lithography for the fabrication of integrated circuits for the most advanced technologies. The newest immersion scanners, in addition to their environment (resist coating track, metrology) easily cost over $50 million each, and it would not be surprising if a price of $100 million was reached with EUV, hence the large amount of research into alternative technologies to optical lithography in order to either significantly decrease the cost or to address very specific applications that do not necessarily need the most advanced lithographic tools.

One alternative technique was established a long time ago: electron beam (often called "e-beam") lithography. This technique is not limited by wavelength or by depth of field, thus making it very attractive. The absence of a mask is an additional advantage when looking at the never ending increase of mask prices, especially in the case of small volume production. The disadvantage of this technique is that pattern printing can only be achieved sequentially (the electron beam writes in the resist pixel after pixel), which does not allow high enough productivity for mass production. In addition, e-beam can no longer claim its superiority in terms of resolution and alignment precision because of the continuous progress of optical lithography. However, new projects are being developed, among which is the idea of massively multiplying the number of independently controlled beams (tens of thousands of beams is the number stated): productivity would then increase significantly, with the prospect of it being applied to small volume production. In addition to this application, electron beam lithography remains a preferred tool for research activities that can combine flexibility, dimension control and affordable price. It can also be used to precisely repair circuits (or to print specific patterns on demand), using either an electron or an ion beam.

Other alternative techniques offer interesting prospects for precise applications:

– NanoImprint lithography, similar to the techniques used to fabricate CDs or DVDs from a master. This enables nanoscale resolutions to be achieved, and could emerge as a contender technology if there were only one lithographic level. It has also been shown that this technique could be used to print 3D patterns. The stacking of dozens of layers in integrated circuits is still to be demonstrated industrially, in particular in terms of alignment precision and defect density due to fabrication.

– Near-field lithography is still the perfect tool when aiming for ultimate resolution (potentially positioning atoms one by one). Its current state suffers from the same intrinsic limitations as electronic lithography (small productivity) as well

as a difficult setting when reaching ultimate resolutions, but this technique could open up to real prospects with tip-matrices of the millipede type.

– X-ray lithography was, for a long period after the major efforts of the 1980s, not considered adequate to become an industrial technique. Source weakness (even if synchrotrons are huge experimental systems), the difficulty of fabrication of transparent masks and the absence of reduction optics have heavily handicapped the future of this technique. However, it remains useful for specific applications (such as the LIGA technique[1]) given its great field depth that can be used in microsystems.

A special note should be made about self-organizing techniques. These rely on a simple fact: nature seems to be able to generate complex structures from apparently simple reactions. More specifically, local interactions can induce unexpected or even complex, emerging behaviors: this is called self-organization. Convincing examples of periodic structures generated by these techniques are regularly submitted to the scientific literature; however, it is hard to find an idea to exploit this technique in order to produce future low cost microprocessors. Thus, two directions now exist:

– the use of these phenomena to locally improve process quality. For example, the use of resists based on copolymers could help improve the line roughness of lithographic patterns; and

– the notion of "directed self-assembly" or "emplated self-assembly", which is the most important direction for more complex structures. This is about defining and implementing limit conditions that, using local self-organization forces, could generate the complex structures desired.

Finally, it is important to remember that the fabrication cost aspect of these emerging technologies remains completely speculative, since the technical solutions to be implemented on an industrial scale are still unknown.

This focus on ultimate resolution as the connecting thread of this book should not hide other technical elements that are also critical for lithography's success. Thus, popular literature often forgets that the capacity to stack two patterns greatly contributes to the capacity to integrate many compounds in a circuit. Indeed if patterns are misaligned, an area around the pattern would have to be freed to ensure the functionality of the circuit, thus reducing the integration density (Figure I.2). Achieving alignment with a precision equal to a fraction of the minimum size of the pattern (a few nm), and measuring it, represents a challenge that lithography has so far been able to meet.

---

1 LIGA is a German acronym for **Li**thographie, **G**alvanoformung, **A**bformung (Lithography, Electroplating, Molding).

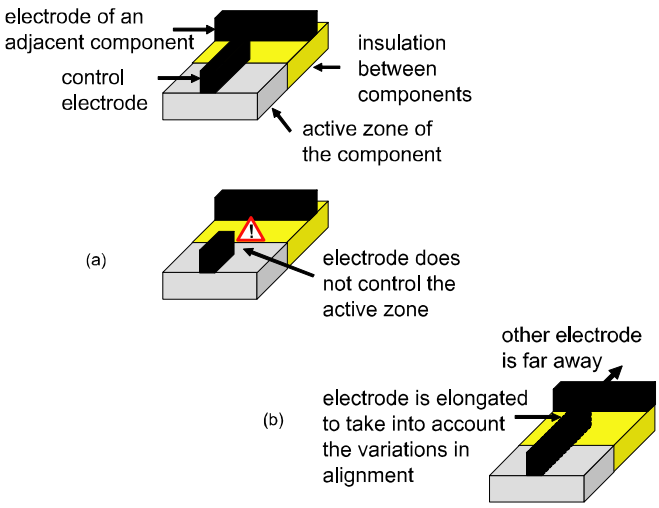

Figure I.2. *The precise alignment of patterns printed at different lithographic levels influences the compound integration density of a circuit. For example, in the case of the command electrode of a transistor: (a) with significant misalignment, the command electrode of a transistor could possibly no longer control the active zone of the compound. (b) In order to avoid this situation, the electrode's size is increased. As a result, those electrodes which are close must be moved, thus inducing a degradation of the integration density*

The functionality of a circuit will depend on the precision at which the patterns on the wafer are printed. Metrology is a key element in mastering the production yield, whereas the demands regarding precision, information integrity and measurement speed keep growing. Previously, optical microscopy techniques were enough to measure, in a relative way, the two critical parameters of a lithographic step, meaning the dimension of its pattern and alignment in relation to the underlying layers. As dimensions have decreased, standard optical techniques were replaced by different approaches:

– the use of an electron beam microscope (and more recently near-field techniques) enabled a natural extension to the smallest dimensions;

– light scattering of periodic patterns (for example scatterometry) gave access to more complete information on the dimensions and shape of the patterns, even though the interpretation of the results remains unsure. A move towards shorter wavelengths (for example SAXS for X-rays) opens up new perspectives (as well as some advantages, for example with substrate transparency).

However, the challenges to be fulfilled keep increasing. A relative measurement is no longer sufficient to guarantee a circuit's performance and the possibility of an absolute metrology on a nanometric scale still remains. In addition, the shape of the

pattern is increasingly a 3D measurement which is essential, at least when considering mass production, even if the techniques used are still in the embryonic stages. Finally, the proximity effects between patterns make the measurement indicators less representative of the complexity of a circuit: the metrology of a statistical collection of meaningful objects in a complex circuit is a field of research that is still wide open.

It is important to mention a technical field which, even if not part of lithography in the strictest sense, is to a large extent connected to it: the measurement of physical defects in a production process. Indeed, two different aspects of the analysis and measurement of defectivity are interesting:

– For defects with an identified physical signature, techniques similar to lithography can be applied because it concerns acquiring an image with optical techniques (in the broad meaning, including charged particle beams) and treating it in order to extract meaningful information.

– Lithography is unique in the way that, in the case of the detection of a defect during this step, it is usually possible to rework the wafer and thus avoid the permanent etching of the defect into the circuit.

In conclusion, lithography has undergone several decades of unimaginable progress, by-passing unproven physical limits thanks to the ingenuity of microelectronics researchers and engineers. Even if questions emerge about the economic viability of dimension decrease at all costs, major steps forward are expected during the coming years, either in terms of the solutions reached, the integration density or capacity to produce cheap complex structures.

Chapter 1

X-ray Lithography: Fundamentals and Applications

1.1. Introduction

The invention of X-ray proximity lithography [SPE 72] dates back to the early 1970s, when the declared objective was overcoming the resolution of the lithographic techniques then employed in the semiconductor industry. At that time, UV projection lithography was the leading technology, having reached a scale resolution of one micrometer [WIL 29]. Nevertheless, a very problematic future was forecast for UV-lithography, given the expected requirements of the microelectronics industry to achieve sizes as small as 250 nm. In fact, the physical barrier represented by diffraction was believed to be insuperable. Therefore, the quite obvious idea of using radiation of shorter wavelengths for exposures was seen as the only viable option to keep pace with Moore's law [MOO 65] and the semiconductor industry roadmaps [ITRS] for device miniaturization.

However, shifting to shorter wavelengths, down to the region of Extreme UV (EUV) which extends between approximately 30 and 250 eV, raises new problems. One fundamental problem is represented by the low transparency of most materials. At these photon energies, the radiation is so strongly absorbed by any dense material that it is difficult or even impossible to find suitable materials to be used as

---

Chapter written by Massimo TORMEN, Gianluca GRENCI, Benedetta MARMIROLI and Filippo ROMANATO.

transparent substrates for photomasks and for the sophisticated demagnification optics of the projection system.

One viable solution to the low transparency problem considered was that of exploring even shorter wavelengths. It has been known, since Röntgen's discoveries concerning the properties of X-rays, that the region of soft to hard X-rays offers a sufficient penetration depth in materials. This possibility of selecting materials with sufficient transparency is likely to have played an important role in convincing the pioneers of X-ray lithography to undertake the development of a new lithographic technique based on the use of electromagnetic radiation in the spectral region of X-rays. One might have expected that jumping from the spectral region of Deep UV (λ~200 nm) to that of X-rays with at least two orders of magnitude shorter wavelengths (λ~1 nm) would have ensured a "resolution reserve" for all the technological nodes ahead in the microelectronics industry. This fact in itself would have represented an enormous advantage for X-ray lithography, compared to DUV lithography which requires the complete renewal of fabrication facilities at every new technological node. It was this fact, therefore, that motivated a large initial effort devoted to establishing X-ray lithography (XRL) as the "next generation" lithography.

Between the 1970s and the end of the century very intense activity was reported in the field of X-ray lithography, in particular in the development of exposure systems (steppers) [SEI 98, SIL 97], in the optimization of different protocols for mask fabrication [RAV 96, ROM 97, SHI 96, ROU 90, WAN 04], in the foundation of the theoretical background, and in the development of codes for quantitative analysis and simulations [AIG 98, GRI 04, ZUM 97, PRE 97]. In the meantime, mainly driven by their use in the study of the physics of matter, in chemistry and biology, third generation synchrotron radiation sources [BIL 05] were reaching a high level of maturity as high brilliance sources of nearly collimated X-ray beams on a wide range of energies. These sources have almost ideal performances for X-ray lithography, and represented a major improvement with respect to X-ray tubes [MAR 95].

A brilliant future seemed to be paved for XRL: it had all the crucial elements necessary to satisfy industrial requirements and accompany microelectronics for many years along the innovation steps forecast by Moore's law. Almost all the crucial elements were matched from XRL: all except one! No refractive lens in the X-ray region exists that is capable of focusing X-ray radiation with high efficiency, and this fact has a series of consequences that will become evident below.

Unlike with UV projection lithography, where a system of lenses is used to project a demagnified image of the mask pattern, the same technique is not possible for lithographic technology based on X-rays. In fact, Fresnel lenses, also known as

"zone plates", can be used to focus X-rays but are limited in diameter (~1 mm) and have a multiplicity of focal spots, corresponding to different diffractive orders, with rather low efficiency (~10% up to 30% in the best cases) [FEN 07]. Moreover, zone plates are highly chromatic optical devices, with a focal length depending on the wavelength of λ^{-1}. Using them to build a projection system would imply the use of monochromatic X-rays to ensure the formation of a demagnified pattern image, in focus, on the substrate. All these problems make X-ray radiation incompatible with the concept of projection lithography.

The development of XRL thus needs to accept proximity as a working configuration, i.e. the mask is placed in close proximity with the surface of the target substrate without interposed optical elements. In this case, a one-to-one replica of the mask pattern is obtained by a simple shadow printing process. The fact that XRL is a proximity lithography has two main consequences from the viewpoint of mask fabrication and alignment. In the case of UV projection lithography, mask fabrication is simplified by the fact that the pattern has to be written on a larger scale to pre-compensate for the rescaling by the demagnifying optics during exposure. In modern steppers, this fact relaxes the typical resolution at which a mask is written by a factor of 4 or 5. Secondly, the tolerances (mask distortion and placement errors, and alignment accuracy) are relaxed by a factor of 4 or 5. In X-ray lithography, the features are instead printed at the same scale as they are on the mask, which makes the lithographic steps for producing the mask much more challenging, and makes the entire process of pattern replication more prone to placement errors or pattern distortion in the mask, which are transferred onto the target substrate at the same scale.

In fact, during the development of XRL technology, several problems began to emerge, the most severe of which related mainly to aspects of the X-ray mask. The latter consists typically of a pattern in a strongly X-ray absorbing material (Au, W, Ta) supported by thin membranes of SiC, Diamond or SiN_x that, for transparency reasons, are just a few micrometers thick and extend over areas of several square centimeters (in order to fit the entire pattern of a chip in a single undivided window). Given the small ratio between thickness and the lateral dimension, the membranes are inevitably prone to distortions. In particular, the main problem is represented by the distortion of the pattern caused by the residual stress in the absorber deposited on the membrane. An additional source of distortion is represented by thermal expansion [DZI 96] which is induced by the heat that the absorbed radiation causes to the mask.

Compensating all sources of pattern distortions proved to be extremely challenging. In fact, the positioning and registration accuracy of two subsequent lithographic levels of over a number of square centimeters has to remain within the

required margin of error, a requirement that today, for microelectronics standards, is of the order of ~10 nm.

A further problem, again related to the mask, is lifetime. Masks are required to last months in order to reproduce the same pattern several thousands to several millions of times. The damage caused by protracted exposure to ionizing radiation and the risks connected to the handling and operation (typically the membrane has to be kept at a distance of 5-10 μm from the substrate in order to keep the diffraction effects low) creates serious risks for the long term survival of the mask. In fact, the membrane can easily be broken by a dust particle that might be present on the wafer when the mask is moved towards it for the exposure.

For several years, X-ray was evaluated as next generation lithography, trying to circumvent all problems and limitations, implementing solutions of increasing complexity. In the meantime, UV projection lithography has continued to serve the purposes of the semiconductor industry, down to the 45 nm node (where '45 nm' refers to the average half-pitch of a memory cell manufactured at that technology level) and will presumably continue down to the 32 nm node with the aid of a variety of additional techniques, such as larger lenses, wavelength reduction by liquid immersion and double patterning. Eventually, the discouraging battle with UV projection lithography was finally lost and XRL was abandoned as being unfit for the purposes of the semiconductor industry.

However, this is just one and probably not the final chapter of the XRL story. As has often happened in the history of science and technology, when all attempts have been made to develop a technology for a very ambitious target, even if that target is not achieved, the technological solutions developed can sometimes be unexpectedly used to target new objectives in different fields of application. XRL failed to satisfy the requirements of the electronics industry. Nonetheless, XRL showed absolutely remarkable properties that make it uniquely suited for many specific purposes in nanodevice design and fabrication. XRL can certainly be considered the best lithographic technique with respect to penetration depth in thick resists and high aspect ratios patterns. It is a unique technique for generating some types of 3D micro- and nanostructures by single or multiple tilted exposures on multi-layer resists. Already, in the fields of micromechanics and optics, LIGA technology, which is based on X-ray lithography with hard X-rays (λ ~0.1 nm), has been used effectively and offers advantages with respect to other competing technologies.

The possibility of X-rays finding niche applications due to the peculiarities of this lithography is possible, avoiding competition with DUV lithography in the field of microelectronics but opening a new frontier of competition in new and innovative applications.

In this chapter we will try to provide a self-consistent description of the key physical concepts and the technology of X-ray lithography, followed by a series of examples and applications. The chapter is organized as follows. The principles of XRL are reviewed and the relevant physical phenomena discussed, in particular the absorption and propagation of X-rays, the equipment used, the role of diffraction in image formation, the interaction of X-rays with matter, and the mechanism of exposure of a resist by X-rays. The fabrication of X-ray masks is described in some detail. Aware that the opportunities for X-ray lithography to be used in the mass production of integrated circuits by the electronics industry have almost vanished, the main focus of the final section is devoted to those applications for which X-ray appears to offer important competitive advantages over all other lithographic technologies. Of particular interest is the technical potential that XRL offers in the field of micromachining, microfluidics and 3D nanopatterning.

1.2. The principle of X-ray lithography

X-ray lithography (XRL) belongs to the class of parallel lithographic techniques, along with UV, deep UV and extreme UV lithography, nanoimprinting, micro contact printing lithography, casting, injection molding, and others. This means that the pattern cannot be originated, just replicated. All constituent points of the pattern are addressed at the same time, and the process is typically fast. However, the pattern has to be first encoded into an object (called a mask) and then transferred entirely in one single parallel step.

X-ray masks consist of absorbing patterns supported by a transparent mask-carrier, which has a weak absorption of X-rays in the range of photon energies required for exposure. They are typically made by patterning by Electron Beam Lithography (EBL) and auxiliary techniques. The process of pattern replication consists of exposing the resist (polymeric material which changes its dissolution rate in a liquid solvent, called a developer, under high energy irradiation) through the mask containing the pattern. Where the beam is not stopped by the adsorbing material, it is transmitted by the membrane and exposes the resist deposited on the target substrate. The resist is defined as positive if the exposed part dissolves in the developer, and defined as negative if it crosslinks upon exposure and the unexposed parts dissolve in the developer. In both cases, after development, the resist exhibits, as a first approximation, the same geometrical features as the original pattern on the mask (see Figure 1.1).

When a feature size approaches the 100 nm scale length, a highly spatially coherent X-ray radiation subjected to a phase and amplitude modulation by high resolution features on the mask leads to a diffracted field that varies, propagating along the gap present between the mask and the target substrate. Therefore,

lithographic structures of higher complexity and which are more difficult to be quantitatively explained can be generated.

The XRL technique can only be implemented effectively employing synchrotron radiation sources, which ensure the desired brilliance and collimation of the X-ray beam.

In the following section, XRL is described from the theoretical point of view (characteristics of synchrotron radiation, how phase and intensity of X-rays are altered by interaction with matter, what happens at the resist upon irradiation, the diffraction effects, and how to select the optimal photon range to obtain the desired final structure). Technical aspects are also addressed: how an XRL beamline works, how it is possible to obtain a uniform exposure of the resist, how to prepare a mask. Finally, some examples of microstructures and microdevices fabricated by DXRL are presented.

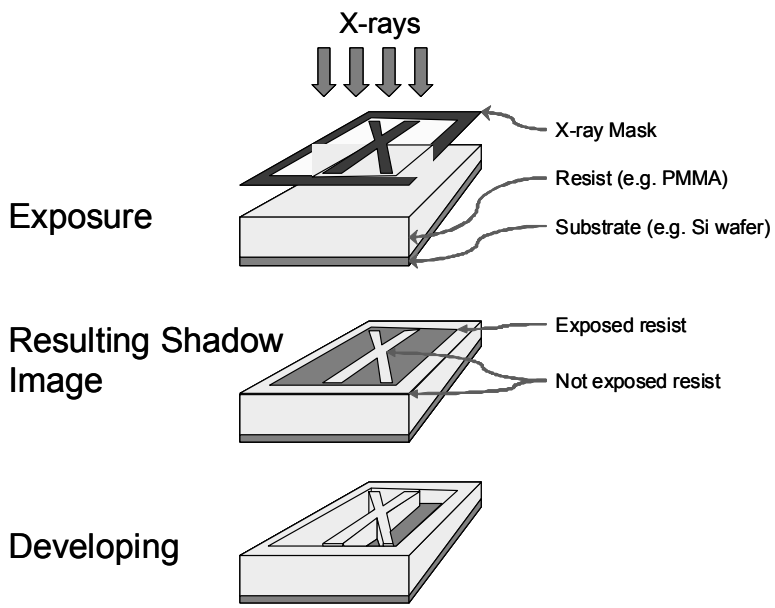

Figure 1.1. *Principle of X-ray lithography, considered to be a parallel writing of a shadow image of a mask using X-rays as the impinging radiation. After exposure, the resist changes its dissolution parameters in a solvent called a developer, and is removed leaving the surrounding pattern in the not-exposed material (a positive resist)*

1.2.1. The irradiation system for XRL

As already mentioned, X-ray lithography is essentially a shadow printing process. Patterning is obtained by means of local chemical changes induced in a radiation sensitive material (a resist) by a spatially modulated X-ray beam. The XRL process comprises three basic steps: (i) irradiation (or exposure); (ii) resist development; and (iii) pattern transfer. The step that mainly characterizes XRL is that of irradiation, for which very specific types of tools (radiation sources, steppers), masks and technical solutions are employed, all very distinct from those in use for all other lithographic technologies. Irradiation is also the step that most affects the quality of the XRL results. Optimizing the irradiation involves optimization of the characteristics of the mask, accurate control of the mask/target substrate gap, selection of the spectral range of radiation and of the total dose delivered to the resist.

By contrast, the resist development step, performed typically in organic solvents, and the subsequent pattern transfer, obtained by additive (lift-off, electroforming, ion implantation) or subtractive (dry and wet etching) methods, do not differ significantly from the corresponding steps in other lithographic technologies, and will therefore not be discussed in detail here.

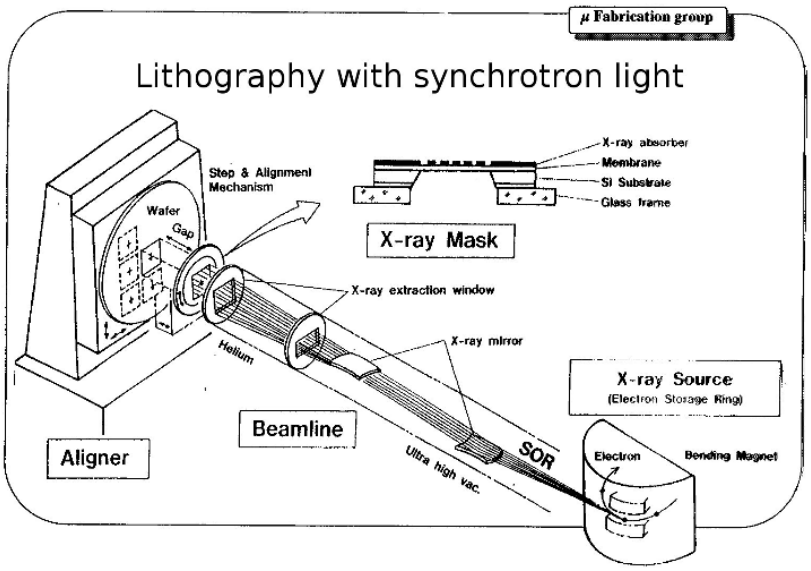

Figure 1.2. *Typical X-ray lithography setup at a beamline station. The radiation from the bending magnet is guided through an evacuated tube to the lithographic station. A series of X-ray mirrors and filters are introduced to shape the beam and select the energy spectrum [DEG 96]*

The main characteristics of X-ray radiation (namely spectral range, beam divergence, spatial and temporal coherence, and power) are determined by the type of source selected for the exposure. Since synchrotron radiation is outperforming all other types of X-ray radiation sources on all relevant aspects for an advanced use of XRL, we will limit ourselves below to a discussion of this source. A schematics of the typical X-ray lithography setup in a storage ring is presented in Figure 1.2 [DEG 96], showing a series of elements interposed between the X-ray source and the mask for filtering the spectrum and for shaping the beam. Typical setups comprise the following elements: source; filters; mirrors; slits-windows; stepper or scanner; and mask/sample assembly.

The radiation produced by a synchrotron radiation source (typically a bending magnet inserted in the trajectory of a high energy electron beam, see below) propagates inside an ultrahigh vacuum beamline. The length of a typical beamline is in the range of tens of meters, which allows the electromagnetic (e.m.) waves to be considered, to a first approximation, as planar at the surface of the membrane of the X-ray mask. Along the beamline, the radiation interacts with a series of different optical elements. Neglecting the unavoidable scattering of X-rays by the residual gas molecules in the beamline, the beam can be allowed to pass through a series of foils of different materials and to impinge on one or more mirrors necessary to select the wavelength spectral window, before reaching the mask.

In fact, synchrotron radiation sources are able to deliver X-rays covering the entire energy range suited to XRL and, in particular, bending magnets can cover a range from the infrared to few tens of keV. However, this is too broad to provide controlled conditions for lithography. Whilst the hard X-ray region with photon energies higher than 5 keV (and up to 10 keV) can be very useful for exposing sensitive materials thicker than hundreds of microns, the highest lithographic resolution can only be achieved by the so called “soft X-ray lithography” (a name that has become synonymous for High Resolution XRL), in the spectral range between 1 and 2 keV.

Many setups have been proposed for the beamline optics. The simplest ones, for example, allow the beam to be delivered directly as generated from the bending magnets source, just filtered with different foils of material of calibrated thickness. These act as high energy pass filters, that is, they cut out the low energy part of the spectrum [XU 01, DIF 99].

In more elaborate setups, the first element the beam impinges on is typically a mirror (or a couple of mirrors), which redirects and reshapes the beam and filters out the high energy part of the spectrum (that is, it acts as a low energy pass filter). The working principle of X-ray mirrors exploits the phenomenon of total external reflection that will be briefly addressed in this chapter. (In X-rays,

the refraction index is lower than 1 which determines that total reflection takes place passing from a lower density to a higher density material).

The combination of mirrors and absorbers represents band pass energy filters that enable the tuning of the spectral distribution of the photon flux employed in the exposures. A beryllium window is generally present to isolate the part of the beamline under high vacuum conditions (10^{-9} mbar or better) and the part of the beamline which is fluxed with helium at a pressure of 1 atm and open to the external atmosphere. In fact, for practical reasons masks and substrate are not kept under the UHV conditions of the beamline, which would make changing the target substrate or mask unpractical. Therefore, the handling of mask and target substrate is always done in a normal atmosphere; however, during exposure, helium is introduced in a final section of the beamline so as to remove the strongly X-ray absorbing atmospheric gases (such as oxygen, nitrogen and water vapor) from the trajectory of the X-ray beam, also keeping the mask and target substrate under the same He atmosphere. The helium also serves to stop or slow down high energy photoelectrons generated by the interaction of photons with the mask that otherwise would cause unwanted exposure of the resist.

1.2.2. Properties of synchrotron radiation

At present, the most mature X-ray sources are third generation synchrotrons. Whilst a fourth generation of synchrotron radiation sources is under development (the so called free electron lasers [NUH 04]), the conditions provided by third generation sources appear already very satisfactory for lithography, in various respects (intensity, low beam divergence, spectral distribution, source size). Other X-ray sources such as X-ray tubes, or hot dense plasma sources [ATW 99], are not comparable to synchrotron radiation and we will not consider them here.

Though a detailed treatment of the physics and technology of synchrotron radiation is well beyond the scope of this chapter (interested readers are referred to a number of different reviews of the topic [WIE 02, MAR 02, MIL 02]), we will briefly summarize a few relevant aspects for a better understanding of what follows.

In synchrotron radiation sources, radiation is generated at the points where the trajectories of “bunches” of ultra-relativistic electrons injected along the storage ring are bent by a magnetic field (the most simple device is represented by bending magnets, which produce a single deflection of the beam, whereas other devices, e.g. “undulators” and “wigglers” produce multiple deflections). The emitted radiation travels inside long tubes in an ultrahigh vacuum and reaches a laboratory where setups for various type of experiments can be installed (such laboratories connected to an X-ray beam are generally referred to as “beam lines”).

The spectrum of the radiation emitted at a bending magnet depends on the electron energy and on the intensity of the magnetic field (or is equivalent to the radius of curvature of the electron trajectory), and can be parameterized by a single value, known as critical energy:

$$E_c = \hbar\omega_c = \frac{3e\hbar B}{2m}\gamma^2 \qquad [1.1]$$

where $\gamma = \frac{E_e}{mc^2}$ is the energy of the accelerated electrons in the storage ring normalized to their rest energy. All curves representing the photon flux from a bending magnet can be superimposed on each other if plotted against the photon energy normalized to the critical energy E_c, and after normalization to their total intensity. Therefore, by knowing the critical energy and the total intensity (which depends linearly on the current circulating in the ring) it is easily possible to obtain the photon flux at any given energy.

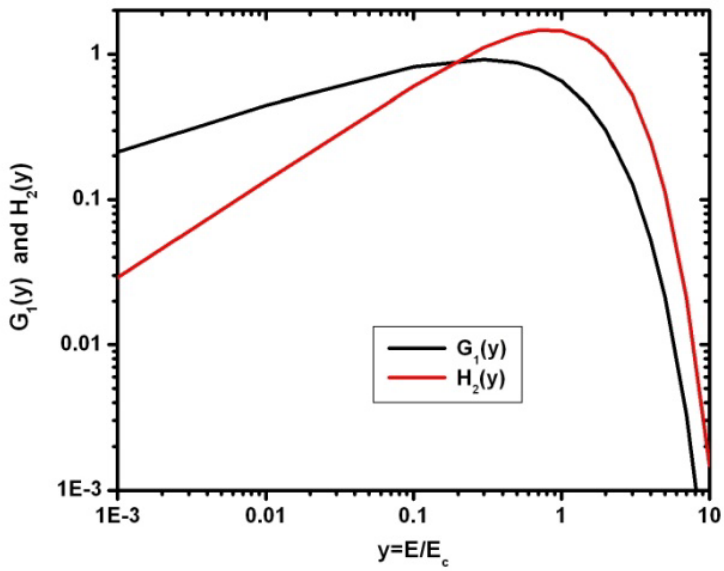

Figure 1.3. *The function* $H_2(y)$*, representing on-axis photon flux from the bending magnet, and* $G_1(y)$*, representing the vertically integrated photon flux, as functions of the photon energy normalized to the critical photon energy*

The lower end of the spectrum is in the IR wavelength regime (in principle the spectrum extends at lower energies but with negligible intensity). The flux raises smoothly as a function of photon energy until critical energy E_c, and then drops rapidly (Figure 1.3).

In physical units, the critical wavelength, corresponding to the critical photon energy is given numerically by:

$$\lambda_c(nm) = \frac{1.864}{E_e^2(GeV)B(T)} \qquad [1.2]$$

where the wavelength is given in nanometers, the magnetic field in Tesla and the electron energy in Gigaelectronvolts (GeV). At the Elettra Synchrotron in Trieste (Italy), for example, two operational regimes are possible corresponding to electron energy of 2.0 and 2.4 GeV, for which values of 1.2 T and 1.45 T are selected for the bending magnets, respectively; these operational modes are alternated several times during the year to provide optimal conditions for different kinds of experiments. Therefore, the critical wavelength in these two operational regimes are 0.39 nm and 0.22 nm corresponding to a critical energy of 3.2 keV and 5.6 keV, respectively.

The radiation from a bending magnet is emitted mostly within a narrow cone of angular aperture γ^{-1} (rad), whose axis is directed along the instantaneous direction of the electron trajectory.

Since the trajectory is circular in the presence of a magnetic field, the emission cone sweeps a "wide" angle, corresponding to the deflection that the electron beam has undergone in the horizontal plane due to the action of the bending magnet. Slits along the beam line are introduced to delimit the width in the horizontal plane of the source. This results in a horizontal "stripe" of radiation that, far from the source, in the experimental station, is typically of 10–50 mm in the horizontal direction and of the order of ~0.5–5 mm vertically.

The exposure of larger areas is obtained by vertically scanning the mask and substrate assembly, held together at a fixed relative position. Scanning the mask/substrate assembly is also fundamental for performing a spectral and intensity average of the photon beam. In fact, while the latter can be considered uniform with respect to the spectral composition and intensity in the horizontal direction (as a result of the superposition of the emission cone at different angles due to the bending of the electrons' trajectory), in the vertical direction it is highly non-uniform, with maximum intensity and harder spectral composition concentrated on

the axis of the emission cone). The difference between the "on-axis photon flux" and the "vertically averaged photon flux" is shown in Figure 1.3.

1.2.3. High Resolution and Deep XRL

Conventionally, XRL is sub-divided into High Resolution XRL (HRXRL) and Deep XRL (DXRL), the latter also known as LIGA when associated with a subsequent step of electroplating and molding (the LIGA acronym derives from the German "LIthografie Galvanofomung und Abformung", i.e. lithography, electroforming and molding) [BEC 86, EHR 95].

HRXRL is devoted to the fabrication of devices with features of a resolution down to a few tens of nanometers, for applications ranging from electronics to photonics and nanomechanics. DXRL (or LIGA) addresses the fabrication of "tall", high aspect ratio structures, with smooth and precise vertical sidewalls, but at lower resolution (few hundred of nanometers), such as is needed for some types of Micro Electro-Mechanical Systems (MEMS), for optics or, more recently, for microfluidics.

Technically, the main difference between them consists of the selected spectrum of the radiation used: while high resolution XRL requires relatively low energy photons (1–4 KeV, λ ~0.3–1.2 nm) distributed within a narrow band, Deep XRL uses a broader and harder spectrum (2–12 KeV), that allows a deeper penetration into materials up to the millimeter range. Today, the flexibility of X-ray beamlines allows both the central energy and bandwidth of the X-ray beam to be selected [ROM 01], and the distinction between DXRL and HRXRL is perhaps less meaningful, given that the best experimental conditions can be selected almost continuously for any specific application, resist thickness or feature size. However, we will maintain this terminological distinction, as it is of widespread use.

1.2.4. Examples of X-ray lithography beamlines

The layout of a beamline for X-ray lithography can be very simple. For Deep X-ray lithography, the beamline consists only of an evacuated tube including valves, filters and windows to protect the vacuum system for the storage ring. The lithography station is positioned a far distance away (about 20 m) from the source (see F. Pérennès *et al.* [PER 01]).

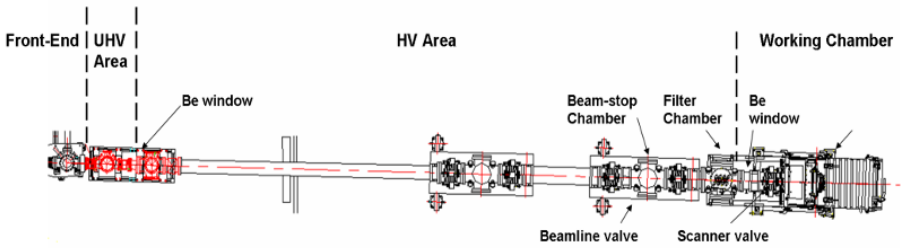

Figure 1.4. *Layout of a beamline (tangential to the synchrotron ring) from the front end to the scanner station*

Just after the front end of the storage ring, a beryllium window separates an ultra high vacuum section (connected to the storage ring, at a very low pressure of 10^{-10}–10^{-11} mbar) and the high vacuum beamline, in which a lower level vacuum is needed. Filter and beam stoppers are used in order to have a minimum amount of control of the beam. The radiation reaches the experimental chamber, where the scanning stage is located, passing through the HV zone (10^{-8}-10^{-9} mbar) and through two chambers in series. One chamber typically accommodates a beam stop where the hardest part of the X-ray spectrum can be removed from the beam by interposition of a thin opaque horizontal strip (a beam-stop), and the central part of the beam is blocked. The beam stop absorbs a large part of the incoming beam reducing the total power impinging on the mask and therefore reducing the thermoelastic deformations of the pattern [NEU 97].

In a second chamber, absorber membranes made of different materials and of different thicknesses allow the low energy part of the beam spectrum to be absorbed selectively, thus acting as a high energy pass filter to tailor the spectrum and the flux that reach the sample under exposure. The physics principles describing the X-ray absorption from the thin films is reported in the sections below.

A major improvement in controlling the spectral composition of the X-ray beam is obtained in beamlines which combine mirrors and absorber foils [ROM 01]. The combination of low and high energy band pass results in a continuous, adjustable band pass energy window that allows a spectrum that optimizes contrast, resolution and resist penetration to be selected for each exposure.

Figure 1.5 shows a sample configuration of the layout of the LILIT beamline settings at the Elettra synchrotron. The beamline consists of one plane mirror (M1) and of a second toroidal mirror. The total length of the beamline is 13.3 m and the angles under which the synchrotron radiation is collected have been fixed at 6 mrad and 0.83 mrad (3σ), respectively, in the horizontal and vertical planes. The latter value corresponds to the natural divergence of the synchrotron radiation in the soft X-rays range under the standard operating condition of the beamline. A beryllium window and an additional energy filter are located before the plane mirror. Further adjustable slits for beam shaping and a photon shutter are placed after the toroidal mirror close to the end of the beam line where, after a second beryllium window, the X-ray beam is delivered for exposure in a helium flux at atmospheric pressure.

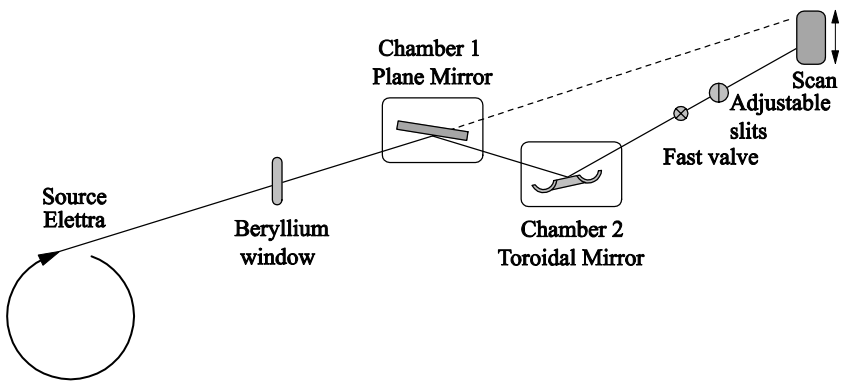

Figure 1.5. *Layout of LILIT beamline at Elettra Synchrothron (Trieste, IT) [ROM 01]*

The mirrors perform a low energy pass filter action and are typically made of silicon coated with a low roughness gold film, typically of the order of 0.5 nm. For a given angle of incidence their reflectivity strongly depends on the wavelength of the X-ray beam.

The value of ϑ_1 can be freely chosen in a range from 0.3 to 2.8 degrees; however, the amplitude of ϑ_2 and the height of second mirror are determined by the constrains imposed by the fixed height from the ground of the source and by the desired beam spot size. Figure 1.6 displays the beam energy spectrum as a function of angle ϑ_1 (ϑ_2 being automatically determined) and shows that the spectral region of interest can be selected. In fact, an increase of the angle ϑ_1 decreases the mirror reflectivity of the lower wavelengths, and provides a rejection of the hard part of the spectrum energy (acting as a low-pass filter). A soft energy spectrum (1–2 keV) is indicated for the best lithographic resolution.

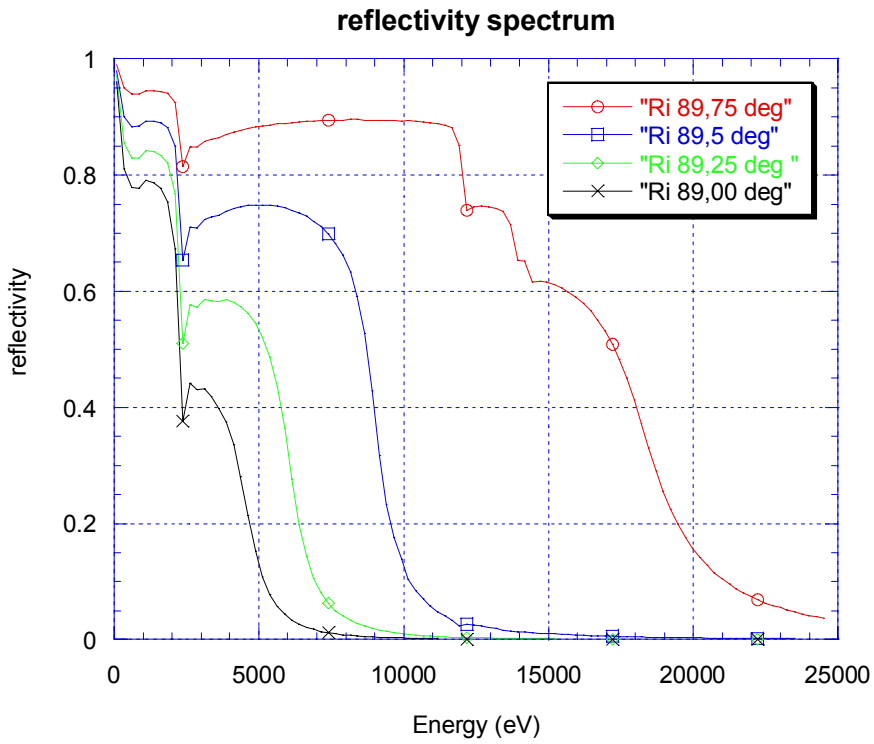

Figure 1.6. *Calculated reflectivity spectrum of the beam as it emerges from the planar mirrors at varying* ϑ_1 *angles*

By contrast, high energies are necessary for deep lithography where the requirement of a high aspect ratio can be obtained reducing the lateral resolution [CAR 98]. In that case, the rejection of the low energy part of the spectrum is performed by a series of eight films of different materials (C, SiC, Cr, Cu) and different thicknesses that are accommodated on two different slits. These can independently intercept the beam providing 16 combinations of different high band pass filter energy.

Figure 1.7 shows the transmittance spectrum in the range of energy interesting for X-ray lithography, providing the effect of a high energy band pass performed by different thin films made of different materials and of different thicknesses. It seems clear that by controlling the thickness and using different materials, an almost continual tuning of low band energy can be achieved. We have simulated the effect of increasing beryllium (Be) thickness up to 300 microns which allows a fine tuning

of the high pass cut off around 2 keV. A higher cut off requires heavier materials and/or greater thicknesses. Cut offs of around 6–8 keV are very useful for deep X-ray lithography in order to obtain homogeneous depth penetration of incoming energetic radiation.

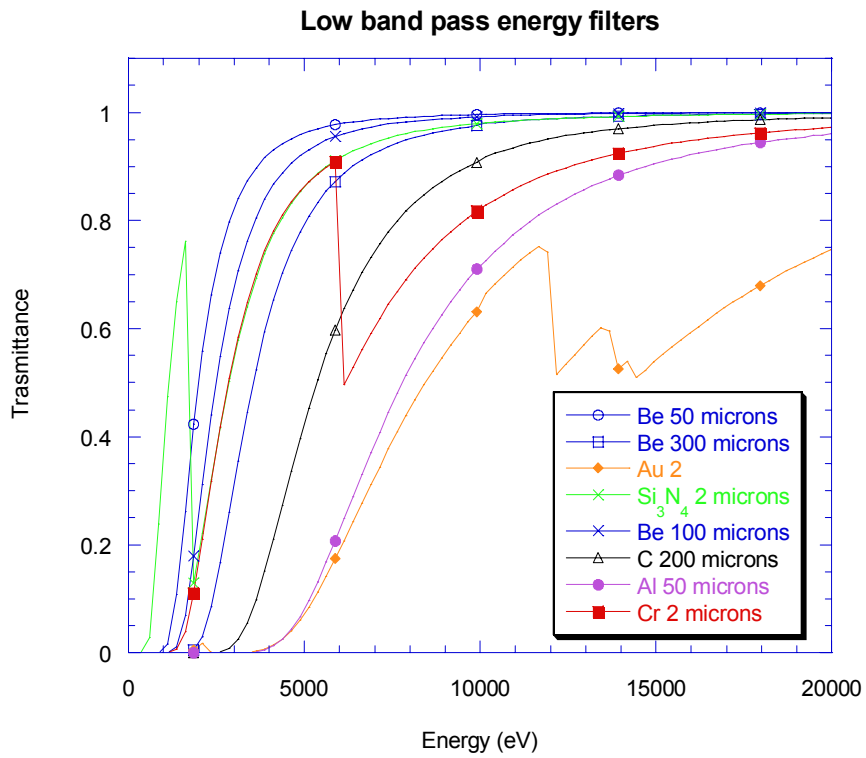

Figure 1.7. *Transmittance values for different materials at different thicknesses, as a function of a photon's energy*

It is interesting to note that filters show abrupt steps in the transmittance correspondence with the atomic absorption thresholds of the material with which they have been made. For example, at 1838.9 eV, silicon nitride has a strong absorption due to K1 line of silicon. That is quite important to notice because X-ray masks often use silicon nitride membranes where a gold absorber is patterned. Chromium has a K1 edge at 5989 eV, whereas gold has a strong absorption at 11.919 eV of L3 edges.

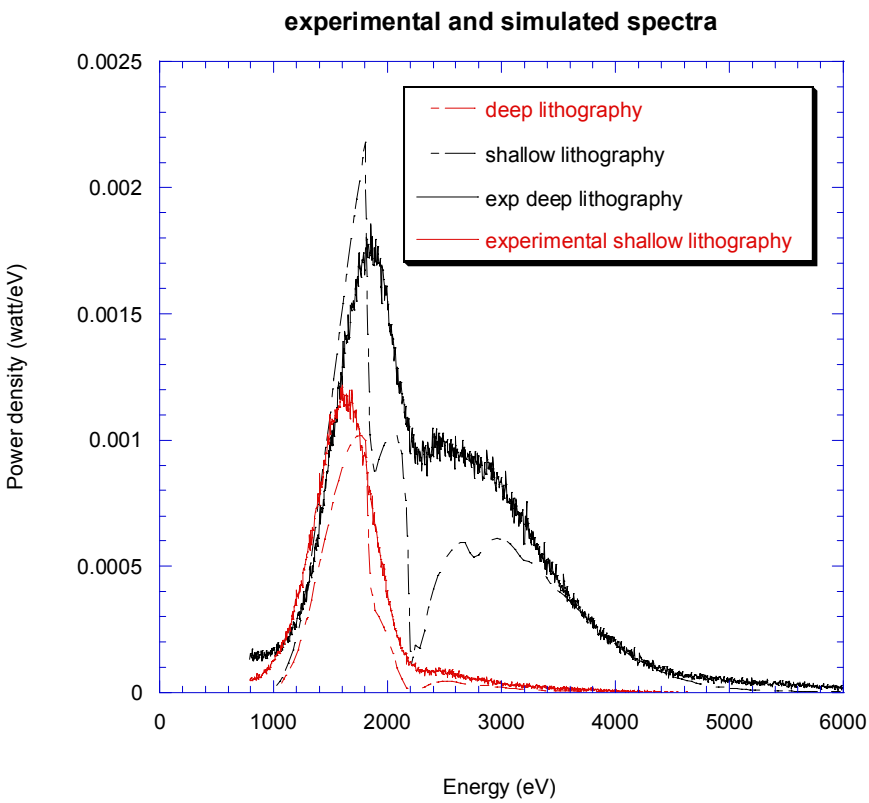

Figure 1.8. *Power emitted by the LILIT beamline at the Elettra synchrotron, corresponding to two different settings of the beamline mirrors (calculated and measured experimentally) and with or without Beryllium foils as absorbers. The broad tuning capability of the photon spectral distribution can be exploited for the exposure of different resist film thicknesses for "shallow" (~ 1 μm) and "deep" (> 10 μm) lithography*

The idea of combining high and low energy passes allows an energy band pass to be obtained. Typical examples are shown in Figure 1.8 where the experimental and simulated spectra are compared for two configurations. A spectrum with a wider energy distribution is more suitable for deep X-ray lithography for a medium resist (of the order of 5–15 μm). The softer spectrum is more suitable for high resolution lithography and thin resists (<300 nm).

1.2.5. Scanner/stepper

The spectral composition and flux of an X-ray beam depends on the precise direction at which photons are collected within the emission cone of $\gamma^{-1} = mc^2 / E$ radians. Therefore, the exposure of a sample in static conditions would produce a non-uniform dose as a function of the relative position of the irradiated area of the resist, with respect to the center of the beam. While horizontally the intensity and spectral distribution is averaged by the sweeping of the electrons in the plane of their orbit, the non-uniformity in the vertical plane can be averaged out by vertically scanning the mask–resist assembly across the beam. In this manner, uniform exposure doses (with residua1 variation of the order of 1%) can be obtained over rectangular areas with dimensions of a few centimeters.

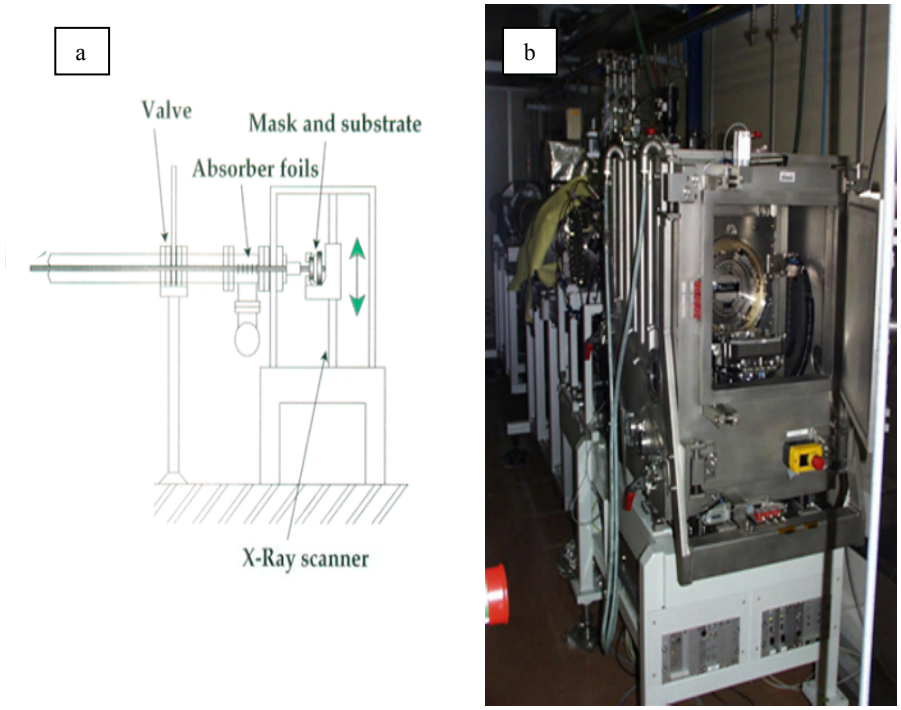

Figure 1.9. *(a) A simple sketch of a scanner, showing the vertical sweeping of the mask-sample assembly, which provides the averaging of the dose applied; (b) the actual X-ray scanner at the DXRL beamline, Elettra (Ts, Italy)*

Ideally, a scanner should be able to allow alignment, fine control of the gap, tilt and rotation of the mask–resist assembly with respect to the beam. Easy handling of the mask and substrate mounting are also requisites for such apparatus. For industrial applications for which repeated exposures of the same pattern (dye) on different areas of the same substrate are required, step and repeat processes are used. Pieces of equipment that allow step and repeat operations to be performed are called steppers. The experimental chamber can be evacuated at a low vacuum of 1 to 10 mbar and fluxed with He at low pressure (of up to 100 mbar), which provides an efficient dissipation of the heat generated during irradiation but avoids a strong reduction of the intensity of the X-ray beam that would happen if other gases (such as O_2, N_2, Ar) were used at the same pressure for the same purpose.

A very simple sketch of a scanner is shown in Figure 1.9, together with a picture of the Jenoptic scanner used at Elettra in its DXRL beamline [PER 01].

1.2.6. The mask

The role of masks in X-ray lithography is to select where the impinging radiation is allowed to reach the resist and where it is not. This section addresses some of the main technical issues in the fabrication of masks, while a deeper discussion concerning the physics of the interaction between radiation and matter (on which their working principle is based) can be found elsewhere in the chapter.

A mask typically consists of a patterned absorber layer (usually a heavy metal such as gold) and a plate or a membrane supporting it, made of a weakly absorbing material with low-atomic number. Beryllium, carbon (amorphous or glassy graphite) and polyimide are suitable substrates with thicknesses ranging from about 50 to 1000 μm, mainly for use with hard X-rays, while thin membranes (0.5 to 4 μm) of silicon nitride, silicon carbide, diamond (Diamond Like Carbon (DLC)) are used with softer radiation. The absorption coefficient as a function of wavelength is shown in Figure 1.11 [BAU 94] for some common materials used for X-ray mask membranes.

The major issue in relation to masks is certainly represented by the requirement that the supporting plate or membrane remains as undistorted as possible against the effect of stress introduced by the absorber layer. In fact, the absorber layer usually has an inner residual stress that, once patterned, induces a non-uniform strain in the membrane, resulting in a distortion of the pattern itself. This effect might be extremely detrimental to the process of alignment of subsequent lithographic levels. Moreover, the membrane has to be highly stable against the distortions caused by heating (i.e. thermal expansion) during irradiation.

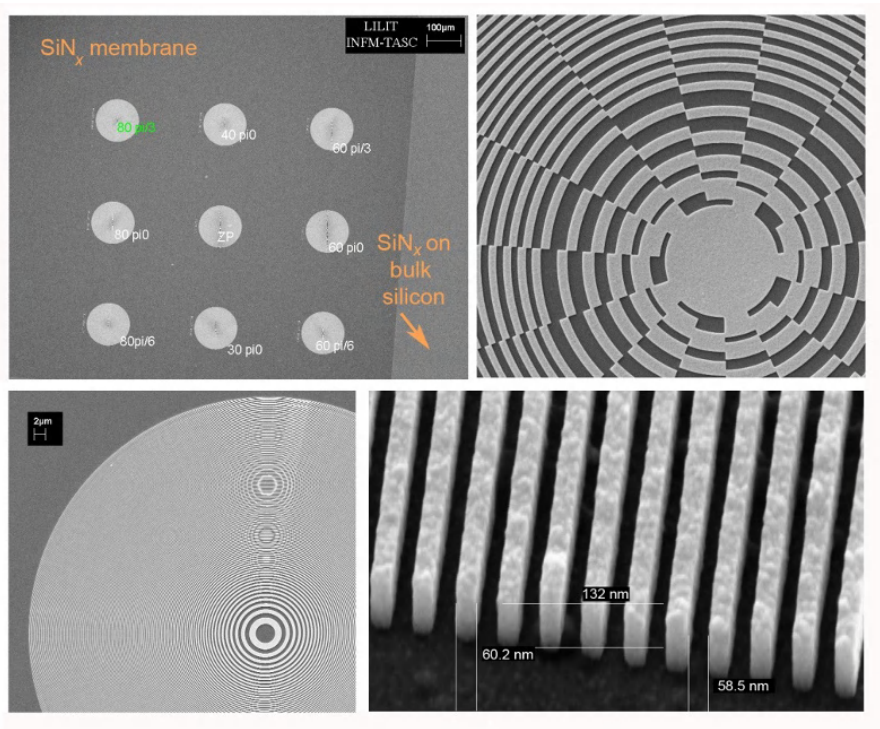

Figure 1.10. *SEM micrographs of XRL masks. Different pattern of diffractive optical elements fabricated by electron beam lithography, and electroplated with gold on a silicon nitrate membrane are shown in the low magnification image (a zone plate in the center surrounded by special elements for Differential Interference Contrast (DIC) microscopy). The other images shows details at various magnifications*

The problem of pattern distortion concerns both Deep and High Resolution XRL, but with different degrees of importance. In the case of Deep XRL the effect is somewhat less severe because of the fact that a much thicker substrate can be chosen (due to the higher penetration depth of the harder spectrum that is used) than the thin membranes used in High Resolution XRL. Moreover, Deep X-ray lithography addresses applications requiring lower lateral resolutions, resulting in a relaxation of the tolerances for subsequent pattern registration.

Beryllium and diamond are among the most favored materials used as mask substrates because of their high X-ray transparency (Figure 1.11) and good mechanical properties (Table 1.1). Beryllium [FEI 95, EHR 86, SCH 91] has slightly poorer mechanical and thermal properties than diamond, but due to its extremely low absorption (enabling the use of substrates about 10 times thicker than diamond)

it would be the first choice material, if it were not for the special safety measures required for its working and handling, due to its toxicity. Diamond is also an excellent material, though very expensive. The most common choice is silicon nitride (Si_3N_4) or silicon carbide (SiC), both of which guarantee a good compromise between properties and cost. For low demanding LIGA applications not requiring the overlaying of subsequent lithographic levels, one possible low cost choice for a substrate is polyimide.

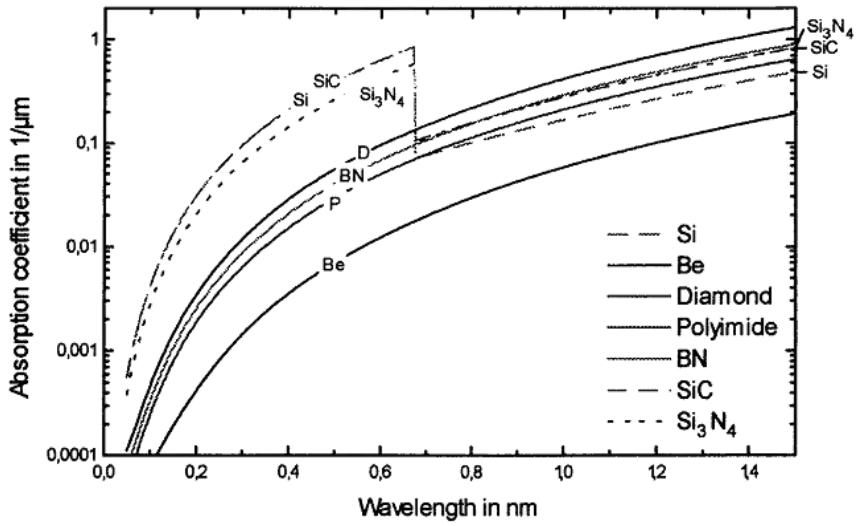

Figure 1.11. *Absorption coefficient of selected materials suitable as XRL mask substrates*

Membrane material	Young's modulus [GPa]	Heat conductivity [W/mK]	Thermal expansion [$*10^{-6}K^{-1}$]
Be	318	205	11.3
Si_3N_4	320	19	2.8
Diamond	1000	900	1.1
Polymide	2–3	0.1–0.35	30–60

Table 1.1. *Mechanical and thermal properties of some suitable materials for mask substrates. Data reproduced from D.W.L. Tolfree [TOL 98]*

The other material that a mask is made of is an absorber. A contrasted shadow pattern can be achieved by interposing high atomic number materials (Au, Pt, W, Ta, either as pure elements or alloyed with others) along the trajectory of the X-ray beam. The choice of the material to be used as a mask absorber is mainly dictated by the type of technological processes selected for their deposition on the substrate and for the patterning. Two different strategies are possible. The first, based on an "additive" process, consists of "adding" the material to the substrate after defining the pattern, which serves as a template for the electrolytic growth of the absorber. The other strategy is based on a "subtractive" process by plasma assisted etching. In this latter case, the absorber structures are obtained by "subtracting" material from a film. This is obtained after patterning a resist film on top of the absorber, which selectively protects areas that are required to be saved from the action of the plasma etching process. The first strategy (the additive process) is convenient for materials for which a plasma etching does not exist or does not work reliably, and for which an electroplating process exists which can be finely controlled exists instead. Gold is the most convenient material for this "additive" strategy. By contrast, materials like tungsten [KAR 87, KU 91], tantalum and their alloys (tungsten or tantalum carbides, nitrides, or silicides) can be etched accurately, with precise vertical sidewalls, using plasmas based on the chemistry of the fluorine.

The wavelength dependent absorption coefficient of convenient X-ray absorbers is shown in Figure 1.12.

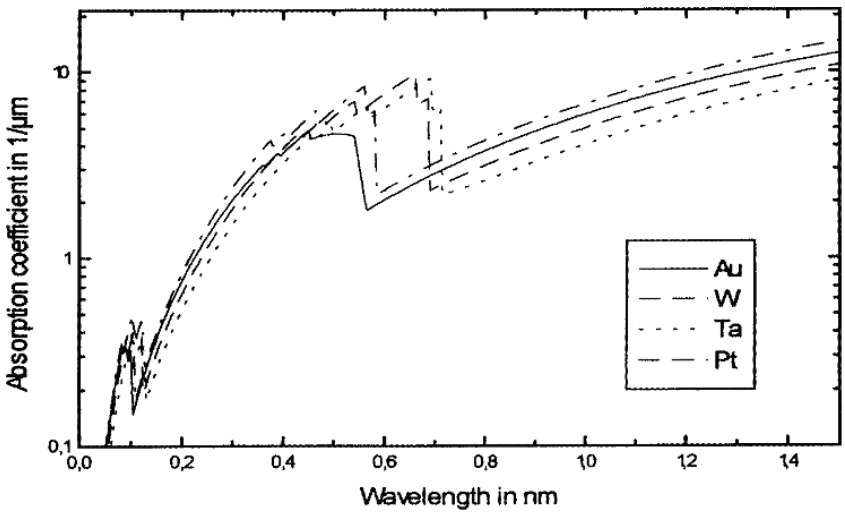

Figure 1.12. *Absorption coefficient of selected materials suitable as XRL mask absorbers*

The value of the absorption coefficients is one of the guiding parameters in the selection of the material and of the absorber thickness. From it, we can see that 1 µm of gold would reduce the radiation intensity down to ~ $e^{-3.5}$, i.e. to the ~3% of its initial value with 0.5 nm wavelength radiation, while down only to ~ $e^{-0.6}$, i.e. to the ~55% with X-rays of 0.2 nm wavelength. This explains why the highest lithographic resolutions with XRL are not achieved with a very short wavelength. Naively, one might perhaps expect that with very a short wavelength radiation (~0.1 nm) the lithographic resolution limit could be improved with respect to that obtained with softer radiation (let's say ~0.5 nm), because of the reduced diffraction effects. However, a practical limitation arises. While the production of, for example, 50 nm wide features (such as dots or lines) of a thickness of 300–400 nm, sufficient to stop 0.5 nm wavelength radiation, is challenging but yet possible, the fabrication of 50 nm wide features of more than 10 µm thickness (with aspect ratios of 200) to stop 0.1 nm wavelength radiation would clearly be beyond the technical capabilities of nanofabrication technologies.

The fabrication of masks is performed in a series of steps, which depend on the materials chosen for the blank and absorber [EHR 86, MAL 96, CAB 05]. Below, we briefly discuss a fabrication scheme for an X-ray mask for hard and soft X-ray lithography, using silicon nitride as the supporting membrane and gold as the absorber. Figure 1.13 illustrates the sequence of steps.

Using gold as the absorber implies (as we have described above) the choice of an "additive" strategy for the fabrication process, where patterning is performed before the deposition of the absorber. The patterning can be done by several techniques. When a high resolution is required, Electron Beam Lithography (EBL) is the first choice as a patterning technique but others, such as laser writing or photolithography could also be used.

The resist structure resulting from the patterning step is then used as a template for the electrolytic growth of Au. In the fabrication scheme shown in Figure 1.13 the formation of a free standing Si_3N_4 membrane is obtained after patterning and electrolytic growth of gold, but a scheme with an inverted sequence of steps is possible. Practical issues related to how absorber stress would strain the membrane can motivate which one of the two options is to be preferred.

The formation of a free standing membrane is obtained by opening a rectangular window in the Si_3N_4 layer present on the reverse of the mask substrate by plasma etching, and wet-etched in a KOH 5M solution to produce a trapezoidal cavity ending at the front of the Si_3N_4 layer, which therefore becomes a silicon nitride membrane fixed to a silicon frame, supporting the gold structures previously grown on it.

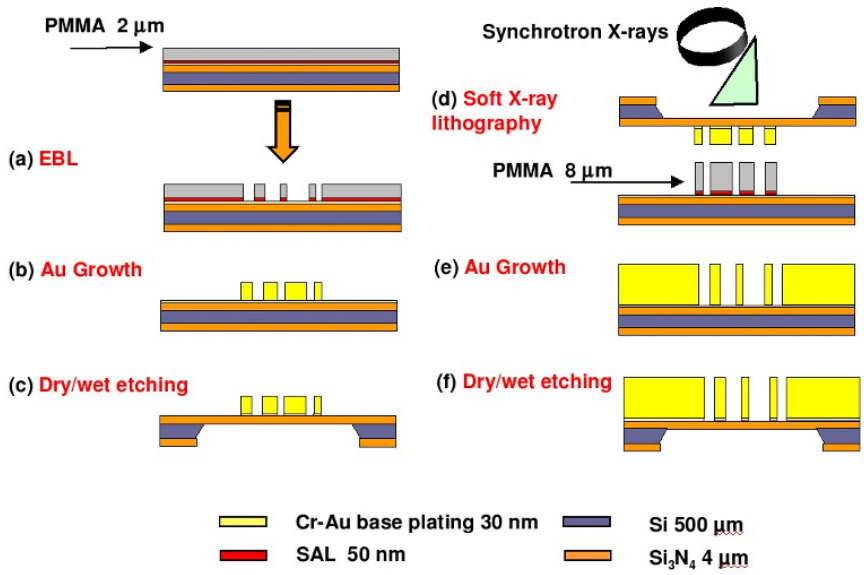

Figure 1.13. *Fabrication of a soft X-ray mask (steps a, b and c) and additional process steps (d, e and f) for the production of a mask for DXRL from a soft X-ray mask by amplification of the aspect ratio of the absorber structures. (a) A silicon (001) substrate with a double sided Si_3N_4 layer deposited by PECVD to a thickness of 1-4 µm, is coated with a metallic bilayer (Cr/Au, 10/20 nm), primed for better resist adhesion (e.g. with a thin layer of negative resist (e.g. SAL)). PMMA (0.5–2 µm), or a different positive resist, is spin-coated and exposed by electron beam lithography (EBL); (b) PMMA is developed, followed by O_2 plasma to clear the bottom of the structure of any residual resist and to expose the surface of the Cr/Au bilayer. Gold structures are electroplated from the seed layer to form the absorber structures; (c) a rectangular window with dimensions along the directions (110) and (1-10) is opened by dry etching with Si_3N_4. A wet etching stage in KOH follows for the anisotropic etching of silicon, stopping on the front of the Si_3N_4 layer. This step leaves a free open membrane of silicon nitride (the mask blank) supporting the absorbing gold layer. The structure obtained is a working mask for soft X-ray lithography; (d) an intermediate mask (alias the soft X- ray mask produced with the previous steps) is used for the fabrication of a DXRL mask. The penetration depth of soft X-rays is sufficient to expose 10–20 µm, producing high resolution structures with vertical sidewalls. Stages (e) and (f) essentially replicate (b) and (c) with structures in a thicker PMMA film. This allows structures with a sufficient absorber thickness to stop the harder radiation used in DXRL to be produced; (e) growth of gold absorbing layer; (f) fabrication of the free standing membrane*

Additional process stages are needed for the fabrication of Deep X-ray lithography masks. Soft X-ray is used instead of EBL for its high penetration depth to transfer the pattern into a much thicker positive resist (up to ~ 20 µm) (in the case of a positive resist). Once the pattern is formed, all other steps (electroplating and formation of the free standing membrane) are performed, essentially in the same

manner as for the fabrication of soft XRL masks, except for the thickness of the grown absorber, which is much larger.

1.3. The physics of X-ray Lithography

1.3.1. *How phase and intensity of X-rays are altered by interaction with matter*

The absorption of X-rays is dominated by the photoelectron effect. X-rays couple effectively with electrons from atomic core levels, inducing the transfer of electrons to unoccupied discrete states (excitation) or to continuum states (ionization). In both cases, the hole left in the core level is filled by an electron decaying from the outer shells, by emission of a photon (fluorescence) or by energy transfer to a third electron (Auger electron) which is ejected into the continuum states. For light elements, the Auger process occurs with the highest probability while fluorescence becomes the dominant process for elements heavier than Cu (Z=28). This is the simplest possible description of the interaction of X-rays with matter.

However, X-rays are electromagnetic waves of wavelength in the 0.1 to 100 Angstroms range (for the particle/wave duality stated by quantum mechanics). Interaction with materials alters both phase and intensity of e.m. waves, and this interaction is described at a macroscopic level (i.e. treating media as continuous) by the complex refraction index n. The interaction of X-rays with matter can be considered weak. The sense of this statement is that photons need to propagate for many wavelengths before they accumulate a phase delay of 2π with respect to the same wave travelling in a vacuum, or before undergoing a reduction to $1/\mathrm{e}$ of their initial intensity. In fact, in the spectral region of X-rays, the refraction index n differs only slightly from unity, and is usually written as $n = 1 - \delta - \mathrm{i}\beta$ where both $\delta, \beta << 1$.

In Figure 1.14 the value of δ and β are plotted in the range of energy and for selected materials of interest for XRL. The attenuation of e.m. waves travelling in a material is related to the imaginary part of the refraction index (the amplitude decays as $\left|\mathrm{e}^{-inkx}\right| = \mathrm{e}^{-\beta kx}$) with an attenuation length of $\eta = \dfrac{\lambda}{2\pi\beta}$. The attenuation length is plotted in Figure 1.15 for various materials in the energy range of 0.5–10 keV, and in the restricted range relevant to soft X-ray lithography, i.e. 0.5–2.5 keV (in a semi-logarithmic scale). X-ray absorption is the fundamental physical phenomenon on which X-ray lithography is based. It is exploited for producing the modulation of transmitted intensity through a patterned absorber, to create a well-defined shadow pattern of resist preventing the target substrate from being exposed.

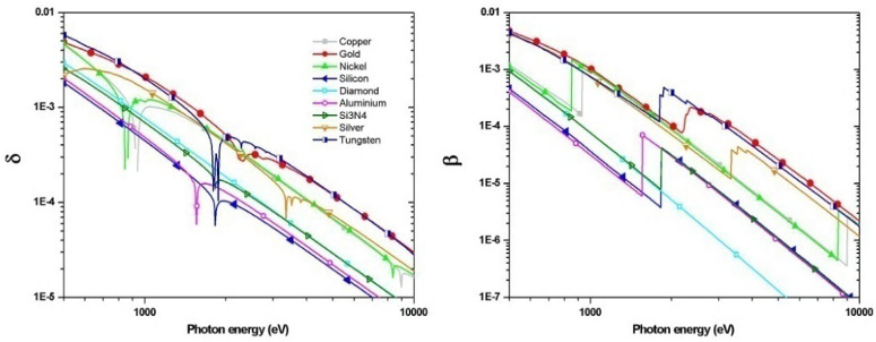

Figure 1.14. *The values of δ and β in the expression of the refraction index n = 1 - δ - iβ are plotted for various materials in the 500 eV to 10 keV photon energy range*

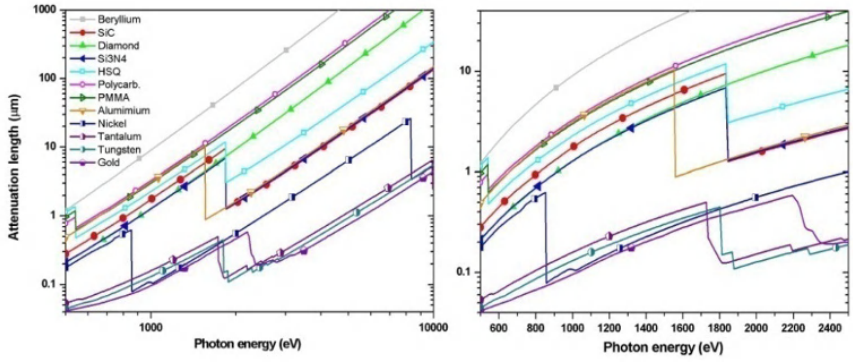

Figure 1.15. *Attenuation length for various materials in the 500 eV to 10 keV photon energy range (left), and zoomed in the 500 eV to 2500 eV range (right) in a semi-log scale*

The phenomenon of total external X-ray reflection is analogous to the total internal reflection occurring in the visible range, and is related to the real part of the refraction index. Total external reflection occurs for rays impinging at a glancing angle ϑ of incidence on a surface below a critical angle $\vartheta_c = \sqrt{2\delta}$ (see Appendix 1).

The effect of total external reflection finds an important application in the technology of X-ray mirrors. These consist of very smooth and flat surfaces that reflect the rays impinging at a grazing angle $\theta < \vartheta_c = \sqrt{2\delta(\hbar\omega)}$. Given that δ

decreases as a function of photon energy (except for energies close to absorption edges), the critical angle also decreases at increasing photon energy. This means that for a given incidence angle ϑ the reflection takes place for photons of energy below a critical value $E_c = \hbar\omega_c(\vartheta)$, while photons above this energy are transmitted into the material and absorbed protecting a well defined pattern. This provides a method for rejecting high energy photons (i.e. creates a low energy pass filter).

We define here the length L_π as the distance that a wave needs to travel into a material before accumulating a phase shift of π with respect to a reference wave propagating in a vacuum. L_π is shown in the left graph of Figure 1.16 for various materials and in the range of interest for X-ray lithography. In the right graph of Figure 1.16, the ratio L_π / η is also presented. If $L_\pi / \eta << 1$ the material can be effectively used as a phase shift material (to make phase shift masks, for example; see D.H. Malueg *et al.* [MAL 04]), whereas in the case where $L_\pi / \eta > 1$ the radiation absorption is the dominant effect, and the radiation is strongly absorbed before penetration in the material to a depth sufficient to produce a significant phase shift.

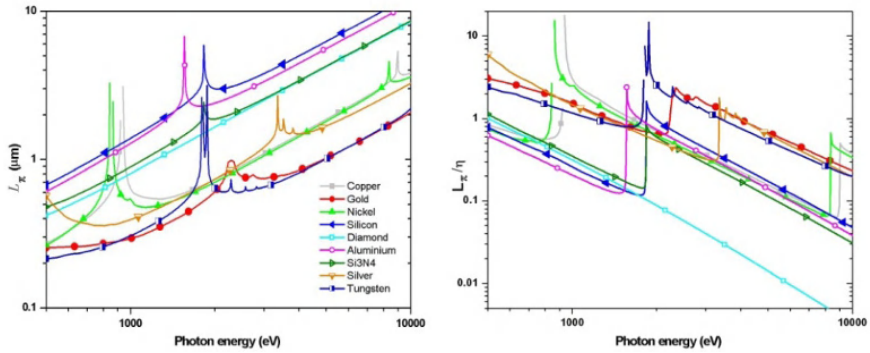

Figure 1.16. *Graph of L_π (left) representing the distance that a wave needs to travel into a material to accumulate a phase shift of π with respect to a reference wave propagating in a vacuum. The ratio L_π / η (right) between the length L_π and the attenuation length*

1.3.2. *X-ray lithography as a shadow printing technique*

Following J. Z. Y. Guo *et al.* [GUO 90], we now introduce some useful terminology. The pattern of intensity (mJ/cm^2) of the transmitted e.m. radiation by the mask at the level of the target substrate (i.e. before being absorbed by the resist),

is called the "aerial image". The energy absorbed in the material volume (mJ/cm^3) is called the "dose image". The distribution of chemical species in the resist created by the absorption of X-rays is termed the "latent image". Finally, the "developed image" is the distribution of material left on the substrate after the resist development. The simplest description of aerial image formation in X-ray lithography represents it as a shadow casting (or shadow printing) process. The laws of geometrical optics are assumed to be valid and diffraction effects are neglected. Refraction at the interface of two media (Snell's law) can be neglected since rays in a typical setup impinge on the mask (on the membrane and on the patterned absorber structures) with almost normal incidence (within a few mrad due to beam divergence), and the real part of the refraction index of materials differs for a value of ~ 10^{-3}–10^{-5} from unity. Therefore, X-rays essentially propagate straight through the different media, and are only attenuated by the membrane and the supported patterned absorber. The flux $\Phi_{out}(\hbar\omega, \vec{x})$ of photons with energy $\hbar\omega$ transmitted by the mask is given by:

$$\Phi_{out}(\hbar\omega, \vec{x}) = T_{mask}(\hbar\omega, \vec{x}) \cdot \Phi_{in}(\hbar\omega, \vec{x}) \qquad [1.3]$$

where $\Phi_{in}(\hbar\omega, \vec{x})$ is the flux impinging at point $\vec{x}$ on the plane of the mask, and $T_{mask}(\hbar\omega, \vec{x})$ is the transmission of the mask at that position for photons of energy $\hbar\omega$. The function $T_{mask}(\hbar\omega, \vec{x})$ factorizes in the product of the absorber transmission $T_{abs}(\hbar\omega, \vec{x}) = e^{-\mu_{abs}(\hbar\omega)t_{abs}(\vec{x})}$ and that of the supporting membrane $T_{memb}(\hbar\omega) = e^{-\mu_{memb}(\hbar\omega)t_{memb}}$ (where dependence on $\vec{x}$ has been dropped because the membrane is typically uniform), i.e.

$$T_{mask}(\hbar\omega, \vec{x}) = e^{-[\mu_{memb}(\hbar\omega)t_{memb} + \mu_{abs}(\hbar\omega)t_{abs}(\vec{x})]} \qquad [1.4]$$

Reflections and multiple reflections (at the air–membrane, membrane–absorber and absorber–air interfaces) are negligible[1] and only absorption has to be considered. Since, generally, the absorber structures have almost vertical sidewalls, the absorber thickness can be mathematically described in most cases as a step function:

---

1 The reflection coefficients for normal incidence are given by $R = \frac{(n-1)(n^*-1)}{(n+1)(n^*+1)} = \frac{\delta^2 + \beta^2}{4}$ [ATW 99]. The reflection at the gold surface, for example, for photon of energy higher than 1 keV is $R < 10^{-6}$.

$$\begin{cases} t_{abs}(\vec{x}) \equiv t_{abs} & \vec{x} \in P \\ 0 & \vec{x} \notin P \end{cases} \qquad [1.5]$$

where P represents the set of points in the protruding areas of the absorber features.

The total transmitted flux is obtained by integrating equation [1.3] over all photon energies:

$$I_{out}(\vec{\mathrm{x}}) = \int T_{mask}(\hbar\omega, \vec{\mathrm{x}})\Phi_{in}(\hbar\omega)d(\hbar\omega) \qquad [1.6]$$

Masks are characterized by several parameters. An important one is modulation, defined as the difference of intensities between the radiation transmitted by the clear and by the opaque areas of the mask, normalized to their sum.

$$M = \frac{I_{out}(\vec{\mathrm{x}} \notin \mathrm{P}) - I_{out}(\vec{\mathrm{x}} \in \mathrm{P})}{I_{out}(\vec{\mathrm{x}} \notin \mathrm{P}) + I_{out}(\vec{\mathrm{x}} \in \mathrm{P})} \qquad [1.7]$$

Modulation is a measure of the capability of a mask to form a contrasted aerial image of the pattern, and assumes a value between 0 and 1. Obviously, the modulation of a mask depends on the spectrum for which it is evaluated. For monochromatic (or, approximately, for narrow distributed) X-ray radiation, the integral (equation [1.6]) reduces to a product of factors, with the cancelation of the membrane absorption as a constant pre-factor common to all terms. In this case, the modulation reads simply as:

$$M = \frac{1 - e^{-\mu_{abs}(\hbar\omega)t_{abs}}}{1 + e^{-\mu_{abs}(\hbar\omega)t_{abs}}} \qquad [1.8]$$

thus making the modulation dependent only on the absorber thickness.

From equation [1.8] it follows that masks with absorber thickness of 1, 2 and 3 times the attenuation lengths have modulation values of 0.46, 0.76, and 0.90, respectively. Generally, a value of ~0.6 for modulation is sufficient for lithographic purposes. In fact, the development process is highly non-linear, with a rather well defined dose threshold. This determines which volumes of resist are selectively dissolved in an appropriate solvent from the volumes that are below threshold and do not develop. With broadband distributed radiation, the concept does not change,

but the calculation of the modulation is slightly less direct, and also the absorption by the membrane affects its value.

In the present description of XRL as a shadow printing process, diffraction effects are neglected in the aerial image formation. In this approximation, the flux reaching the surface of the resist corresponds exactly to that found beyond the mask (we also neglect here the small divergence of the beam). In order to obtain the absorbed dose distribution one needs to calculate the absorbed energy flux at different depths in the resist.

The dose of energy in an infinitesimal layer of thickness *d*, at depth *z* in the resist, absorbed from photons of energy between $\hbar\omega$ and $\hbar(\omega + d\omega)$ is:

$$D(\hbar\omega, \vec{\mathrm{x}}, \mathrm{z})d(\hbar\omega)dz = \mu_{res}(\hbar\omega) \cdot e^{-\mu_{res}(\hbar\omega)z} \cdot \Phi_{out}(\hbar\omega, \vec{\mathrm{x}})d(\hbar\omega)dz \qquad [1.9]$$

where $\mu_{res}(\hbar\omega)$ is the attenuation length in the resist for photons of energy $\hbar\omega$.

Often, the attenuation length in a resist is much larger than the thickness of the resist. In that case, the energy absorbed per unit volume (mJ/cm^3) has a negligible dependence on the depth inside the film. However, for thick films, the different absorption at different photon energies causes a change of the relative weight of the spectral components of the beam with the depth. In particular, since absorption tends to decrease with increasing photon energies (with the exception of the regions of the edges where new absorption channels are opened), the beam becomes "harder", i.e. richer in short wavelength photons, as it proceeds into the material (this refers to the relative weight of the components, not to the absolute intensity of each spectral component, which obviously decreases).

1.3.3. *X-ray absorption in a resist and physical mechanisms involved in its exposure*

The absorption of X-rays within a resist creates photoelectrons in a small volume surrounding the event. Modeling of the photoelectron energy distribution in the photoresist has been carried out by Cerrina *et al*. [CER 92]. The distribution of the directions of photoemitted electrons is concentrated around the plane perpendicular to the incident X-rays. The resulting non-local energy transfer causes a blurring of the energy distribution with respect to the shadow pattern. An estimate of the maximum penetration depth, R_e, of the electrons scattered out into the shadowed region of the resist is given, approximately, by the Grün range $R_g(\mu m) = (0.046/\rho)E^{1.75}$ (Everhart & Hoff [EVE 71]), where ρ is the density of the resist in g/cm^3, and *E* is the electron energy expressed in keV.

In order to refine the picture outlined above, we have to go deeper into the physical mechanisms of resist exposure by X-rays. It is important to understand that the 3D distribution of photoabsorption events (i.e. the actual atomic site where a photon is absorbed) is not reflected accurately in the distribution of absorbed energy by the resist. In fact, the ejected photo and Auger electrons resulting from photoabsorption events redistribute their energy to the surroundings of the absorption site, by traveling in the material and producing several generations of secondary electrons by scattering. The fact that primary and secondary electrons distribute their energy around the photoabsorber results in a blurring of the dose image. The accurate prediction of the final shape of the structures after resist development requires this effect to be taken into account. Below, we summarize some of the published work on this subject [MUR 85, OCO 93].

In electron-beam lithography, the photoresist is exposed by the chemical changes induced by electron energy loss. In X-ray lithography, the same physical chemical mechanisms are involved in the exposure of the photoresist by fast photo and Auger electrons originated by the photoemission of core electrons. The fact that the direct mechanism of resist exposure in X-ray lithography is electronic (in fact, the direct scission of a bond by photoemission of a valence electron is a rather rare process compared to photoemission from the core level, and can be neglected) has two important practical consequences:

i) all resists suited for electron-beam lithography are also suited for X-ray lithography and vice-versa; and

ii) models developed for the effects of exposure of resists to electron-beams can be applied to the study of the response of a resist to X-rays.

Although we are not very interested here in exploring the first point, it is worth mentioning that common resists such as PMMA, ZEP, SAL, SU-8, HSQ, NEB, etc. have been used successfully in X-ray lithography after first being introduced in electron-beam lithography. We concentrate here more on the second point, i.e. on the possibility of applying the models that describe resist exposure by energetic electrons to the case of X-ray exposure.

As described in Figure 1.17, the main difference between exposing a resist by an electron beam and by X-rays is that, in the latter case, the primary electrons do not form a monoenergetic and almost collimated beam but are distributed both in energy and emission direction. The energy and angular distribution of primary electrons needs to be implemented into the models describing X-ray induced exposure.

As for the chemical effects induced by energetic electrons in a resist, various modeling strategies have been developed since the mid-1980s. The simplest phenomenological models are based on the assumption, proven to be rather accurate,

that the effects on resists, in particular the solubility rate and change in the average molecular weight, can be parameterized by a single quantity, i.e. the density of locally absorbed energy $D(\vec{r})$ (eV/nm^3). In recent years, more refined models have been developed that also allow us to distinguish between different types of electron-matter interaction (elastic scattering, ionization, electronic and plasmonic excitations), and attribute the associated chemical effects accordingly (G. Han *et al.* [HAN 02]). By this latter approach, the different types of interaction are taken into account with their respective cross-sections in a first principle calculation scheme. The treatment is rather complicated and will only be outlined briefly here, after discussing the simplest approach.

In the simplest description in which the effects of exposure are parameterized by the density of absorbed energy, it is important to make a clear distinction between the energy of absorbed photons $D_{photon}(\hbar\omega,\vec{r})$ and that obtained after the redistribution operated by the electrons $D_{el}(\vec{r})$. If Green's function $G(\hbar\omega,\vec{r}-\vec{r}')$ (also known as the Point Spread Function) describes the non-local effect of energy deposition at a point $\vec{r}$ caused by the absorption of a photon with energy $\hbar\omega$ at position $\vec{r}'$, $D_{el}(\vec{r})$ can be obtained from $D_{photon}(\hbar\omega,\vec{r})$ via a convolution integral extended over the resist volume and summing over all photon energies:

$$D_{el}(\vec{r}) = \int G(\hbar\omega,\vec{r}-\vec{r}')D_{photon}(\hbar\omega,\vec{r}')d\vec{r}'d\omega \qquad [1.10]$$

The dependence of G on $\vec{r}-\vec{r}'$ and not on r and r′ separately, expresses the fact that the Point Spread Function is assumed to be translationally invariant. This is not true in volumes of material close (within the range of primary electrons) to interfaces with other materials, as in the case of thin films on a substrate. In such cases, the function G dependents separately on $\vec{r}$ and $\vec{r}'$, and the function G has to take into account the fact that the spreading of the energy caused by secondary electrons around the photoabsorber is altered by the presence of other materials in proximity to the resist.

We conclude outlining the scheme of calculation that allows a prediction of the post-development resist structure, but postpone the problem of determining $G(\hbar\omega,\vec{r}-\vec{r}')$. After determining the energy loss density $D_{el}(\vec{r})$ of equation [1.10] the next step is to introduce it as an input parameter in models (mostly phenomenological) describing the solubility rate $R(D_{el})$ (nm/sec) of the resist as a function of the dose locally delivered. This quantity describes the local velocity at which the resist's front of dissolution proceeds, and depends on the type of resist, on

the initial molecular weight and is affected by processing conditions (such as pre-bake temperature and time, whose effect is reflected in the amount of residual solvent in the resist film, and the temperature of the developer). As an example, we briefly describe the case of a family of positive-tone resists, consisting of high molecular weight polymers, which undergo chain scission during exposure. Chain scission resists are characterized by a reduction of molecular weight owing to chain scission of the original molecules. Polymer chains have to be thought of as an intricate distribution of molecules entangled with each other. Only a strong solvent can swell this network and make the relative motion of polymer chains possible. However, if radiation breaks them into smaller pieces it becomes easier for them to move. In the appropriate developing solution, usually an organic solvent, the higher solubility resulting from a reduction of the average molecular weight allows the selective dissolution of the volume of polymer that has been irradiated with a dose above a threshold value.

The relationship between the original molecular weight M_n (in general assumed to be monodispersed), the average fragmented molecular weight $\overline{M_f}$ and the exposure parameters are described in terms of the absorbed energy density, D (i.e. $D_{el}(\vec{r})$), by [GRE 75]:

$$\overline{M_f} = \frac{M_n}{1 + \frac{gDM_n}{\rho A_0}} \qquad [1.11]$$

where ρ is the resist density, A_0 is Avogadro's number, and g is an efficiency factor that represents the number of scission events per absorbed energy (events/eV). The above equation descends directly from the observation that each scission event splits a single polymer chain into two polymer chains, with an average molecular weight corresponding to half of the molecular weight of the initial chain.

The solubility rate can be calculated using an empirical formula:

$$R = (R_0 + \frac{\beta}{\overline{M_f}^{\alpha}})e^{-E_a/KT} \qquad [1.12]$$

where the rate R_0 , the exponent α, the coefficient β, and the activation energy E_a are considered as fitting parameters. The combination of equations [1.11] and [1.12] allows the dissolution rate to be related to the absorbed energy density.

The first and classic example of a chain-scission resist for e-beam applications, employed since the late 1960s [HAL 68, HAR 82, KAK 77] is poly(methyl methacrylate), or PMMA. This simple resist material has been shown to provide resolution that is among the highest for any resist for any lithographic application.

Using PMMA as a resist with initial molecular weight in the range from 100 to 1000 kDa, the X-ray dose required for the resist to become soluble in a common developer solution (isopropyl alcohol, IPA, or methyl isobutyl ketone, MIBK, diluted IPA) can be as low as ~3.0 kJ cm^{-3}. There is an upper dose limit (to be calculated on the surface of the resist) of ~30 kJ cm^{-3}. This must not be exceeded, as above this value gaseous products associated with thermal effects cause the formation of microbubbles in the resist. For doses less than 100 J cm^{-3}, no dissolution of PMMA is observed. These values determine what part of the X-ray spectrum from the synchrotron should be used for a given resist material, its thickness and the thickness of the absorber on the mask.

We now resume the discussion, so far postponed, of how the point spread function $G(\hbar\omega, \vec{r} - \vec{r}')$ (relating $D_{el}(\vec{r})$ to $D_{photon}(\hbar\omega, \vec{r})$) is determined.

The energy redistribution operated by primary and secondary electrons in a material is usually performed in the framework of Monte Carlo simulations. In fact, each electron can be involved in several scattering events, producing trajectories that are better described in terms of stochastic processes, rather than deterministically.

In Monte Carlo simulations the entire trajectory of an electron is "constructed" by generating a sequence of segments delimited by points where some type of interaction takes place. At each step, the energy E and direction $\vec{v}$ of the electron emerging from an interaction is updated. In addition, in the case of ionization events, a secondary electron with a given initial energy and direction of emission is created. Also, the trajectory of the secondary electron is simulated from there with the same stochastic model used for the primary photoelectrons.

In practice, the computation proceeds as follows. For a given electron energy E, the total cross-section $\sigma_T(E)$ (which includes all kinds of scattering. i.e. elastic, ionization, excitations) is computed, and the mean free path $\Lambda(E)$ in the material is derived from it:

$$n\sigma_T(E) = \sum_{\mathrm{i}} n_i \sigma_{el,i}(E) + \sum_{\mathrm{i}} n_i \sigma_{inel,i}(E) + n\sigma_{plasm}(E) \qquad [1.13]$$

$$\Lambda(E) = \frac{1}{n\sigma_T(E)} \qquad [1.14]$$

where n is the numeric density of (all) atoms, n_i the numeric density of atoms of type i. $\sigma_{el,i}(E)$ and $\sigma_{inel,i}(E)$ are the elastic and inelastic cross-sections for electron scattering with atom i, and $\sigma_{plasm}(E)$ is the cross-section for plasmon excitation (normalized to a single atom). The distance $l \in (0,\infty)$ that is assumed to be travelled before the next interaction takes place is generated stochastically by choosing a uniformly distributed random number $\gamma \in (0,1)$ and mapping it into the value $l = -\Lambda(E)\ln\gamma$ (which leads to a probability distribution for the mean free path $P(l) = Exp[-l/\Lambda(E)]$). The value of l and the position of the previous interaction point and the direction $\vec{v}$ determines where the new interaction point will take place. Next, the interaction is further specified, by determining which type of interaction event will actually occur on the basis of their relative probabilistic weights, i.e. their total cross-sections. This is again obtained by dividing the interval (0,1) into segments whose lengths are proportional to the relative probabilistic weight of each different type of event they are representing. The type of event that it is assumed to occur is identified by the segment in which a number randomly chosen in the interval (0,1) falls. Finally, the new energy E and direction $\vec{v}$ of the electron are updated. Also at that step, a map between distribution of random numbers and the distribution probabilities for the occurrence of a scattering event with given scattering parameters (e.g. in an inelastic process the change of energy ΔE and direction θ) is established on the basis of differential cross-sections. Each electron in the simulation is followed until it reaches an energy at which it cannot further induce chemical effects on the material, which is typically assumed to be ~10 eV. The trajectory of many electrons with the same initial energy is simulated in order to obtain distribution of interest (spatial distribution of the ionization events, spatial distribution of deposited energy etc.).

1.3.4. *Physical model of electron energy loss in resists*

The scheme outlined above can be implemented at different levels of accuracy, depending on how the scattering events are classified and on the accuracy of the scattering cross-section used in the computations.

For example, a relatively simple treatment has been developed by K. Murata [MUR 85], which separates the scattering events into elastic and inelastic. In this case, the continuous loss of energy is not associated with a specific scatter but rather

to the polarization of the material surrounding the traveling electron. Each trajectory is divided into small steps of variable length distributed exponentially around the mean free path for elastic scattering. The angular distribution and the energy loss are calculated at each step. The model uses the screened Rutherford equation [1.15] for elastic scattering with the nuclei of atoms (with electron screening of columbic potential) and the Bethe law for continuous energy loss (equation [1.16]):

$$\frac{d\sigma}{d\Omega} = \frac{Z(Z+1)\mathrm{e}^4}{4E^2(1-\cos\theta+2\beta)^2} \qquad [1.15]$$

$$-\frac{dE}{ds} = \frac{2\pi\mathrm{e}^4 nZ}{E}\ln\frac{1.166E}{J} \qquad [1.16]$$

where Ω is the solid angle, Z is the atomic number, θ is the scattering angle, β is the screening parameter, ds is the element of distance along the electron trajectory and J is the average atomic excitation energy. It is well known that Bethe's law is accurate at high energies but needs to be modified for low energies ($E < \mathrm{E}_{\mathrm{inf}} = 6.338J$) into:

$$-\frac{dE}{ds} = \frac{2\pi\mathrm{e}^4 nZ}{1.26(JE)^{1/2}}. \qquad [1.17]$$

However, even with modification for electron energies, the Bethe formalism is not adequate to describe electron energy loss below 5 keV. Therefore, more recently, an approach using the dielectric response of the material has been used to describe energy loss mechanisms. The complex dielectric function $\varepsilon(k,\omega)$ describes the response of a medium to a given energy transfer $\hbar\omega$ and momentum transfer $\hbar k$. The dielectric function contains contributions from both valence and core electrons.

The complex dielectric function describes how the medium is polarized by a variable electric field. This can be produced by an external field, or by a charged particle travelling in the material, creating an e.m. field that can be decomposed by Fourier modes (both for temporal and spatial coordinates). Fast electrons polarize the medium in which they travelling, exciting their modes at a momentum $\hbar k$ and $\hbar\omega$ (which are linked by mode dispersion curves).

For an electron of energy E, the probability of an energy loss $\hbar\omega$ per unit distance is given by:

$$\tau(E,\hbar\omega) = \frac{1}{\pi a_0 E}\int_{k_-}^{k_+}\frac{dk}{k}\mathrm{Im}\left[\frac{-1}{\varepsilon(k,\omega)}\right] \qquad [1.18]$$

where $\hbar k_{\pm} = \sqrt{2m}(\sqrt{E} \pm \sqrt{E-\hbar\omega})$ and $a_0 = \hbar^2/me^2$. The quantity $\tau(E,\hbar\omega)$ is known as the differential inverse mean free path, because by integrating it over all allowed energy transfers the inelastic mean free path is obtained. Furthermore, an integration of $\hbar\omega\tau(E,\hbar\omega)$ overall allowed energy transfers gives the energy loss per unit path length, or stopping power $S(E)$. The stopping power can then be used to calculate the distance it takes to slow an electron down to a given energy. This distance is called the continuous slowing down approximation (CSDA) range, because the calculation assumes that the electron slows down continuously from the initial energy E to the final energy, which is usually taken to be 10 eV. The CSDA range R (E) is given by:

$$R_0(E) = \int_{10eV}^{E}\frac{dE'}{S(E')} \qquad [1.19]$$

The calculations for the mean free path and stopping power have been carried out down to 10 eV for a number of materials, including SiO_2, polystyrene, polyethylene, silicon, aluminum, nickel, copper, and gold.

A description of the energy loss in materials such as resists has been attempted with Monte Carlo simulations, using the CSDA in between discrete events of elastic scattering. Also, the treatment of elastic scattering has been improved by adopting the relativistic Mott cross-section in the Born approximation for electron elastic scattering with atoms instead of screened Rutherford cross-sections [CZY 90, GRE 74]. Alternatively, Mott cross-sections are reproduced analytically by empirical models based on a few fitting parameters, and the analytical representations of the data are introduced into the calculations [BRO 94].

In more recent research, models of electron energy deposition based on the Monte Carlo method have been further improved by separating inelastic scattering events into various contributions i.e. ionization, excitation and plasmon [HAN 02]. In fact, CSDA only gives the expected value of energy deposition, but is unable to provide detailed information about the generation of secondary electrons. The model developed by G. Han *et al.* [HAN 03] is based on knowledge of the cross-sections for the different scattering process involved, i.e. elastic, ionization excitation and

plasmons, and also gives the spatial distribution of all types of events, with the possibility of identifying those that lead to chain scission events in the case of polymer materials acting as resists [HAN 03].

The typical range of secondary electrons is of the order of angstroms and, therefore, cause chemical modification locally in a resist where they are generated. However, the more energetic primaries (photoelectrons and Auger) can travel a longer distance. Their range depends on the material, on the initial electron energy and on the final energy that is assumed to be a threshold to consider it as ineffective to cause further ionization in the material. The range at which the primary electrons are able to affect the chemical-physical nature of the resist, by scission of bonds and creation of radicals, determines a blurring of the exposed resist volume with respect to the volume where X-ray radiation is absorbed. Although elastic scattering does not contribute (by definition) to the loss of energy, it affects nevertheless the range at which electron energy is deposited in the material by inelastic scattering. In fact, elastic scattering, with its rather large differential cross-section for scattering at large angles, contributes to reducing the range of electrons, due to multiple changes in the direction in their trajectory. Inelastic scattering events (ionization, excitation), are characterized instead by smaller scattering angles.

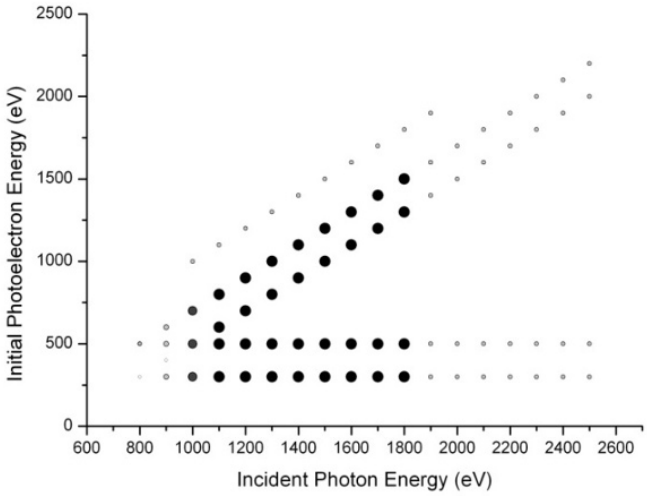

Figure 1.17. *Probabilities of photoelectron emission within the spectrum range of an X-ray lithography beamline for discrete energies (Al Kα). The probabilities are represented in grey, with darker areas corresponding to higher probabilities. Reproduced from L E. Ocola [OCO 93]*

For monochromatic X-ray radiation, photo and Auger electrons are distributed according to a discrete spectrum of energies given by $E_{pe,A} = \hbar\omega - E_A$ for a photoelectron generated from a level A, and $E_{ABC} = E_A - E_B - E_C$ for an Auger electron generated from level C, with the energy transferred in the transition of an electron from level B to the empty level A, where E_X represents the binding energy of the level X. In resists, which are typically made of low atomic weight elements (O, C, Si), Auger electrons are produced in *KLL* transitions. In that case, given that $E_L << E_K$ the photon energy is essentially split between the kinetic energy of the photoelectron and that of the Auger electron, with energy $E_{pe,K} = \hbar\omega - E_K$, and $E_{KLL} \approx E_K$, respectively. It is important to notice that while the photoelectron energy depends linearly on the energy of the absorbed photon, the Auger level is independent of it. This determines the fact that while the blur induced by photoelectrons depends on the exciting photon energy, the blur associated with the Auger electrons is independent of it.

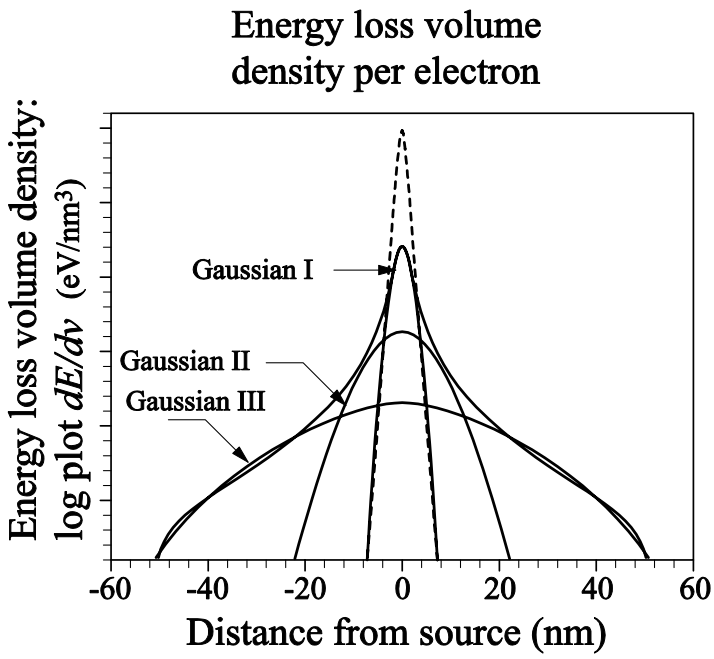

Figure 1.18. *Example of 3D point spread function of a 1.3 keV photon in PMMA, fitted with the sum of three Gaussian distributions. The dose per unit volume is represented as a function of the distance from the source. Reproduced from L.E. Ocola [OCO 93]*

As resists are mainly organic polymers consisting of light elements – H, C, O, (and in some cases also S, Cl or Si) – Auger electrons are produced with probability close to 1 at each event of photoemission (except of course for H, as Auger is a two-electron process). Therefore resist exposure is the result of the combined effect of photoelectrons and Auger electrons.

The knowledge of the absolute ionization cross-sections allows the calculation of the number of electrons generated at different energies by a monochromatic X-ray beam. This is known both theoretically [OCO 93] and experimentally [HAN 02].

	1 KeV	1.5 KeV	2.0 KeV	3.0 KeV	5.0 KeV	10.0 KeV
H	12.6	3.73	1.79	0.88	0.65	0.65
C	43833.2	14147.5	6124.8	1806.8	369.9	43.9
O	122161.6	41708.1	18762.0	5823.5	1258.5	150.8
Si	74968.7	25314.7	127032.3	46474.1	11815.1	1604.2
Cl	163380.8	59056.0	27381.4	84332.2	23374.5	3468.9

Table 1.2. *Table representing the X-ray cross-sections for a few elements found in resist materials for a few selected values of photon energies, in barn/atom. Adapted from W.H. McMaster,* et al. *[MCM 69]*

1.3.5. *Diffraction effects in X-ray lithography*

In addition to the blurring caused by Auger and photoelectrons, the picture of X-ray lithography as a simple shadow printing process has to be corrected to take into account diffraction effects. The fact that diffraction cannot be neglected, even for a short wavelength λ of ~0.1–1 nm, can be easily seen from the displacement of the first satellite peak in the diffraction pattern. The equation that gives the angle θ_n at which the diffraction maxima of n-th order occurs when monochromatic radiation is passing through a slit of width d is:

$$d \cdot Sin\,\theta_n = n\lambda \qquad [1.20]$$

The first diffraction maximum in the approximation of small angle can be found at $\theta_{\max,1} = \frac{3\lambda}{2d}$. Considering a gap g between mask and substrate, the position of the first max would be found at a distance of $\Delta = \frac{3g\lambda}{2d}$.

For typical values of the X-ray wavelength used in proximity lithography, λ =1 nm, and for an aperture width of d = 150 nm, that we identify with a mask feature and a mask–substrate gap g of 10 μm, the satellite peak displacement Δ from the central peak would be 100 nm. Therefore, the contribution of the first diffraction peak would alter the dose in the region of the edge of the geometrical shadow of the feature. The linear dependence of Δ on the mask–substrate gap shows that only a zero gap eliminates any diffraction effect. However, because a residual gap cannot be avoided, diffraction plays an important role in one-to-one mask pattern replication, an issue that is widely discussed in the literature [HEC 92, GUO 92].

Fresnel diffraction effects can generate strong modulations of the illumination of the resist. A proper simulation of these effects can be exploited to differentiate the exposure and then the development of the resist. One of the experimental parameters that can be controlled with a degree of freedom is the gap between the mask and the sample spun with the resist. Generally, the wider the gap, the stronger the effect of diffraction, which can be avoided with a zero gap, i.e. placing the mask in full contact with the resist. In the past, simulation programs such as TOOLSET [KHA 94, KHA 97A] have been specifically developed to simulate diffraction effects and the development of a resist in X-ray proximity lithography. The parameters that are required to be given as input are the natural divergence of the incoming beam, the layering of the mask and its pattern, the mask–substrate gap distance, the type of resist (thickness, chemical composition, dissolution rate), the atmosphere where the exposure takes place, the exposure dose and parameters related to the way resists are affected by radiation (contrast, threshold dose).

1.3.6. *Coherence of synchrotron radiation from bending magnet devices*

A mask illuminated by a spatially coherent source induces diffraction effects that propagate along the mask–substrate gap.

In the theoretical limit of a point source oscillating at a single frequency for all time from $-\infty$ to $+\infty$, the radiated field would be perfectly correlated everywhere. That is, if one knows the electric amplitude and phase at a given point and time, one would know these quantities for all time and throughout space. Real physical sources, however, are made up of spatially distributed radiators that emit a

finite spectral bandwidth for a finite period of time. Moreover, in normal sources the emission of individual radiators are not correlated in phase, in contrast to what happens for lasers. Consequently, well defined phase relationships between amplitude and phases at different points in time–space are restricted to a finite spatial–temporal region of coherence.

In synchrotron radiation the radiators are ultra-relativistic electrons spatially distributed in bunches that radiate at specific points of the storage ring where their trajectories are bent by a magnetic field. From bending magnets, the emission of electrons is a white spectrum, and the phase of e.m. waves emitted from each electron is temporally uncorrelated with that from another. In Figure 1.19, a bunch of electrons is depicted, each independently emitting from a point that is in view of the mask. Each electron has its own emission cone of angular aperture γ . The e.m. field of each electron produces a diffraction pattern after the mask. Being uncorrelated in phase, the total intensity pattern is obtained by the superposition of the intensity patterns relative to each independent diffracted photon. However, if the diffraction patterns are not too dissimilar from each other, the modulation of intensity due to diffraction will still be present and recognizable on the final exposed features.

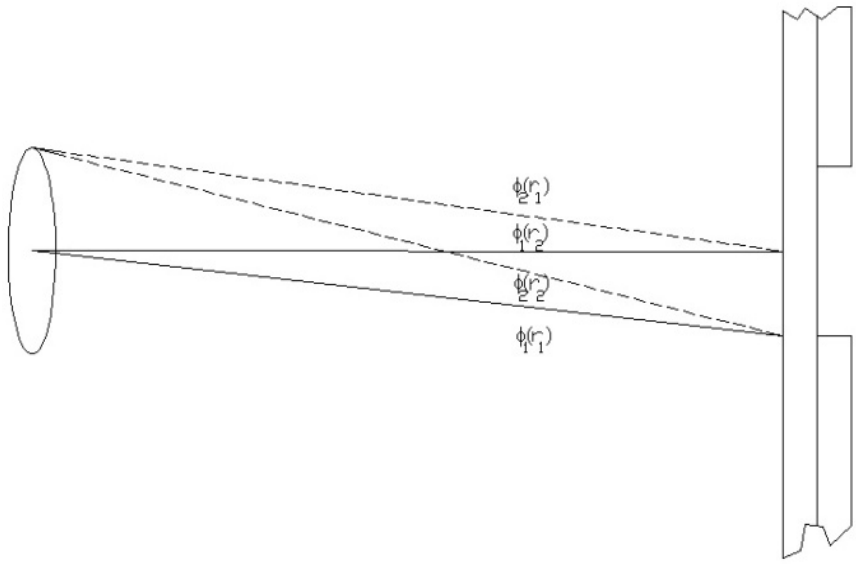

Figure 1.19. *Sketch of a bunch of electrons and phase delay introduced by the path that e.m. waves have to travel from different positions inside the bunch to different positions inside a transparent feature on the mask*

Our purpose here is to show by a simple and intuitive calculation when the conditions of coherence are sufficient to produce recognizable diffraction effects. With reference to Figure 1.19, the phase at point x on the mask is given by

$$\phi(x,s) = \sqrt{L^2 + (s_i - x)^2} / \lambda \approx \frac{L}{\lambda} + \frac{(s-x)^2}{2L\lambda} \approx \phi_0 + \frac{(s-x)^2}{2L\lambda} \qquad [1.21]$$

Now we look at the phase relationship between the wave front on x_1 and x_2 relative to a photon emitted by an electron at position s in the bunch. We find that the relative phase shift is given by:

$$\begin{aligned} &\delta\varphi(x_1, x_2, s) = \varphi(x_1, s) - \varphi(x_2, s) = \\ &[\sqrt{L^2 + (s - x_1)^2} - \sqrt{L^2 + (s - x_2)^2}] / \lambda \approx s(x_1 - x_2) / L\lambda \end{aligned} \qquad [1.22]$$

To understand whether the diffraction pattern of an aperture on the mask will be approximately the same (or not) for photons emitted at point s_1 and s_2 we have to consider if relative phases of a photon on the points of aperture x_1 and x_2 are approximately the same for photon waves emitted at s_1 and s_2 in the bunch. In other words, we have to verify:

$$\Delta\phi(x_1, x_2, s_1, s_2) = \delta\phi(x_1, x_2, s_1) - \delta\phi(x_1, x_2, s_2) \approx (s_1 - s_2)(x_1 - x_2) / L\lambda$$

[1.23]

If $\Delta\phi$ is small with respect to 2π, the photons (with the same energy) generated at different points in the bunch and impinging on an aperture diffraction, the effects will not be cancelled out.

What we have obtained above is essentially the Van Cittert–Zernike theorem, which states that the spatial coherence length is given by:

$$l_c^{spatial} = \frac{\lambda}{2\pi}\frac{L}{S} \qquad [1.24]$$

If we take $s_1 = 0$, $s_2 = 100$ µm, $x_1 - x_2 = 10$ µm, $L = 10$ m, $\lambda = 1$ nm,

$$\Delta\varphi(x_1, x_2, s_1, s_2) \approx 10^{-4} \times 10^{-5} / (10 \times 10^{-9}) = 0.1 \qquad [1.25]$$

In this case, the distribution of relative phases between different points on the aperture will be approximately the same for the waves generated at s_1 and s_2, with only a small "distortion" of 0.1 radians over the aperture of 10 um, and 0.01 radians for aperture of 1 um. This means that the diffraction pattern obtained after the aperture will be just slightly different for two field components with the same energy but generated by two electrons spatially separated within a bunch. Therefore, the two diffracted patterns almost superimpose over each other.

1.3.7. *Basic formulation of diffraction theory for a scalar field*

Here, we outline the treatment of the problem of aerial image formation in X-ray lithography in the presence of diffraction effects. As the purpose of this section is not to provide a scheme for quantitative prediction, but more to illustrate the fundamental concepts, we will make further simplifying assumptions, i.e that (i) the mask has a modulation M=1 (i.e. the transmission assumes only the binary values 0 or 1) and (ii) the impinging radiation is a monochromatic plane wave propagating orthogonally to the plane of the mask. Moreover, the use of scalar diffraction theory is justified in this context [GOO 96].

The derivation of the main results will be obtained in the framework of the Rayleigh–Sommerfeld formulation of diffraction, according to the discussion and notations of [LUC 06], to which we refer readers for more details.

The calculation of the complex disturbance U (which represents the complex amplitude of the e.m. field as a scalar) can be obtained with the help of Green's theorem. Let U(P) and G(P) be any two complex-valued functions of position, and let S be a closed surface surrounding a volume V. If U, G, and their first and second partial derivatives are single-valued and continuous in the volume V and on S, then we have:

$$\iiint_V (U\nabla^2 G - G\nabla^2 U)dV = \iint_S (U\frac{\partial G}{\partial n} - G\frac{\partial U}{\partial n})dS \qquad [1.26]$$

The surface integral contains the derivative of the functions in the normal direction to the local orientation of the surface.

From this theorem and with the additional assumption that both functions U and G satisfy the wave equation, i.e. $(\nabla^2 + k^2)G = 0$, and $(\nabla^2 + k^2)U = 0$ it follows that the surface integral vanishes:

$$\iint_S (U\frac{\partial G}{\partial n} - G\frac{\partial U}{\partial n})dS = \iiint_V (U\nabla^2 G - G\nabla^2 U)dV = \iiint_V (-Uk^2 G + Gk^2 U)dV = 0$$

[1.27]

A useful integral-differential equation can be derived from the above equation. This will allow us to deduce the value of U at a generic point P_0 inside the volume V from the knowledge of U and $\frac{\partial U}{\partial n}$ on the surface S.

To derive this expression, we consider G as the function $\mathrm{G}_{\mathrm{P}_0}(\mathrm{P}_1)$ of the generic point P_1, defined as:

$$\mathrm{G}_{\mathrm{P}_0}(\mathrm{P}_1) = \frac{e^{ik|P_1 - P_0|}}{|P_1 - P_0|} = \frac{e^{ikr_{01}}}{r_{01}} \qquad [1.28]$$

where P_0 plays the role of a parameter (i.e. it parameterizes a family of functions of P_1). This function can be verified to satisfy the wave equation $(\nabla^2 + k^2)G = 0$, and it is continuous with continuous derivatives, with the exception of the point at which $\mathrm{P}_1 = \mathrm{P}_0$.

The theorem (equation [1.27]) remains valid with the function G expressed by equation [1.28] by excluding, from its domain, an infinitesimal sphere containing the point of divergence; that is, it remains valid if applied to the volume $V' = V - V_\varepsilon$ from which an infinitesimal sphere V_ε (where the condition of continuity of the function G is not verified) of radius ε has been removed around the point P_0 (as shown in Figure 1.20). Given the surface, S_ε, of the infinitesimal sphere V_ε, it follows from [1.27] that:

$$\iint_{S\varepsilon} (U\frac{\partial G}{\partial n} - G\frac{\partial U}{\partial n})dS = -\iint_S (U\frac{\partial G}{\partial n} - G\frac{\partial U}{\partial n})dS \qquad [1.29]$$

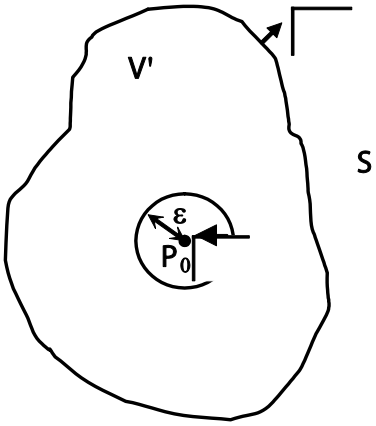

Figure 1.20. *Surface of integration*

We calculate the derivative of the function $G_{P_0}(P_1)$ along the outward-pointing normal to the surface of the volume V':

$$\frac{\partial G}{\partial n}(P_1) = \cos(\vec{n}, \vec{r}_{01})(ik - \frac{1}{r_{01}})\frac{\exp(ikr_{01})}{r_{01}} \qquad [1.30]$$

where $\vec{r}_{01}$ is the vector $P_1 - P_0$ and r_{01} its modulus.

For P_1 on S_ε, $\cos(\vec{n}, \vec{r}_{01}) = -1$, hence:

$$\frac{\partial G}{\partial n}(P_1) = -(ik - \frac{1}{\varepsilon})\frac{e^{ik\varepsilon}}{\varepsilon}. \qquad [1.31]$$

Introducing [1.31] into the expression for $\iint_{S\varepsilon}(U\frac{\partial G}{\partial n} - G\frac{\partial U}{\partial n})dS$ in the left side of equation [1.29] and taking the limit $\varepsilon \to 0$, we obtain:

$$\lim_{\varepsilon\to 0}\iint_{S\varepsilon}(U\frac{\partial G}{\partial n} - G\frac{\partial U}{\partial n})dS = \lim_{\varepsilon\to 0} 4\pi\varepsilon^2[U(P_0)(\frac{1}{\varepsilon} - ik)\frac{e^{ik\varepsilon}}{\varepsilon} - \frac{\partial U(P_0)}{\partial n}\frac{e^{ik\varepsilon}}{\varepsilon}] = 4\pi U(P_0) \qquad [1.32]$$

Where here in evaluating the limit for $\varepsilon \to 0$ we have used the continuity of the derivative of $\frac{\partial U}{\partial n}$. Finally, the result of the above calculation can be cast into the following equation:

$$U(P_0) = \frac{1}{4\pi} \iint_S \{ \frac{\partial U}{\partial n} [\frac{\exp(ikr_{01})}{r_{01}}] - U \frac{\partial}{\partial n} [\frac{\exp(ikr_{01})}{r_{01}}] \} dS \qquad [1.33]$$

Equation [1.33] is known as the Helmoltz and Kirchhoff integral theorem, and expresses in integral-differential form the relationship between the value of the function U at a generic point P_0 of the volume V to the values that the same function and its derivative assume on the surface S.

As is shown below, the diffraction by a planar screen can be treated using the formalism above, using a function G satisfying the wave function equation and suitable boundary conditions. In fact, there is some arbitrariness in the choice of function G. In particular, the choice made above of $\mathrm{G}(\mathrm{P}_1) = \frac{e^{ikr_{01}}}{r_{01}}$ as a Green's function, is not the most convenient, since the surface integral [1.29] contains both the terms U and $\frac{\partial U}{\partial n}$ (Fresnel-Kirchhoff) and, as a consequence, the evaluation of the integral [1.29] requires the knowledge or assumption of boundary conditions for both U and its derivative $\frac{\partial U}{\partial n}$.

1.3.8. *Rayleigh–Sommerfeld formulation of diffraction by a planar screen*

In this section, we derive the basic equation describing the diffraction by a planar screen, making use of the results of the previous section. However, a different choice for the function $\mathrm{G}_{\mathrm{P}_0}(\mathrm{P}_1)$ will be made. In fact, it is well known that the choice of the function $\mathrm{G}_{\mathrm{P}_0}(\mathrm{P}_1) = \frac{e^{ikr_{01}}}{r_{01}}$ as Green's function in a diffraction problem has the drawback that, for the evaluation of the integral [1.33] both U and $\frac{\partial U}{\partial n}$ need to be known or somehow "guessed" and imposed as boundary conditions on a surface enclosing the volume where the field U has to be calculated. This has the drawback that specifying these conditions independently can engender

inconsistencies between the assumptions made about U and $\frac{\partial U}{\partial n}$, and their values calculated instead via the use of equation [1.33].

The origin of this inconsistency is that U and $\frac{\partial U}{\partial n}$ are not fully independent on the surface S. In some problems, however, the geometry of the problem makes possible the choice of a Green's function G that either vanishes or has a vanishing derivative $\frac{\partial G}{\partial n}$ on the surface S where the boundary conditions have to be imposed. The problem is demonstrated in Figure 1.21, which presents diffraction by a planar screen in such circumstances.

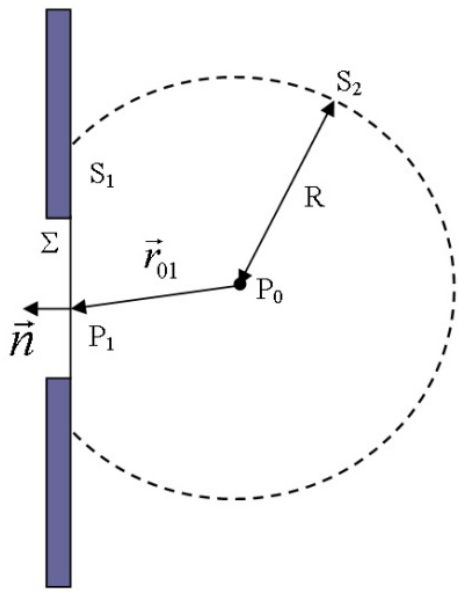

Figure 1.21. *Schematic representation of the problem of diffraction by a planar screen*

By choosing a function G that satisfies the condition $G|_S \equiv 0$, the integral [1.33] becomes independent of $\frac{\partial U}{\partial n}$. As a consequence, the boundaries have to be imposed only on the field U, thus removing all inconsistencies in the calculation.

With reference to Figure 1.21, the conditions requested are that the function G vanishes on the plane of the screen, i.e. $\mathrm{G}\big|_{S1} \equiv 0$, while, on the spherical surface S_2 and in order for the term $G\dfrac{\partial U}{\partial n}$ to be neglected, the product $\mathrm{G}\dfrac{\partial U}{\partial n} \to 0$ is faster than $\dfrac{1}{R^2}$ for $R \to \infty$, a condition that can be verified *a posteriori* after finding the solution for U .

The function G^{RS} which satisfies such a condition in the case of a planar diffractive screen was found by Sommerfeld [SOM 96]. It is obtained by subtracting the function $\mathrm{G}_{\mathrm{P}_0}(\mathrm{P}_1)$ from the function $\mathrm{G}_{\mathrm{P}_2}(\mathrm{P}_1)$, which is parameterized by the point $\mathrm{P}_2 = \mathrm{P}_0 - 2\vec{\mathrm{n}}(\vec{\mathrm{n}} \cdot \mathrm{P}_0)$ which is the mirror image of point P_0 with respect to the plane of the diffractive screen:

$$\mathrm{G}^{\mathrm{RS}}_{\mathrm{P}_0}(\mathrm{P}_1) = \frac{e^{ik|P_1 - P_0|}}{|P_1 - P_0|} - \frac{e^{ik|P_1 - P_2|}}{|P_1 - P_2|} = \frac{e^{ikr_{01}}}{r_{01}} - \frac{e^{ikr_{21}}}{r_{21}} . \qquad [1.34]$$

By construction, the function $\mathrm{G}^{\mathrm{RS}}_{\mathrm{P}_0}(\mathrm{P}_1)$ has a parity -1 with respect to the inversion of the axis perpendicular to the screen, and therefore it vanishes at all points P_1 that lie on it.

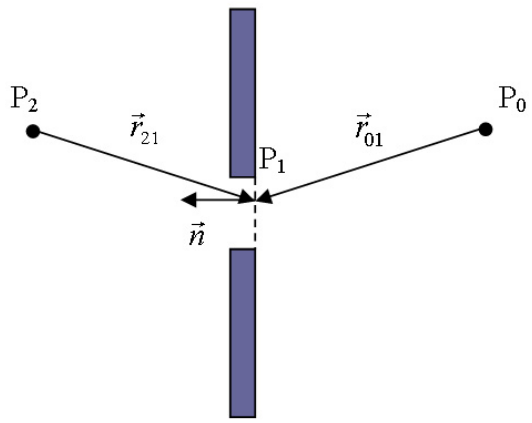

Figure 1.22. *Schematic representing the Rayleigh –Sommerfeld construction for the problem of diffraction by a planar screen*

From this, and from the assumption that in the limit $R \to \infty$ both $\mathrm{G}\frac{\partial U}{\partial n} \to 0$ and $\mathrm{U}\frac{\partial G}{\partial n} \to 0$ are faster than $\frac{1}{R^2}$ (which can be verified easily after finding the solution for U), it follows that [1.33] becomes:

$$U^{RS}(P_0) = \frac{-1}{4\pi}\iint_S U\frac{\partial \mathrm{G}^{\mathrm{RS}}_{\mathrm{P}_0}}{\partial n}dS \qquad [1.35]$$

The derivative of $\mathrm{G}^{\mathrm{RS}}_{\mathrm{P}_0}(\mathrm{P}_1)$ reads:

$$\frac{\partial \mathrm{G}^{\mathrm{RS}}_{\mathrm{P}_0}}{\partial n}(P_1) = \cos(\vec{\mathrm{n}}, \vec{\mathrm{r}}_{01})\left(ik - \frac{1}{r_{01}}\right)\frac{e^{ikr_{01}}}{r_{01}} - \cos(\vec{\mathrm{n}}, \mathrm{r}_{21})\left(ik - \frac{1}{\mathrm{r}_{21}}\right)\frac{e^{ik\mathrm{r}_{21}}}{\mathrm{r}_{21}} \qquad [1.36]$$

For points P_1 on the screen we have $r_{21} = r_{01}$ and $\cos(\vec{\mathrm{n}}, \vec{\mathrm{r}}_{01}) = -\cos(\vec{\mathrm{n}}, \vec{\mathrm{r}}_{21})$, which leads to:

$$\frac{\partial \mathrm{G}^{\mathrm{RS}}_{\mathrm{P}_0}}{\partial n}(P_1) = 2\cos(\vec{\mathrm{n}}, \vec{\mathrm{r}}_{01})\left(ik - \frac{1}{r_{01}}\right)\frac{e^{ikr_{01}}}{r_{01}} \qquad [1.37]$$

If we are interested in the field at distances much larger than the wavelength of the radiation impinging on the mask, the approximation $\lambda << r_{01}$ could be used to simplify the expression above into:

$$\frac{\partial \mathrm{G}^{\mathrm{RS}}_{\mathrm{P}_0}}{\partial n}(P_1) = 2ik\cos(\vec{\mathrm{n}}, \vec{\mathrm{r}}_{01})\frac{e^{ikr_{01}}}{r_{01}} \qquad [1.38]$$

This approximation in particular applies to the case of X-ray lithography where the wavelength is of the order of 0.1–1 nm and the gap between the mask and the resist film where the diffraction pattern is recorded is typically more than 5 μm.

Inserting the expression [1.38] into [1.35] we obtain:

$$U^{RS}(P_0) = \frac{1}{i\lambda}\iint_S U(P_1)\cos(\vec{n}, \vec{r}_{01})\frac{e^{ikr_{01}}}{r_{01}}dS \qquad [1.39]$$

In the next section we will show how it is possible to obtain the far field solution $U^{RS}(P_0)$ from the assumption of the field $U(P_1)$ just behind the screen.

1.3.9. *An example of diffraction effects: Poisson's spot in X-ray lithography*

We want to illustrate here how diffraction plays a role especially in high resolution X-ray lithography. For this purpose, we present an example of how diffraction affects the shape of the printed structures in the resist, making them differ from the absorber. In particular, we show an example of the formation of Poisson's spots.

Here, we are following a very didactic paper by R.L. Lucke [LUC 06]. In the introduction, Lucke supplies a definition of the effect:

> "Poisson's spot, also known as the spot of Arago, is the name given to the bright on-axis spot behind a circular obscuration illuminated by a plane wave: on the axis of the disk, all light diffracted at the rim of the disk arrives in phase and interferes constructively. Consequently, even for angles approaching 90°, i.e., for observation points close to the disk, diffraction can result in a significant intensity."

Here, we will briefly derive the analytical expression of the on-axis and near axis diffracted field amplitude and intensity produced by an obscuring circular disk illuminated by a plane monochromatic wave (in a scalar approximation). The results will be used to interpret the results of a pattern generated by X-ray lithography.

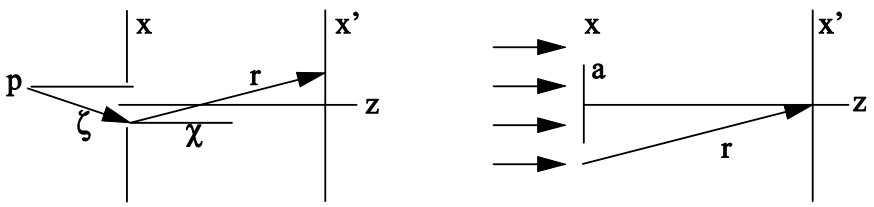

Figure 1.23. *Geometry of the Poisson's spot problem*

We apply the Rayleigh–Sommerfeld diffraction integral [1.39] to the case of an obscuring disk, with reference to Figure 1.23:

$$U^{RS}(x', y', z) = \frac{1}{i\lambda}\iint_S U(x, y, 0)\cos\chi \frac{e^{ikr}}{r} dS \qquad [1.40]$$

As boundary conditions for the field U on the plane of the screen, we assume that it equals the input field in the unperturbed field in the transparent areas of the screen, denoted by T, and that it vanishes in the obscuring part of the screen. These conditions, known as the Rayleigh–Sommerfeld conditions, can be written as:

$$\begin{cases} U(x, y, 0) = U_i(x, y, 0) & (\mathrm{x}, \mathrm{y}) \in \mathrm{T} \\ U(x, y, 0) = 0 & (\mathrm{x}, \mathrm{y}) \notin \mathrm{T} \end{cases} \qquad [1.41]$$

In the case we are analyzing, the pattern of the mask is an obscuring disk of radius a.

We now exploit the cylindrical symmetry of the problem by defining the cylindrical coordinate system, by $(x, y, z) = (\rho\cos\phi, \rho\sin\phi, z)$, $0 \le \varphi < 2\pi$. From the cylindrical symmetry it follows that the complex field amplitude at the point $(x', 0, z)$ represents all points $(\rho\cos\varphi, \rho\sin\varphi, z)$ with $\rho = x'$ and $0 \le \varphi < 2\pi$.

Therefore, in [1.40] $r = [(x - x')^2 + y^2 + z^2]^{1/2}$ represents the distance between the point $(x', 0, z)$ where the field is observed, and the generic point $(x, y, 0)$ on the diffracting screen, χ is the angle formed by the vector that joins $(x, y, 0)$ to $(x', 0, z)$ with the normal to the screen. With these definitions, we can write $\cos\chi = \frac{z}{r}$. The surface element $dS = dxdy$ can be written in cylindrical coordinates as $dS = \rho d\rho d\varphi$.

Furthermore, from $r^2 = z^2 + (x - x')^2 + y^2 = z^2 + (\rho\cos\varphi - x')^2 + \rho^2\sin\varphi^2$ it follows that $rdr = (\rho - x'\cos\varphi)d\rho \approx \rho d\rho$ as long as $\rho \ge a >> x'$ (i.e. the point of observation $(x', 0, z)$ is close to the z axis). For an on-axis point of observation $(x' = 0, 0, z)$ the equation $rdr = \rho d\rho$ is exact. The surface element can be written $dS = \rho d\rho d\varphi \approx rdrd\varphi$ for $\rho \ge a >> x'$, which become exact for $x' = 0$.

In such a case, equation [1.40] reads:

$$U^{RS}(x',0,z) = \frac{U_i}{i\lambda}\int_0^{2\pi}\int_a^{\infty}\frac{e^{ikr}}{r}\frac{z}{r}\rho d\rho d\varphi \approx \frac{zU_i}{i\lambda}\int_0^{2\pi}\int_{R(\varphi)}^{\infty}\frac{e^{ikr}}{r}drd\varphi \qquad [1.42]$$

where changing from ρ to r as an integration variable we have to change the lower integration limit from a to:

$$R(\varphi) = \sqrt{z^2 + a^2 + x'^2 - 2x'a\cos\varphi} \approx r_0 + \frac{x'^2}{2r_0} - \frac{x'a\cos\varphi}{r_0} \qquad [1.43]$$

where $r_0 = \sqrt{z^2 + a^2}$. The integral on r can be evaluated by parts, as:

$$\int_{R(\varphi)}^{\infty}\frac{e^{ikr}}{r}dr = \frac{1}{ik}\left(\frac{e^{ikr}}{r}\bigg|_{r=R(\varphi)}^{r=\infty} + \int_{R(\varphi)}^{\infty}\frac{e^{ikr}}{r^2}dr\right) = \frac{i}{k}\frac{e^{ikR(\varphi)}}{R(\varphi)} + O\left(\frac{1}{(kR(\varphi))^2}\right) \qquad [1.44]$$

where we have kept only the leading term in the approximation $rk >> 1$.

In the example of X-ray lithography illustrated below, the approximation consisting of neglecting the term $O\left(\left(\frac{\lambda}{2\pi R(\varphi)}\right)^2\right)$ with respect to $O\left(\frac{\lambda}{2\pi R(\varphi)}\right)$ is fully justified, as the wavelength is of the order of 1 nm, $a \sim 100$ nm and $R(\varphi) \sim g$ is the gap between the mask and resist which is of the order of 10 μm. Finally, we can insert equation [1.44] into [1.42] and, using the approximation:

$$U^{RS}(x',0,z) \approx \frac{gU_i}{2\pi}\int_0^{2\pi}\frac{e^{ikR(\phi)}}{R(\phi)}d\phi \approx \frac{ge^{ik(r_0+\frac{x'^2}{2r_0})}U_i}{2\pi r_0}\int_0^{2\pi}e^{-ik\frac{x'a\cos\phi}{r_0}}d\phi = \qquad [1.45]$$

$$U_i\frac{g}{r_0}\exp(ikr_0)\exp(\frac{i\pi x'^2}{\lambda})J_0(\frac{2\pi x'a}{\lambda r_0})$$

where $J_0(\xi) = \frac{1}{2\pi}\int_0^{2\pi}e^{-i\xi\cos\varphi}d\varphi$ is the Bessel function of zero order.

The relative intensity of the diffracted beam $U^{RS}(x',0,g)$ with respect to the input field U_i, in the additional hypothesis that the gap is much larger than the dimensions of the radius of the obscuring disk, $g >> a$, which leads to the approximation $g \approx r_0$, is given by:

$$I_{rel}(\rho') = \frac{I^{RS}(\rho',g)}{I_i} = \left|\frac{U^{RS}(\rho',0,g)}{U_i}\right|^2 = \left(\frac{g}{r_0}\right)^2 \left[J_0\left(\frac{2\pi\rho' a}{\lambda r_0}\right)\right]^2 \approx \left[J_0\left(\frac{2\pi\rho' a}{\lambda z}\right)\right]^2$$

[1.46]

The plot of $I_{rel}(\rho')$ with ρ' represented in units of $\frac{\lambda z}{2\pi a}$ is shown in Figure 1.24.

The conditions in our experiments were E~2 KeV, i.e. $\lambda = 0.56$ nm, $g = 10$ µm $a = 90$ nm. The full width at half max (FWHM) is 2 in units of $\frac{\lambda z}{2\pi a} = 9.9$ mm. Therefore a hole of ~20 nm diameter is expected.

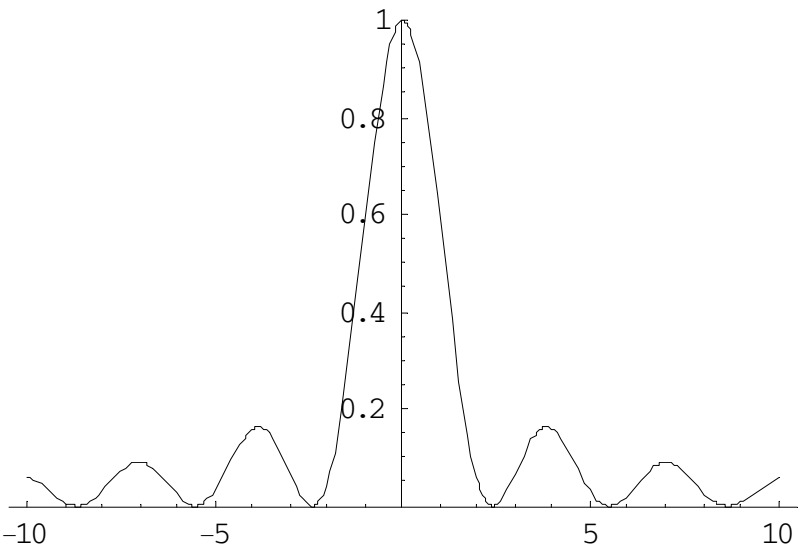

Figure 1.24. *Plot of* $I_{rel}(\rho')$ *with* ρ' *represented in units of* $\frac{\lambda z}{2\pi a}$

1.4. Applications

Here we present a series of examples of High resolution and Deep XRL.

1.4.1. *Optimal photon energy range for High resolution and Deep X-ray lithography*

In general, the optimization of any procedure needs to be done to maximize or minimize a figure of merit that represents how close the parameter or a weighted combination of parameters is from a desired target value.

In X-ray lithography the choice of the optimal conditions depends very much on the class of applications that are addressed. In particular, two main classes of applications have caused the differentiation of X-ray lithography into High Resolution X-ray Lithography (HRXRL) and Deep X-ray Lithography (DXRL). Though the principle is the same, the applications, technology, equipment, masks and problems all differ.

The main focus of HRXRL is high resolution nanopatterning. The objective is to overcome the resolution limitations of DUV lithography for its main use in the microelectronics industry. In DXRL the target application is micromechanics and MEMS, with tall (hundreds of micrometers) and high aspect ratio (i.e. the ratio between height and lateral size) structures, but with resolutions that are in the range of micrometers. This requires the use of a much more penetrating X-ray radiation, with respect to HRXRL, in order to expose thick resist films.

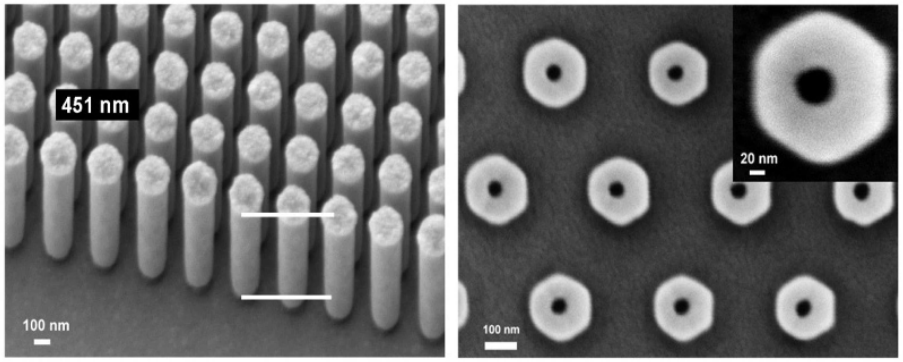

Figure 1.25. *Left: Array of gold absorber pillars on an X-ray mask. Right: Pattern of pillars obtained by X-ray lithography with a mask containing an array of pillars similar to those on the mask on the left, but arranged in an hexagonal array. Strong diffraction effects result in the formation of a hole in the middle of the dots as well as in the modified shape of the dots, reflecting the hexagonal symmetry of the array*

In deep X-ray lithography there are two main limitations to achieving high resolution patterning. One is related to the thickness of the absorber, typically gold, where the required thickness is in the range of ~ 10–20 μm in order to provide a sufficient contrast. Therefore printing features at the sub 100 nm resolution would require structures in the absorber with an aspect ratio in excess of 100, which is almost impossible to achieve. The second, more basic limitation, is that the photoelectrons generated by X-ray of 10 keV energy have a correspondingly much higher spreading range in the resist, of up to 100–200 nm.

1.4.2. *Diffraction effects on proximity lithography*

In this section, we address a study of the diffraction effects using the spectrum generated at LILIT (Elettra, Trieste, Italy). Due to the finite source size and the poly-chromaticity of the spectrum, typically 1+/-0.5nm in wavelength, the electromagnetic field responsible for the lithographic aerial image formation is partially coherent. From the Van Cittert–Zernike theorem, the spatial coherence length of the Lilit beamline is:

$$l_c^{spatial} = \frac{\lambda}{2\pi}\frac{L}{S} \cong 20\mu m$$

a value much larger than for typical patterned structures. (The beam line is characterized by a length L=25 m and by a source with cross-section of diameter S=200 μm).

Simple considerations of the role of diffraction effects on proximity lithography can be argued taking into account the diffraction pattern generated by a thin rectangular aperture. The displacement of the first satellite peak in a diffraction pattern is given by: $\delta = g\lambda / d$. For typical values of an X-ray wavelength used in proximity lithography, λ = 1 nm, with an aperture width d = 200 nm that we identify with a typical mask, and with a slit-screen distance that in our example coincides with the mask–substrate gap: g = 15 μm, the displacement, δ, is 75 nm. The linear dependence of δ on the mask–substrate gap shows that only a zero gap eliminates any diffraction effect. Typically in X-ray proximity beamlines, the residual mask–substrate gap can be decreased down to 5 μm, corresponding to a diffraction limit for one-to-one proximity lithography close to 25 nm. Since a residual gap cannot be avoided completely, the result is that diffraction plays an important role in one-to-one mask pattern replication, an issue that is widely discussed in the literature.

Here, we present an experimental investigation of diffraction effects as a function of the gap g between mask and substrate.

Three samples prepared with SAL 601 (negative tone resist) and called S5, S10 and S15 were exposed by setting the mask–substrate gap to 5 μm, 10 μm and 15 μm, respectively (Figure 1.26(a)–(c)). A fourth sample, P15, spun with PMMA (positive tone resist) was exposed with a 15 μm mask–substrate gap (Figure 1.26(d)).

What is interesting to notice is the dependence of the lattice unit cell on the mask–substrate gap distance. In the case of the 5 μm mask–substrate gap (Figure 1.26(a)) the mask features are well reproduced. This is the case for proximity X-ray lithography where almost a one-to-one replica of a mask can be achieved and where diffraction effects are almost completely suppressed by minimizing the mask–substrate gap.

By contrast, the effects of diffraction are evident on the samples exposed with a 15μm mask–substrate gap, with both negative and positive resists (Figure 1.26(c) and (d)). The square shape of the unit cell is strongly smoothed on the corners with a hole (or a pillar, depending on the tone of the resist) at the center. The patterning obtained exposing a negative resist appears to be composed of an array of rings with thin lateral walls (<50 nm). In this case the filling factor of the pattern ranges from 9% with a 15 μm gap to 28% for a 5 μm gap. Of course an opposite patterning with a very high filling factor (78%) can be achieved using a positive (PMMA) resist (Figure 1.26(d) which provides a final structure composed of thin rings etched into the epitaxial multi layer.

An even more complex case is shown by sample S10 exposed with a 10 μm mask–substrate gap (Figure 1.26(b)). In this case, a further central pillar appears, of 100nm diameter and 70 nm away from the external ring whose wall is 45 nm thick.

Several combinations of internal and external radii of the rings or a controlled smoothing of the squared angles can be achieved by choosing the right experimental conditions. The key parameter in this case is the contrast between the absolute and local maxima (and minima) of the diffraction pattern (Figure 1.26) that is high enough (more than 20%) to guarantee the modulation of the lithographic structures. The importance of the mask–substrate gap on the internal and external diameters of the rings for three different development times (30 s, 60 s and 120 s) are reported in Figure 1.28 for a PMMA resist and a dose of 3.5 J/cm^2. The results show that a large range of configurations can be achieved. At 30 s, no holes are opened in the base of the lattice that, by contrast, can be obtained at 60 s. A further increase of the development time decreases the external radius and increases the internal one, resulting in a thinning of the ring walls.

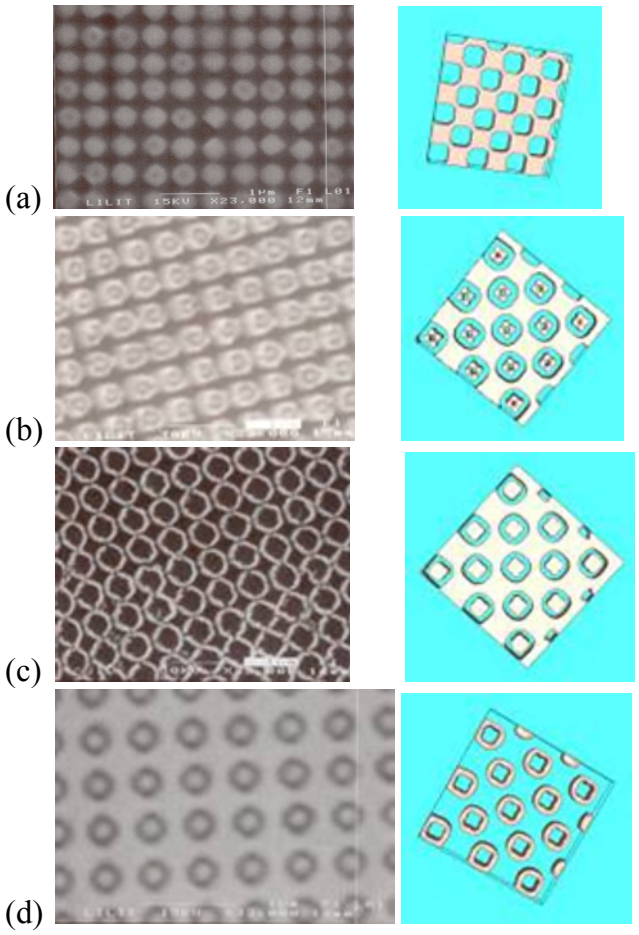

Figure 1.26. *Images obtained showing the changing mask–substrate gap. (a) sample S5: resist SAL601, 5 µm gap; (b) sample S10: resist SAL601, 10 µm gap; (c) sample S15: resist SAL601, 15 µm gap; (d) sample P15: resist PMMA, 15 µm gap. For each sample, the relative X-ray lithography simulations performed by TOOLSET code have been attached*

Modeling the diffraction pattern is important to evaluate and compensate for the distortion generated by diffraction. For this purpose, we used TOOLSET [KHA 97A, GOO 96], a computer program specifically developed to simulate the exposure and development of a resist in X-ray proximity lithography. The program requires knowledge of the parameters describing the X-ray source and X-ray mask. The input parameters are, therefore, the natural divergence of the incoming beam, the layering of the mask and its pattern, the type of resist (thickness, chemical

composition, dissolution rate), the atmosphere where the exposure takes place, the exposure and development time, and finally, the mask–substrate gap distance.

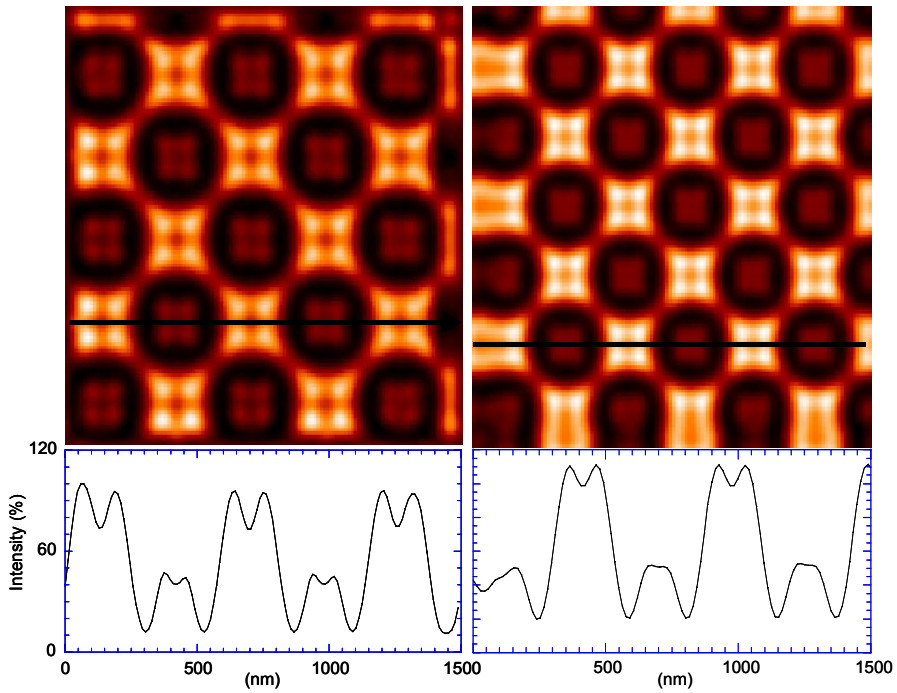

Figure 1.27. *Comparison between aerial diffraction pattern simulations generated by: (left) an X-ray mask pattern obtained by increasing the spatial blur from the real value of 1nm; and (right) a spatial blur of 10 nm. In both cases a 15 µm mask–substrate gap has been used. The bottom panels report the intensity profiles along the cut linesin the aerial diffraction patterns*

Figure 1.27(a) shows the aerial diffraction pattern obtained for a gap of 15 µm, i.e. the gap used for samples S15 and P15 (Figures 1.26(c) and 1.26(d)). The presence of peaks and troughs with position and intensity dependent on the geometrical configuration of the lattice appears clearly. The diffraction pattern intensity along a straight line crossing the squares of the pattern is shown to highlight the resist profile. It is worth noting the single strong minimum of the center of the transmitted beam that is responsible of the hole in the lattice unit base in Figure 1.26(c).

In order to show the previously discussed effect of X-ray beam coherence, in Figure 1.27(b) we have reported for comparison the diffraction pattern obtained by increasing the blur of the beam from 1 nm to 10 nm. In the latter case, we noticed a

strong decrease in the intensity modulation of the illumination pattern. The evolution of diffraction patterns along the same cut lines simulated for different values of the mask–substrate gaps and for 1nm blur is reported in Figure 1.29 showing the appearance and the development of several diffraction maxima and minima. The single strong minimum of the center of the transmitted beam for a 15 µm gap and the small secondary peak for an 11 µm gap are responsible, respectively, for the hole in the sample in Figure 1.27(a) and for the central pillar in the sample in Figure 1.26(b).

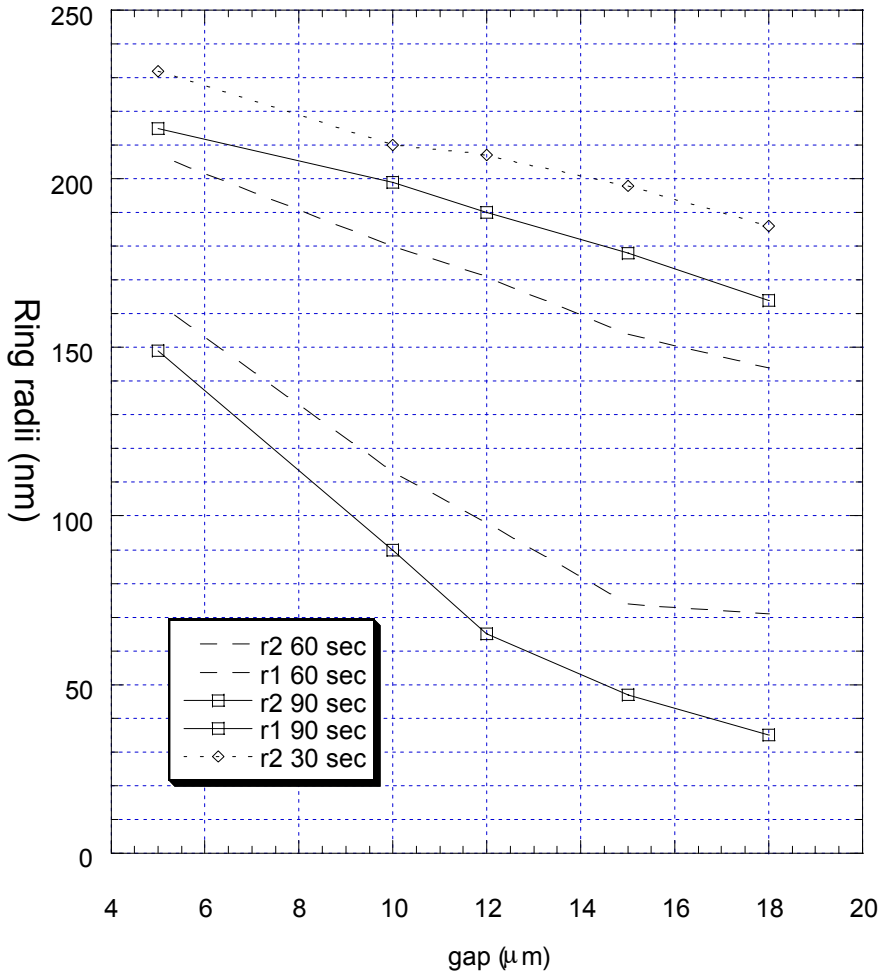

Figure 1.28. *Internal and external radius of a 2D lattice basis obtained for different mask–substrate gaps and developing times*

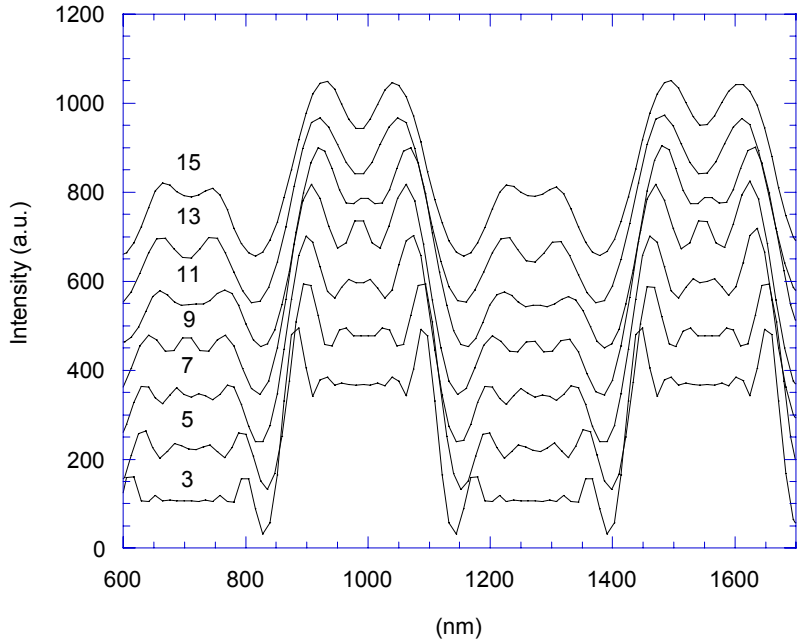

Figure 1.29. *Comparison of the intensity profiles obtained by varying the mask–substrate gap from 3 to 15 µm*

Diffraction is not the only effect that must be controlled to achieve the final lithographic pattern. In order to correctly develop the exposed resist, an accurate optimization of the exposure dose and development time are required. A study of these has also been performed exploiting the part of TOOLSET devoted to resist development. PMMA and SAL 601 resist dissolution rates [KHA 97B] were introduced to compute the evolution of resist development time on a representative area. A good agreement with the experimental features has been obtained; as an example, the square shape of the internal hole in Figure 1.26(d) is reproduced well.

1.4.3. *High resolution 3D nano structuring*

3D high resolution structures can be obtained using hybrid lithographic techniques. In fact, by combining different fabrication techniques it is possible to overcome the limitations and fully exploit the advantages of every single process, and to enlarge the class of micro- and nanostructures that can be fabricated. Below, two examples of such an approach are presented in order to give an idea of what can be achieved. We will describe the fabrication of optical waveguides embedded in 3D

photonic crystals fabricated by a binary resist process, using X-ray Lithography (XRL) and Electron beam Lithography (EBL).

Photonic crystals (PhC) are periodic dielectric structures exhibiting a photonic band gap (PBG) – a wavelength range in which light cannot propagate [YAB 87, YAB 91, JOH 87, JOA 95, SAK 01]. Because of their ability to efficiently trap [FOR 97], reflect [JOA 97], and guide [LIN 98] light in 3D, photonic crystals designed for optical wavelengths are expected to greatly increase the density of integrated optical circuits. The ability of directing light is based on the capability of designing and fabricating structural defects locally breaking the discrete translational symmetry of the PhC lattice. Isolated photonic levels arise inside the PBG compelling light of the appropriate energy-frequency to be effectively confined in the region defined by the defect itself [JOH 02]. In the case of a waveguide, a line-defect in the regular lattice of a PhC compels light to follow the defect path through a µm-scale sharp bend [ZHI 03]. This scheme had already been successfully implemented for the realization of two dimensional (2D) PhC using a layer-by-layer fabrication approach [BAB 01]. However, such waveguides in 2D PhC show strong dissipation effects due to an unavoidable loss of light out of the plane [LI 04, AND 03]. A complete photonic band can occur only in 3D PhC [LIN 99], widely studied theoretically. However, their experimental fabrication still remains a challenge. An original fabrication method was proposed by Yablonovitch using millimeter-scale periodic arrays of holes drilled into a dielectric medium to realize 3D PhC at microwave frequencies. The resulting lattice structure is called Yablonovite (after his name) [YAB 91]. A parallel lithographic approach suitable for mass production has been implemented using tilted X-ray lithography on PMMA for the fabrication of Yablonovite structures with lattice parameters in the range of hundreds of micron [FEI 97] and subsequently in the range of 1 µm by Cuisin *et al.* [CUI 00a].

We applied a hybrid lithography method for the fabrication of linear defects embedded in a 3D metallic Yablonovite structure that satisfies the requirements for a waveguide.

The process developed exploits the combination of two resist exposures by using a protocol sequence of EBL and XRL (Figure 1.30). A 5 µm thick PMMA was previously spun on a silicon substrate coated with a base plating layer and successively baked. On top of this layer, a 500 nm thick film of SAL-601 negative resist is spun and pre-baked (Figure 1.30(b)). EBL is performed (Figure 1.30(c)) with an exposure dose high enough to expose SAL-601 but unaffecting the bottom PMMA resist layer.

After the EBL exposure, post exposure baking and development are performed resulting in a chemical polymerization of SAL-601 shaped in the designated pattern lying on the top of the first PMMA layer (Figure 1.30(d)). Subsequently, a second

5 µm thick PMMA layer is spun on top of the previously patterned sample and baked to assure the perfect homogeneity of the two PMMA layers, embedding the predefined SAL-601 pattern (Figure 1.30(e)). XRL is then performed in a multi-tilted configuration (Figure 1.30(f)).

XRL has been performed on the LILIT beamline located at the Elettra Synchrotron (Trieste) [ROM 01]. After XRL, the whole block of the PMMA layer pattern is developed without any further baking. The SAL-601 structure at this point is completely embedded in the PMMA resist structure, which is used as a template for a final electroplating metal growth, followed by stripping of the PMMA in a warm acetone at 50°C (Figure 1.30(g)).

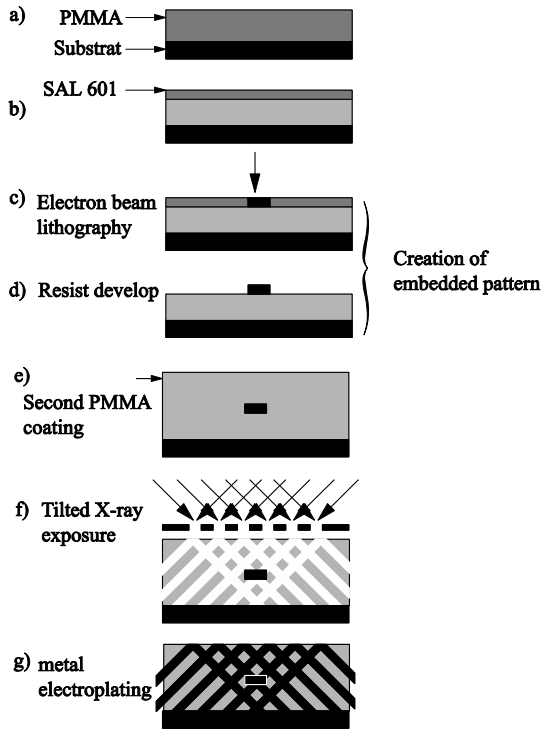

Figure 1.30. *Flowchart of a hybrid lithography process. Resists of opposite tone are combined in two distinct lithographic processes. After a first PMMA coating and baking (a), a second resist SAL-601 is spun, baked (b), exposed by electron beam lithography (c) and developed with MF312 (d). Following this, a second PMMA coating is spun and baked (e). X-ray lithography is performed in the tilted configuration (f) without affecting the SAL-601 patterning. The final structure can be used as a template for a final electroplating metal growth (g)*

From a fabrication point of view, a metallic structure can be used as a more stable and resistant template for infiltration of high refraction index materials. Metallic structures *per se* can have, however, interesting photonic crystals as verified by preliminary optical characterization [ROM 03b]. The resulting structure, a line-defect in a 3D metallic Yablonovite structure, is shown in Figure 1.31. The resist wire is perfectly embedded in the structure and thereby defines a perfect tube-like defect.

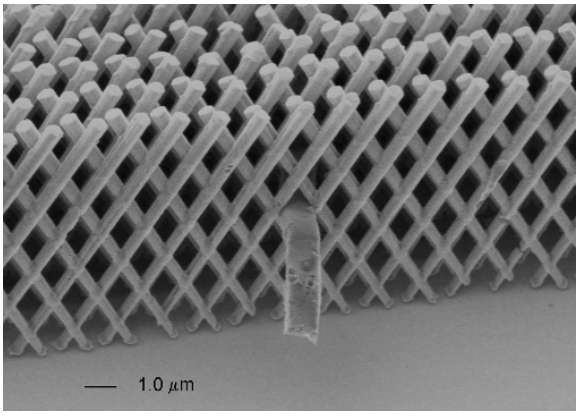

Figure 1.31. *Waveguide defect made of a resist included in 3D metallic Yablonovite structures without any distortion of the lattice structure. The defect runs along the whole length (500 μm) of the sample and can be seen through an occasionally un-grown zone of the 3D lattice*

1.4.4. *3D polymer structures by combination of NanoImprint (NIL) and X-ray lithography (XRL)*

NIL is a high resolution (sub-10 nm), low cost, high throughput technique that has intrinsically 3D replication potential, having the capability to form smooth curved surfaces over large areas [MIN 01]. Due to these characteristics it is emerging as a possible mass-production technology in the field of micro- and nanosystems. A large variety of 3D master profiles can be transferred into a polymer film by NIL. However limitations exist for arbitrary shapes. First, there is the difficulty of fabricating arrays of structures non-perpendicular to the substrate or having overhanging parts. This problem relates to the possibility/impossibility of releasing the mold from the polymer, due to the interlocking of the nanostructures of the stamp and polymer. A further limit is the maximum aspect ratio (~3) of the structures due to the stresses produced by shear and tensile forces at the surface of micro/nanostructures during the release of the master.

By contrast, XRL is well known to provide aspect ratios attaining values of ~20 (for structures with µm scale resolution), and a resolution that, in its present state of development, can go below 50 nm. Geometrically, the structures obtainable by XRL can be described as the intersection of (a) the volume shadowed by a two-dimensional pattern defined on a mask with (b) the volume of the resist film. As the two-dimensional pattern of the mask can be projected in arbitrary directions with respect to the resist film, XRL also allows tilted structures to be defined. Furthermore, by performing single or multiple exposures at tilted angles, it has been possible to build complex 3D structures containing voids and overhanging parts [CUI 00b, [ROM 03a].

We have developed an innovative lithographic approach that combines NanoImprint (NIL) and X-ray lithography (XRL) for fabricating unconventional 3D polymer structures. The use of XRL to structure a pre-patterned resist by NIL gives rise to high-resolution high-aspect-ratio structures whose overall profile is enveloped by the original 3D imprinted profile [TOR 04]. A master with continuous 3D profile was fabricated using isotropic etching of a fused silica substrate in order to form an array of hemispherical cavities of ~20 µm diameter. For the imprinting step, a silicon substrate was coated with 6 µm of PMMA, and hot embossing was performed according to standard procedures, at a pressure of 20 MPa and a temperature of 210°C [MIN 03].

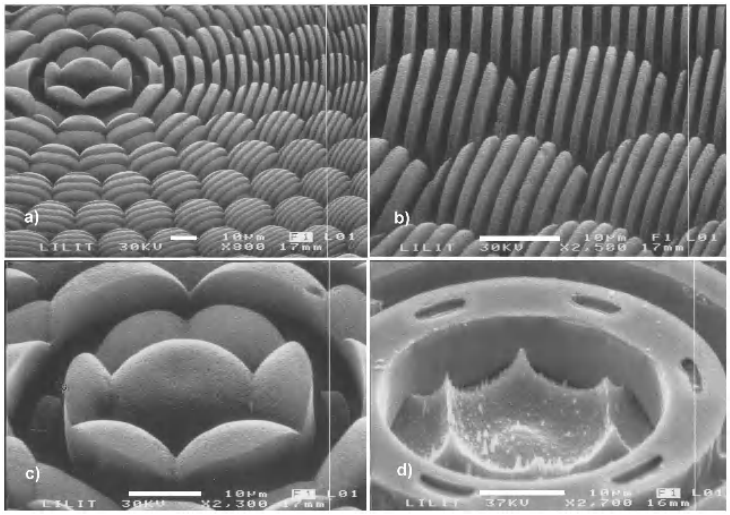

Figure 1.32. *(a–c) Zone plate structure superimposed on the 3D profile of an array of hemispheres; (d) inverted 3D structure by nickel electroplating. Scale bars correspond to 10 µm*

After the process of hemisphere imprinting, a set of samples was exposed at the XRL LILIT beamline selecting a spectrum energy window that allowed the full exposure of the thickest (9 μm) part of the hemispheres. One of the samples three-dimensionally structured by NIL/XRL was further processed in order to demonstrate the possibility of generating a master for imprinting or injection molding, and therefore suitable for mass production. The sample was sputter coated with a 40 nm film of palladium-gold which was used as base plating for the electrochemical growth of Ni. Figures 1.32(a–c) show the results of the process demonstrating that special optical elements containing refractive and diffractive components could be produced. Figure 1.32(d) shows the negative of the central part of the 3D object obtained by nickel electroplating.

Such a technique could become particularly suitable for prototyping masters for imprinting and injection molding, thus requiring the limited use of a highly expensive technique, while mass production would be committed to low cost techniques.

1.4.5. *Micromachining and the LIGA process*

DXRL is a competitive technology for the production of micro-fabricated parts of high accuracy and high aspect ratio. It can be used in small or medium volume production batches or to supply high throughput replication techniques, such as injection molding, with very high quality metal molds. In recent years, in addition to micro-electro mechanical systems (MEMS), interest from the scientific community, start-ups and industries has been growing for the production of microfluidic systems. Microfluidics is a field of applied science and technology, whose aim is to develop ways of using, mixing and multiplexing fluids (liquids and gases, typically highly expensive or only available in small amounts) in channels and reservoirs which range in size from 1–1000 μm. In a microfluidic system, micro channels, micro pumps, micro valves and filters have to be integrated, as well as providing a connection to the macroscopic world (involving liquid reagents, pressures, temperatures) [WHI 06]. The characteristics of DXRL [SCH 94] can offer important advantages to the development of some microfluidic applications, for the following reasons:

1. It is possible to do a sequence of aligned exposure in order to integrate different levels and parts in the same device;

2. DXRL provides high aspect ratio for the production of deep channels with smooth surfaces (optically finished);

3. DXRL permits the use of plastic materials, for the production of disposable and cheap devices (very interesting for bio-medical applications).

Three examples follow in which DXRL has been very useful in solving the technological challenges imposed by the applications.

1.4.5.1. *Micro-mixer*

The purpose of the device we present here is the study of the evolution of chemical reactions within the first milliseconds and with high time resolution (i.e. monitoring the consumption of reagents and growth of products) [MAR 09].

Two reagents have to be mixed to initiate a chemical reaction. Mixing two liquids at the macroscopic level introduces a large uncertainty in the time that can be taken as t=0 for the reaction, as this depends on the timescale at which intermixing occurs, which is mainly determined by convection. Therefore, different volumes of the mixture of the reagents can be at different stages of the reaction. A micromixer with a configuration like the one shown in Figure 1.33 was selected because the flux is laminar in the microchannels even at high flow rates, and mixing is based only on diffusion which can be precisely described, leading to a much lower uncertainty in setting t=0 for the reaction [KNI 98]. One of the two chemical reagents is inserted in the central channel, while the other is put in the two lateral ones. The central flux is squeezed by the lateral ones, obtaining a so-called hydrodynamic focusing.

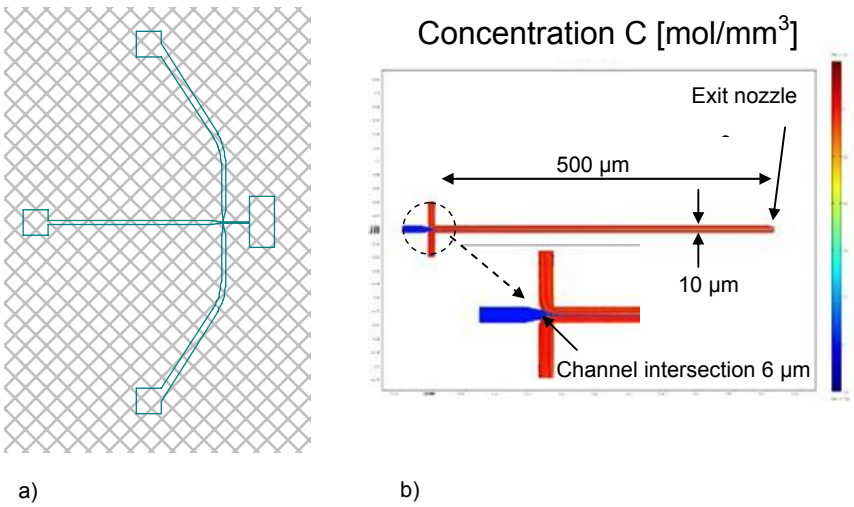

Figure 1.33. *(a) Device layout optimized for rapid mixing of two reagents; and (b) simulated concentration of chemical species. The inlet and outlet nozzles were designed to obtain complete mixing inside the mixer and a jet at the exit with a velocity of 10 m/s*

Simulations of microfluidics (conducted with COMSOL multiphysics commercial Finite Element Analysis software) have been based on the following requirements:

1. Channels with high aspect ratio (>10).

2. A 6 μm inlet nozzle with a particular shape to avoid recirculation of fluids and better focusing performance.

3. A precise profile of the features, with vertical walls down to the bottom of the device (otherwise the mixing of liquid A and B at the top and the bottom of the micro channels would occur at different timescales).

4. A transparent plastic body, transparent for ease in assembling the parts and plastic to guarantee a chemical compatibility with the reagents of interest.

5. A stable free jet at the exit of the device, where measurements of the chemical reaction evolution can be conducted without interference from the channel walls. The mixing of the reagents is obtained inside the device, while the measurements start just at the outlet nozzle.

The geometry of the channels should be able to provide perfect control of the flux of the reagents, as the reproducibility and consistency of the measuring results depend on knowledge of the mixing zone (i.e. time) and on the flow rate inside and outside the device.

The resulting velocity of the jet from the nozzle is ~10 m/s, which ensures a time resolution of less than 100 μs. In this experiment, the measurements have been conducted with Small Angle X-ray Scattering (SAXS), using the SAXS beamline at Elettra [AME 98].

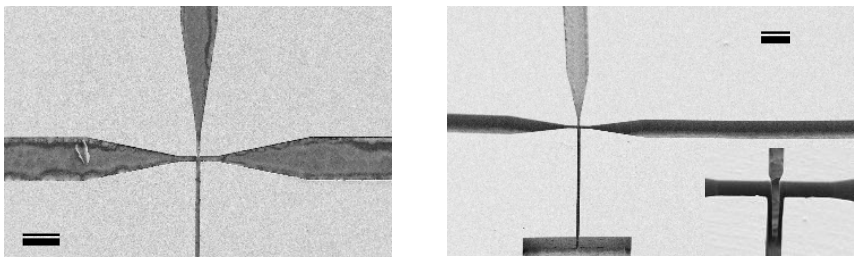

Figure 1.34. *(a) SEM picture of the final mask; the thickness of the gold layer is 1.7 μm; (b) device channels after developing the exposed PMMA slab; a close up view of the inlet channels is shown in the inset (bottom right)*

Such stringent requirements on the device geometry required the use of DXRL. First, a DXRL mask was obtained using a two step process based on the fabrication of an X-ray mask by EBL, which is replicated with soft X-ray lithography, to obtain the final working mask (see Figure 1.13). The final mask, together with an SEM image of the device after exposure and development, is shown in Figure 1.34.

The exposure was made on a slab of PMMA 1 mm thick. The sample was mounted on the mask using a 50 µm Kapton© foil as a spacer to avoid dangerous contact between the surface of the sample and the fragile nitride membrane of the mask. A *Jenoptic* Gmbh scanner provides an average constant dose on the exposed area, scanning in the vertical direction with a velocity of 20 mm/s; the dose was calculated to obtain a depth in the channels of 60 µm, where the dose imposed should be between 3 and 4 kJ/cm^3.

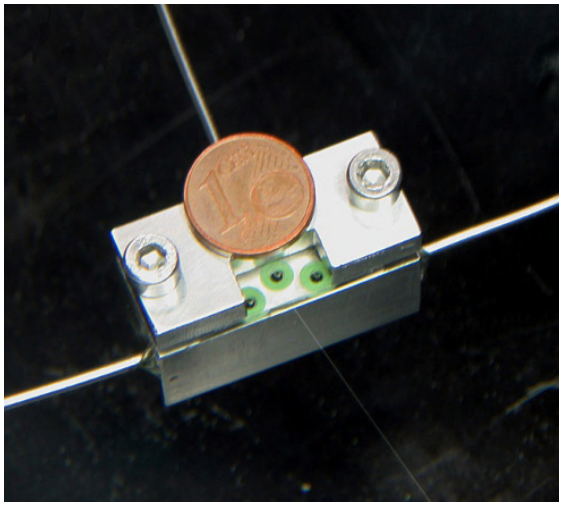

Figure 1.35. *Image of the free jet obtained at the exit of the final device mounted in the steel sample holder. The three inlets are fed by means of syringe pumps connected via HPLC-type connections (not visible in the photograph)*

The microfluidic device was sealed by thermally bonding a thin sheet of PMMA (0.5 mm thick). A pumping system composed of three syringe pumps, able to provide constant flux of reagents at high pressure (up to 16 bar), was used to introduce liquids A and B. Figure 1.35 shows the device mounted with the sample holder, and fed by the pump; the free jet is also visible, with a cross-section of 8x60 µm and speed of ~10 m/s.

The device for micro-mixing, producing a free jet suitable for the measurement of the kinetics of chemical reactions in ultra-fast regimes (i.e stable in air and with laminar flow) is shown to work as predicted by simulations in the design step process. By using DXRL, very high quality micro-channels, using PMMA sheets, have been fabricated. The sealing system and the assembly set-up engineered for this experiment made it possible to use devices produced with ease and fast mounting, implementing the idea of fast and reliable use of disposable devices in a new kind of time-resolved scientific experiments.

1.4.5.2. *Micro-needle fabricated by LIGA and casting*

The controlled delivery of drugs to specific organs or parts of the body at a well defined rate is becoming an important therapeutic objective in modern medicine. Several invasive and non-invasive techniques have been developed already, such as silicon micro needles, implanted micro-chips or micro particle reservoirs [TAO 03]. Transdermal delivery based on micro needle arrays is recognized as one of the most promising methods, because of the possibilities of offering a wide range of delivery rates compared to other systems, and of using disposable devices, minimum invasiveness and high patient comfort.

Human skin is made up of three layers, as shown in Figure 1.36. The outer layer (the epidermis or *Stratum Corneum*), is 20 µm thick and is mainly made up of dead cells. The layer underneath (the dermis), consists of capillaries with blood vessels and living cells, but contains few nerves; its thickness is around 50–100 µm. The bottom layer is the hypodermis, which forms the bulk of the skin's volume, and contains nerves and capillaries.

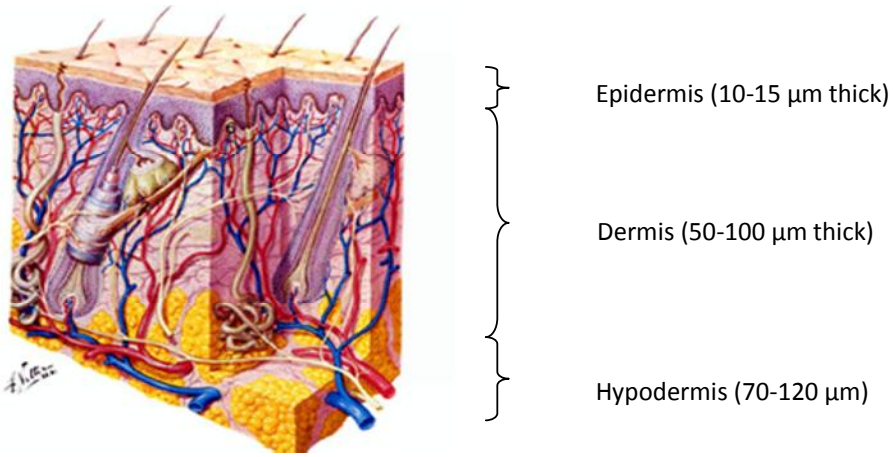

Figure 1.36. *Structure of human skin, in which three layers are visible*

Effective delivery of drugs through the skin requires reaching the hypodermis layer so that interstitial fluid can absorb the drug and then diffuse it into the blood stream through capillaries; at the same time, skin penetration has to be limited to lower the chance of causing pain through nerve pinching.

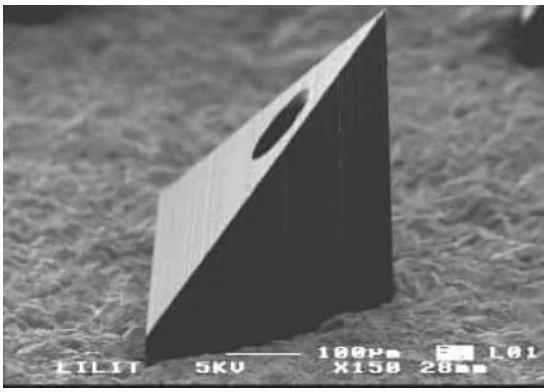

Figure 1.37. *SEM image of a polymeric micro needle fabricated by DXRL*

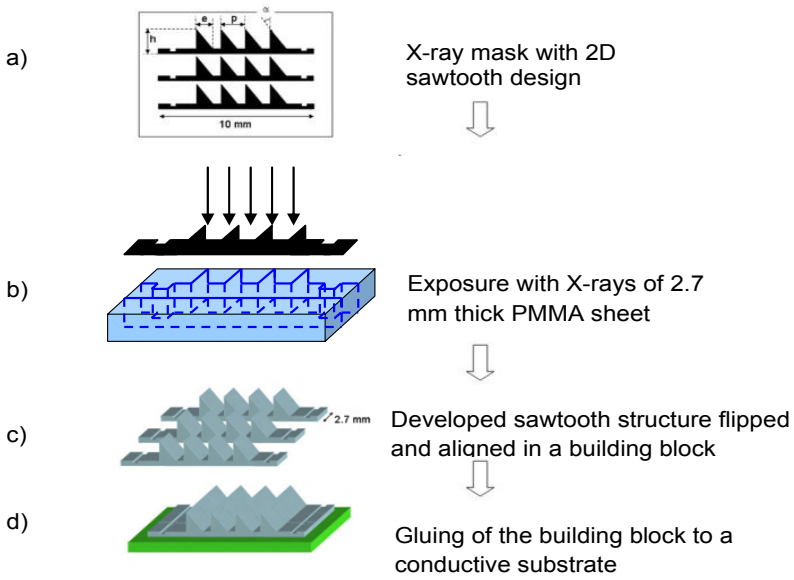

Figure 1.38. *(a) Pattern of a DXRL mask; (b) exposure of a sawtooth grating, laying on a 2.7 mm thick PMMA sheet substrate; (c) and (d) fillets of PMMA with sawtooth structures assembled and glued on a conductive substrate*

The first process used to fabricate hollow microneedles was based on silicon technology [MCA 00]. However, silicon is a brittle material. Instead, we used DXRL to build micro needle arrays made of polymer materials [PER 06]. The SEM image in Figure 1.37 shows the final result.

Using an X-ray mask with sawtooth pattern (shown in Figure 1.38(a)), a series of 2.7 mm thick slabs of PMMA are exposed. Three of them are glued onto a conductive substrate. The resulting structure is shown in Figure 1.38(c), with a total area covered of 8x10 cm. This assembly is then exposed again using DXRL, with a second mask containing an array of equilateral triangles. Each of them has a hole of controlled diameter and positioned near a corner which will act as the future needle tip, and symmetrically distant from the other two (see Figure 1.39).

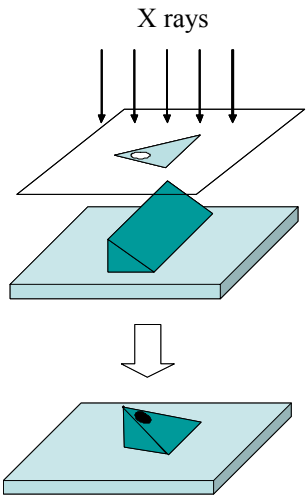

Figure 1.39. *Using a mask with a pattern made by an equilateral triangle with a hole near one corner. Exposure to X-rays produces the needles array starting from the building block prepared before*

The developing of the assembled structure after this second exposure is stopped before fully opening the internal holes. Since the developing rate is different between large and small open areas, inside the holes a residual PMMA layer, remains, as shown in Figure 1.40(a).

Copper is then deposited by electrolytic growth on the fully developed parts around the needles, and not in the holes where residual undeveloped PMMA remains. The thickness of this metal layer will determine the offset h_m between the base of the needle and the central pillar that will serve for molding holes through the

entire thickness (see Figures 1.40(a) and (b)). Growth is stopped leaving the tip free, for a thickness which is that of the final device's tip. A final development of the structure opens the bottom of the holes.

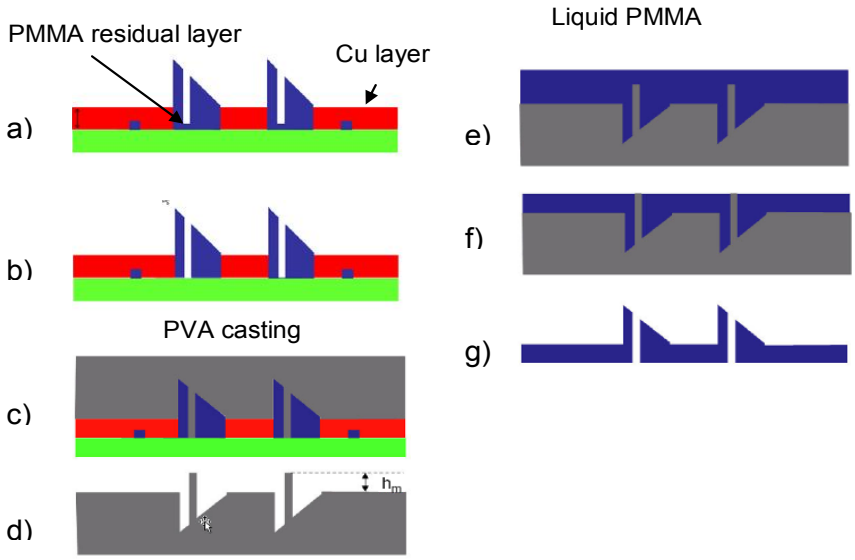

Figure 1.40. *Mold preparation and replication via soft polymer casting: (a) electrolytic growth of Cu layer in the partially developed structure (outside the needle triangles; (b) full development after Cu layer growth; (c) casting with soft polymer (i.e. PVA); (d) Negative replica of the mold; (e) casting of liquid PMMA in the negative replica; (f) back polishing to open the needle hole; (g) release of the PMMA replica from the PVA; this is the final device*

The structure obtained in this way is the working master for the replication process. A soft material (PVA) is cast in its liquid state and peeled off once it has solidified (Figures 1.40(c) and (d)). The soft replica is filled with liquid PMMA and left to polymerize into its solid state using appropriate heat treatment. The base of this casting is usually closed, because the casting of the polymer is thicker than the master base. To open the needle channel, this excess thickness must be removed, avoiding damage to the structure: for a few microns thickness, a dry etching using oxygen plasma is used; otherwise mechanical lapping is used.

Once the PMMA has hardened, the needle array has to be de-molded. Since PVA is soluble in water while PMMA is not, the de-molding process consists of dissolving the master in water, leaving the PMMA device undamaged (Figures 1.40(e–g)).

1.4.5.3. *Microturbine rotors for power generation in portable systems*

LIGA can be employed for the production of metallic structures with a high aspect ratio and surface roughness better than that usually obtained with micro-mechanical tools. The example presented here describes the whole process from lithography to micro-machining for the production of microturbine rotors [MAR 04].

Figure 1.41 shows a rocket engine layout. It is based on a microturbine powered by compressed gas to generate electricity. Such a power generator is of interest in astronautics, in particular for micro-satellites, for position and orientation control, and could be applied to provide energy requirements for small portable devices for a long term stability and functionality without recharge. The application field benefits very much from a lowering of the size and weight of the structural and service parts of the device.

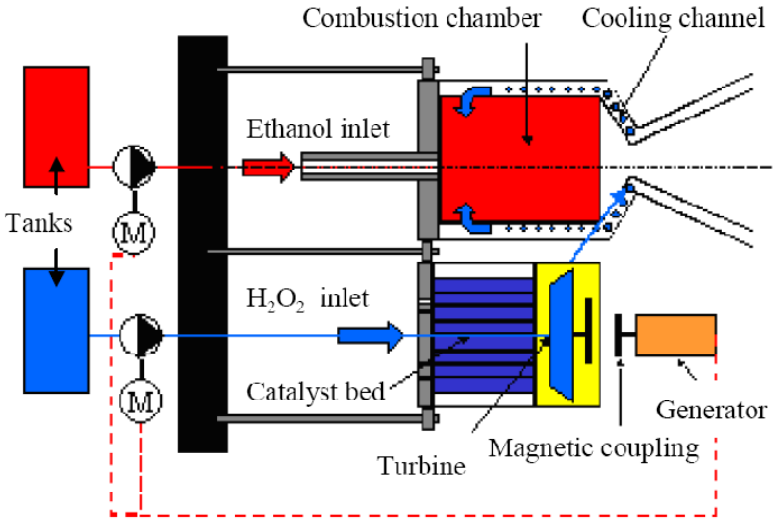

Figure 1.41. *Diagram of a rocket engine layout. A micro turbine is used as an electrical generator for satellite applications. The combustion of ethanol and oxygen peroxide produces pressurized gases, which drive the turbine. The rotation of the rotor is coupled with a micro motor, used in reverse mode for power generation*

The turbine in this system was designed to be magnetically coupled with a commercial micro motor, working in reverse mode as a generator, and driven by pressurized gas produced by the combustion of a mixture of ethanol and hydrogen peroxide. The blades of the turbine were designed with a constant section area

(Figure 1.42(a), so that the gas flowing in the channels between them could expand only at the exit nozzle. In this way, only kinetic energy is exchanged, without a contribution from enthalpic phase changes (which occur only in the nozzle).

Whereas most of the microturbine components had dimensions compatible with conventional high precision micromachining techniques, the complex shape of the rotor blades required LIGA and electro discharge machining (EDM) (details of this technology are well discussed by Ajit Singh and Amitabha Ghosh [SIN 99]). The fabrication process is shown in Figure 1.42(b).

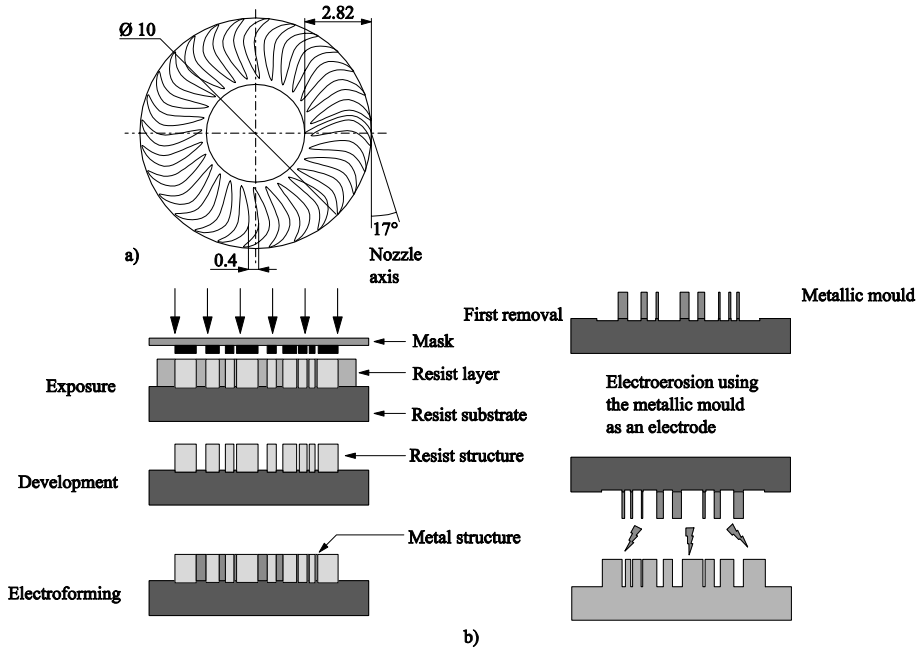

Figure 1.42. *(a) Design of the turbine rotor, with geometrical dimensions; (b) DXRL and electroforming process for production of the rotor's metallic mold. The metallic mold is then used as a template for electro discharge machining, producing a replica of the rotor in a bulk metallic ingot*

PMMA, 1 mm thick, is glued to a conductive substrate (a silicon wafer covered by a 2 μm thick layer of TiO) and exposed to X-rays through an appropriate mask. After development of the shadow image, a metallic structure is grown in a copper sulphate electrolytic bath. At the end of this process, the top surface of the sample is polished in order to obtain electrodes with a smooth surface. The silicon wafer is then etched in a KOH bath to release the structures.

The final product is an array of copper microelectrodes and microrotors, each with a diameter of 10 mm (see Figure 1.43). Each of them is then cut and mounted on a copper holder for the EDM machine. Electro Discharge Machining consists of the generation of pulsed electric sparks between an electrode and the electrically conductive work piece which are separated by a dielectric liquid. The sparks melt and erode the material, which is then removed by mechanical impact and flushed away by the dielectric liquid.

Figure 1.43. *Rotors obtained after electroplating. The structure is used as a master electrode for the Electro Discharge Machining process*

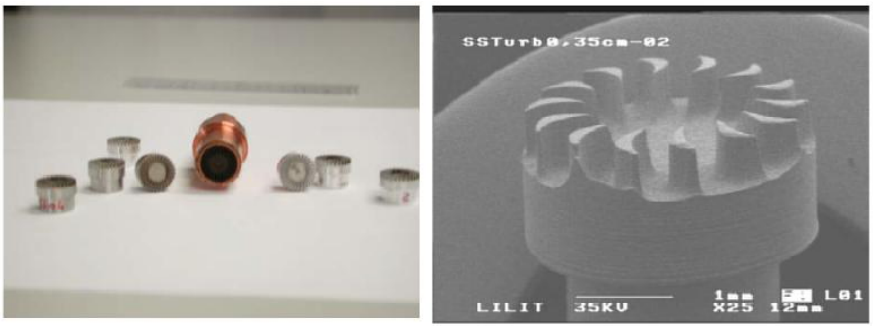

Figure 1.44. *Rotors produced by EDM: (left) showing a 10 mm diameter structure; and (right) an SEM image of a 3.2 mm diameter rotor*

EDM allows the parts to be obtained by erosion from a solid bulk ingot of metal, instead of forming it by electroplating which leads to metallic parts of lower mechanical strength, and limits the choice of materials to the available electrolytic solutions. Rotors with diameters of 10 and 3.2 mm were fabricated using different metallic materials such as stainless steel, aluminum and a magnetic alloy (FeNdB). Images are presented in Figure 1.44.

Tests performed with the stainless steel rotors of 10 mm diameter, using cold air as a driving fluid, showed the capability of this system to deliver a power up to 4 W at 80,000 rpm with an inlet pressure of 0.5 MPa.

1.4.9. *Micro-optical element for distance measurement*

Positioning measurement is one of the most important features of equipment and system characteristics in factory automation (FA) and semiconductor manufacturing. Among the different possibilities, a micro optical distance sensor based on the triangulation principle is widely chosen because of its non-contact inspection and high resolution.

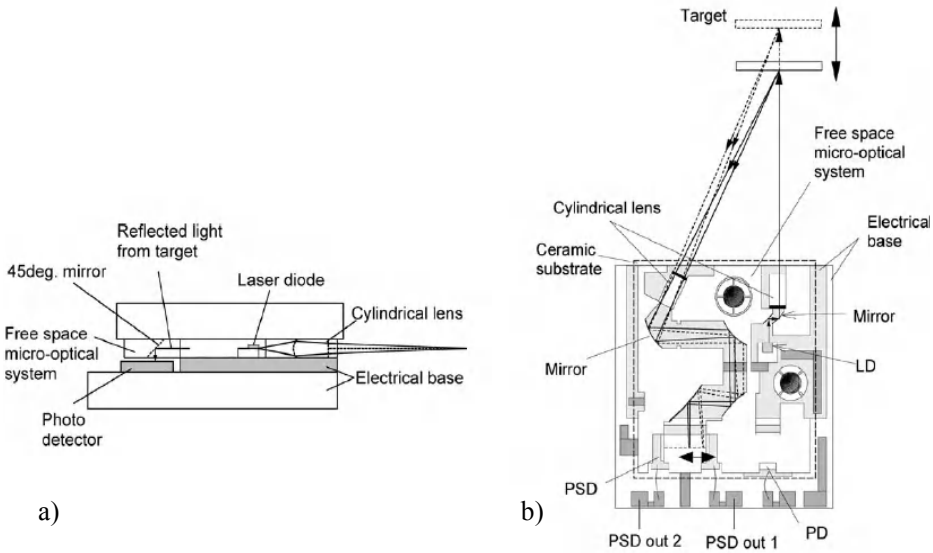

Figure 1.45. *(a) Side view of an optical system for distance measurement; (b) top view of the device: a laser diode illuminates the target, from which reflected light is collected by a cylindrical lens, and travels through several mirrors to the photo detector*

T. Oka *et al.* [OKA 03] presented a production scheme based on LIGA and injection molding. Their optical triangulation distance sensor consists of an illumination optical system and a detection optical system, both shown in Figure 1.45.

The operating principle of this class of device is as follows. An electronic photo sensitive detector (PSD) is used to record the position of a target object. The target object is illuminated by a photo diode emitter embedded in the device; the light produced by the diode is focused horizontally by the mirror and vertically by the cylindrical lens. Then, part of the scattered light returns to the device, where it comes in through a window and meets a second cylindrical lens. To enhance the resolution of the measurements, the optical path of this light is increased using four mirrors; a final 45° mirror just above the PSD deflects the light by 90°. As the incident position of the light on the PSD depends on the target position, the distance between the sensor and the target can be measured.

All mirrors and lenses should have surface roughness suitable for optical applications and be of a shape calculated for the geometry of the sensor. These requirements, together with the necessity to integrate small parts in a small system, achieving a light pathway inside the device that is as long as possible, suggest the LIGA process for fabrication of a suitable master, and injection molding for the high throughput achievable.

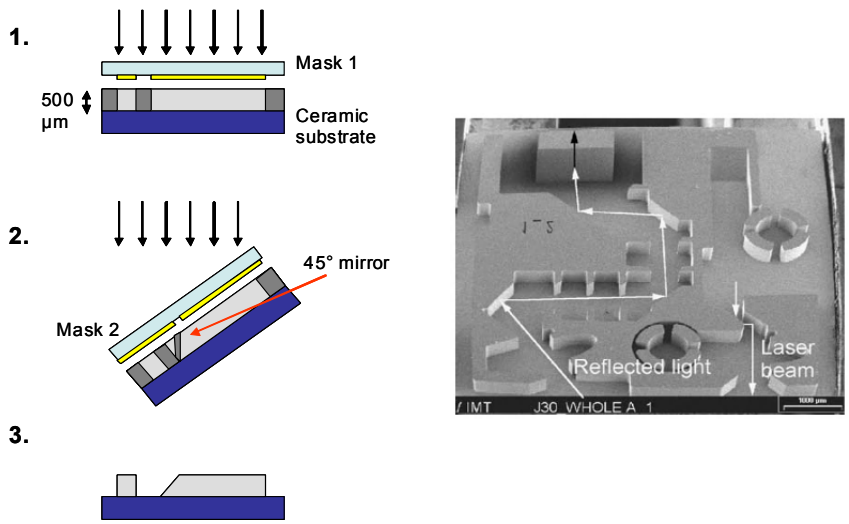

Figure 1.46. *Left: fabrication procedure for the free space micro optical system: 1. the perpendicular structure is first exposed; 2. a 45° mirror is patterned, then tilts the target and mask together; 3. the resulting structure after development. Right: an SEM image of the structure obtained*

This device was produced in PMMA with the fabrication procedure shown in the left part of Figure 1.46. The right part shows a SEM picture of the resulting structure, where the pathway of the laser light is shown.

For the final application, the device is plated by evaporation with a thin layer of gold, to improve the reflectivity of the mirrors' surfaces. The two cylindrical grooves visible in the SEM image are used for alignment in the mounting of the device with a packaging system.

The final device is then a sensor with an electrical I/O interface (embedded in the base of the package) able to measure displacement in the range 5.5 to 6.5 mm with an error of less than ± 2.0 %, and repeatability of the single measure with an error of 0.3 % (3 µm absolute maximum value).

1.5. Appendix 1

This Appendix comes from Snell's law (or the law of refraction), $n_1 \sin\varphi_1 = n_2 \sin\varphi_2$ which is reduced to $n \sin\varphi_{\mathrm{v}} = n_m \sin\varphi_{\mathrm{m}}$ where φ_{v} and φ_{m} are the angles that a refracted ray makes with the normal to the surface in vacuum and inside the material, respectively. The phenomenon of total reflection (internal in the visible range, external in the case of X-rays) is explained by the bifurcation in Snell's equation, corresponding to the physical condition that the refracted ray is parallel to the surface, i.e. $\theta \equiv \pi/2 - \varphi = 0$ where θ is the angle of incidence with the surface. For X-rays traveling in a vacuum and impinging at a grazing angle on a material, the bifurcation condition in Snell's law is written as $\sin(\pi/2 - \theta_c) = n_m \sin\pi/2$, which can be approximated for the small angle θ by $1 - \theta_c^2/2 \approx 1 - \delta(E = \hbar\omega)$, from which follows $\vartheta_c = \sqrt{2\delta(\hbar\omega)}$.

1.6. Bibliography

[AIG 98] AIGELDINGER G., CRAFT B. & MENZ W., "Simulating 3-Dimensional Deep X-ray Lithography Using the CXrL Toolset", *MSM 98 Technical Proceedings of the 1998 International Conference on Modeling and Simulation of Microsystems*, Nano Science and Technology Institute, 1998.

[AME 98] AMENITSCH H., RAPPOLT M., KRIECHBAUM M., MIO H., LAGGNER P. & BERNSTORFF S., "First performance assessment of the small-angle X-ray scattering beamline at ELETTRA", *Journal of Synchrotron Radiation*, 5, 506–508, 1998.

[AND 03] ANDREANI L.C. & AGIO M., "Intrinsic diffraction losses in photonic crystal waveguides with line defects", *Appl. Phys. Lett.* 82 (13), 2011–2013, 2003.

[ATW 99] ATWOOD D., *Soft X-rays and Extreme Ultraviolet Radiation: Principles and Applications*, Cambridge University Press, Chapter 6, 1999.

[BAB 01] BABA T., FUKAYA N. & MOTEGI A., "Clear correspondence between theoretical and experimental light propagation characteristics in photonic crystal waveguides", *Electronics Letters* 37 (12): 761–762, 2001.

[BAU 94] BAUER, H.D., (ed.*). LIGA Technique*, *Training in Microsystems UETP MEMS course*, 1994.

[BEC 86] BECKER EW, EHRFELD W, HAGMANN P, MANER A & MÜNCHMEYER D, "Fabrication of microstructures with high aspect ratios and great structural heights by synchrotron radiation lithography, galvanoforming and plastic molding (LIGA process)", *Microelectron. Eng* 4, 35–36, 1986.

[BIL 05] BILDERBACK D.H., ELLEAUME P. & WECKERT E., "Review of third and next generation synchrotron light sources", *Journal of Physics B: Atomic, Molecular and Optical Physics*, 38 (9) S773–S797, 2005.

[BRO 94] BROWNING R., LI T.Z., CHUI B., YE J., PEASE R.F.W., CZYIEWSKI Z. & JOY D.C., "Empirical forms for the electron/atom elastic scattering cross-sections from 0.1 to 30 keV", *J. Appl. Phys.* 76, 2016, 1994.

[CAB 05] CABRINI S, PÉRENNÈS F, MARMIROLI B, OLIVO A, CARPENTIERO A, KUMAR R, CANDELORO P & DI FABRIZIO E, "Low cost transparent SU-8 membrane mask for deep X-ray lithography", *Microsystem Technologies* 11(4–5), 370–373, 2005.

[CAR 98] DE CARLO F., MANCINI D.C., LAI B., "Characterization of exposure and processing of thick PMMA for deep X-ray lithography using hard X-rays", *Microsys. Technol.* 4 (2), 86–88, 1998.

[CER 92] CERRINA F., GUO J.Z., TURNER S., OCOLA L., KHAN M. & ADERSON P., "Image formation in X-ray lithography: Process optimization", *Microelectron. Eng.* 17, 135–139, 1992.

[CUI 00A] CUISIN C., CHELNOKOV A., LOURTIOZ J.M., DECANINI D. & CHEN Y., "Fabrication of three-dimensional photonic structures with submicrometer resolution by X-ray lithography", *J. Vac. Sci. Technol. B*. 18 (6): 3505–3509, 2000.

[CUI 00B] CUISIN C., CHELNOKOV A., LOURTIOZ J-M., DECANINI D. & CHEN Y., Submicrometer resolution Yablonovite templates fabricated by X-ray lithography; *Appl. Phys. Lett.* 77(6), 770–772, 2000.

[CZY 90] CZYZEWSKI Z., O'NEILL MACCALLUM D., ROMIG A. & JOY D.C., "Calculations of Mott scattering cross-section", *J. Appl. Phys.* 68, 3066, 1990.

[DEG 96] DEGUCHI K., *et al.* Adapted from "Recent Progress In Synchrotron Radiation Lithography", *J. Electr. Spectr. and Rel. Phenom* 80, 1996), 321–327.

[DIF 99] DI FABRIZIO E., NUCARA A., GENTILI M., CINGOLANI R., "Design of a beamline for soft and deep lithography on third generation synchrotron radiation source", *Review of Scientific Instruments* 70 (3), pp. 1605–1613, 1999.

[DZI 96] DZI-CHI L., LI D-C., CHEN J-T., CHYUAN S-W. & SUN C-Y., "Computer Simulation for mask structure heating in X-ray lithography", *Computers and Structures* 4, 825–834, 1996.

[EHR 86] EHRFELD W, GLASHAUSER W, MUNCHMEYER D & SCHELB W, "Mask making for synchrotron radiation lithography", *Microelectron. Eng.* 5, 463–70, 1986.

[EHR 95] EHRFELD W. & LEHR H., "Deep X-ray lithography for the production of three dimensional microstructures from metals, polymers and ceramics", *Radiat. Phys. Chem* 45(3), 349–365, 1995.

[EVE 71] EVERHART T.E. & HOFF P.H., "Determination of Kilovolt Electron Energy Dissipation vs Penetration Distance in Solid Materials", *J. Appl. Phys.* 42, 5837–5846, 1971.

[FEI 95] FEIERTAG G, SCHMIDT M & SCHMIDT A, "Thermoelastic Deformations of Masks for Deep X-ray Lithography", *Microelectron. Eng.* 27, 513–516, 1995.

[FEI 97] FEIERTAG G., EHRFELD W., FREIMUTH H., KOLLE H., LEHR H., SCHMIDT M., SIGALAS M.M., SOUKOULIS C.M., KIRIAKIDIS G., PEDERSEN T., KUHL J. & KOENIG W., *Appl. Phys. Lett.* 71, 11, 1997.

[FEN 07] FENG Y., FESER M., LYON A., RISHTON S., ZENG X., CHEN S., SASSOLINI S. & YUN W., "Nanofabrication of high aspect ratio 24 nm X-ray zone plates for X-ray imaging applications", *J. Vac. Sci. Technol. B* 25, p.2004, 2007.

[FOR 97] FORESI J.S., VILLENEUVE P.R., FERRERA J., THOEN E.R., STEINMEYER G., FAN S., JOANNOPOULOS J.D., KIMERLING L.C., SMITH H.I. & IPPEN E.P., "Photonic-bandgap microcavities in optical waveguides", *Nature* 390, 143, 1997.

[GOO 96] GOODMAN J.W., *Introduction to Fourier Optics*, McGraw-Hill, 1996.

[GRE 74] GREGORY D. & FINK M., *Atom. Data Nucl Data Tables* 14, 39, 1974.

[GRE 75] GREENEICH J.S., "Developer Characteristics of Poly-(Methyl Methacrylate) Electron Resist", *J. Electrochem. Soc.* 122, 970, 1975.

[GRI 04] GRIFFITHS S.K., "Fundamental limitations of LIGA X-ray lithography: sidewall offset, slope and minimum feature size", *J. Micromech. Microeng.* 14, 999–1011, 2004.

[GUO 90] GUO J.Z.Y., CHEN G., WHITE V., ANDERSON P. & CERRINA F., "Aerial image formation in synchrotron-radiation-based X-ray lithography: The whole picture", *J. Vac. Sci. Technol. B* 8, 1551, 1990.

[GUO 92] GUO J.Z.Y., QUINN L., CERRINA F., DI FABRIZIO E., LUCIANI L., GENTILI M. & GEROLD D., "Experimental and theoretical study of image bias in X-ray lithography", *J. Vac. Sci. Technol. B* 10, 3150–3154, 1992.

[HAL 68] HALLER I., HATZAKIS M. & SRINIVASAN R., *IBM J. Res. & Dev*. 12, 251, 1968.

[HAN 02] HAN G., KAHN M., FANG Y. & CERRINA F., "Comprehensive model of electron energy deposition", *J. Vac. Sci. Technol. B* 20, 2666–2671, 2002.

[HAN 03] HAN G., KHAN M. & CERRINA F., "Stochastic modeling of high energy lithographies", *J. Vac. Sci. Technol B* 21, 3166, 2003.

[HAR 82] HARADA K., TAMAMURA T. & KOGURE O., *J. Electrochem. Soc.* 129, 2576, 1982.

[HEC 92] HECTOR S.D., SCHATTENBURG M.L., ANDERSON E.H., CHU W., WONG V.V. & SMITH H.I., "Modeling and experimental verification of illumination and diffraction effects on image quality in X-ray lithography", *J. Vac. Sci. Technol. B* 10, 3164–3168, 1992.

[ITRS] International Technology Roadmap for Semiconductors (ITRS), http://www.itrs.net/reports.html.

[JOA 95] JOANNOPOULOS J.D., MEADE R.D. & WINN J.N., *Photonic Crystals - Molding the Flow of Light*, Princeton University Press, 1995.

[JOA 97] JOANNOPOULOS J.D., VILLENEUVE P.R. & FAN S., "Photonic crystals: putting a new twist on light", *Nature* 386, 143, 1997.

[JOH 02] JOHNSON S. & JOANNOPOULOS J.D., *Photonic Crystals, The Road from Theory to Practice*. Kluwer Academic Publisher, Norwell, Massachusetts USA, 2002.

[JOH 87] JOHN S., "Strong localization of photons in certain disordered dielectric superlattices", *Phys. Rev. Lett.* 58, 2486, 1987.

[KAK 77] KAKUCHI M., SAGAWARA V.S., MURASE K. & MATSUYAMA K., *J. Electrochem. Soc.* 124, 1648, 1977.

[KAR 87] KARNEZOS M., RUBY R., HEFLINGER B., NAKANO H. & JONES R., "Tungsten: An alternative to gold for X-ray mask", *Journ. Vac. Techn. B* 6, 283–287, 1987.

[KHA 94] KHAN M., MOHAMMAD L., XIAO J., OCOLA L. & CERRINA F., "Updated system model for X-ray lithography", *J. Vac. Sci. Technol. B* 12, 3930–3935, 1994.

[KHA 97A] KHAN M., BOLLEPALLI B.S. & CERRINA F., *CNTech Toolset User's Guide*, Univ. of Wisconsin Madison Report, 1997.

[KHA 97B] KHAN M., BOLLEPALLI S.B. & CERRINA F., "A Semi-Empirical Resist Dissolution Model for Sub-micron Lithographies", *Proceedings MSM conference Tokyo* 21–23 July, 1997.

[KNI 98] KNIGHT J.B., VISHWANATH A., BRODY J.P. & AUSTIN R.H., Hydrodynamic focusing on a silicon chip: mixing nanoliters in microseconds, *Phys. Rev. Lett*., 80, 3863–3866, 1998.

[KU 91] KU Y-C., NG L-P., CARPENTER R., LU K., SMITH H.I., HAAS L.E. & PLOTNIK I., "In situ stress monitoring and deposition of zero-stress W for X-ray masks", *J.Vac. Sci. Tech. B* 9, 3297–3300, 1991.

[LI 04] LI Z.Y., HO K.M., "Anomalous propagation loss in photonic crystal waveguides", *Phys. Rev. Lett*. 92 (6), Art. No. 063904, 2004.

[LIN 98] LIN S-Y., CHOW E., HIETALA V., VILLENEUVE P.R. & JOANNOPOULOS J.D., *Science* 282, 274, 1998.

[LIN 99] LIN S.Y., FLEMING J.G., SIGALAS M.M., BISWAS R. & HO K.M., "Photonic band-gap microcavities in three dimensions", *Phys. Rev. B* 59 (24), R15579–R15582, 1999.

[LUC 06] LUCKE R.L., "Rayleigh-Sommerfeld diffraction and Poisson's spot", *Eur. J. Phys.* 27, 193, 2006.

[MAL 96] MALEK C.K., JACKSON K.H., BONIVERT W.D., HRUBY J., "Masks for high aspect ratio X-ray lithography", *J. Micromech. Microeng*, 6, 228–235, 1996.

[MAL 04] MALUEG D.H., TAYLOR J.W., THIELMAN D., LEONARD Q., DHUEY S. & CERRINA F., "Modeling, fabrication, and experimental application of clear X-ray phase masks", *J. Vac. Sci. Technol. B* 22(6), 3575–3580, 2004.

[MAR 95] MARKS N, "Synchrotron radiation sources", *Radiat. Phys. Chem*. 45(3), 315–331, 1995.

[MAR 02] MARGARITONDO G., *Elements of Synchrotron Light: For Biology, Chemistry and Medical Research*, Oxford University Press, USA, 2002.

[MAR 04] MARMIROLI B., PÉRENNÈS F., TURCHET A., GOSPARINI A., MIOTTI P., TAJMAR M., LANG M. & DI FABRIZIO E., "Design and Fabrication of Microturbine Rotors for Small Power Generation", *Proceedings of CANEUS 2004 Conference on micro-nano technologies for aerospace applications*, AIAA 2004-6710, 42–48 (Monterey, California 1–5/11), 2004.

[MAR 09] MARMIROLI B., GRENCI G., CACHO-NERIN F., SARTORI B., FERRARI E., LAGGNER P., BUSINARO L. & AMENITSCH H., "Free jet micromixer to study ultrafast chemical reactions by small angle X-ray scattering", *Lab Chip*, 2063–2069, 2009.

[MCA 00] MCALLISTER D.V., ALLEN M.G. & PRAUSNITZ M.R., "Microfabricated microneedles for gene and drug delivery", *Annu. Rev. Biomed* 2, 289–313, 2000.

[MCM 69] MCMASTER W.H., DEL GRANDE N.K., MALLETT J.H. & HUBBELL J.H., *Lawrence Livermore National Laboratory Report*. UCRL-50174 Section II Revision I, 1969.

[MIL 02] MILLS D.M., *Third-Generation Hard X-ray Synchrotron Radiation Sources: Source Properties, Optics, and Experimental Techniques*, Wiley-Interscience, 2002.

[MIN 01] MINGTAO L., CHEN L. & CHOU S.Y., "Direct three-dimensional patterning using nanoimprint lithography", *Appl. Phys. Lett*., 78(21), 3322–3325, 2001.

[MIN 03] MINGTAO L., CHEN L., ZHANG W. & CHOU S.Y., "Pattern transfer fidelity of nanoimprint lithography on six-inch wafers", *Nanotechnology* 14, 33–36, 2003.

[MOO 65] MOORE G.E., "Cramming more components onto integrated circuits", *Electronics* 8, 1965.

[MUR 85] MURATA K., "Theoretical studies of electron scattering effect on developed pattern profiles in X-ray lithography", *J.Appl Phys*. 57, 575–580, 1985.

[NEU 97] NEUMANN M., PANTENBURG F.J., ROHDE M. & SESTERHENN M., "Heat transport in masks for deep X-ray lithography during the irradiation process", *Microelectronics Journal* 28, 349–355, 1997.

[NUH 04] NUHN H-D., "From storage rings to free electron lasers for hard X-rays", *J. Phys.: Condens. Matter* 16, S3413–S3421, 2004.

[OCO 93] OCOLA L.E. & CERRINA F., "Parametric modeling of photoelectron effects in X-ray Lithography", *J. Vac. Sci. Technol. B*. 11, 2839–2844, 1993.

[OKA 03] OKA T., NAKAJIMA H., TSUGAI M., HOLLENBACH U., WALLRABE U. & MOHR J., "Development of a micro-optical distance sensor", *Sens. and Actuat. A* 102, 261–267, 2003.

[PER 01] PÉRENNÈS F., DE BONA F. & PANTENBURG F.J., "Deep X-ray lithography beamline at Elettra", *Nuclear Instr. and Meth. in Phys. Res. A*, 467–468, 1274–1278, 2001.

[PER 06] PÉRENNÈS F., MARMIROLI B., MATTEUCCI M., TORMEN M., VACCARI L. & DI FABRIZIO E., "Sharp beveled tip hollow microneedle arrays fabricated by LIGA and 3D soft lithography with Poly vinyl alcohol", *J. Micromech. Microeng.* 16, 473–479, 2006.

[PRE 97] PRESTON WHITE K. JR & TRYBULA W.J., "Simulation study of an X-ray lithography cell: background and objectives" in *Computational Cybernetics and Simulation: 1997 IEEE International Conference on Systems, Man, and Cybernetics*, vol.1, 444–447, 1997.

[RAV 96] RAVET M.F. & ROUSSEAUX F., "Status of diamond as membrane material for X-ray lithography masks", *Diamond and Related Materials* 5 (6–8), pp. 812–818, 1996.

[ROM 01] ROMANATO F., DI FABRIZIO E., VACCARI L., ALTISSIMO M., COJOC D., BUSINARO L. & CABRINI S., "Microelectron LILIT beamline for soft and deep X-ray lithography at Elettra", *Eng* 57 (8), 101–107, 2001.

[ROM 03a] ROMANATO F., BUSINARO L., VACCARI L., CABRINI S., CANDELORO P., DE VITTORIO M., PASSASEO A., TODARO M.T., CINGOLANI R., CATTARUZZA E., GALLI M., ANDREANI C. & DI FABRIZIO E., *Microelectronic Engineering* 67–68, 679, 2003.

[ROM 03b] ROMANATO F., COJOC D., DI FABRIZIO E., GALLI M. & BAJONI D., "X-ray and electron- beam lithography of three-dimensional array structures for photonics", *J. Vac. Sci. Technol B* 21 (6) 2912–2917, 2003.

[ROM 97] ROMANKIW L.T., "A path from electroplating through lithographic masks in electronics to LIGA in MEMS", *Electroch. Acta* 42 (20–22), pp. 2985–3005, 1997.

[ROU 90] ROUSSEAUX F., HAGHIRI-GOSNET A.M., KHAN M.C., KEBABI B., LAUNOIS H. & DURAND J., "X-ray lithography at the super-ACO storage ring of Orsay (France)", *Microelectronic Engineerin*g 11 (1–4), pp. 229–232, 1990.

[SAK 01] SAKODA K., *Optical Properties of Photonic Crystals*, Springer, Berlin, 2001.

[SCH 91] SCHOMBURG W.K., BAVING H.J. & BLEY P., Ti and Be X-ray masks with alignment windows for the LIGA process, *Microelectronic Engineering* 13, 323–326, 1991.

[SCH 94] SCHOMBURG W.K., VOLLMER J., BÜSTGENS B., FAHRENBERG J., HEIN H. & MENZ W., "Microfluidic components in LIGA technique", *J. Micromech. Microeng* 4, 186–191, 1994.

[SEI 98] SEIZER R., "A fully integrated X-ray stepper program for 0.15 micron MMIC devices", *IEEE Lithography-98 Workshop*, Banff, AB, VT 05403, 1998.

[SHI 96] SHIGEHISA O. & SUNAO I., "An overview of X-ray lithography", *Micr. Eng*. 30 (1–4), pp. 171–178, 1996.

[SIL 97] SILVERMAN J.P., "X-ray lithography: Status, challenges, and outlook for 0.13 µm", *Journal of Vac. Sc. and Techn. B* 15 (6), 2117–2124, 1997.

[SIN 99] SINGH A. & GHOSH A., "A thermo-electric model of material removal during electric discharge machining", *International Journal of Machine Tools & Manufacture* 39, 669–682, 1999.

[SOM 96] SOMMERFELD A. "Mathematische Theorie der Diffraction," *Math. Ann.* 47, 317-374, 1896.

[SPE 72] SMITH D.L. & HENRY I., High-resolution pattern replication using soft X rays, *IEE Electron. Lett.* 8, 102–104, 1972.

[TAO 03] TAO S.L., DESAI T.A., "Microfabricated drug delivery systems: from particles to pores", *Adv. Drug. Deliv. Rev.* 55, 315–28, 2003.

[TOL 98] TOLFREE D.W.L., "Microfabrication using synchrotron radiation", *Rep. Prog. Phys.* 61, 313–351, 1998.

[TOR 04] TORMEN M., ROMANATO F., ALTISSIMO M., BUSINARO L., CANDELORO P. & DI FABRIZIO E.M., "Three-dimensional micro- and nanostructuring by combination of nanoimprint and X-ray lithography", *Journal of Vacuum Science and Technology B* 22, 766, 2004.

[WAN 04] WANG L., DESTA Y.M., FETTIG R.K., GOETTERT J., HEIN H., JAKOBS P. & SCHULZ J., "High resolution X-ray mask fabrication by a 100 keV electron-beam lithography system", *Journal of Microm. and Microengineering* 14(5), pp. 722–726, 2004.

[WHI 06] WHITESIDES G.M., "The origins and future of microfluidics", *Nature*, 442: 368–373, 2006.

[WIE 02] WIEDEMANN H., *Synchthron Radiation*, Springer, 2002.

[WIL 29] WILCZYNSKI J.S., "Optical Step and Repeat Camera with Dark Field Automatic Alignment", *J. Vac. Sci. Technol.* 16, No. 6, p.1929, 1979.

[XU 01] XU C., PAN G., XU F., WEI S., TIAN Y., ZHAO D. & WANG F., "X-ray beamlines at the superconducting wiggler of NSRL", *Nuclear Instruments and Methods in Physics Research, Section A: Accelerators, Spectrometers, Detectors and Associated Equipment* 467–468, 639–642, 2001.

[YAB 87] YABLONOVITCH E., "Inhibited Spontaneous Emission in Solid-State Physics and Electronics", *Phys. Rev. Lett.* 58, 2059, 1987.

[YAB 91] YABLONOVITCH E. & LEUNG K.M., "Hope for photonic bandgaps", *Nature* 351, 278, 1991.

[ZHI 03] ZHI-YUAN LI & KAI-MING HO, "Light propagation through photonic crystal waveguide bends by eigenmode examinations", *Phys. Rev. B* 68 (4): 045201 1–12, 2003.

[ZUM 97] ZUMAQUÉ H, KOHRING GREGORY ALLEN & HORMES J, "Simulation of Energy Deposition in Deep X-ray Lithography", *PARCO conference*, Wissenschaftszentrum, Bonn, Germany, 16–19 September, 1997.

Chapter 2

NanoImprint Lithography

2.1. From printing to NanoImprint

Today, printing has become a common thing thanks to several technological revolutions. After the development of the first written forms 30,000 years B.C., cuneiform writing, invented by Mesopotamian Sumerians, appeared 4000 years B.C. This form of writing was mainly produced using a sharpened reed on a clay tablet. The Sumerians also created the cylinder seal, today considered to be the first impression technique: symbols were carved into a stone cylinder which was then rolled over fresh clay; the imprinted pattern constituted a seal.

It was only in 1908 that an Italian archeologist, Luigi Pernier, discovered what is considered to be the earliest imprinted item: the Phaistos disk (Figure 2.1), dating from the 17th Century B.C, which is a clay disk covered with hieroglyphs embossed by stamps. It has a 16 cm diameter, is only 1.2 cm thick and was made by pressing sculpted symbols into wet clay, which was then baked and attached to a support. The disk is covered with unknown pictograms on both faces. The first traces of seals or stamp impressions on clay can thus be dated from many centuries before our age.

Ten centuries later, the first imprinted coins appear in ancient Greece and Asia. The impressions consist of a symbol to represent a value, and that value in writing. They are therefore considered to be the first examples of products from a mass impression technique. In Western Europe, between the 1st and the 15th Century A.D., books were copied by scribe monks, called copyists, who handwrote them with a goose feather. However, during the 6th Century in China, xylography was

---

Chapter written by Stefan LANDIS.

invented. An impression was accomplished thanks to sculpted wood or engraved ceramic blocks. In 868, a Chinese man, Wan Jie, printed the first book. It was a xylographical edition of the *Diamond Sutra*, a buddhist text, of which only a few fragments are left and kept at the British Library in London. A century and a half later, in 1401, Corean Pi Cheng, printed the first book using mobile clay characters.

Figure 2.1. *Pictures of the Phaistos disk.*
Heraklion Archaeological Museum, Crete [PHA 10]

Around 1400, the first metallographic books appeared. Molten lead was deposited on a copper plate which had been struck with punches. The lead block was then taken out of its mold, covered with ink and placed under a sheet of paper. A few decades later, in about 1430, the lead matrix was replaced with wooden boards, carved in reverse. Once the boards were coated with ink, they were pressed against paper sheets. In 1436, Johannes Gutenberg invented the printing press with removable wood or metal characters.

It was only in 1517, with Luther and the Reformation, that these impression techniques became a way of spreading mass information. And it was only in c.1790 that a rotary motion was introduced into the process, with the invention of the first impression cylinder by William Nicholson.

Lithography, based on the incompatibility between ink (oil) and water, was created in 1796 thanks to Senefelder's work. But it was only in 1829 that relief lithography was invented by the Frenchman Louis Braille, to allow blind people to have access to information media. With the help of progress in science and the twentieth century's developments in technologies, numerous techniques have appeared and modified impression methods (Figure 2.2).

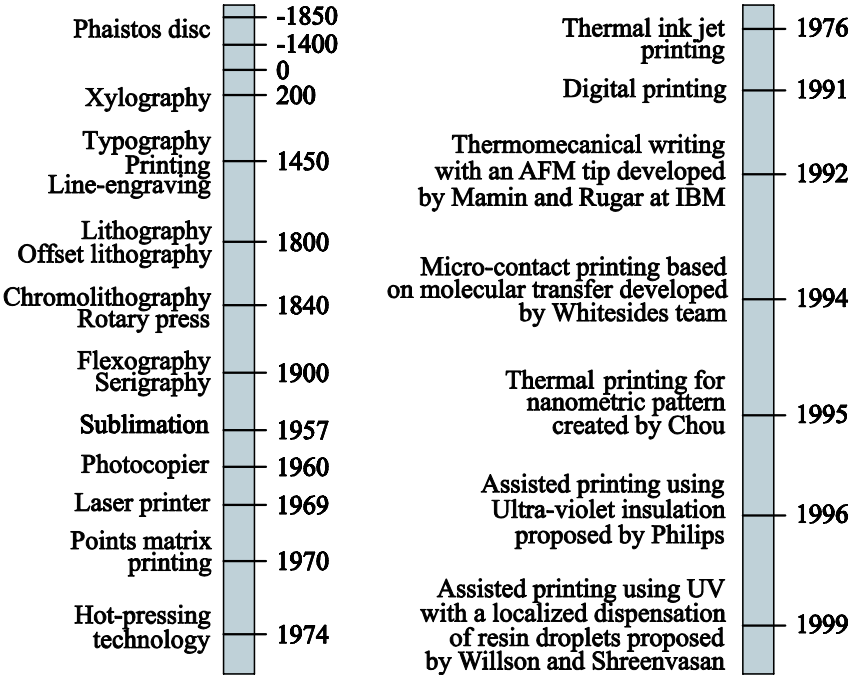

Figure 2.2. *From imprint to NanoImprint*

It was only in about 1974 that hot embossing of millimetric and micrometric structures appeared. Stephen Benton and Michael Foster first developed a process using this technology to produce holograms on plastic. In 1983, MasterCard International became the first user of this reproduction technique for security holograms on their cards.

In 1992, two IBM scientists, Mamin and Rugar, developed a thermomechanical writing process using an AFM tip [MAM 92]. This method consisted of embossing a locally heated polymer with the tip of a near-field microscope. Initially this approach was used to manufacture data storage supports. However, since the information is written as a chain, the process was quite slow.

In the mean time, Whiteside's team, at Harvard University, developed the microcontact imprint technique [KUM 94], allowing them to generate molecular transfers from a stamp to a specific substrate. This technology is based on the alkanethiol adsorption principle on a gold surface (a monolayer) at the scale of from 0.2 to 100 µm. To do so, a soft elastomer stamp was used to process the areas where the gold surface was covered with this organized monolayer.

In 1995, Stephen Chou [CHO 95] from the University of Michigan published thermal imprints of patterns smaller than 200 nm. Although the concept was very similar to that developed by IBM at the same time, here, the printing was done in parallel. The support (a mold) contained numerous patterns and was embossed in a melted polymer. As de-embossing happened once the polymer was hardened, a mirror image was reproduced: nanoimprinting was born. In the same year, Kim [KIM 95] published an article about the first imprints made by filling a mold using capillary effects between a liquid resist and the surface ("micromolding in capillaries", or MIMIC).

In 1996, a research team from Philips [HAI 96] wrote an article about the first results for UV assisted impressions to create CDs. The idea consisted of using a liquid polymer at room temperature and shaping it with a mold engraved with patterns. The final stack was stabilized by a UV flash through the transparent mold. Chou, on the other hand, used a silicon mold. Even though the targeted application was CD fabrication, the authors [HAI 96] mentioned a possible use of this technology as a lithographic process.

Based on work done at Philips, Wilson and Sreenvasan's teams [COL 99], from the University of Texas, elaborated the first UV assisted imprinting equipment with a local resist drop dispenser. This technology optimized the volume of resin required locally to fill the die. Transparent molds of a reasonable size (a few cm^2) used the same concept of photorepetition in photolithography to print much larger surfaces than the size of the mold.

After these three original breakthroughs, countless research teams started studying NanoImprint. Numerous variations and enhancements on Chou, Whiteside and Wilson's articles emerged and established NanoImprint as one of the ten technologies that could change the future [MIT 03].

2.2. A few words about NanoImprint

NanoImprint is a generic technology involving various approaches but keeping a common goal: the use of a stamp or mold to transfer a 2D or 3D pattern onto a surface or in a material's thickness. All these technologies assume an intimate contact between the original information media (the mold) and the receiving support (the substrate).

A full description of all these techniques (presented in Table 2.1) goes way beyond the frame of this chapter and we will focus instead on two of the technologies which have had the biggest impact on micro- and nanofabrication of

electronic, optical, biological or magnetic devices: thermal and UV assisted nanimprint lithography (see Figure 2.3).

NanoImprint techniques stick out from other more conventional lithography processes (photolithography, electronic lithography, X-ray, EUV lithography, etc.) because of the fundamental mechanism of creating the structures. In classical approaches, structures are created through a physical and chemical contrast. The resist positive or negative can be selectively developed. In the case of NanoImprint, the contrast is topographic and the flow of the resist through the stamp's cavities shapes the pattern.

Name of the technique (acronym)	Specificities for the mold	Shaped materials	Physical principle behind the shaping
Thermal NanoImprint or hot embossing (NIL)	Hard (Si, Ni…) [CHO 95] Soft [PER 07]	Monomers [LIA 07b] Polymers Sol-gels [LI 03]	Constrained flowing
			Selective de-wetting [KIM 03]
		Hard organic materials [STU 02] or minerals [CHO 02]	Constrained flowing
UV assisted NanoImprint lithography (UV-NIL)	Soft Transparent to UV [BEN 00]	Monomers Polymers Sol-gels	Capillarity Constrained flowing
	Hard Transparent to UV [COL 99]	Monomers Polymers Sol-gels	Constrained flowing
Microcontact lithography (μCP)	Soft	Organometallic [KUM 94]	Adsorption and creation of covalent links
	Soft Hard	Metal [MEL 03]	Adsorption and creation of covalent links
	Soft	Metal [JAC 01]	Injection and trapping of electric charges
Micromolding through capillary effects (MIMIC, micromolding in capillaries)	Soft	Organic materials	Auto-organization Capillarity [KIM 95, SUH 01]
Micromolding using solvent evaporation (SANIM)	Soft Porous	Organic materials	Capillarity Evaporation of the material's solvent through the mold [KIM 97]

Table 2.1. *Different technologies using a mold brought into contact with a surface to structure*

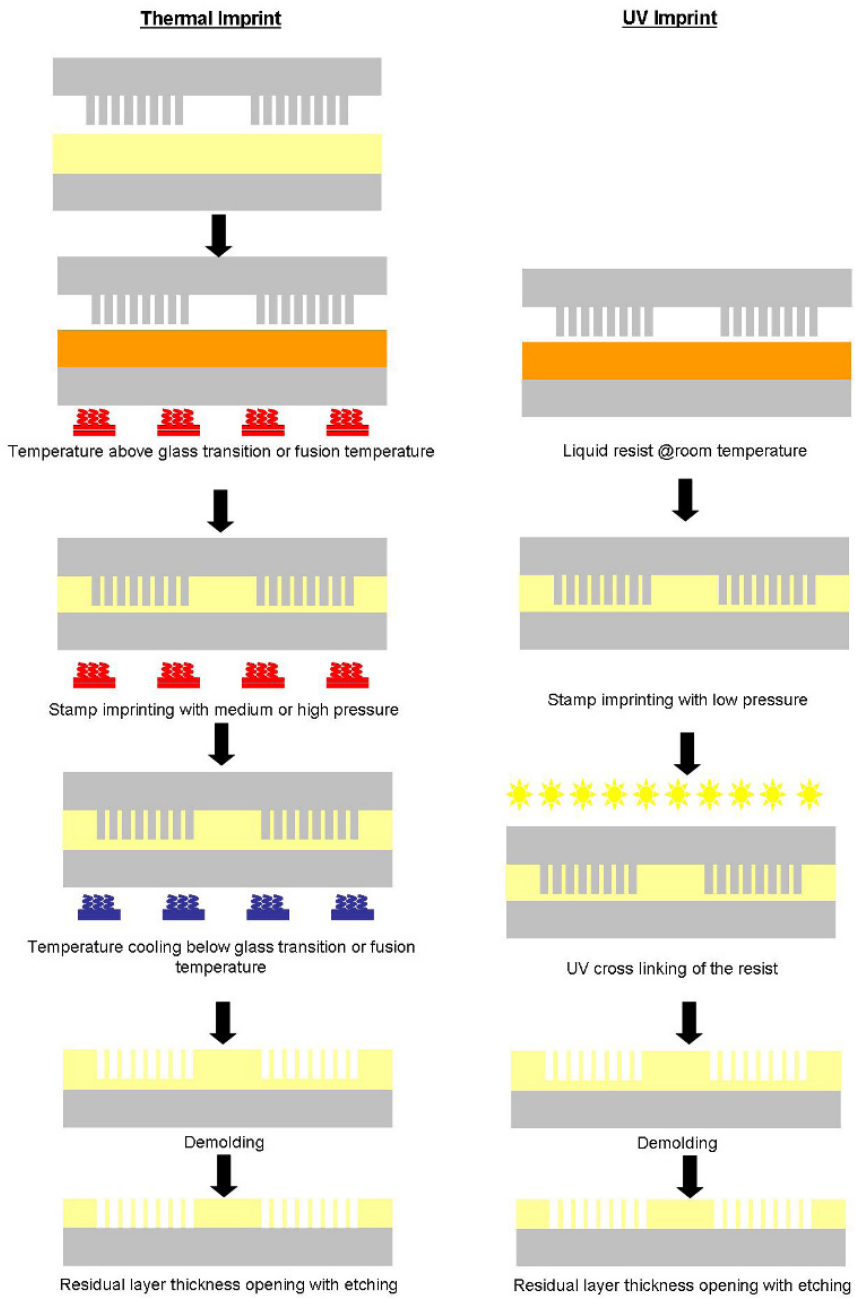

Figure 2.3. *Description of thermally and UV assisted NanoImprint processes*

Based on this principle, two solutions (thermal or UV NIL) are employed to solidify the displaced matter. Either the thermal properties of the material are used (in thermally assisted NanoImprint) by exploiting its liquid and solid states, or its physical and chemical properties are thermally modified (with thermoset materials) or modified by exposing to utlraviolet (UV assisted NanoImprint), establishing a crosslinkage or polymerization process.

Dispensing the resist requires it to be liquid with the lowest possible viscosity to reduce printing time. For thermal NanoImprint this operating point is reached by heating the material above its glass point (for polymers) or fusion transition temperature. Then a force is applied on the reverse of the mold to deform the liquid material. Depending on the structures to be reproduced and the flowing properties (mainly surface energy and viscosity), the force and heating applied to the stamp is held from a few seconds to several minutes. Then the system cools down under the glass transition or fusion temperature to harden the structures created. The mold and the substrate can be separated (de-embossing). Once all this is done, a thin layer of resist is still present below the imprinted features (residual layer) and needs to be removed to obtain a resin mask on a substrate, as in other traditional techniques (Figure 2.3).

For UV assisted impression, the resist is aleady liquid at room temperature and generally has a lower viscosity (a few mPa/s). The temperature cycle is no longer needed, allowing an improvement of throughput. The solidification of the material is done by photocrosslinking (Figure 2.3). We can immediately see that the mold has to be transparent to the wavelengths used, making its fabrication a lot more complicated. Once the resist is crosslinked, it is then solid enough to allow the separation of the mold. As with thermal NanoImprint, the residual layer has to be removed. Alignment between different pressed levels is achieved with a precision lower than 50 nm thanks to the transparency of the mold [FUC 04]. For obvious reason, the same cannot be done for thermal NanoImprint and alignment is still a major issue.

In UV assisted NanoImprint, a technique using a local drop dispenser was proposed by Colburn [COL 05]. This solution has the advantage of optimizing the volume of matter required locally to fill the mold cavities but keeps the residual layer as thin as possible. This is why this solution was widely developed for application in nanoelectronics [SCH 07].

These techniques are contact technologies since the mold embosses the resin. However, during the last decade, significant efforts have been made to overcome the contact between the material containing the information and that receiving the transfer. This has helped limit the defects and increase resolution (mainly for optical lithography). Moreover, the dimensions of the imprinted pattern correspond to the

those of the mold's object; this technology is called 1x, unlike scanners or step and repeat tools for optical lithography that use reduction factors of 4 or 5.

Finally, even though the topographic contrast (unlike chemical contrast) allows exact reproduction of the inverse image of the stamp, the existence of a residual layer (unlike with a chemical contrast) requires an extra etching step to end up with a classical resist mask on a substrate ready to be etched. We present the consequences of such specificity below. The main asset of this technology is the ability to reach better resolutions than optical lithography, with higher yields than with electronic lithography.

Their respective potentials led to a huge development, in ten years, of fabrication processes for the stamps, equipment, and their respective processes. Even though these technologies were created to imprint relatively small plane surfaces (of a few square microns [CHO 95]), it is interesting to notice that larger surfaces can now be imprinted [PER 04].

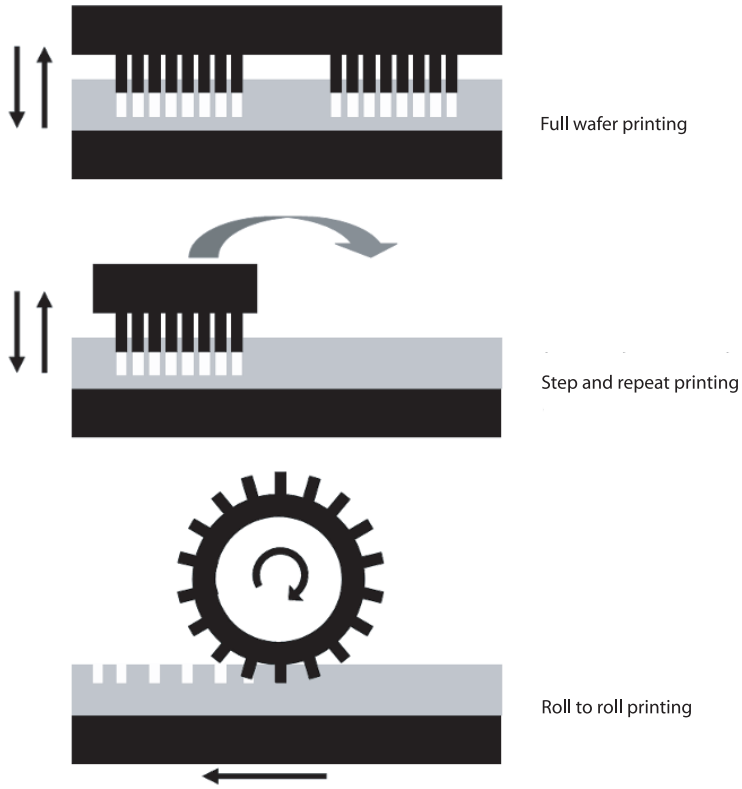

Figure 2.4. *Different NanoImprint modes: full wafer, step and repeat, and roll to roll*

Three reproduction modes can now be clearly identified (see Figure 2.4):

– wafer to wafer NanoImprint [PER 04];

– step and flash imprint lithography [COL 99], or thermorepeated (step and stamp imprint lithography) [HAA 00];

– roller imprint or roll to roll, either thermal [TAN 98] or UV assisted [AHN 06].

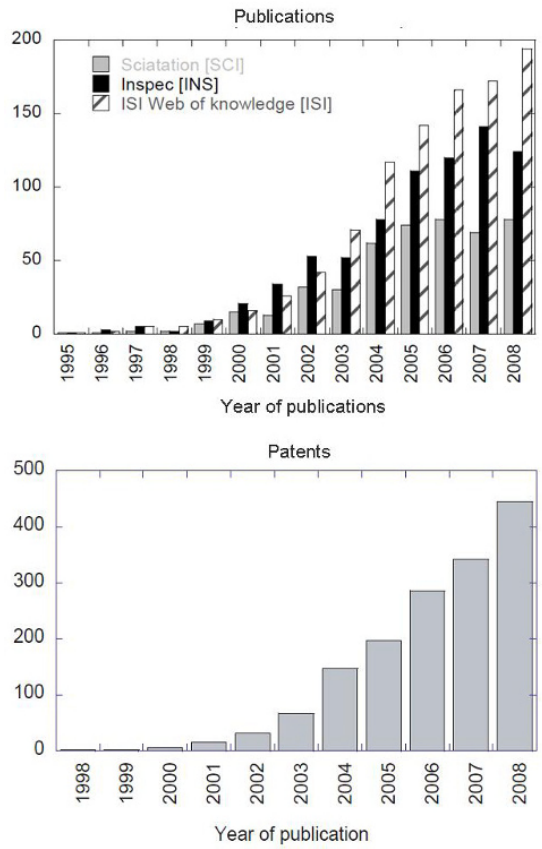

Figure 2.5. *Evolution of the number of publications (top) and patents (bottom) mentioning NanoImprint, over the years. Three databases were searched for publications [INS, ISI, SCI]. The Micropatent database [MIC] was interrogated for patent*

There has been a growing interest in these technologies, proposed over a decade ago. Figure 2.5 shows a significant evolution in the amount of publications (from three databases) directly related to the technology itself or using NanoImprint to design objects or components. This tendency confirms the enthusiasm for the subject

and is strengthened by the constantly growing number of patents deposited each year that mention NanoImprint (Figure 2.5). These two factors show that NanoImprint is of industrial as well as academic interest, a necessary condition to ensure its future.

Moreover, in 2003, less than ten years after the first paper was published, NanoImprint appeared in the International Technology Roadmap for Semiconductors (ITRS) as a potential solution to ensure the shrinkage of future electronic components [ITR]. This document is established through an agreement of industrial, academic and equipment partners, and bring together the major actors of the microelectronic industry: Europe, Japan, Korea, Taiwan and the United States. The point of the document is to identify blockages for future technologies but also the innovative solutions. It also sets future markers and technical objectives required to overcome micro- and nanoelectronic constraints.

The presence of NanoImprint in this roadmap significantly boosted interest in this technology, creating a link between research technology and industry.

2.3. The fabrication of the mold

The key element of the process, the mold or stamp, is to NanoImprint what the mask is to optical lithography. However, unlike optical lithography through projection, NanoImprint is called a 1x technology because there is no reduction factor between the mask and the resist. Therefore, the structures reproduced in the resist have the same size as the ones on the mold. The conception of such an object requires advanced micro- and nanofabrication processes (mainly etching and lithography). An exhaustive review of all the more or less standard processes and tricks used for the fabrication of such objects go beyond the limits of this chapter.

The most common approach consists of using other highly resolving lithography techniques for stamp manufacturing: electron beam lithography, EUV, X-rays, advanced optical (193 nm dry immersion lithography), or even FIB lithography, to cite a few. Readers can refer to [LAN 10] to understand the limits of these technologies. All these approaches are commonly called *top-down* because the organization of matter is realized via a mechanical (etching), chemical (development of a resist) or mechanical and chemical (Reactive Ion Etching (RIE)) machining. However other approaches take advantage of the auto-organizing capacity of matter at a scale of a few nanometers, or even tenths of nanometers. These techniques are generally classified as *bottom-up* solutions and are able to reach resolutions comparable with electronic lithography and with a much simpler implementation.

To conclude this discussion of the different approaches, there is one method which consists of taking advantage of certain materials' capacity to be deposited as

ultra thin films. The technique is to realize a multilayer deposition on a substrate, which is diced. This way the multilayer coatings are accessible and can be selectively etched. Thus, the edge of the wafer contains nanometric structures defined by the thicknesses of the deposited layers [AUS 04, MEL 03]. Despite the exceptional resolutions accessible through this method, the size of the stamp created is far too small because it is limited by the number of layers deposited. However, it is possible to extend this approach to larger surfaces by coating the edge of a predefined pattern with multiple layers. This process is commonly called the "PEDAL process" (PEDAL being an acronym of "planar edge defined alternate layer") [SON 05].

By choosing a two materials wisely, so that one can selectively remove one of them through an etch step, it is possible to achieve very dense and large wafers (up to 8 or 12 inches, or 200 to 300 mm) of nanometric patterns (of a few nanometers depending on the thickness of the layer deposited for the material), by using structures with larger dimensions (of a few hundred nanometers). In this configuration, the multilayer is revealed by etching, or by a chemical mechanical polishing/planarization (CMP) step (Figure 2.6).

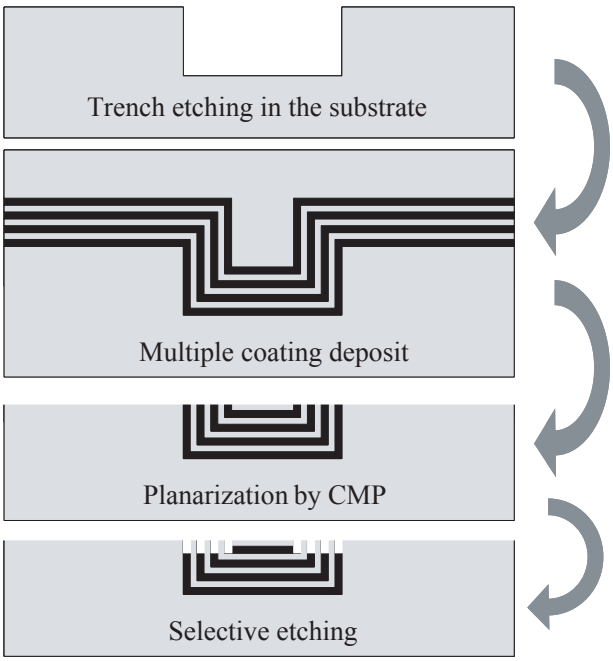

Figure 2.6. *Illustration of the PEDAL stamp manufacturing process*

All these approaches have specific benefits and limitations. Depending on the application targeted with NanoImprint, they can be used together or separately. So-called *top-down* techniques generally constitute the majority of the methods encountered in NanoImprint.

Further, improvements in micro- and nanoelectronic equipment have made stamp manufacturing over very large surfaces possible (up to hundreds or thousands of centimeters square), even though the process can take several days for serial writing lithography (with Gaussian beam electronic lithography, for instance). Resolutions around 10 nm can be obtained thanks to electron beam lithography (Figure 2.7) with either positive or negative resists (see [LAN 10], Chapter 3).

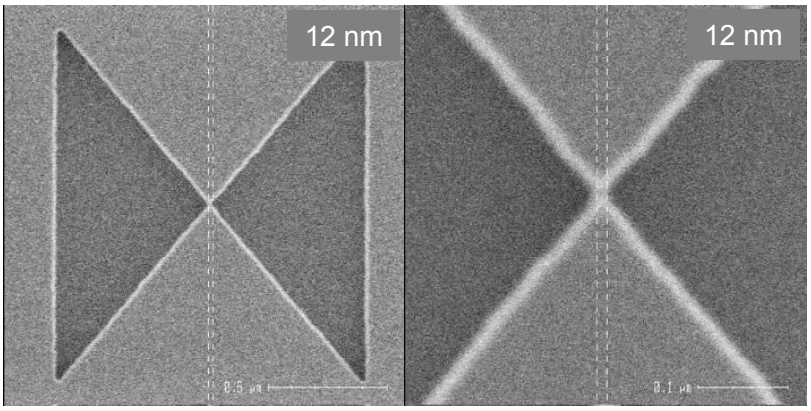

Figure 2.7. *SEM pictures. Top views of an object made with (left) electron beam lithography and (right) after RIE etching in silicon with a minimal size of 12 nm*

By contrast, the less expensive *bottom-up* solutions like copolymer systems (for which resolutions around a few nanometers can easily be achieved) can be used for stamp manufacturing. The main issues with these approaches are: the limited choice in the form and density of patterns imposed by the auto-organization of the system itself; the relatively small total surface; and, very often, the lack of ways to position a given pattern accurately. Nevertheless, recent papers [BIT 08, RUI 08, SEG 08] have raised the possibility of solving these main issues, like the size of the structured surface and positioning of nano-objects, through a combination of *top-down* and *bottom-up* techniques. Finally, it can be noticed that these *bottom-up* approaches are often achieved using coatings with thicknesses lower than one hundred nanometers. It is therefore very complicated or even impossible to obtain molds with aspect ratios (pattern height/width) of above one.

UV assisted NanoImprint technologies can be implemented with hard stamps, like quartz, or soft stamps usually made of organic materials. Quartz molds are generally limited to a few centimeters square but soft stamps can be as big as an 8 or 12 inch wafer, or even larger. Hard stamps are fabricated with silicon molds by lithography and an etching step (usually more challenging than using silicon) for the substrate. When creating a soft stamp, a first mold (usually in silicon) has to be fabricated. A liquid material (cured thermally or through UV exposure) is deposited on the mold to create a mirrored copy. Then the copy is used as a soft stamp for further steps. In that case, good mechanical behavior of the patterns during the imprint is required [MIC 01]. Various polymers can be used to realize these molds; elastomer is, amongst others, a very attractive choice. The material most used so far is poly(dimethyl-siloxane) (PDMS). Other materials like polyurethane (PU), polymide or a Novolac cured resist have been used to manufacture such molds. Poly(dimethylsiloxane) is particularly adapted to the fabrication of molds for soft lithography. In fact, it is just a silicon rubber. It is rather stable with time, non-toxic, inert with most materials required to be structured, and resistant to most solvents except many apolar solvents [LEE 03]. Furthermore, it is transparent to wavelengths over 300 nm, thermally stable under 150°C, flexible (Young modulus of 1.8 MPa), and undergoes 160% stretching. PDMS can be cured at low temperature (from ambient to 60°C) minimizing thermal expansion. This material is low cost and simple to implement. Besides, it is compatible with a large variety of organic or organometallic molecules, ceramics, sol-gels, colloids, biological micromolecules, acids or silane [XIA 98B, XIA 98B]. Its surface energy is only 22 mJ/m^2 and can even be reduced to 12 mJ/m^2 by using fluoropolymer-based treatments [PER 98]. This low surface energy enhances the demolding of the stamp from the shaped material and limits the contamination of the mold by particles or organic vapors. Its elasticity improves the conformity of the contact at the molecular scale, removing Van der Waals forces.

In reality, the mold, structured by lithography and etching, is realized by coating a stiff substrate. Sylgard 184 is the most commonly used PDMS formulation. Even though this material presents lots of advantages, some restrictions arise depending on the density and the size of the patterns. The standard formulation of PDMS allows the reproduction of features with sizes around 300 nm, with no significant deformations. The main issue is a low Young modulus that can induce many different types of mechanical deformations of the stamp, therefore limiting the potential resolution of this technique. A study of the collapse of the mold versus curing time of the PDMS enabled shrinkage of the printed structures by using a mold with higher elastic modulus and surface hardness. However, if those two components are too large, the stamp becomes fragile and contact with the substrate can be less homogeneous. To counter this problem, Schmid [SCH 00] suggested using a mixture of prepolymer bases with vynilic and hyrdosilane functions, and varying the length of the polymer chains between crosslinking points. Schmid

[SCH 00] emphasized the fact that a thermal curing of the PDMS intrinsically limits the fabrication of the stamp for high resolutions. In fact, the cooling cycle can induce mechanical stress in the material and therefore restrict its resolution. Even though using a thin film can solve this issue, it seems very important to create molds with no residual constraints to enhance the resolution and the alignment of the imprinted patterns. The use of photo-crosslinkers or curing agents at room temperature seems to be an attractive solution, in spite of the few results available today.

For the roller imprint method, fabrication of the mold remains to this day the limiting factor for the development of this technology. Indeed, well-known nanostructuring tools and associated processes are perfectly adapted for planar samples. The adaptation of these approaches to curved substrates is not possible yet and the fabrication of cylindrical stamp is done by coating a thin and deformable metallic [TAN 98] or soft [AHN 08, LEE 08] layer. Even though this trick has allowed a few research teams to achieve very good results in terms of imprint, the issue of connection fields between each wafer edge on the cylindrical stamp is still unsolved.

Even though the methods presented can help realize high-resolution molds on various sizes of surface, in most cases the structures have different heights (so-called 3D). Unlike most of the other lithography techniques, NanoImprint can easily achieve patterns of different heights on the same sample (true 3D) if the mold is also 3D [TOR 07].

The fabrication of 3D stamps is thus a major scientific and technologic challenge for the near future. The implementation of such processes would allow the application fields of NanoImprint to be significantly extended.

2.4. Separating the mold and the resist after imprint: de-embossing

2.4.1. *The problem*

The specifics of NanoImprint processes, namely the intimate contact between the surface of the mold and the material, most of the time organic, require the development of strategies to make the separation of the support containing the information (the mold) and the shaped polymer easier. This demolding is a key step in the implementation of NanoImprint.

The mechanisms acting during this separation can affect not only the mold but also the resist printed, creating many irreversible defects. Adhesion at the interface and friction between the surface of the mold and the resist can induce elastic

[HIR 01, MOH 06] or plastic [CHE 06, CRO 05] deformation or even lifting of the patterns (Figure 2.8) [GOU 07, HIR 03].

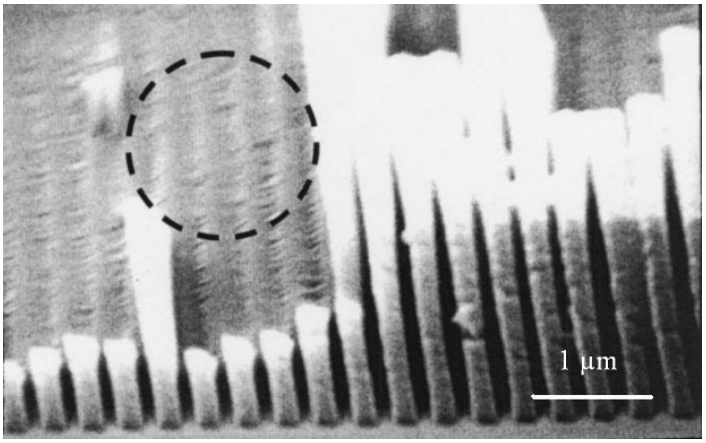

Figure 2.8. *Cross-section SEM image of a line network in a resist after the lifting of the structure during demolding [HIR 03]*

Right from the start, the NanoImprint scientific community tried not only to optimize this de-embossing step to reduce the defects generated but also reduce the mechanical stress on the mold and in the resist, allowing an improvement in the resistance of the mold and its life expectancy.

Given the few theoretical results dedicated to the study of the mechanisms in action during de-embossing, most results presented are process oriented or experimental findings, and offer more qualitative than quantitative solutions for their implementation. For the experimenter, there are two possibilities to separate the stamp from the resist: either a parallel separation of the mold and the resist [MER 07, TRA 08] (parallel demolding); or the insertion of a thickness between the substrate and the mold creating the propagation of a crack line (a separation wave) at the interface [HOU 07a, LAN 08] (peeling de-embossing).

The parallel separation of a mold from a resist requires a perfectly vertical relative motion, which constitutes a major experimental challenge. This is the reason why, in most situations, the de-embossing is either done by propagating a crack at the interface or by mixing parallel de-embossing and peeling. In all cases, it is necessary to consider both adhesion and friction phenomena during this stage (Figure 2.9(b) and 2.9(c)).

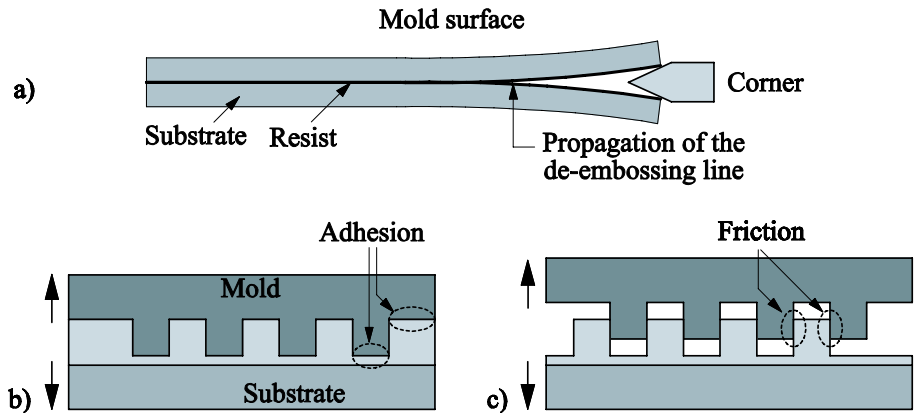

Figure 2.9. *(a) Peeling demolding principle with propagation of the de-embossing line between the resist and the mold; (b) and (c) adhesion and friction effects during the demolding stage*

Even if the mechanical and adhesion behaviors of the mold on the resist are key parameters for the de-embossing process, most effort has been focused on an enhancement of the physicochemical properties of the mold–resist interface [BUN 00, DEV 04, HOU 07b, MEN 84, SCH 05a, SIL 91]. This results in a reduction of the surface energy, making the demolding easier.

2.4.2. *Adhesion*

Adhesion involves physico-chemical phenomena arising when two surfaces are in contact. These phenomena can generate specific interactions or linking between materials. The causes of adhesion, and things contributing to it, can be numerous and complex. Mechanical anchorage, strong or weak electrostatic and acido-basic interaction, inter-diffusion phenomena, the creation of covalent bonding or wetability of the components can all factor in the de-embossing process, together or separately [DAR 03].

Since most of the fundamental adhesion mechanisms in solids are not fully understood, many models have been proposed. Nevertheless, to this day there is no unified theory for adhesion and sticking.

The computation of the attraction force (adhesion force), whether on a micro- or nanoscopic scale, as a function of the distance between the solids, does not imply the strength of adhesion. Therefore, the transposition and implementation of knowledge on this de-embossing step in thermally and UV assisted NanoImprint are not trivial.

A precise and complete analysis of this stage is still missing today. However, many research teams have shown that an improvement of the surface properties (mainly surface energy) of the different materials used reduces the adherence between the mold and the shaped resist. The main studies performed so far consist of reducing the surface of the mold to reduce the work of adhesion of the system.

2.4.3. *Adhesion and physico-chemical surface properties*

A complete description of surface properties and wetting theory go beyond the aim of this book; see the specialized literature for further details [DAR 03, GEN 04].

The goal of this section is to recall a few essential definitions and concepts, to get a better grasp of the experimental results obtained.

During the NanoImprint process, a mold with a solid surface is placed in contact with a liquid polymer or organic material with a viscosity between a few mPa/s and a few GPa/s. This contact between a solid and a liquid refers directly to wetting theories. The capacity of a liquid to fully or partially wet a solid surface is directly linked to one of its surface properties: surface energy.

Internal intermolecular forces ensure the cohesion of a material. Inside its own volume, each molecule comes under the influence of its neighbors. On the surface of the material, this symmetry is broken and a force is generated. Each atom or molecule on the surface sustains an attraction pulling it back into the volume. This force tends to reduce the surface of the material versus its available volume.

The surface tension, or surface energy γ, can be defined as the effort dW required to increase the surface by an elementary area dS:

$$dW = \gamma\, dS$$

We can also link surface energy to the cohesion effort W_{co} of a solid or liquid. W_{co} corresponds to the required reversible effort per surface unit to bring two identical surfaces in contact, in a vacuum:

$$W_{co} = 2\gamma$$

Ideally, this surface energy should correspond to the energy needed to split a body in two. However, since this process is irreversible and disperses energy, it is

important to introduce an adhesion effort W_{ad} and interface energy γ_{12}. If we consider two surfaces 1 and 2, this adhesion effort or Dupré's adhesion energy is defined by:

$$W_{ad} = \gamma_1 + \gamma_2 - \gamma_{12} \qquad [2.1]$$

with γ_i the surface energy of phase i with respect to the vapor phase (Figure 2.10).

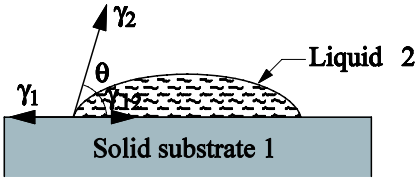

Figure 2.10. *Definition of the contact angle between phases 1 (solid) ad 2 (liquid) and interface energy γ_{12}. This representation gives rise to Young's equation*

In the case of a liquid phase 2 and a solid substrate 1, wetting is only effective if the adhesion energy W_{ad} is higher than the cohesion energy $W_{co.}$

$$\gamma_1 + \gamma_2 - \gamma_{12} > 2 \cdot \gamma_2 \qquad S = \gamma_1 - \gamma_2 - \gamma_{12} > 0 \qquad [2.2]$$

This equation is commonly called the wetting factor or criteria, and S is defined as the spreading parameter. With $S \geq 0$ wetting is full and the liquid deposited on the solid spreads completely; in the case where $S < 0$, the wetting is only partial and the liquid will remain as drops. By combining the Young equation:

$$\gamma_1 = \gamma_2 \cos\theta + \gamma_{12} \qquad [2.3]$$

and Dupré's equation [2.1], the adhesion effort of the liquid on the solid, the spreading parameter, can be expressed under the form:

$$W_{ad} = \gamma_2 (1 + \cos\theta) \qquad [2.4]$$

$$S = \gamma_2 \left(\cos\theta - 1 \right) \qquad [2.5]$$

with θ the contact angle of phase 2 on phase 1.

As a consequence, the measurement of the contact angle of a liquid on a solid allows the adhesion energy to be determined. At this point, various approaches have been studied to decompose the surface energy of a liquid or a solid as a dispersive (linked to dispersive, induction or dipole-dipole interactions) and a polar or acid-base component (linked to Debye, Keeson or hydrogen interactions).

When a liquid comes in contact with a surface (or another non-miscible liquid), numerous microscopic forces act and allow it to wet, to a greater or lesser extent. These forces are among others, van der Waals, or dispersive forces, created by the relocation of electron clouds of the two bodies, and polar forces regrouping electrostatic forces (electronegativity of atoms) and eventually surface charges, and hydrogen bonds. These forces can be computed through macroscopic values, surfaces energies that can be expressed in $mN.m^{-1}$ or $mJ.m^2$.

The surface energies of the liquid (surface tension) or of the substrate are the sum of their dispersive (γ^d) and polar (γ^p) components. Various models can numerically estimate these components and sub-components.

Owens *et al.* [OWE 78] assumed that surfaces could have a dispersive and a polar fraction. In the same way, polar surface energy can be divided into two components [WIE 99], one linked to electrostatic bonds (γ^e), and the other linked to hydrogen bondings (γ^H).

$$\gamma = \gamma^d + \gamma^p = \gamma^d + \gamma^e + \gamma^H \qquad [2.6]$$

To compute the surface energy of a substrate based on its contact angle with a known liquid (specifically its surface energy), we need to calculate the interface energy γ_{12}. The adhesion effort of a liquid on a substrate can be determined thanks to a geometrical mean between surface energy of a substrate and a liquid (see Girifalco & Good [GOO 60], Fowkes [FOW 64]):

$$W_{ad} = 2\sqrt{\gamma_1 \gamma_2} \qquad [2.7]$$

Using equation [2.6], this becomes:

$$W_{ad} = 2\left(\sqrt{\gamma_1^d \gamma_2^d} + \sqrt{\gamma_1^e \gamma_2^e} + \sqrt{\gamma_1^H \gamma_2^H}\right) \quad [2.8]$$

If we allow only similar interactions to remain (for instance: dispersive-dispersive), namely only the same type of effort exist, then:

$$W_{12} = W_{12}^d + W_{12}^e + W_{12}^H \quad [2.9]$$

After combining [2.4] and [2.8], we obtain the following relation:

$$0 = \gamma_2 (1 + \cos\theta) - 2\left(\sqrt{\gamma_1^d \gamma_2^d} + \sqrt{\gamma_1^e \gamma_2^e} + \sqrt{\gamma_1^H \gamma_2^H}\right) \quad [2.10]$$

which corresponds to the equation used in the extended Fowkes method.

Fowkes, extended Fowkes (EF), and Owens *et al.* are a part of the same family in which the adhesion effort corresponds to the geometrical mean value of the particle surface tensions (components). These methods, in particular extended Fowkes, answer an important range of surface energy values. The difference between the Fowkes method (or EF) and Owens' approach is the computation technique: Owens *et al.* use linear regression to solve the equation system, whereas Fowkes and EF use iterative determinations with different liquids allowing the exclusion of some components after each calculation step.

Nevertheless, other models exist. The Wu model [WU 82] is more adapted to small surface energies (< 35 mN.m^{-1}) than for large surface energies, as it diverges strongly. In this model, the adhesion effort corresponds to the harmonic mean of the surface tensions. The Wu method is solved using two unknown parameters in a two equations system, but it is possible to solve it by excluding components, as in the Fowkes' method:

$$0 = \gamma_2 (1 + \cos\theta) - 4\left(\frac{\gamma_1^d \gamma_2^d}{\gamma_1^d + \gamma_2^d} + \frac{\gamma_1^p \gamma_2^p}{\gamma_1^p + \gamma_2^p}\right) \quad [2.11]$$

Finally, the Oss and Good [OSS 90] method, which is also based on a geometrical mean value of the two components of the surface energy, considers that the polar fraction is divided into two components, an acid fraction (γ^+) linked to the

presence of acid groups at the surface (proton donors), and a basic fraction (γ^-) caused by the existence of basic groups on the surface (electron donors):

$$0 = \gamma_2 \left(1 + \cos\theta\right) - 2\left(\sqrt{\gamma_1^d \gamma_2^d} + \sqrt{\gamma_1^+ \gamma_2^-} + \sqrt{\gamma_1^- \gamma_2^+}\right) \qquad [2.12]$$

All these models can be useful, even though the extended Fowkes model is probably the best known for surface energy calculations.

Even if adherence is not simply linked to adhesion effort, it is possible, in certain cases [DAR 03], to establish a relationship between Dupré's adhesion energy and the rate of energy returned to the system (G in J/m^2) that allows the energy required for a crack to propagate in a material or a system to be calculated, which corresponds perfectly to the de-embossing step in NanoImprint.

The consideration of these elastoviscoplastic energy dissipation phenomena during the de-embossing of the mold and the resist would allow Dupré's adhesion and the adherence with an amplification coefficient that can achieve 10^3 to be linked. To this day, no research has been conducted with such detailed descriptions of NanoImprint processes. On the other hand, it seems clear today that the evolution of adherence is linked to Dupré's adhesion. Reducing W_{ad} implies an adherence reduction. According to equation [2.8], a reduction in adhesion means a reduction in the components of the surface energy of both materials implemented. This is the reason why most research done so far has focused on enhancing the release step, through the reduction of the surface energy of the mold or, more rarely, the resist.

2.4.4. *Surface treatment of the mold*

Fluorine compounds are known for their anti-adhesive properties. They are used in various fields with mechanical applications like kitchen tools, waterproof coatings for fabrics, in electronics and also for medical applications. Because of their chemical components and the strong presence of fluorine atoms, these products have very low surface energies (a few mJ/m^2). In general, the wetting of organic surfaces is set by the nature and the organization of the atoms on the surface. Shafrin and Zisman [SHA 60] demonstrated that the surface with the lowest achievable surface energy is obtained by condensation of a monolayer of perfluoroloric acid. The surface presents a dense arrangement of CF3 groups, and this was later confirmed by Nishino's work [NIS 99]. Table 2.2 summarizes surface energy as a function of surface chemistry.

Composition of the surface	Surface energy (mJ/m^2)	Composition of the surface	Surface energy (mJ/m^2)
Fluoride surface		Chlorinated surface	
-CF3	60 000	-CClH-CH2-	39 000
-CF2H	15 000	-CCl2-CH2	40 000
-CF3 & -CF2-	17 000	=CCl2	43 000
-CF2-	18 000	Hydrogenated surface	
-CH2-CF3	20 000	-CH3	21 000
-CF2-CHF-	22 000	-CH3	23 000
-CF2-CH2-	25 000	-CH2-	31 000
-CFH-CH2	28 000	-CH2- & -¨CH¨-	33 000

Table 2.2. *Surface free energy as a function of the chemical composition of the surface; from [SHA 60]*

It appears that the mold's surface needs to have the largest number of CF3 at the surface to reduce the adherence with the resist. To achieve this result, many processes have been suggested. The second constraint of these approaches, is the fact that the deposition has to be homogeneous on the stamp's patterns to reduce not only adherence at the top of the structures and on the bottom of the trenches, but also friction on the sidewalls of the micro- and nanostructures. Finally, the lifetime of such a coating also has to be considered (several thousands of imprint cycles). For this, the film has to be mechanically and thermally stable, have covalent bonds with the surface of the mold if possible, and be inert regarding the chemical reactions taking place during thermal or UV curing.

The first processes implemented to reduce the surface energy of a mold consisted of a very thin fluoropolymer film deposition (a few nanometers). These polymers need a composition and properties similar to polytetrafluoroethylene (PTFE). The main techniques used for deposition are plasma enhanced chemical vapor deposition

[GOU 02, GOU 04, JAS 99] or sputtering [JAS 99]. In the case of PECVD, precursor gases like octofluorocyclobutane (C4F8) or tetrafluoromethane (CF4) can be used. Sputtering uses a Teflon target with trifluoromethane (CHF3) as a carrying gas.

A layer deposited in this way has many carbon and fluorine based chemical species and they need to be quantified to optimize the anti-adhesive properties. To do so, X-ray photo-electron spectroscopy (XPS) is used to quantify the amount of the species present: CF3, CF2, CF, CCF, CCC.

A high quantity of CF2 species and a small amount of CF and CCF ensure good anti-adhesive properties very close to Teflon (PTFE 18 mJ/m^2).

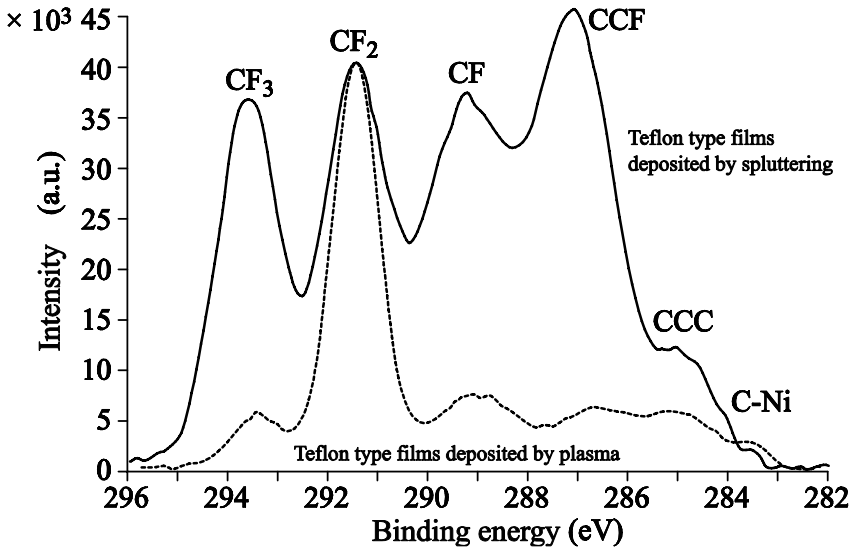

Figure 2.11. *Comparison between the surface composition of Teflon type films deposited by plasma or sputtering. Spectra intensity are normalized with respect to the CF2 signal intensity. The presence of this CF2 ray, higher in the case of a plasma deposited layer, shows the presence of a long linear chain similar to the composition of pure PTFE [JAS 99]*

Figure 2.11 [JAS 99] represents different species deposited by sputtering (ion sputtered film) and plasma deposition (plasma polymerized film). These depositions have been realized on nickel substrates as (C-Ni), appearing on the XPS spectra.

It is interesting to notice that the deposition technique influences the chemical composition of the surface and therefore its properties. Obviously, fine adjustments in the deposition process enable an improvement in the CF2 proportion of the layer

[ROO 01]. The sputtering deposition creates a more heterogeneous deposition than PECVD, which is closer to a Teflon film.

Jaszewski *et al.* [JAS 99] showed that imprinting using a mold covered with coatings such as polycarbonate (PC) or methyle polymethacrylate (PMMA) generated a transfer of fluorine species to the imprinted polymer. Jaszewski *et al.* also demonstrated that two mechanisms were responsible for the fluorine transfers: a diffusing mechanism, mainly active during the first ten imprints, then an abrasive mechanism is responsible for the fluorine transfer in the resist film.

Even though it is possible to obtain a high proportion of fluorine in the unmolding agent after deposition, a good amount of the fluoride molecules is weakly bonded to the carbon-rich polymer network and therefore easily transferable to the resin. It is important to notice that the printing time presents a cumulative effect in the diffusive regime, whereas only the number of imprints is relevant in the abrasive regime. Jaszewski *et al.* finally showed that more than half of the CF2 species are transferred in the polymer after only 50 imprints.

Even though the procedures for such depositions are relatively simple, the coatings obtained have a few downsides: a premature aging of the layer with a strong decrease in the CF2 proportion (20%) after 24 hours when it is kept in vacuum; a complicated deposition process, hard to optimize to achieve an ultra thin film homogenous with the nanostructures; and a high transfer rate of fluorine from the mold and therefore a limited life expectancy, namely lower than 100 impressions.

A solution to counter the thick and non-homogeneous depositions of those fluoropolymers is to use an organic monolayer that has fluoride terminations. For UV NIL technology, Colburn [COL 99] suggested a solution that is widely used nowadays, using fluoride based alkylsilanes to reduce the surface energy of the mold. As a matter of fact, these products set off an auto-assembled homogeneous deposition on very thin structures, of about a few nanometers [JUN 05]. Also, a silicon or silicon oxide mold's surface energy is reduced from 60 mJ/m^2 to values close to 15 mJ/m^2. Their covalent bonds to the subtrate provide a good resistance to external, mostly thermal (for temperatures above 200°C) and mechanical, aggressions.

These materials' deposition processes are done by silanization of the substrate. In other words, a reaction of $SiCl_3$ takes place on a surface with hydroxyl groups (OH). This process, initially developed for chromatographic applications, became used, much later, to realize monolayers with antisticking properties [BIG 46].

A detailed description of the deposition process and a procedure were then proposed to achieve a sufficient yield to expand the field of applications of such materials. Brzoska [BRZ 94] obtained critical surface energies for deposition of around 6 ± 1 mJ/m^2 by silanizing a silicon oxide with a solution of $C_{10}F_{21}(CH_2)_2SiCl_3$. These products are now widely used in NanoImprint and can be deposited in vapor [BEC 02] or liquid [LAN 06a] phase. The silanization reaction requires the presence of SiOH groups on the surface, which restricts these depositions to silicon, or silicon oxide surfaces [GAR 07, PAR 04], or even titanium oxide [KEI 05]. The transplantation process is presented in Figure 2.12.

In the process described in Figure 2.12, the substrate is first carefully cleaned, either by a piranha like cleaning, or ozonolysis, to remove all traces of organic left-overs. The native oxide of silicon or silicon oxide's surface being very hydrophilic, because of the OH groups, a thin water layer is thus present.

The hydrophilic function of the products places itself spontaneously at the surface of the water film. This is called the physisorption mechanism (step 1). The molecules spontaneously deposit themselves on the substrate as a film, and ideally all are oriented perpendicular to the substrate forming a dense and well-organized structure with a low surface tension.

The hydrolysis reaction between the $SiCl_3$ group and the OH function forms a strongly polar trisilanol group (step 2) and goes along with a release of hydrochloric acid. The presence of a very thin liquid film allows the mobility of silane chains to be enhanced. Their reorganization is thus facilitated to form a dense monolayer with a compact arrangement of CH3 or CF3 groups at the surface. Then, condensation and formation of covalent bonds (step 3) lets a molecular coating form itself at the surface of the mold. Finally (step 4), a transverse cross-linking reaction happens between neighbor molecules and stabilizes the monolayer.

As far as antisticking applications targeted by NanoImprint are concerned, the main compounds used for deposition are [SCH 05a]:

1. tridecafluoro-1,1,2,2-tetrahydrooctyl-dimethylchlorosilane or F_{13}-OMCS;

2. tridecafluoro-1,1,2,2-tetrahydrooctyl-trichlorosilane or F_{13}-OTCS which contains three (SiCl) groups;

3. heptadecafluoro-1,1,2,2-tetrahydrooctyl-trichlorosilane or F_{17}-DTCS which possesses a longer alkyl chain and three reactive groups.

The molecules are all constituted of a hydrophobic surface group (CF_3) and a reactive group ($SiCl_3$) both linked by an alkyl chain (Figure 2.13). These compounds can be used separately or mixed [SCH 05a] to enhance the properties of the monolayer.

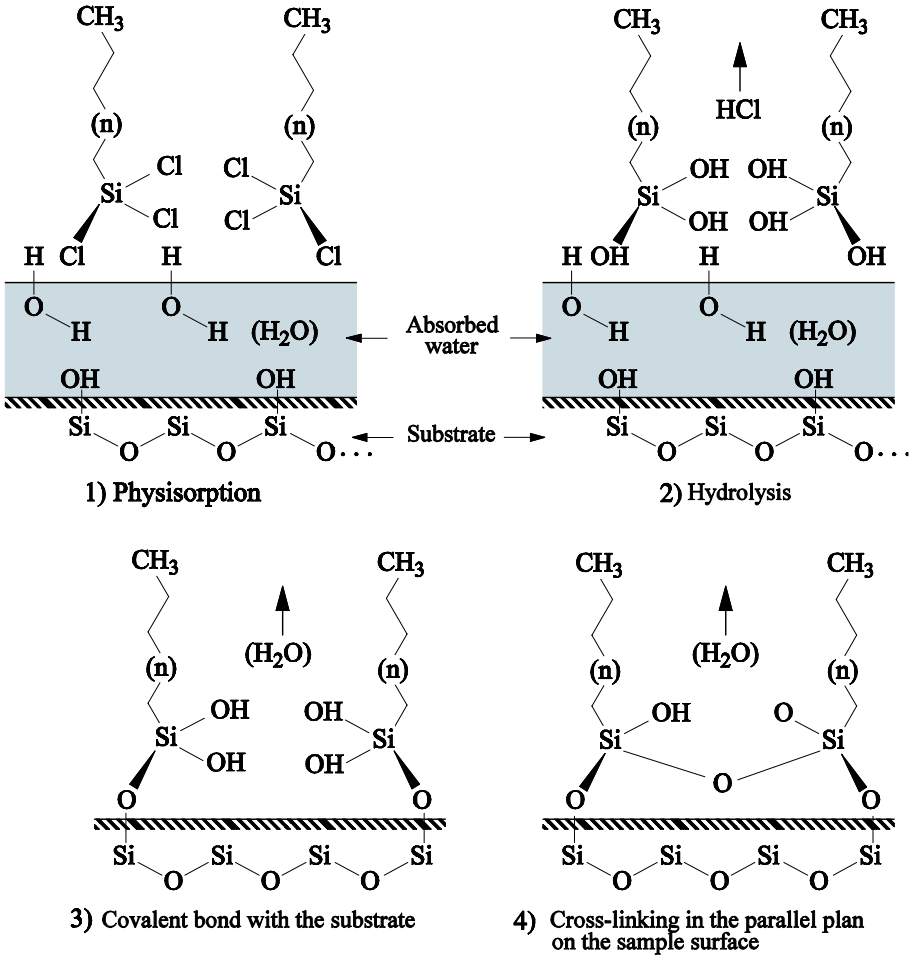

Figure 2.12. *Transplantation mechanisms of a monolayer on a silanol group according to Brzoska [BRZ 94]*

The description of this process (Figure 2.12) remains schematic because condensation and covalent transposition of the molecules can interact simultaneously during the deposition. This generates deflections regarding a perfect

auto-assembly on the surface and is characterized mainly by a lack of CF3 groups or a disorientation of molecules with respect to the mean orientation of the alkyl chains.

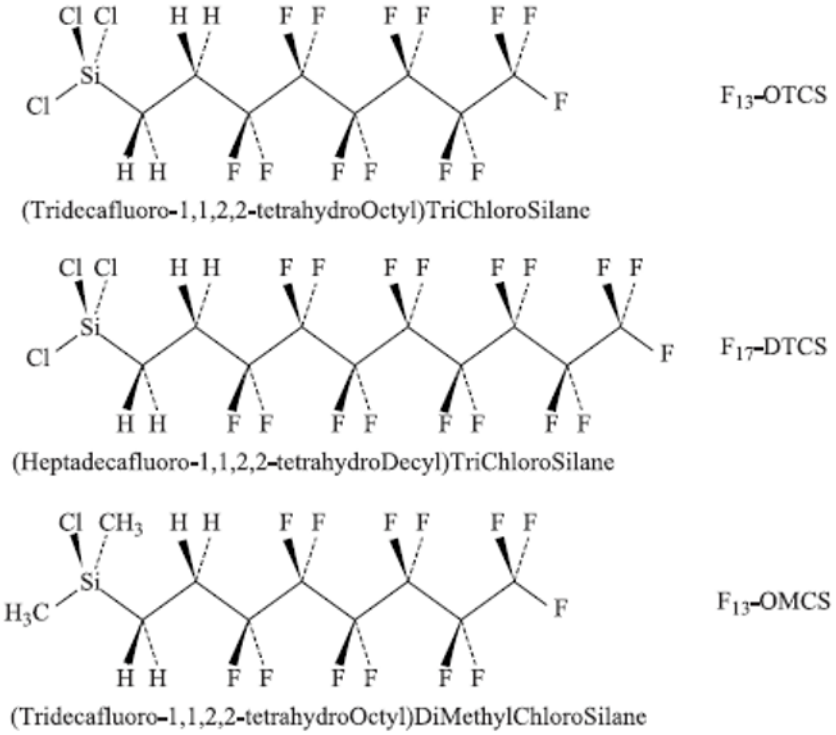

Figure 2.13. *Representation of the principal molecules used for the surface treatment of the molds used in NanoImprint, according to [SCHI 05]*

Nevertheless, trends can be identified. This monolayer transplantation process improves the reproduction capacity regarding surface properties, with a wide variety of procedures. The amount of water present during the deposition plays a crucial role on the quality and organization of the layer. The transverse silane chain cross-linking is favored over a transfer to the mold because of too high a proportion of water. Furthermore, a low deposition temperature favors the organization of molecules and thus increases the density of CF3 functions at the surface. The deposition of a blend of F13-OMCS–F13-OTCS or F17-DTCS–F13-OMCS, significantly reduces the polymerization of silane chains with each other and the roughness of the monolayer [SCH 05a]. Moreover, unlike fluoride polymer deposition of a Teflon type, the transfer of fluoride species in the imprinted resist

has not to this day been demonstrated, showing the stability of this type of monolayer.

2.4.5. *Treatment of the resist*

Even though the treatment of the mold is usually enough to ensure a proper unmolding, while maintaining the integrity of the patterns formed, the life expectancy of this surface treatment was raised from the start. How many imprints can be realized with a single surface treatment?

This question raised even more interest with the development of UV assisted NanoImprint and its potential application in micro-electronic device fabrication. Thanks to the photo cross-linking process that is specific for this process, it has been shown [GAR 07] that successive imprints, especially exposures, generate chemical reactions between the free radicals and the surface treatment of the mold. As a consequence, after just a few tens of imprints, the antisticking properties deteriorate, which is a major setback for industrial applications.

Very quickly, a solution was developed [BEN 02] to improve the anti-adherence of the mold and the resist. To do so, the composition of the resist is modified by adding fluoride compounds [BEN 02, KIM 05, LIN 08, WU 07] so that their migration at the resist–mold interface is controlled.

The goal of such a procedure is to create an asymmetry between the substrate–resist and mold–resist interfaces. Furthermore, the resist needs to have a strong adhesion with the substrate and a weak one with the mold. This is the reason why the portion of fluoride has to be carefully controlled, several percent in mass [BEN 02, LIN 08, WU 07].

2.4.6. *Characterization of the demolding process*

The quality of the de-embossing is based on a controlled balance of the adhesion forces between the substrate–resist and mold–resist interfaces. To this day, only a few theoretical studies have been conducted and most of the experimental researches give a qualitative approach to this step. There exist two commonly employed solutions for performing a demolding step: a separation through a vertical motion of the mold relatively to the resist (parallel demolding) or via a so-called peeling process (peel demolding, Figure 2.14).

In most peel demolding cases, the step is realized manually thanks to a scalpel blade inserted between the mold and the imprinted resist. For parallel demolding, it

is implemented via automatic systems and uses smaller molds (20×20 mm^2) in thermal or photo-repeated approaches (Figure 2.4). However, even in a parallel demolding configuration, it is difficult to get execute a peeling motion for a mold–resist separation. Moreover, the imprint stack usually contains soft layers (compliance layers) to obtain a more uniform print. The evaluation of the required de-embossing force is then extremely complicated or even impossible.

Because of the friction and adhesion generated during the de-embossing of the mold, it seems obvious that the unmolding force greatly depends on the geometry of the stamp (size, density, and shape of the patterns). Therefore, the separation force needs to be locally controlled so that it never exceeds the stress fracture limit of the material.

To master this step, it becomes necessary to understand the macroscopic (mechanical deformation of the mold during separation) and both micro- and nanoscopic mechanisms (friction and adhesion at those structures' levels) in place. Thereby, it is possible to figure out an automatic separation process applying sufficient effort to keep the resist intact. The computation of the separation force, in the case of parallel demolding, requires equipping the parts applying pressure with a fixation system to hold the mold and the substrate.

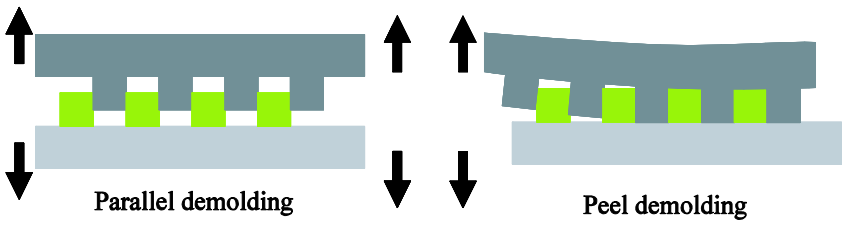

Figure 2.14. *Schematic representation of parallel and peel demolding*

In fact, during the de-embossing step, the applied force progresses from a set point (from a few bars to several hundreds of bars) to zero. By measuring the evolution of the force felt by the piston as a function of time, the separation of the mold from the wafer can be studied.

Figure 2.15 shows the evolution of the applied pressure as a function of printing time. The curve on the left illustrates the full evolution of the force applied along the various steps (vacuum in the chamber, contact, imprint, unmolding, venting); the curve on the right is a magnified image of the force applied on the piston during the demolding step. We have labeled the spike on the force curve the de-embossing force.

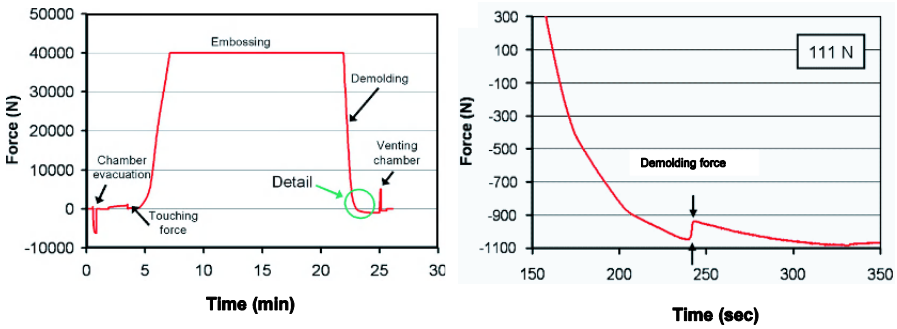

Figure 2.15. *Evolution of the force applied on a mold during an impression process [TRA 08]. The diagram on the left shows a full cycle, including a step where vacuum is established in the chamber, the imprint step, the de-embossing and the venting of the chamber. The graph on the right is a detailed view of the negatives forces acting at the end of the demolding step*

This irregularity is also studied by Park [PAR 09] using another experimental setup. In both cases the unmolding force required is estimated at around a few tens of Newtons, for a total surface close to 100 cm^2.

When the demolding is realized by introducing an air gap between the mold and the imprinted resist (Figure 2.16), the induced bending is usually so low that the separation of the stack can be considered vertical, thus easing a quantitative approach. Although a huge research effort has been concentrated on understanding the mechanisms acting during molecular bonding [VAL 05] and issues relating to propagation of fracture [MAU 00], there are, to this day, only a few results concerning a predictable demolding.

Maszara [MAS 88] obtained results when measuring the sticking energy between a mold and a wafer by using the double cantilever method (DCB, Figure 2.9). Therefore it is possible to estimate the impact of nanostructures on the propagation of a split in a stack [LAN 08], or to measure the aging of an anti-sticking treatment [HOU 07a, HOU 07b].

The experimental implementation (Figure 2.16) of this test cannot be linked back to demolding. Actually, it gives access to a split energy G [GIL 60, GIL 64, MAS 88] required to separate the wafers, such that:

$$G = \frac{3Eh^3 y^2}{16L^4}$$

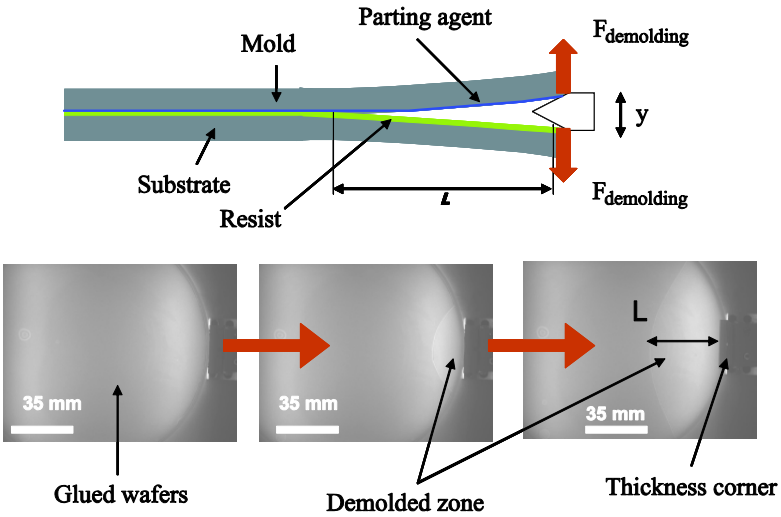

Figure 2.16. *Peeling demolding realized by introducing a air gap between the mold and the wafer. All three images have been captured by an infra-red camera and reveal the propagation of a unmolding crack between both plates. The unmolded zone corresponds to the lighter parts on the pictures*

which depends on Young's modulus E of the mold and substrate (usually the same), on the thickness of the used substrates h, and on the thickness of the object inserted y and the distance L between the edge of the object and the splitting line.

The computation of G can be understood as a way of testing the efficiency of a specific surface treatment. The use of molds and square wafers (Figure 2.17) can present a more developed quantitative approach [LAN 08]. In fact, it has been established that the presence of structures on the mold implies a significant rise in the splitting energy G and thus in the demolding force [LAN 08].

Moreover, Landis *et al.* [LAN 08] have shown that the energy required to unmold trenches with their length parallel to the splitting wave (Figure 2.17, right) is much lower than the energy required to de-emboss trenches with their length perpendicular to the splitting wave (Figure 2.17, left). The equation of the mold and the deflected mold–substrate system [KAN 74, PEN 93] can be used to calculate the elastic energy stored during the peel test and to compare it with the adhesion energy. Considering a mold and a substrate with a width b (m), a detachment energy G (J/m2), and a constant (8,446) determined by the geometry of the system (plate, mold and resin), the force per unit length required to unmold the system can then be expressed simply by [LAN 08]:

$$\frac{F_{op}}{b} = 8446\sqrt{G} \qquad (\mathrm{N.m^{-1}})$$

For the standard configurations usually encountered in NanoImprint, energy G is close to several tens or even hundreds of mJ/m2 which translates into a force release of a few tens to hundreds of newtons for a 35 mm wide mold. This result agrees with measurements made in the case of parallel release [TRA 08, PAR 09].

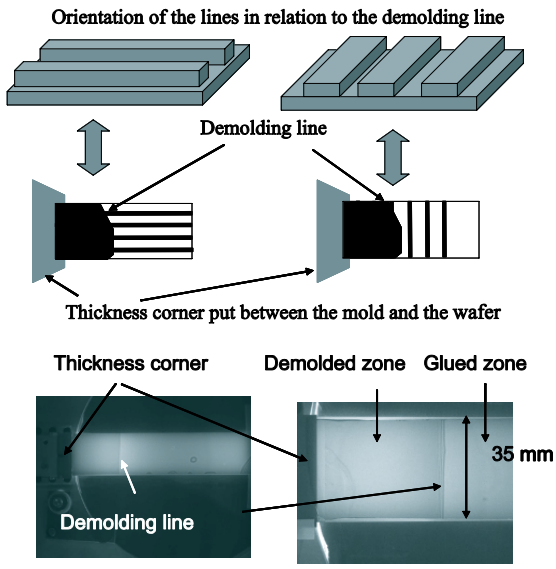

Figure 2.17. *Peeling demolding realized on rectangular samples with two pattern geometries. Both images were captured by infra-red cameras and reveal the propagation of the crack between the substrate and the mold. The unmolded zone corresponds to the darker zone on the pictures*

2.5. The residual layer problem in NanoImprint

2.5.1. *The residual layer: a NanoImprint specific issue*

Without taking into account issues related to the creation of defects due to the intimate contact between the mold and resin [CHE 05, HIR 03, LAN 07, MCM 08], this technique of NanoImprint, at first glance, could present another major drawback: the repeated contact between the nano-scale geometries of the mold and the substrate's surface. These points of contact between two hard materials could then mechanically weaken the patterns, especially smaller ones.

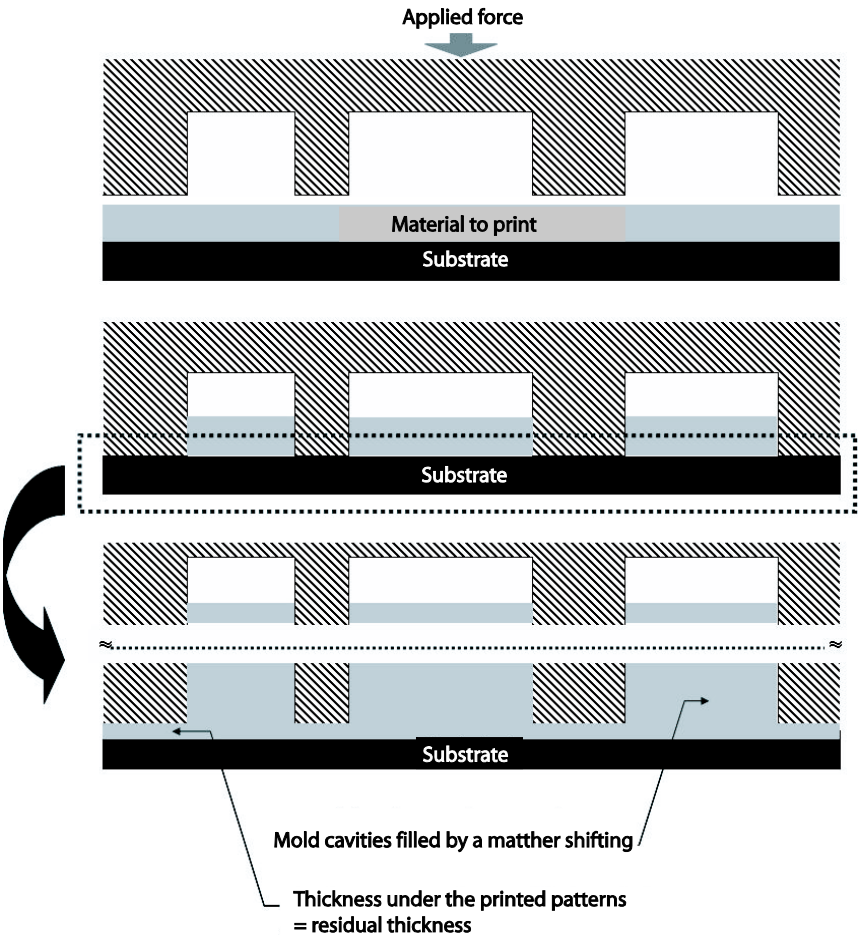

Figure 2.18. *Schematic representation of resist printing with a stamp, showing the definition of a residual layer under the imprinted features*

The properties of materials used as resists (monomers, oligomers or polymers) are such that in most experimental conditions, i.e. pressure, temperature and pressing time of less than 100 bars, Tg + 100°C and 1 hour, respectively, the mold does not reach the resist–substrate interface. Therefore, a resist layer, with thickness depending on imprint conditions, initial available resist volume and the mold's geometry, exists between the surface of the wafer and the mold's structure (Figure 2.18). This residual layer can be considered as a cushioning layer that reduces the mechanical stress on the mold's patterns.

2.5.2. *Is the thickness of the residual layer predictable?*

An early demonstration of the high resolution capabilities of this technology [CHO 97, AUS 04] and its straightforward implementation gave rise to an important development in the academic world. Users rapidly showed interest in a predictive approach to the printing process, especially with regard to the residual layer, as a function of mold geometry and the available resist volume. During the imprint, the vertical motion of the stamp with respect to the resist, induces very complex flows of polymer into the mold cavities (by vertical flow) but also parallel to the substrate's plane, called planar flow (Figure 2.19) which can generate patterns very different from the initial design of the mold [SCH 01b].

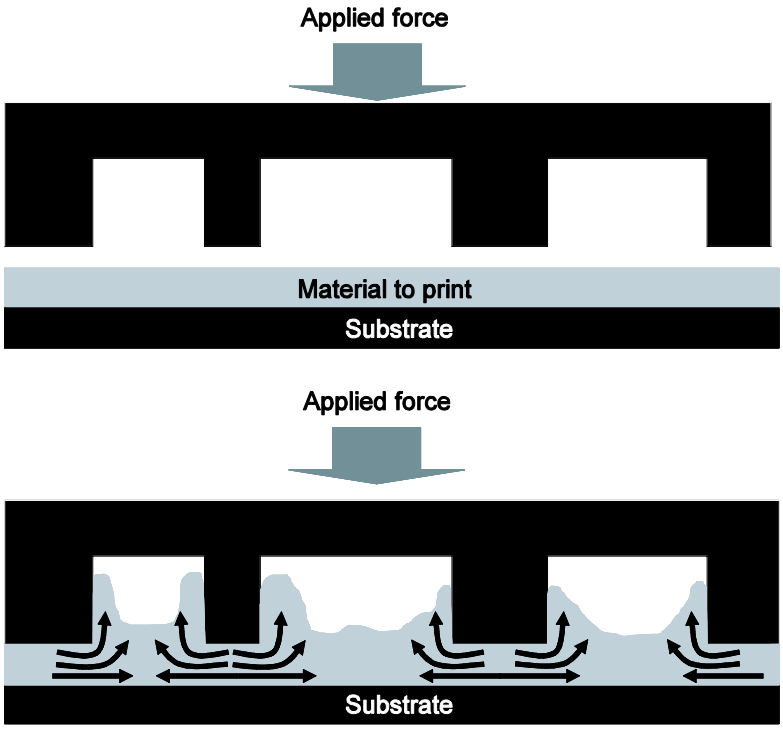

Figure 2.19. *Resist imprinting with a stamp. Arrows schematically indicate the complexity of the resist flow*

These material flows can both minimize the residual thickness and fill cavities. Depending on the flow properties (viscosity and surface energy) of the material to be embossed, we can expect that the extension of such planar flows may vary by several orders of magnitude. Consequently residual thickness control requires an

understanding and control of these two flows. An analogy with a simple and cheap experiment illustrates the importance of these flows. Take a thin piece of clay (a thermoplastic resin) between your thumb and forefinger. Tighten it firmly between your fingers (representing the mold and substrate). It will initially replicate your fingerprint on an area about the size of the piece of clay and, as you increase the pressure applied, the pressed surface becomes larger. This little experiment shows that the clay initially fills the fingerprints with the up and down movements (in the mold cavities) and then spreads to the rest of the finger (planar flow). Based on this experiment, we can wonder if the imprint can be considered roughly as:

– a filling regime for a stamp's structure with mainly vertical short displacements of the imprinted material (from a few to a few hundred nanometers);

– a planar flowing regime for the pressed material between the substrate and the mold over larger distances (a few micrometers to a few millimeters).

Even though the current state of research does not establish a relationship between the viscosity of the imprinted material, the volume to fill in the mold, the pressing conditions and the distance traveled by the planar flow, experimental results have been used to deduce some trends for thermally [HEY 00, LAN 06A, SCH 01a] and UV assisted NanoImprints [VOI 07].

Considering that the copy material may flow over distances similar to that of the sample, it is possible to establish a simple test for whether the mold can be completely filled or not. Figure 2.20 represents an arbitrary profile of a 3D structure to print, with h_i the initial thickness of the resist, S the surface of the substrate and the mold and p (x, y) the mathematical function describing the profile of the mold. The calculation of the ratio (f) between the volume to be filled in the mold (Vm) and the volume of incompressible material available (Vi) identifies three configurations:

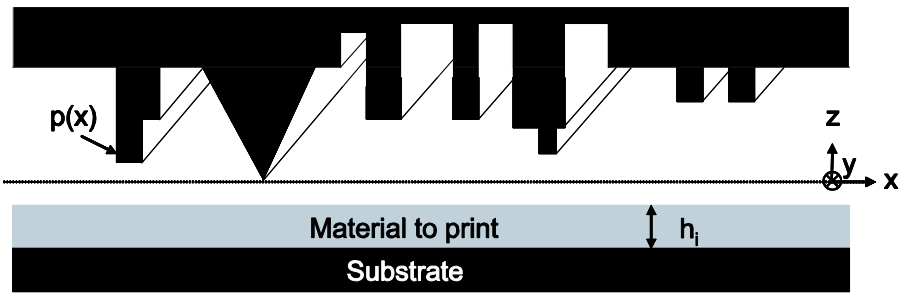

Figure 2.20. *Imprint of a 3D surface described by a function p(x) in a material's thickness h_i*

$$f = \frac{Vm}{Vi} = \frac{\iint_S p(x,y)dxdy}{h_i S} \begin{cases} <1 \\ =1 \\ >1 \end{cases} \qquad [2.13]$$

For a ratio f <1, the complete filling of the mold is possible because the material is present in excess. In this case the theoretical residual thickness (h_r) could be calculated and is given by:

$$h_r = h_i - \frac{\iint_S p(x,y)dxdy}{S} \qquad [2.14]$$

A ratio of 1 implies that the volume of material available is equivalent to the volume to be filled, thus implying a theoretical residual layer equal to zero.

Finally, for a ratio greater than 1, the mold cavities cannot be completely filled.

Note that this relationship does not show the printing conditions (temperature, pressure, time of printing) or material properties (viscosity, surface energy) and therefore cannot be considered to describe the dynamics of the process. It can only reflect an ideal static state of the process.

Although this simple analysis of the flow of a material does not take into account the full complexity of the system, it nevertheless allows the thickness of resin required to be optimized.

Let us consider initially a network of lines on a uniform large area of several square millimeters, as shown in Figure 2.21. Many results [CHA 07, GOU 07, LEE 05b] have shown that in such cases, specifically when symmetry is kept for the density and size of the design to be printed, the thickness of the final residual layer could be predicted using the formula above. In this simple case, widely implemented for many applications [AHN 05, CHE 02, WAN 99, WU 98], computing the residual thickness, given the geometry of the mold and the initial thickness, is calculated by the formula:

$$h_r = h_i - \frac{h_{mold}}{1 + L/S} \qquad [2.15]$$

This relationship simply reflects the conservation of volume at a local level. Therefore, we see an excellent agreement between experimental results and equation [2.15]. It is, however, important to note that these situations are representative of ideal cases, by the uniformity of the density or the size of the patterns on the mold.

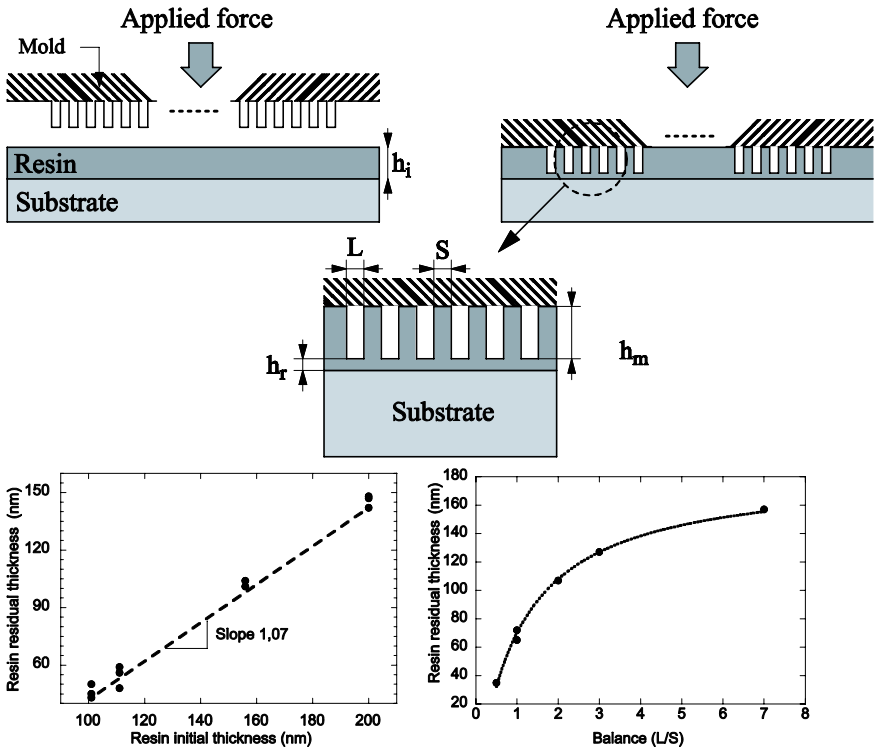

Figure 2.21. *Imprint of a lines array with a height h_m in a material with initial thickness h_i and a width L separated by a distance S. Both curves show the evolution of the residual thickness of resist for a 1 mm^2 network and a 110 nm deep stamp [GOU 07], as well as the ratio L/S for a 5mm^2 network and a 227 nm deep stamp with an initial layer of 185 nm [CHA 07]. The dots represent experimental values and the dotted line equation [2.15]*

If we now look at the distribution of the residual thickness at the edge of a uniform network pattern, typically a network of lines (Figure 2.22), we find a significant variation in the printed profile, even though the structures are all identical.

The presence of a symmetry breakdown in the imprinted design can be expressed either by a variation in the size or density (position x = 0, Figure 2.21), and

translates systematically in an inhomogeneous distribution of the residual thickness. Depending on the relative position of the area with no pattern at the top of the printable structures, two scenarios are possible even if the physical (mechanical description of the bending of thin plates) behavior of the mold is identical [FUA 05, MER 08, LAN 06b].

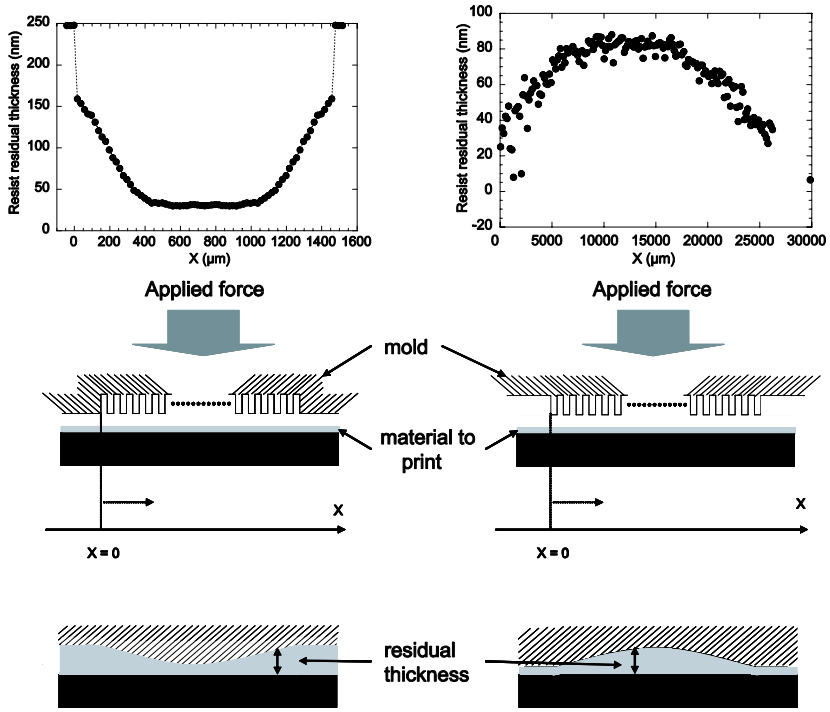

Figure 2.22. *Distribution of residual layer thicknesses along a line array as a function of the stamps' design in the structure-free areas. The design of the mold and the deformations occurring during the imprint are also pictured*

In a situation where the unstructured region of a mold is at the same level as the top structures to be printed (Figure 2.22, left), the average residual thickness obtained is more important than in the case shown on the right side of the figure. We will see later (fluid section) how this behavior can easily be interpreted with the so-called Stefan law. When the unstructured area is at a different level to the patterns (Figure 2.22, right) the minimum residual thickness is along the edges of the network. These two situations, quite representative of the impact of a stamp's design on the process, show that the greater the contact area between a mold and resin is (in

regions where there are no special reasons for printing), the slower the resist flows and penetrates into the mold.

As a consequence, in the case of Figure 2.22 (left), at the edge of the network close to a large mold contact surface, the resist penetrates less rapidly than at the center of the network. The opposite configuration applies in the other case, in Figure 2.22 (right). Having no immediate contact between resin and the mold during the first moments of imprint, near the edge of the network, these structures have a penetration rate far higher than those at the center of the network.

These distributions relate to both the mechanical properties of the mold and the intrinsic flowing properties of the pressed material. The adjustment of the operating points of the process (namely temperature, pressure or printing time) can, to some extent, homogenize the distribution of residual thickness without completely overcoming it [GOU 05, LAZ 04].

These results also show that for most thermoplastic resins used in thermal NanoImprint, the flow of matter in its viscous state over long distances, that is to say a few tens of microns, is nearly impossible. This limitation comes from the high values of dynamic viscosity, usually greater than 10^4 Pa/s [SCH 05b, LEV 07] for temperatures between Tg + 10°C and Tg + 70°C. Voisin *et al.* [VOI 07] showed that by using low viscosity (tens or even hundreds of mPa/s) formulations for UV-assisted NanoImprint (UV-NIL), this non-uniformity in the distribution of the residual thickness could be substantially reduced or eliminated.

The analysis of such networks of lines, very simple in terms of design rules, shows very clearly the main experimental issue in thermal NanoImprint: how to obtain an homogeneous residual thickness over the entire printed area. The situation becomes complicated when the imprinted patterns have different shapes [LAN 06B].

2.5.3. *How can the process impact the thickness of the residual layer?*

This question still raises a lot of interest in the scientific and technological community and many teams have presented various more or less simple approaches to address the issue. There are three main approaches:

– optimize the operating process points, namely temperature, time and imprint pressure as a function of the mold's geometry [BOG 05, GOU 03, GOU 04];

– develop a specific printable material that will present specific flow properties [CHA 06, GUO 07, LEE 05a, SCH 05];

– optimize the stamp's geometry [HOC 07, LAN 06a, MER 08, PED 08] or the imprinted stack [LEV 06].

The first option appears to be the most natural and easiest to implement experimentally. It mainly consists of adjusting the temperature, imprint pressure, and duration of printing. Figure 2.23 shows the impact of the shape of the structures, and especially their density, on the residual layer thickness. For equivalent printing conditions (the patterns are on the same mold) this thickness varies from 30 nm for a dot diameter of 400 nm to 140 nm for a ring of 2 µm outside diameter. This shows that during the thermal imprint, when materials with viscosities close to even a few fractions of MPa/s are employed, matter only flows over very short distances for standard process conditions (Tg + 40°C / 50 bar/5 minutes) [HEY 00].

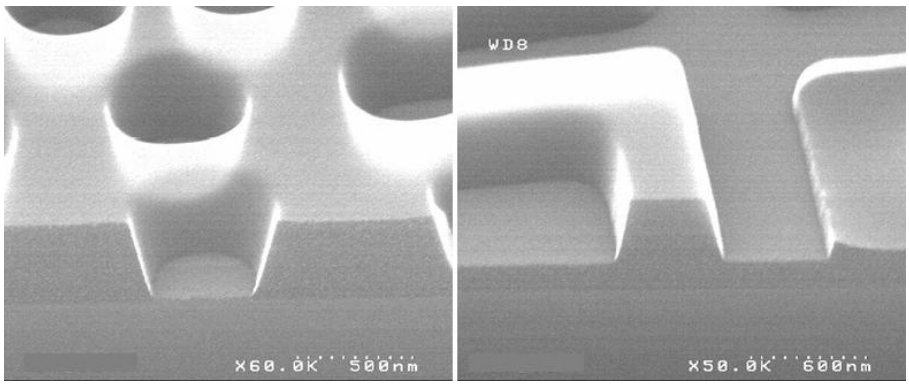

Figure 2.23. *Cross-section SEM images of a printed dot (left image) and a ring (right image), according to [GOU 03]*

The results obtained by Gourgon [GOU 03] on a simple structure such as a network of lines printed in an aperiodic thermoplastic resist film, clearly show the impact of pattern density on the residual layer thickness (Figure 2.23).

When the density of the patterns to be printed increases, the penetration of the mold in the material decreases. The residual thickness is thus more important than in an area where the structures are almost isolated. This implies an inhomogeneous distribution of residual thickness: a 27% variation between areas of high (top width = 1 micron) and low density (top width = 10 microns). However, we note that these inhomogeneities depend significantly on process conditions. Indeed, an increase in the printing temperature for the same printing time (Figure 2.24) highlights the possibility of achieving a relatively uniform distribution of residual thickness (less than 4% changes) regardless of the density. This phenomenon is directly related to the viscosity reduction of the imprinted material as the temperature increases. Usually, with the organic materials used in nanoprinting, viscosity is divided by ten when the temperature increases 10°C [LEV 07, SCH 06].

Meanwhile, increasing the printing time at a constant temperature (Figure 2.24) can also avoid these inhomogeneities, but at the expense of a very low throughput. Obviously, we primarily seek to increase the printing temperature, when the material allows it (which is to say, a working temperature below the degradation temperature of the material) to significantly reduce its viscosity and the printing time, rather than working with high viscosity and thus a longer printing time. It is important to note that the distributions of residual thicknesses result systematically in deformations of the mold itself [FUA 05, LAN 06b, LAZ 04, MER 08].

This deformation of the mold can lead to great stresses on the patterns themselves, and especially where the pattern density varies greatly. If the mold is completely filled by the polymer and the yield stress fracture of the material forming the mold is exceeded, a portion or all of the structures can be broken and embossed into the resin itself (Figure 2.25). Furthermore, it has been shown that these deformations and residual thickness distributions could lead to the emergence of structures in the resist in areas where the mold does not have any structures [LAN 05 LAZ 04, SCH 01a, SCH 01b].

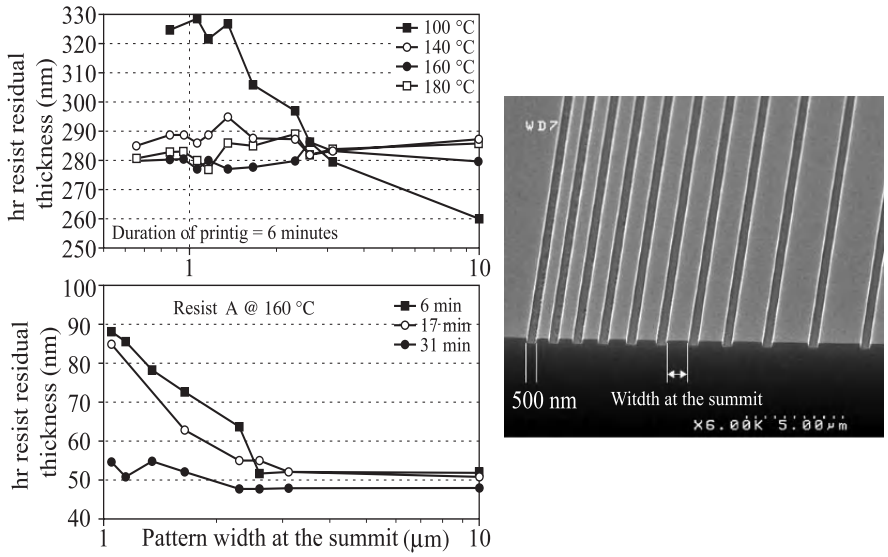

Figure 2.24. *Cross-section SEM image (right) of a 500 nm wide line network with a variable imprinted period in a thermoplastic resist. Evolution of the residual layer thickness (graphs on the left) as a function of printing conditions (temperature and time) for a pressure of 50 bars [GOU 03]*

The second approach is to use thermosetting formulations, which are liquid at room temperature, and therefore have dynamic viscosity (h <1 Pa) much lower than thermoplastics (h ~ 10^4 Pa). The imprint process is now changed because pressure can be applied at room temperature. The temperature increase is no longer to cross the glass transition temperature (Tg) (to decrease the viscosity of the polymer) but instead to achieve the crosslinking temperature (Tr) to make the formulation strong and stable at room temperature after the demolding step (Figure 2.26).

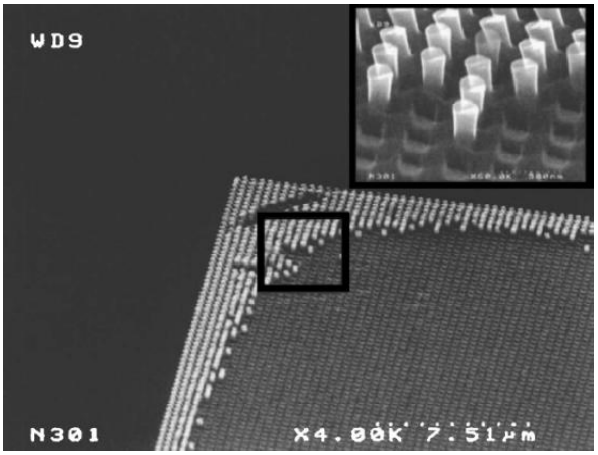

Figure 2.25. *SEM images of a 200 nm dot array pressed in a polymer. Note that some of the mold's elements have been transferred in the resist at the edges and corners of the die (from [LAZ 04])*

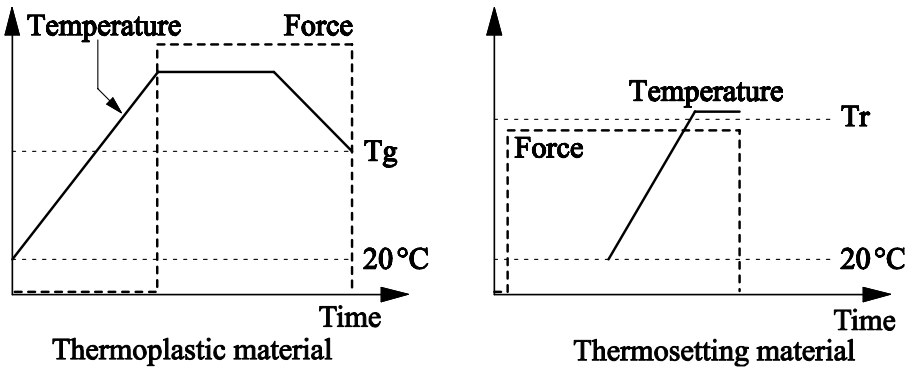

Figure 2.26. *Imprint process with thermoplastic and thermoset resist*

Results obtained by Lee [Lee 05a] show (Figure 2.27) that it is possible to obtain a residual thickness close to zero even when pressing surfaces larger than 100 cm^2. However, even though this path sounds promising, many efforts are still needed to reach a level of understanding similar to that developed for more standard formulations and chemistries typically used for resins dedicated to micro- and nanofabrication. This is why many of the results show that it is only possible to impact the capacity of the material to accurately reproduce the mold's patterns by modifying the molecular weight and not the chemistry of the formulations used [CHA 06, SCH 05b].

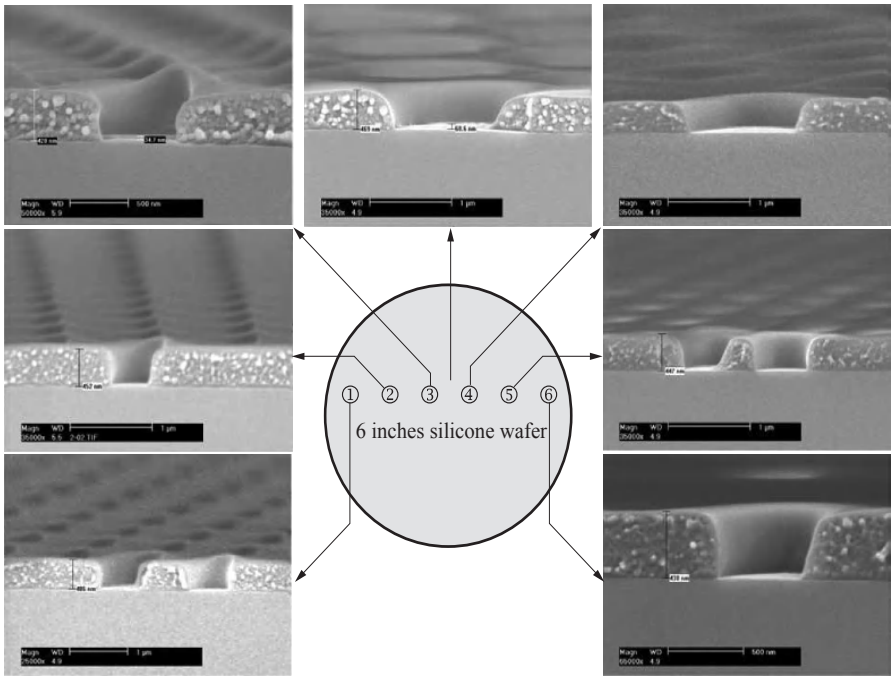

Figure 2.27. *SEM cross-section images of an imprinted resist using Lee's process [LEE 05a]. The various measuring points made on a 150 mm sample highlight the uniformity of the process. A residual layer with thickness almost equal to zero is obtained thanks to this process*

More generally, the compounds developed must meet certain requirements to be shaped by NanoImprint. Their Young's modulus must be less than the material's used to make the mold. The pressure used must be greater than the shear modulus of the formulation. The printed material must adhere well to the substrate supporting it

but must not stick to the mold, in order to facilitate the release and minimize defects. Moreover, these materials can be either functional, that is to say directly usable as such for the developed application, or resist an etching step to allow the transfer of the patterns formed into the substrate.

It should be noted that, even in the case of a complete filling of the mold, the distribution of residual thickness does not reflect the steady state of the system. Indeed, if the distances over which the polymer can flow are generally a few microns, there is apparently no limit if the printing time is long enough. Whatever the structures on the mold, a much longer printing time (of several hours) than the regular duration accepted for a realistic implementation process (a few minutes), would homogenize the distribution of the residual thickness. In practice, as we saw earlier, it is possible to use materials with lower viscosity to achieve the final state faster. It is also possible to change the stack itself [LEV 06].

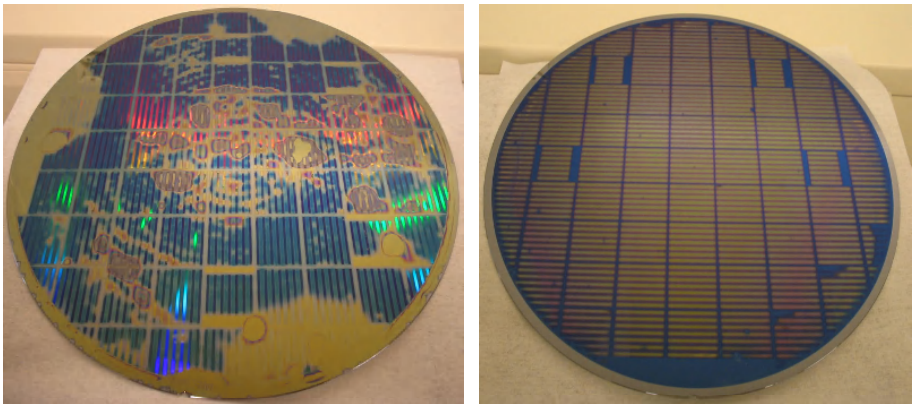

Figure 2.28. *Imprint of a 200 mm wafer without (left) and with (right) the use of a soft layer in the pressing stack; from [LEV 06]*

This latter approach is particularly relevant when the pressure on the back of the mold is applied mechanically with a piston. In this configuration, and because of the roughness on both sides of both the print sample and the mold, the pressure points are not uniformly distributed and fully compliant contact can be achieved only if deformation of the mold and sample are possible. Adding stack layers with low Young's modulus (compared to the mold and the sample) allows a regulation of the pressure applied on the reverse of the mold. The impact is significant, as pictured in Figure 2.28. Leveder [LEV 06] quantified the impact of this experimental trick and demonstrated that uniformity of residual thickness distribution at a short distance (of a few millimeters) and long distance (several tens of centimeters) could be improved

from 100% to 1% residual layer thickness. Therefore, it is possible to obtain distributions of residual thickness that do not vary by more than 1% on a whole 200 mm wafer.

Figure 2.29. *Schematic representation of a uniformly thinned mold (left) and a locally refined one (right) by Pederson [PED 08].The larger zones are 525 µm and the thinnest are 150 µm*

More recently, a solution that consists of modifying the mold itself to allow a larger deformation was proposed with a local thinning of the back of the mold [HOC 07, PED 08]. Figure 2.29 shows schematically the two molds' structures proposed by Pederson [PED 08]. In both cases, the thinnest areas have a thickness of about 150 µm, while the rest of the mold is 525 µm (standard thickness for a 100 mm silicon substrate). Each mold supports areas of 1 mm² on which lines of 25 µm wide and 1 mm length were realized. Pederson has also characterized the influence of line density on the resulting distribution of residual thickness, by varying the number of line from 8 to 24 in a unit cell (pattern density of 20–60%).

The uniform thinning of the entire reverse of the mold provides a uniform contact while applying light pressure (or force). But this also implies that the active areas (areas that support designs to be printed) will deform more easily. On the other hand, locally thinned molds have thick areas supporting structures that can reduce local deformation of the mold, while allowing a consistent contact thanks to thin membranes.

Figure 2.30 shows the evolution of residual thickness (in angstroms) for both configurations of molds, evenly tapered (Figure 2.30, left) and locally thinned (Figure 2.30, right) with structure densities ranging from 20–60%. In both cases, the higher the filling factor is, the lower the residual thickness because the mold cavities are more important. One can also notice that the residual thickness distribution is less homogeneous when the mold is uniformly thinned, agreeing with the greater capacity of this mold to be deformed. It is therefore quite possible to impact the distributions of residual thickness without changing the points of processes or materials, but only by optimizing the structure of the mold.

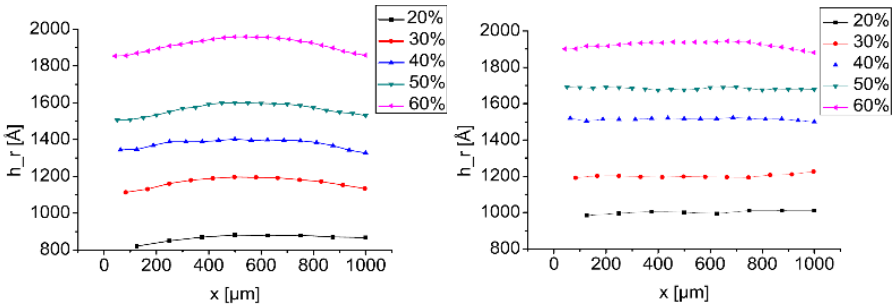

Figure 2.30. *Distribution of the residual layer (in angstroms) through an elementary cell of 1 mm^2 for various filling factors (from 20– 60%) and for both configurations, i.e. uniformly (left) or locally thinned (right) [PED 08]*

However, this attractive solution does not resolve the issues concerning differences between absolute values of residual thicknesses for various densities of structures. In fact, allowing a greater deformation of the mold reduces the residual thickness variations but, even for very long pressing times (several hours), it cannot make it uniform.

2.6. Residual layer thickness measurement

The presence of the residual layer of resin, which does not exist with standard lithography techniques, except by using resins with no threshold effect (called a gray scale resist [MUR 06]), is specific to NanoImprint. It gives rise to two completely new issues for the scientific community:

– how to remove the resist layer after printing without affecting the shape and dimensions of the imprinted design, in order to obtain a resin mask with the same characteristics as those obtained by other lithography techniques?

– how to measure its absolute value, commonly called residual thickness, and especially its distribution on a surface?

The first point is not a technological obstacle when the imprinted material will be directly used as an active element in the component [ICH 03, KIM 07, REB 07]. However, in most situations the imprinted resist is used as a mask to transfer topographic information in the underlying material via a wet or dry etching process. Consequently, it is necessary to have the highest anisotropic etching process with a lowest etch rate perpendicular to the substrate. Otherwise every etching step of the remaining thickness would cause changes in dimensions of the imprinted patterns and therefore an unacceptable loss of information (Figure 2.31). The development of

a very anisotropic etching process between two materials is a very common constraint in the field of micro- and nanotechnology. It is less common to get such results on a single organic material.

The second point is even more difficult to solve. Indeed, the various techniques commonly used in metrology allow the lateral and vertical dimensions patterns to be measured precisely, or the thickness of a flat film of a given material to be measured. In this case, the information sought is the thickness of a film covered by a gathering of patterns. Before the use of NanoImprint, measurement of the layer thickness could be done before micro- or nano-pattern manufacturing, as these technological flow were made of two different steps: material was first coated and then patterned.

The printing process creates the topography in a single step and with a residual thickness comparable to a continuous layer. The standard metrology techniques available, then, have many limitations for extracting both the topographic characterization and measurement of residual layer thickness.

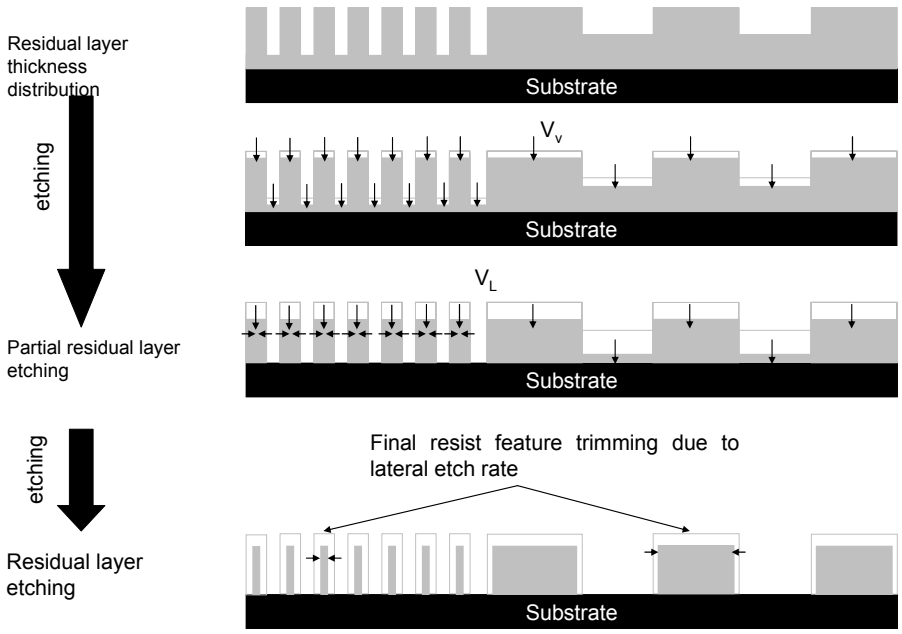

Figure 2.31. *Diagram of an imprinted resist pattern later etched in the subtrate, highlighting the impact of the horizontal and vertical etch rate on the original design*

2.6.1. *Macro-scale approach: coherence between film color and thickness*

The simplest characterization consists of observing the areas printed in the resin by optical microscopy. Obviously this technique has its inherent limitations, and cannot be used for quantitative metrology of structures much thinner than one micron. However, in terms of measuring the residual thickness, even if a local measurement is not possible, this approach, through the color distribution observed, qualitatively assesses the distribution of the residual thickness in the measurement field.

Indeed, the reflection coefficient of the resins is directly connected to the thickness of the observed film. Therefore, a small variation in thickness occurs when the color of the film changes as it is exposed to white light. Although it is possible to establish a mathematical link between the thickness of the film with its reflection coefficient and therefore its color, the implementation of a quantitative technique still faces certain difficulties involving:

– the non-bijective function over the whole domain of resist thickness used;

– the transfer function of the microscope;

– the need to have a reference point in the observation window and that the thickness does not vary too much.

However, this approach can still easily and qualitatively give access to the distribution of the residual thickness at different points of the processed sample. Its implementation is thus fully justified for process development. Figure 2.32 is an example of a 200 mm wafer and the information that can be obtained with such a characterization method. The figure shows the full wafer and five optical microscopy views of different areas of the substrate. The structures are much larger than one micrometer and the color uniformity is typical of an area with a homogeneous residual layer.

Moreover, we note that the color is also similar and consistent between different areas, indicating that the process leads apparently to a uniform result across the entire wafer.

This analysis can therefore very quickly evaluate the quality of a print. The non-uniformity of color does not always mean that the process is or is not poorly controlled. Indeed, depending on the patterns observed, the color distribution may be a direct image of a variation of the residual thickness.

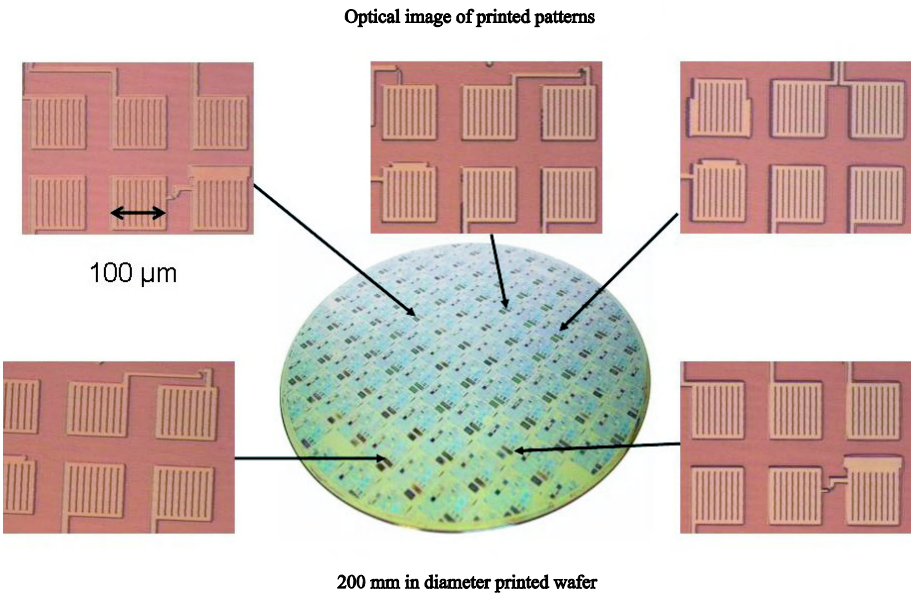

Figure 2.32. *A 200 mm wafer printed with 5 different close-ups from different areas of the wafer from [PER 04]*

In the case shown in Figure 2.33, a mold containing a 200 µm line array with a 1 micron period, with line width ranging from 150–850 nm, was printed in a 200 nm thick resist. The lines were made so they stick out of the mold with a height of 150 nm. An optical characterization of the printed pattern shows a consistent color around the network meaning that, in this area, the thickness is constant. As the mold contains no structures in this part, the resin has not been printed. In the 200 µm line array, we notice a change in color between the two ends. Given the asymmetry of this pattern on the mold it can be seen that the volume available between the lines varies uniformly between the two ends of the network of lines.

For this experiment, the initial volume of resist is much greater than required to completely fill the mold's cavities. We also know that the resin flows in the layer's plane occurs only for a few micrometers (the case of a thermal imprint). Therefore, the resist cannot compensate residual layer thicknesses over distances greater than a few tens of micrometers. The optical image is thus a representation of the distribution of residual thickness. Without being able to determine the values shown in two cross-sections along the network (Figure 2.33), this method allows the evaluation of a process and the distribution of residual thickness created is either as a result of the mold or the experimental conditions.

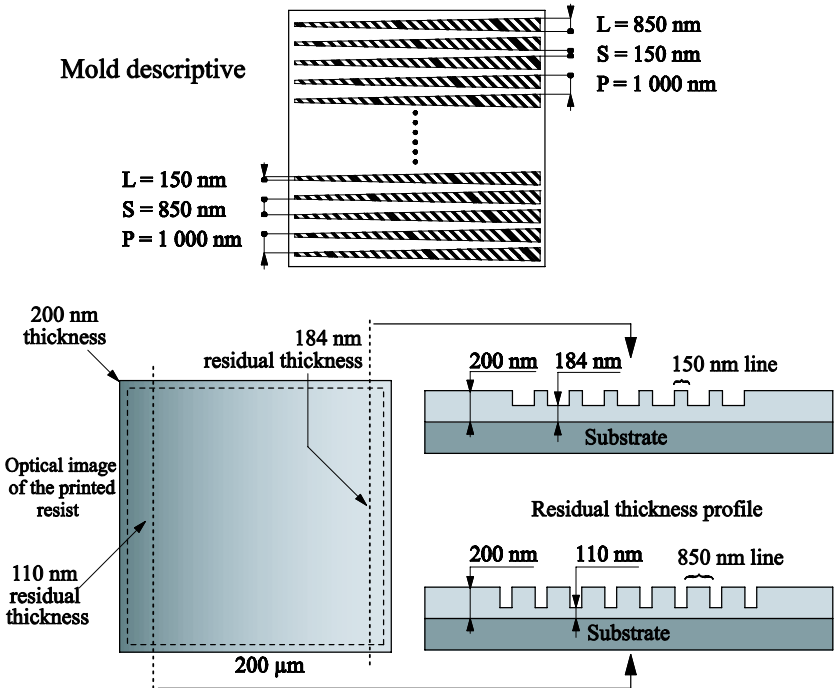

Figure 2.33. *Stamp pattern description. 200 µm × 200 µm line array with a 1µm period and line width ranging from 150–850 nm. Optical microscope images of a 200 nm resist layer imprinted, and a schematic representation of the imprinted pattern on both side of the array*

2.6.2. *Microscopic approach*

Quantitative information may be obtained by several approaches. However, these techniques are not simple to carry out experimentally. They can be destructive or not, with a field of view from several μm^2 up to a 200 mm wafer. Some are indirect measurement, and others apply only in cases of very specific processes.

2.6.2.1. *Scanning electron microscopy (SEM)*

Since scanning electron microscopy (SEM) is widely use to characterize micro- and nano-fabrications it is a very attractive and straightforward technique for the characterization of printed patterns. Two approaches are possible: an observation view (called top view SEM) that does not require a special treatment of the sample but does not measure the residual thickness, and a cross-section observation of a test sample; this latter method is destructive and requires a pre-metallization of the

surface to prevent a charge effect during the characterization that could change the printed topography and therefore induce measurement errors.

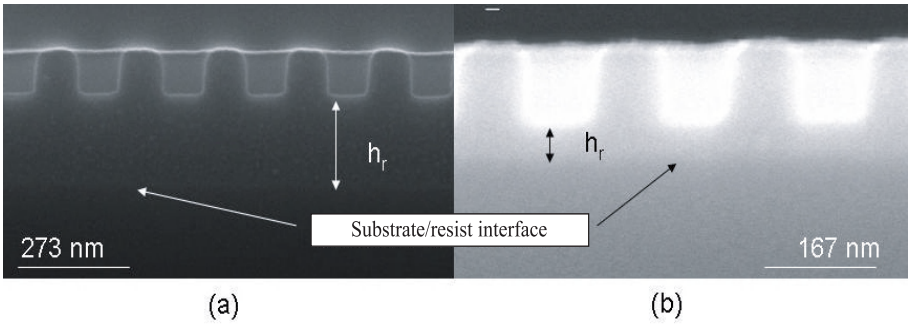

Figure 2.34. *Cross-section SEM image of a hole array of 110 nm with a 90 nm pitch imprinted in a polymer: (a) we can clearly identify upper and lower interfaces of the resist; (b) the observation conditions make the observation of various interfaces more difficult*

This characterization remains very local with a measuring range of a few micrometers (Figure 2.34) and does not establish a mapping (except with a large number of observations) of the residual thickness over areas of several millimeters. It is important to note that the SEM cross-section observation also presents some constraints in obtaining very precise quantitative measurements. Indeed, because of the various aberrations inherent to electronic columns, the scale calibration in the directions perpendicular and parallel to the surface of the sample can be difficult to perform. Depending on the nature of the substrate and the resin to be observed, charging effects can occur during image acquisition making the identification of interfaces impossible (Figure 2.34(b)) and even changing the geometry observed. In addition, the electron beam must be as perpendicular as possible to the plane defining the section view, in order to observe the actual heights and not their projection.

2.6.2.2. *Atomic force microscopy (AFM)*

Atomic force microscopy has the advantage of being harmless to the samples. It allows easy determination of printed geometries (width, length and height), taking into account the convolution of the tip and the patterns characterized. The measurement range can reach 40 µm × 40 µm and be repeated (manually or automatically) at several points on the wafer. However, it is only possible to access the residual thickness under certain conditions. Indeed, AFM characterizations are not absolute measurements of the height but measure relative changes in height. There is no absolute reference for the determination of thicknesses and heights give access to the distribution of the printed depth in the resin. Figure 2.35 clearly shows

that two samples with very different initial residual thicknesses but printed with the same patterns present different residual thicknesses, but will lead to the same AFM measurement.

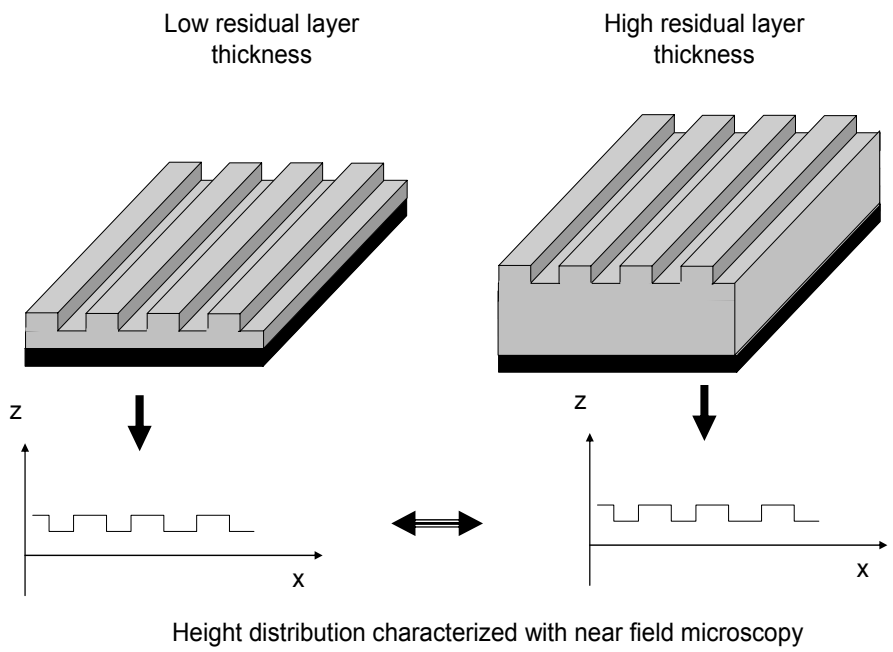

Figure 2.35. *Schematic representations of the imprint in two very different initial resist thicknesses and their corresponding profiles obtained by near field microscopy, or profilometry*

However, there are some configurations that favor the use of atomic force microscopy or profilometry. The main problem of these techniques is the absence of a reference height. Therefore, with a reference on sample, the absolute measurement of the residual thickness becomes possible. This is likely when the design of the mold, the initial thickness of resin and the process conditions lead to a partial filling of the mold's cavities. If the structures on the mold are sufficiently spaced so that the unprinted resin's surface is not perturbed by the resist flow around the structures, this region of the sample is therefore a reference thickness equivalent to the initial resist thickness. The depth of the imprint is measured by AFM or profilometry. The difference between these two quantities gives direct access to the remaining thickness (Figure 2.36).

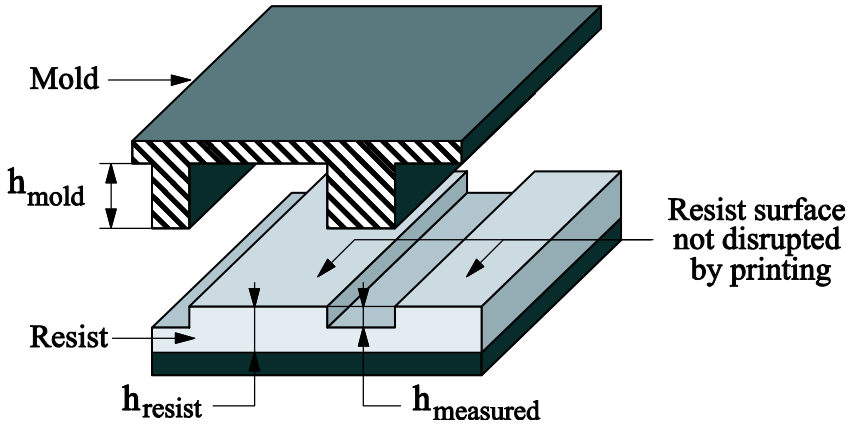

Figure 2.36. *Schematic representation of an imprint configuration for which a partial filling of the structures of the mold is observed. The unperturbed resist surfaces can establish a reference altitude point for AFM or profilometry measurements*

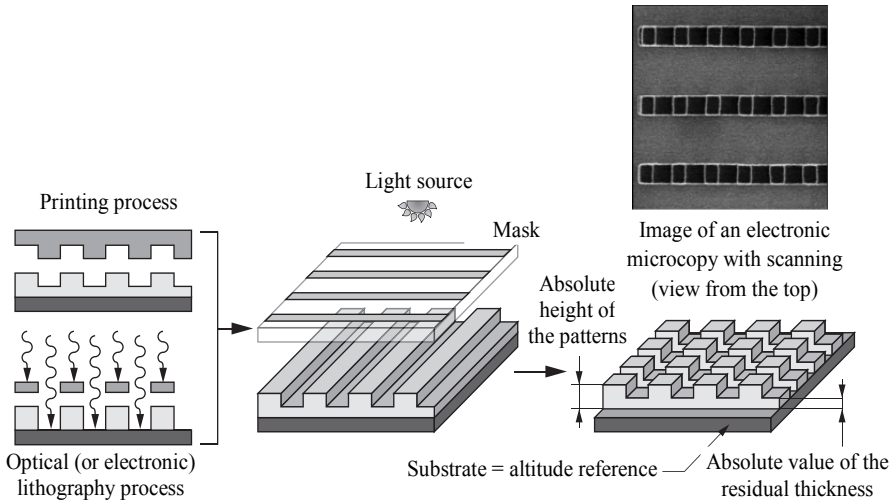

Figure 2.37. *Hybrid process combining an imprinting step and an electronic or optical exposure of the imprinted resist to locally strip the subtrate's surface. Top view SEM image of the formed patterns. Dark areas represent the resin and the lighter zone is the surface of the wafer*

In cases where the printing conditions do not give a reference value, after pressing, some areas of the resist (for which the resin should be photosensitive or

electrosensitive) can be exposed to photons or electrons and therefore obtain a reference point for the thickness of the resin (Figure 2.37).

The initial imprinted structures being substantially modified, this process should be considered destructive. It may help, however, in making resin patterns with different heights for 3D molds, i.e., with different heights for different patterns.

2.6.2.3. *Optical scatterometry characterization*

Scatterometry is not an optical imaging technique. It is based on the measurement of an optical signal scattered by an array and the simulation of the same spectrum. J.R. Coulombe first proposed this concept in 1998 [COU 98]. The analysis of the diffraction spectrum of a coherent beam on a periodical pattern allows the theoretical characterization of 2D (typically lines) and 3D (holes and dots) structures. This approach can be split into two stages:

– the measurement of the diffraction spectrum;

– the determination of the shapes of the array leading to the measured signal.

The first stage is a measure of the average response of a pattern array. This characterization is therefore less sensitive to local variations in geometry, unlike scanning electron microscopy. It appears very clearly that this measuring method will not be affected by localized or isolated printing defects.

The second stage is thus the reverse problem; the geometry of the diffracting system should be identified. The methodology used for this type of problem involves comparing the experimental spectrum with a calculated one. The theoretical spectrum, calculated from a set of parameters describing the periodic pattern, minimizing the mean square error with the experimental spectrum, can then determine the most plausible geometry for the sample. This optimization step can be achieved by creating a library of scattered signals for all geometries considered [COU 98] or standard approaches such as the Levenberg–Marquart algorithm [LEV 44, MAR 63].

To do this, the geometry is set periodically. Maxwell's equations, appropriate boundary conditions and a rigorous diffraction model, typically based on the modal MMFE method (with Fourier expansion) and a rigorous coupled wave analysis (RCWA) are then used to calculate the diffracted light for each set of parameters. This technique has many advantages:

– there is no physical contact between the probe and the sample, thereby reducing any risk of degradation or contamination;

– it is non-destructive since it requires no special preparation of the sample;

– it is very accurate because the information is contained in the phase of the diffracted signal, and the resolution is thus much smaller than the wavelength(s) used. Therefore it is also very sensitive and allows very small changes (~1 nm) in size to be identified;

– it is perfectly reproducible;

– it allows fast characterization of very large areas (several cm^2), the acquisition time of a spectrum being of the order of a few seconds;

– simulations of the spectra can take into account multilayer stacks.

This very last point makes the determination of the residual thickness possible. Furthermore, the width, height, slope of the sides of the structures, and the depth and thickness of the printed sub-layers present on the substrate can also be determined.

The main drawbacks of this technique lies in the fact that it is not possible to characterize non-periodic patterns and that this indirect method of determination of geometrical quantities does not measure the sizes of the structures outside of a range of values predetermined by the user. This scatterometry technique can be implemented at different levels of complexity.

2.6.2.3.1. Quantitative approach

The simplest approach [JUC 04] is to measure the scattered signal from a pattern array and monitor the intensity of a particular diffraction order, usually 1 or - 1, which is very sensitive to the quality of the imprinted features. Without going into the problem of inverse method, this simple approach allows a process window to be determined, i.e. temperature and printing time and the demolding temperature, which maximizes the scattered signal and hence the quality of printed patterns.

Figure 2.38 shows the evolution of the first diffraction order for a line array with a 770 nm period, for three different pressure values (P = 0.2, 0.4, 0.6 kN) versus time and printing temperature. At constant pressure, it is clear that the reproduction of the network is enhanced when temperature and pressing time are high. However, we note that at high pressure (0.6 kN cases), demolding at a temperature above 130°C, depending on the imprint time, may induce a deformation of the patterns measured by the reduction of the scattered signal, implying a deterioration of the printing process. The flowing mechanism responsible for this evolution of the printed shapes has been the subject of many studies. The control of the latter allows us to consider thermal printing processes at high production rates.

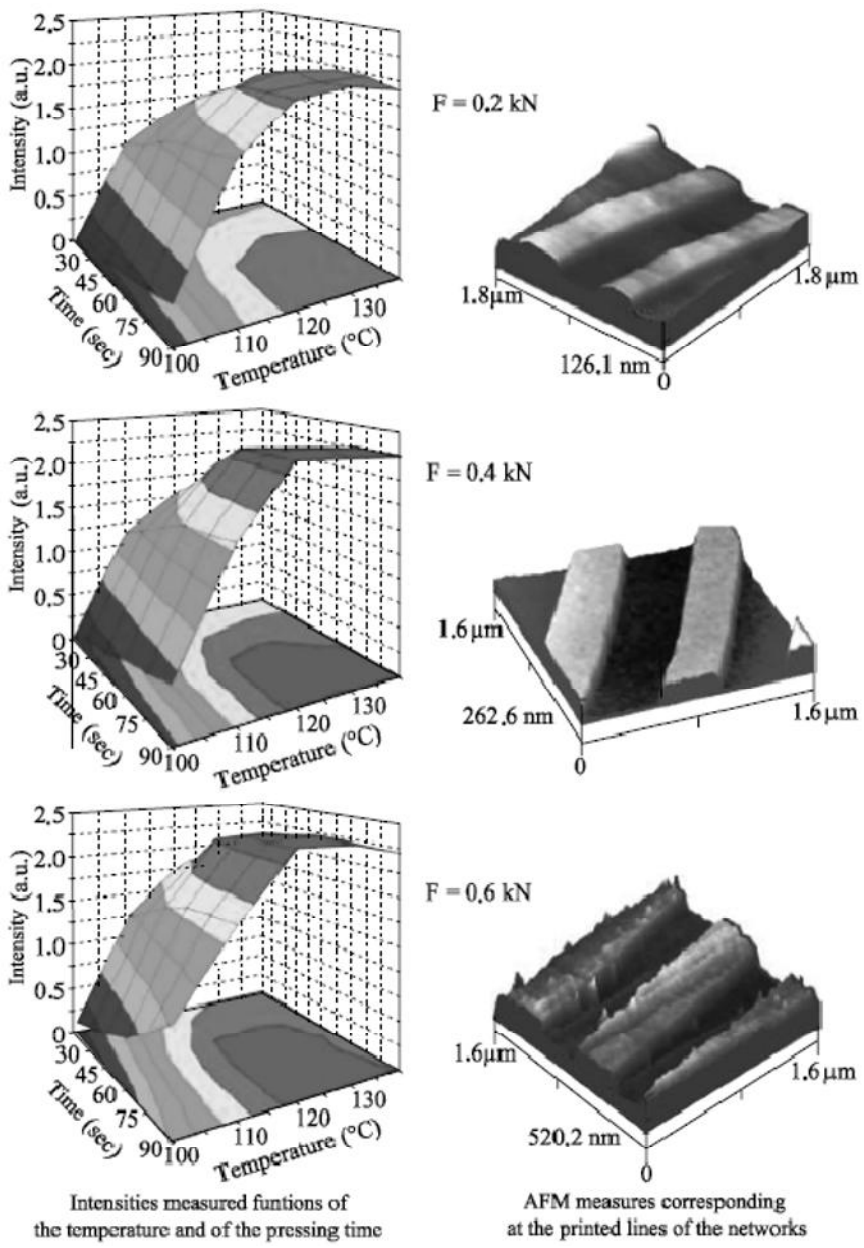

Figure 2.38. *Evolution of the first diffraction order for a line array with a 770 nm period imprinted with a force ranging from 0.2– 0.6 kN. The dependence on time and temperature and corresponding AFM images are presented for 3 imprints; results from [JUC 04]*

2.6.2.3.2. Quantitative usage

The implementation of this technique for a quantitative approach is more complex both experimentally and in terms of analysis of measured spectra. In this case, it is necessary to measure not only the scattered spectra but also to generate a library of simulated spectra. For this last point, it is essential to know the values of optical indexes (*n* and *k*) of materials making up the system, as well as ranges of geometries to be simulated. Experimentally it has been demonstrated that a simple measurement of the diffraction signal is not sufficient; the determination of materials' indexes in the electromagnetic spectrum used for measurement can be a very complex problem. In 2005, Fuard [FUA 05] showed that scatterometry appeared the most suitable quantitative method to characterize nanoimprinted patterns.

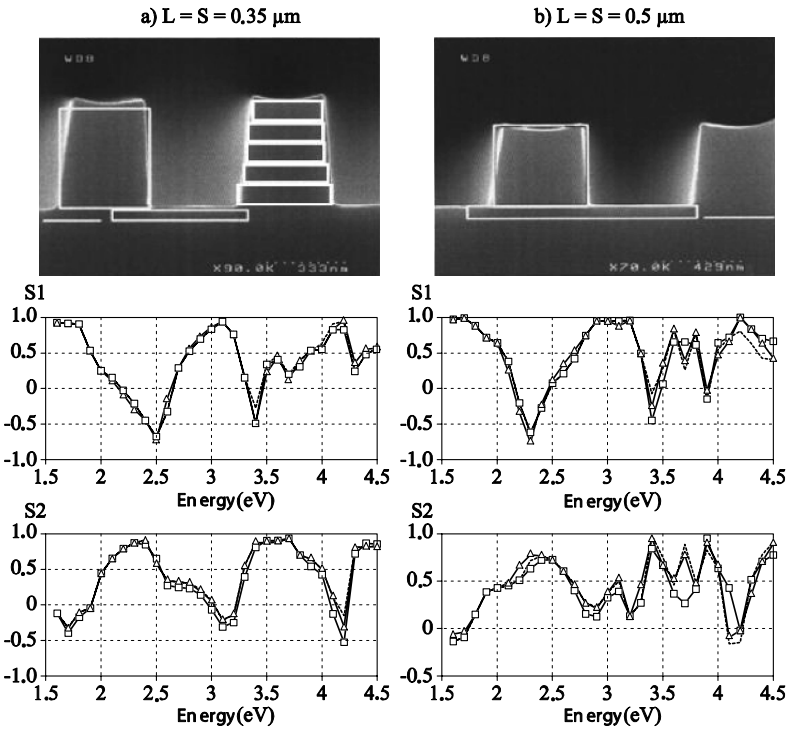

Figure 2.39. *Comparison between experimental spectra (dotted graphs) and scatterometry computed ones (graphs with symbols). Squares/triangular symbols correspond respectively to the rectangular and trapezoidal models. Spectra have 31 energies ranging from 1.5–4.5 eV. Two iso dense 350 and 500 nm line arrays were characterized; from [FUA 05]*

Figure 2.39 is a comparison between a sectional scanning electron microscopy characterization and the result of a scatterometry for two dense lines arrays with 350 nm and 500 nm periods. There is also good conformity between the spectra (S1 = cos (2Ψ) and S2 = sin (2Ψ) cos (Δ), with Ψ and Δ angles used in ellipsometric mode) and experimental (dotted curves) and calculated diffractions (curves with square and triangular symbols).

Two models were considered for this study (Figure 2.39): a rectangular description for the pattern printed in the resin and a trapezoidal description divided into five rectangular slices (triangular symbols). The second approach takes into account the slope of the sides of the printed patterns, caused by either the mold or resist flows during the demolding process, for example. If this description is actually more accurate (Table 2.3) and more representative of reality, it requires longer computation times (CT parameter in Table 2.3) for the simulation of the spectrum.

Feature 1/2 pitch	**SEM-cs**	**Rectangular Model**			**Trapezoidal Model**		
(line = space) (nm)	**RRT (nm)**	**RRT (nm)**	**Error**	**CT (s)**	**RRT (nm)**	**Error**	**CT (s)**
350	49	47.5	0.81×10^{-2}	43	47.8	0.21×10^{-2}	150
500	61	57.6	2.8×10^{-2}	66	59.3	0.57×10^{-2}	341
1 000	67	60.3	1.8×10^{-2}	156	59.7	1.4×10^{-2}	357
1 500	67	119	9.9×10^{-2}	136	135	16.5×10^{-2}	244

SEM-cs = SEM cross-section view

Table 2.3. *Comparison between residual thickness measurements (RRT in nm) obtained with SEM and scatterometry methods with two models, considering a rectangular and trapezoidal description. For scatterometry results, the error (in %) and the computation time (CT in s) are specified; from [FUA 05]*

Figure 2.39 and Table 2.3 summarize the conformity that can be obtained between measurements made by scanning electron microscopy and scatterometry. We notice very clearly that the error obtained with the trapezoid model is much

lower than with the rectangular design. This numerical error can be converted into an error in nanometers; however the conversion factor will depend on the geometrical model considered for simulation, and the size of the measured patterns (Figure 2.40).

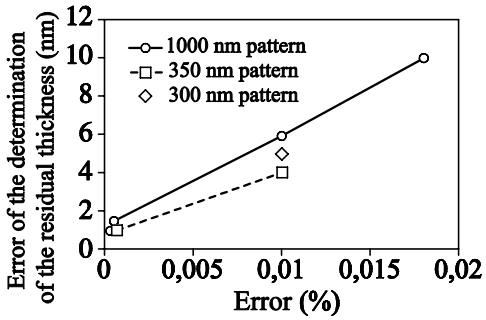

Figure 2.40. *Comparison between the error measured during the recognition of the best scatteromtrical signature phase and the real equivalent error in nm on the dimension of the pattern simulated from [FUA 05]*

Table 2.3 summarizes the results obtained in the case of a partial filling of the mold cavities (the case for a 1,500 nm pattern). In this case, one notices a significant difference between the results of electron microscopy and scatterometry. In this context, this metrology technique becomes quite inappropriate. Indeed, scatterometry, using scattered signal, presupposes a complete filling of the mold or partial but consistent filling from line to line. This configuration is very unlikely, since it has been shown that during the printing, mold filling was not homogeneous [FUA 05].

Even if the numerical error in this case appears to be much greater, it has not yet been determined as a test to discriminate quickly and securely the relevance of the results of scatterometry. Together with the need to minimize the simulated geometric space and, therefore, the number of spectra, these are the main drawbacks of this reverse metrology method.

2.6.2.3.3. Using real-time tracking of the imprint

The final implementation proposed for this method is to perform a real-time monitoring of the resist flow into the mold [XIA 06, YU 04]. This time-resolved diffractive scatterometry approach (TRDS) can follow the intensity of the first diffraction order on a pattern array during the mold filling stage in real time (for time scales of seconds or even tens of nanoseconds). The use of a transparent mold with a wavelength probe is necessary. During the imprint, the resist fills the mold

cavities, gradually changing the refractive index of these areas. The diffraction pattern and thus the measured signal are then directly related to the filling rate of the mold.

Figure 2.41 is an example of the measured signal for a line array of 650 nm wide, with a 1000 nm pitch. The mold and resin are put into contact at room temperature and the whole system is then gradually heated above the glass transition temperature of the polymer to allow the mold to penetrate into the resist layer. The mold cavities are filled with resin, thus changing the refractive index of this area.

The filling of the mold cavities with the resin results in a variation of the average refractive index in these regions, thus changing the intensity of the diffracted signal. Since the indices of the silica used for the mold (n = 1.46) and polymers used for NanoImprint (n > 1.5) are greater than the index of air, an increase in the average index and therefore a reduction of the diffracted intensity is observed during the filling. Although this result does not achieve a real-time tracking of the resist–air interface, the two corresponding points at the beginning (start) and end (end), respectively of the mold filling process is a valuable contribution to the process optimization. Indeed, this approach allows a direct verification of the impact of the applied pressure, the mold's geometry, the resist viscosity or the printing temperature on the filling kinetics of the mold. These experimental results can be understood and simulated with rigorous numerical modeling. However, a scalar theory of diffraction is sufficient to reproduce the experimental results [YU 04].

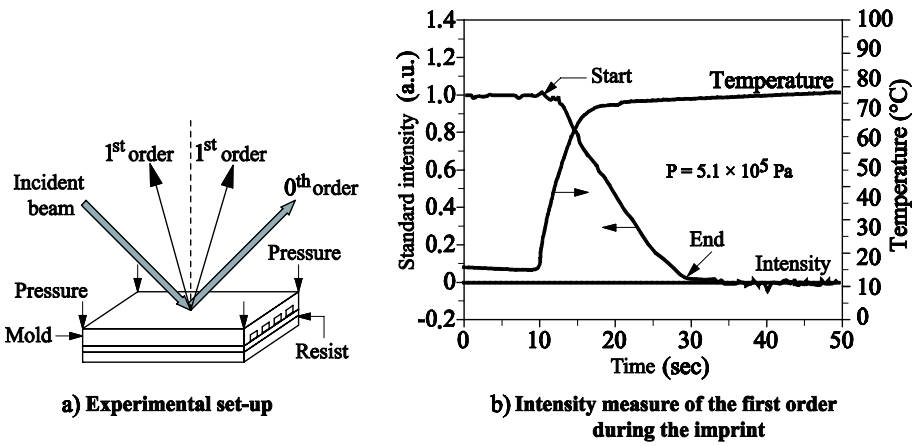

Figure 2.41. *(a) Experimental set up for real time monitoring of the mold displacement into a resist; (b) experimentally measured signal during the imprint (full line) and process temperature (dotted line)*

2.6.2.4. *Characterization by X-ray specular reflectivity*

Scatterometry implementation is not limited to wavelengths in the visible range. The use of much smaller wavelengths in the X-ray field has been proposed by Lee [LEE 05c]. This technique is based on X-ray specular reflectivity, usually used to measure the thickness, density and roughness of thin films (typically a few nm to several hundred nanometers). This technique, without changing the experimental protocol, can be applied to layers with topography.

Although this approach allows a much better resolution than offered by optical scatterometry to be considered, it requires a harder and more complicated experiment. Moreover, its use for a qualitative assessment of the imprint is not possible and the use of models based on quantum mechanics is needed to interpret and use the reflectivity spectra. Figure 2.42 shows the evolution of the reflected intensity (in log scale) as a function of the angle of incidence of the X-ray beam expressed in wave vector Q ($Q = 4\pi/\lambda \sin(\theta)$). Two regimes can be identified on these spectra: the first, for small wave vectors ($< 40 \times 10^{-3}$) representing the critical angle of reflection, is directly related to the atomic composition of the material probed [PAR 54] and therefore to its density profile; the second scheme, from which we can identify so-called Kiessig fringes [KIE 31], can usually determine the thickness, surface roughness and density profile of the material deposited in thin layers. Detailed analysis of the position of critical angles identifies the average density of different regions of the sample as shown in Fig 2.42. The density of a layer being directly related to the size of the grounds and spaces filled with air, it is possible to trace the size of the objects characterized.

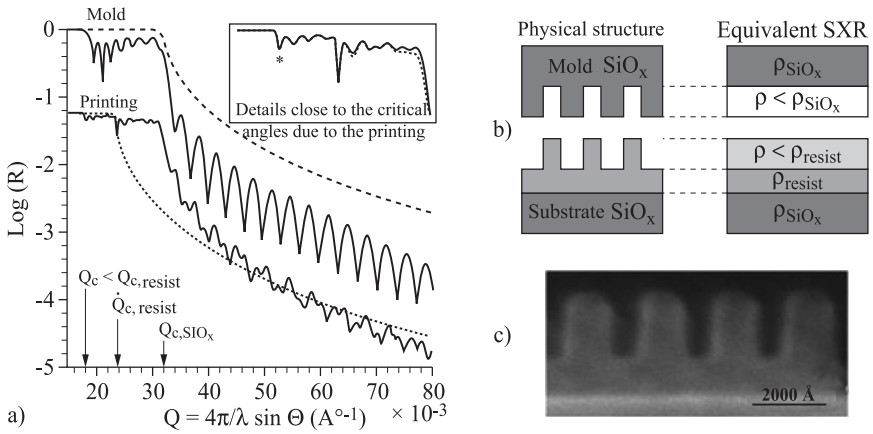

Figure 2.42. *(a) Evolution of reflected intensity as a function of the incident angle of the X-ray beam; (b) schematic representation of equivalent densities in printed structures; and (c) corresponding SEM image. Results from [LEE 05c]*

Although the theoretical foundations are different, the philosophy is similar to optical scatterometry. However, while a rough knowledge of quantities that we seek to determine (line width, height pattern, residual thickness, etc.) is sufficient for optical scatterometry, RX scatterometry gives access only to the line–space ratio of the patterns measured. The determination of the absolute value of the width of the line requires the use of another method of characterization to calibrate the simulation, by measuring the width of either the line or the trench (in the case of a line network). Moreover, it is not possible to differentiate the left and right corners of the patterns and the simulation yields only to a mean angle. Finally, this method seems best for characterizing patterns with dimensions of the order of a hundred nanometers, significantly reducing its range of application compared to optical scatterometry.

2.7. A few remarks on the mechanical behavior of molds and flow properties of the NanoImprint process

The complete modeling of a manufacturing process makes the optimization of process windows easier. This approach, generally well controlled in the macroscopic domain, is fully transferable to NanoImprint with some adjustments. Without considering the physical chemistry of interfaces, i.e. the wettability of a polymer in its molten state on an area of the mold with low surface energy, modeling the printing process requires consideration of fluid (polymer pressed)–structures (mold) interaction. Although we have seen that it is possible in most situations to predict the final state of the system based on a simple conservation of volume of materials moved, knowledge of the state of the system can be considered at any moment by an analytical approach. The real-time penetration monitoring of an assembly of patterns in the resin above its glass transition temperature requires the use of specific numerical approaches.

Many authors [HIR 04, MEN 06, ROW 04, CRS 07] have proposed various solutions to enhance experimental results modeling. However, for given geometries (we consider, in the following case, infinitely long line arrays), it is possible to provide an analytical description of the mold penetration within the resin at any moment. This oversimplified representation of the imprint, allows a better understanding of some experimental results [COL 04, LEV 07, SCH 03] and of the impact of the properties of material used during pressing. The scope of such representation is relatively small and only applies to designs with low aspect ratios (height/width of the pattern to be printed) and very low densities (almost isolated). In other situations, the assumption of laminar flow is no longer sufficient to describe more complex configurations.

Considering that the flow, in the material we want to model, is homogeneous, two assumptions can simplify the equations of conservation (conservation of mass and motion) used: the hypothesis of a Stokes flow and the lubrication approximation. A Stokes flow is a flow in which inertial effects are negligible compared to viscous effects. To determine if this flow regime is reached, the Reynolds number, Re ($\mathrm{Re} = \rho UL/\eta$) is usually estimated, where ρ is the density of the material (~ 1040 kg/m3 for resins), U the characteristic velocity of flow (~ a few tens of nm/s, or less), L a characteristic dimension of the system (typically the pressed line width ~ 10-^{6} m across) and η the dynamic viscosity of the printed material (~ 10^5 Pa).

In the context of nanoprinting, this Reynolds number is extremely low (~ 10-^{17} or less), thus validating the assumption of a Stokes flow. As for the lubrication approximation, it is justified when a flow is very small compared to the others. In this case, this implies that the width of these lines (a few hundred nanometers) is very small compared to its length (several millimeters). This assumption allows the restriction of spatial dependencies of the components of the velocity field and pressure, which makes an analytic integration possible.

The last simplifying assumption reflects a greater surface stress than volume stress (gravity) and is quantified by the capillary length κ^{-1} ($\kappa^{-1} = \sqrt{\gamma/\rho g}$ (where ρ is density, g is the gravitational constant and γ the surface energy of the polymer) [GEN 89]. The characteristic dimensions of our system are well below the capillary length, so gravity is negligible, thus simplifying the flow equation.

Given these considerations, in the absence of a mass source term (no creation or destruction of fluid) and body force, the laws of conservation of mass balance and momentum, respectively, may be written as:

$$\frac{\partial \rho}{\partial t} + div(\rho \vec{v}) = 0 \qquad [2.16]$$

$$0 = -\overrightarrow{grad}\, P + \eta \Delta \vec{v} \qquad [2.17]$$

with ρ the density of the fluid and $\vec{v}$ its velocity, P the corrected pressure ($P = Ps + \rho g z$ with Ps being the static pressure) and η the dynamic velocity of the fluid.

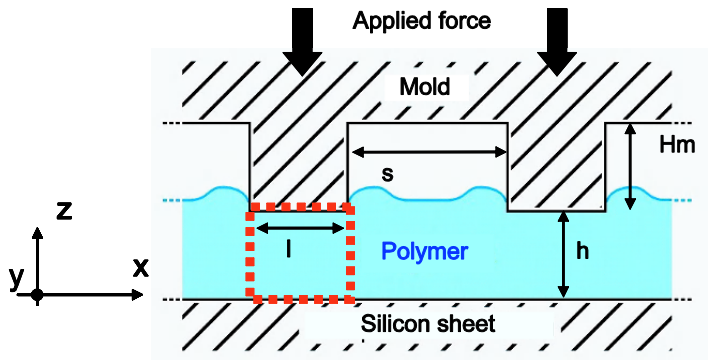

Figure 2.43. *Representation of the model used to imagine the penetration of a line of width l and height Hm in a resist film with thickness h*

The surfaces of the mold and the substrate are resist-proof; the x and z components of the velocity field are zero at z = 0 and z = h (Figure 2.43). In addition, assuming a two-dimensional system and lubrication we can also consider that the pressure field is constant under z. By using and integrating equations [2.16] and [2.17] along z in the unit pattern printing the fluid, we can then determine the component of the velocity field along the line of the mold:

$$u_x(x,z,t) = x\frac{6}{h}\left|\frac{\partial h}{\partial t}\right|\left(\frac{z^2}{h^2}-\frac{z}{h}\right)$$

with z being the altitude between the surface of the substrate and the mold line. The Stokes equation can then determine the field pressure in the fluid and, by integrating over *x*, the force felt by the line of the mold. It is then possible to establish a relationship between the rate of sinking of a single line, its geometric characteristics, the pressing conditions and the viscosity of the material:

$$\frac{\partial h}{\partial t} = \frac{1}{\eta}\frac{F}{L}\frac{h^3}{l^3}$$

with η the viscosity of the resist, F the applied force by a single pattern on the fluid, L the dimension of the line along y, h the height of the resist under the structure at any time and *l* the width of the imprinted line. Considering an initial thickness of resist h_0, the following relation expresses the evolution of the thickness of resin under the structures:

$$h(t) = \frac{h_0}{\sqrt{1 + t/\tau}}$$

with:

$$\tau = \frac{\eta L l^3}{2 F h_0^2}$$

Note that increasing the viscosity or the width of the line increases the characteristic time τ and vice versa for an increase of the initial thickness or the applied force. An increase in τ implies a slowdown in the penetrating rate of the mold in the resin (Figure 2.44).

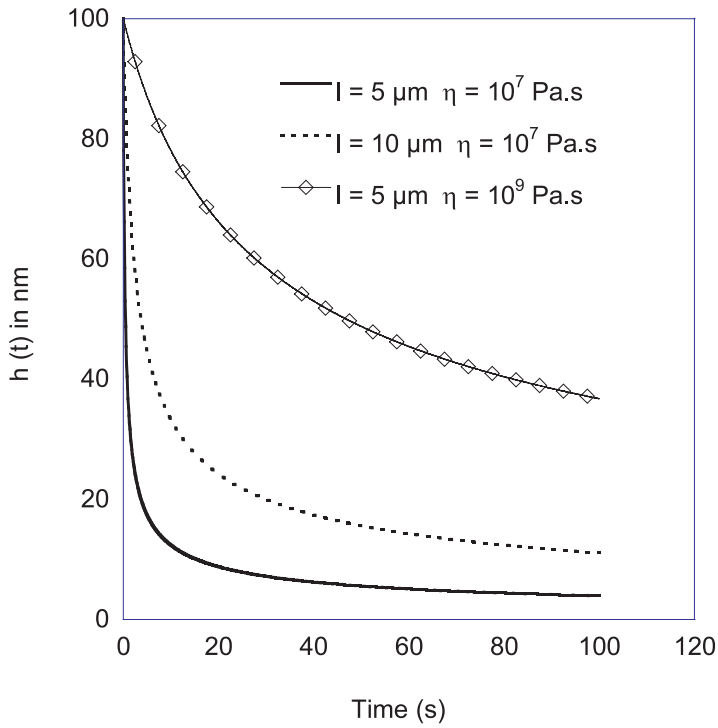

Figure 2.44. *Evolution of resist thickness under a 5 µm or 10 µm long and 1 mm wide line. Initial thickness is 100 nm with a 400 N force applied on each line and a 10^7 or 10^9 Pa/s viscosity*

To carry out further quantitative analysis, it is necessary to implement numerical approaches. To do so, three approaches can be considered to simulate thermal NanoImprint: finite differences; finite elements in which the resin is considered as a viscous solid [HIR 04]; a mixed approach with a finite element to model the behavior of the mold and a Volume of Fluid (VOF) approach, specific to the inclusion of specific behaviors, to model the resist fluid. Only the latter approach allows consideration of the fluid structure during printing, essential to take into account the deformation of the mold during a pressing. It should be noted, however, that the latter approach, despite being the most accurate, requires a significant computing time of several hours, for an area far less than the size of an entire stamp/mold.

King's team [ROW 05] from the Georgia Institute of Technology has specifically studied the various filling modes in different cavities. According to available experimental results [ROW 04, HIR 01, CRO 04, HEY 00], Rowland [ROW 05] was able to model the deformation of the free surface of a resist in the viscous regime during filling, identified as the single peak and dual peak filling modes (Figure 2.45). In the first mode, we notice that the filling of the mold cavity is essentially a vertical motion of the resin with a principal strain at the center of the cavity. For the second mode, there is flow both through the sidewalls of cavities but also in a plane parallel to the substrate, thus spreading the deformation of the free surface of the resin in the middle of the cavity. This behavior, also observed by Mendels [MEN 06], has been systematically studied in terms of the geometry of a mold and the initial thickness of a resist to flow with low Reynolds and capillary numbers, which are, respectively, very low (<<1, i.e. dominant viscosity) and high (>> 1, i.e. dominant viscous forces over forces related to surface tension).

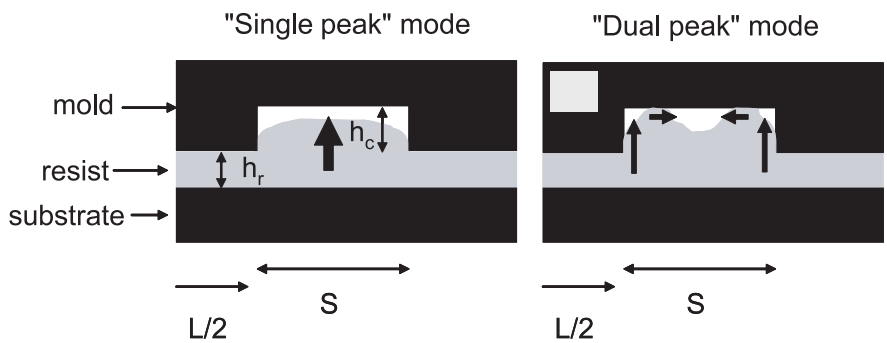

Figure 2.45. *Single and dual peak filling modes of a cavity by a resist*

Rowland [ROW 05] was able to show that the ratio of the cavity width and the initial thickness of resin $S/2h_i$ allowed the identification of the filling mode (Figure 2.45) in the cavity (predominantly horizontal or vertical resin flow). Furthermore, the relationship between the size of the printed pattern and thickness of resist available at any moment under this structure, *L/2hr*, identifies the nature of the flow, squeeze or shear flow, which impacts the filling time. Finally, the definition of a capillary number specific to NanoImprint ($Ca_{NIL} = \eta V_{NIL} / \sigma$, where V_{NIL} is the characteristic velocity, η the viscosity and σ the surface energy of the resist) can predict what major mechanism acts during filling (Table 2.3). V_{NIL} can be obtained, for example, by dividing the time needed to fill the cavity by its height h_c.

$S/2h_i$ < 0,5	whatever $L/2h_r$ value Forced flow		$t^a{}_{NIL} = \frac{12\eta h_c^2 L}{PS^2(L+S)}$	$Ca^a{}_{NIL} = \frac{PS^2(L+S)}{12\sigma h_c L}$
$S/2h_i$ > 0,5			$t^b{}_{NIL} \approx \left[3\times t^a{}_{NIL};\ 5\times t^a{}_{NIL}\right]$	$Ca^b{}_{NIL} \approx \left[\frac{Ca^a{}_{NIL}}{5};\frac{Ca^a{}_{NIL}}{3}\right]$
$S/2h_i$ > 1	$L/2h_r$ > 1	Squeeze flow	$t^c{}_{NIL} = \frac{\eta L^2}{8P}\times\frac{L+S}{L}\times\left(\frac{1}{h_r^2}-\frac{1}{h_i^2}\right)$	$Ca^c{}_{NIL} = \frac{8Ph_i^2h_r^2}{\sigma(h_i+h_r)L(L+S)}$
	$L/2h_r$ < 1	Shear flow	$t^d{}_{NIL} = \frac{12\eta}{P(S+L)}\times(h_i-h_r)$	$Ca^d{}_{NIL} = \frac{P(L+S)}{12\sigma}$

Table 2.3. *Characteristic filling time and capillary numbers associated as a function of mold geometries [ROW 05]*

Rowland's work allowed a detailed analysis of a cavity, or a few cavities, from the stamp/mold. However, NanoImprint mold modeling requires a multi-scale approach: across the entire mold in order to understand the pressure distribution, its deformations and its residual thickness distributions; at the patterns level, to accommodate the flow of displaced fluid; and, finally, at the relevant molecular scale for molecular interactions at the interface between the fluid and the mold. Each level of simulation involves the use of specific tools and concepts.

Mendels [MEN 06] proposed a multi-scale approach based on finite element modeling to determine the correct boundary conditions at the mold scale. Although significant efforts have been made to model at the molecular level, the choice to describe the system with a continuum approach is used to represent the flow in a volume adapted to the mold's geometry. To date, molecular modeling cannot easily achieve such modeling by standard means.

Initially, a finite element modeling of the fluid–structure interaction is performed on a single cavity. Subsequently, the mold is described as an assembly of elementary cells by exploiting the symmetries of the system and making sure of the connections of boundary conditions between each cell, namely: continuous force and displacement for the solid system and continuous velocity and pressure for the fluid parts. The calculations were compared with experimental results and the contribution of simulation has been highlighted (description of the resist edge, influence of structures' density) even for very simple geometries [SIR 06, SIR 07].

UV-NIL modeling requires new phenomena neglected in thermal NanoImprint to be taken into account. Printing a layer of resist with high viscosity (in the case of thermal printing) does not look as attractive and effective, at first glance, as the impression of a liquid with very low viscosity (the case of UV assisted printing) dispensed in drops and taking advantage of filling the micro- and nanocavities by capillary effects. Indeed, the printing time in the second case can be significantly reduced [COL 04]. Apart from modeling the flow of fluid between a mold and a substrate, UV-assisted NanoImprint coupled with a drop dispense unit raises new problems: what might be the impact of the number of drops and their respective volumes on the filling of the mold? The imprint being carried out at room pressure, what might be the impact of potential air bubbles trapped between the mold and the edge of the printed monomer [LIA 07b]? Can capillary effects fully compensate viscous dissipation?

In this case, the comprehension of the mechanisms governing the motion of a liquid (with a very low capillary number $\sim 10^{-3}$) through a rectangular nano-scale cavity is essential to predict its air-filling or air-trapping within the cavity (Figure 2.46). Bonnecaze's team [RED 05a, RED 05b, RED 06] proposed a 2D model of the

motion of such a fluid, considering the capillary but also the viscous flow and deformation of the mold in the lubrication regime.

The fluid–structure interaction manifests itself in the equations governing the evolution of the mold or substrate (then regarded as a thin plate) and height available for liquid flows between the mold and the substrate. Through an iterative approach and a coupled resolution of the two systems (fluid flow and deformation of the mold) until convergence of deformation fields and pressure, the dynamic filling (horizontal and vertical movement) of the mold has been simulated. It has been shown that in the absence of a force applied on the reverse of the mold, a capillary effect generates a force high enough to attract the mold and counterbalance viscous dissipation. In this case, the deformation of the mold is negligible. Of course, the application of a printing force reduces the imprint time but also results in an increased pressure within the fluid, causing significant distortions in the mold or the substrate [RED 06, VOI 07].

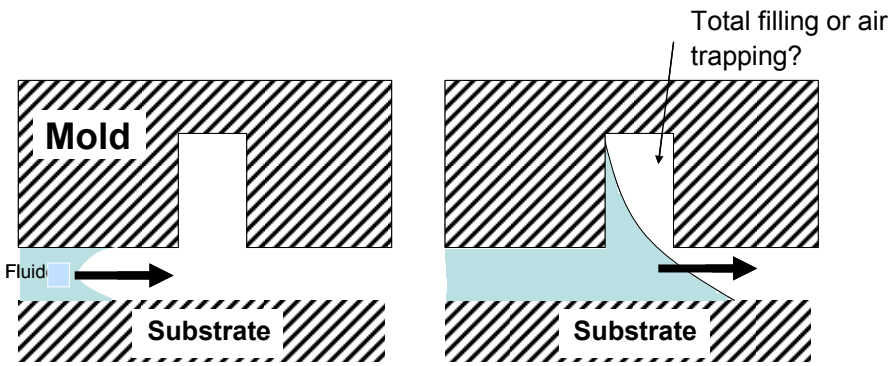

Figure 2.46. *Resist edge during a UV-NIL coupled with a drop dispense unit*

When the mold is pressed into the resist, it generates a flow of resist, resulting in a pressure gradient in the fluid (from the center toward the edges of the printed chip), as described in Figure 2.47. This pressure gradient in the resin puts pressure on the sidewalls in contact with the resin (mold and substrate), which then generate a deformation. In UV-assisted NanoImprint lithography, the mold is considered rigid and dimensionally stable compared to the silicon substrate, thus implying a deformation mainly of the substrate. This deformation is then translated by a non-uniform resin thickness in the chip after exposure and stripping. This pressure gradient is enhanced when the chip size increases and implies an increase in the distribution of the residual thickness (Figure 2.47).

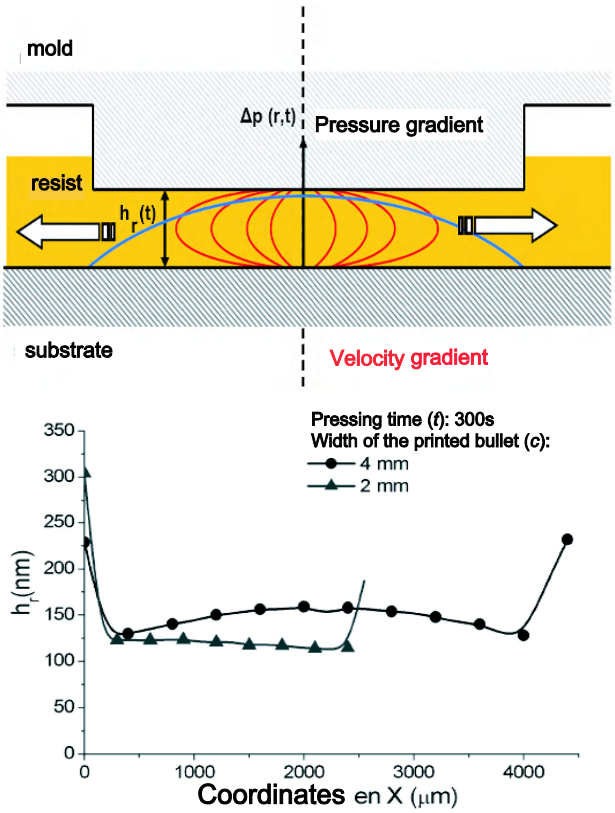

Figure 2.47. *Flow velocity and pressure gradients distribution within the resist during the imprint of a chip with no patterns (experimental measurements of h_r through two chips, of different areas, printed with a pressing time of 300 seconds; from [VOI 07]). The stamp used supported different die areas (from 2 × 2 mm to 4 × 4 mm stamp size) and a 145 nm depth. The pressure applied is 1 bar over 300 seconds in a 185 nm thick resist film of NILTM105*

Reddy [RED 06] has well demonstrated that the use of a large number of droplets in UV-assisted NanoImprint, allowed reducing the printing time. Indeed, the use of 50 drops is equivalent to applying a 50 N force (at the back of the 25 mm × 25 mm mold) when a single drop is used [RED 05a]. Although this research has shed light on the moving edge of fluid through a nanometer-sized cavity, and the impact on the number of drop on pressing time and capillary forces, the application of this approach to a group of patterns representative of a mold (different densities, sizes, orientations, etc.) is not yet possible.

2.8. Conclusion

Through the various aspects discussed in this chapter, NanoImprint really appears as a low-cost nano-lithography technique that achieves small structures over large areas. In less than a decade and with les financial investment than other solutions such as EUV lithography, immersion at 193 nm, or electronic multibeam, its incredible development suggests an increase of nanomanufacturing workshops. Indeed, it opens the doors to laboratories, R&D centers or small-scale businesses manufacturing technologies to structure matter at the nano-scale, to explore new properties and to develop new features.

However, as with most alternative technology solutions, transition from the research and development stage to the production process will require more time. Indeed, this evolution towards economic sectors will only happen if the gains in production costs are significantly reduced by the use of NanoImprint. These industries always seek to minimize the risk of introducing new technologies in developing solutions, even if sometimes it is very expensive to push the boundaries of processes and equipment already in place in an industrial environment. An incremental development will always be preferred to a big leap into the unknown.

The development of new objects, or the discovery of new properties of matter requiring a structure that cannot be achieved with current process technology could be a factor promoting the introduction of NanoImprint in an industrial context.

It took less than ten years for NanoImprint to evolve from a laboratory process to an R&D process in pre-industrial environments. Will it need another decade to reach the stage of a mass production process for nano-object fabrication?

2.9. Bibliography

[AHN 05] AHN S.W., LEE K.D., KIM J.S., KIM S.H., PARK J.D., LEE S.H., YOON P.W., "Fabrication of a 50 nm half-pitch wire grid polarizer using nanoimprint lithography", *Nanotechnology*, vol. 16, no. 9, p. 1874–1877, 2005.

[AHN 06] AHN S., CHA J., MYUNG H., KIM S.M., KANG S., "Continuous ultraviolet roll nanoimprinting process for replicating large-scale nano- and micropatterns", *Appl. Phys. Lett.*, 89, p. 213101, 2006.

[AHN 08] AHN S.H., GUO L.J., "High-speed roll-to-roll nanoimprint lithography on flexible plastic substrates", *Adv. Mater.*, 20, p. 2044–2049. 2008.

[AUS 04] AUSTIN M.D., GE H., WU W., LI M., YU Z., WASSERMAN D., LYON S.A., CHOU S.Y., "Fabrication of 5 nm linewidth and 14 nm pitch features by nanoimprint lithography", *Appl. Phys. Lett.*, 84, p. 5299, 2004.

[BEC 02] BECK M., GRACZYK M., MAXIMOV I., SARWE E. -L., LING T. G.I., KEIL M., MONTELIUS L., "Improving stamps for 10 nm level wafer scale nanoimprint lithography", *Microelectronic Engineering*, 61–62, p. 441, 2002.

[BEN 00] BENDER M., OTTO M., HADAM B., VRATZOV B., SPANGENBERG B., KURZ H., "Fabrication of nanostructures using a UV-based imprint technique", *Microelectron. Eng.*, 53, p. 233, 2000.

[BEN 02] BENDER M., OTTO M., HADAM B., SPANGENBERG B., KURZ H., "Multiple imprinting in UV-based nanoimprint lithography: related material issues", *Microelectronic Engineering*, 61–62, p. 407–413, 2002.

[BIG 46] BIGELOW W.C., PICKETT D.L., ZISMAN, W.A.J., "Oleophobic monolayers I. Films adsorbed from solution in non-polar liquids", *Colloid Sci.*, 1, p. 513, 1946.

[BIT 08] BITA I., YANG J.K.W., JUNG Y.S., ROSS C.A., THOMAS E.L., BERGGREN K.K., "Graphoepitaxy of self-assembled block copolymers on two-dimensional periodic patterned templates", *Science*, 321, p. 939, 2008.

[BOG 05] BOGDANSKI N., WISSEN M., ZIEGLER A., SCHEER H.C., "Temperature-reduced nanoimprint lithography for thin and uniform residual layers", *Microelectronic Engineering*, vol. 79, p. 598, 2005.

[BRZ 94] BRZOSKA J.B., AZOUZ I.B., RONDELEZ F., "Silanization of solid substrates: a step toward reproducibility", *Langmuir*, 10, p. 4367, 1994.

[BUN 00] BUNKER B.C., CARPICK R.W., ASSINK R.A., THOMAS M.L., HANKINS M.G., VOIGT J.A., SIPOLA D., DE BOER M.P., GULLEY G.L., "The Impact of Solution Agglomeration on the Deposition of Self-Assembled Monolayers", *Langmuir*, 16, p. 7742, 2000.

[CHA 06] CHAIX N, GOURGON C, LANDIS S, PERRET C, FINK M, REUTHER F, MECERREYES D, "Influence of the molecular weight and imprint conditions on the formation of capillary bridges in nanoimprint lithography", *Nanotechnology*, 17, no. 16, p. 4082, 2006.

[CHA 07] CHAIX N., GOURGON C., PERRET C., LANDIS S., LEVEDER T., "Nanoimprint lithography processes on 200 mm Si wafer for optical application: Residual thickness etching anisotropy", *J. Vac. Sci. Technol.*, B 25, p. 2346, 2007.

[CHE 05] CHEN L., DENG X., WANG, J., TAKAHASHI K., LIU F., "Defect control in nanoimprint lithography", *J. Vac. Sci. Technol.*, B 23 pp.2933, 2005.

[CHE 06] CHEN S.Z., LIU J.F., CHEN H.J.H., HUANG F.S., "Study of nanoimprint pattern transfer on hydrogen silsesquioxane", *J. Vac. Sci. Technol.*, B 24, p. 1934, 2006.

[CHE 02] CHENG X., HONG Y., KANICKI J., GUO L.J., "High-resolution organic polymer light-emitting pixels fabricated by imprinting technique", *J. Vac. Sci. Technol.*, B 20, p. 2877, 2002.

[CHO 95] CHOU S.Y., KRAUSS P.R., RENSTROM P.J.," Imprint of sub-25 nm vias and trenches in polymers", *Appl. Phys. Lett.*, 67, pp. 3114, 1995.

[CHO 97] CHOU S.Y., KRAUSS P.R., ZHANG W., GUO L., ZHUANG L., "Sub-10 nm imprint lithography and applications", *Journal of Vacuum Science & Technology*, B15 (6), p. 2897–2904, 1997.

[CHO 02] CHOU S.Y., KEIMEL C., GU J., "Ultrafast and direct imprint of nanostructures in silicon", *Nature*, 417, 835, 2002.

[COL 99] COLBURN M., JOHNSON S., DAMLE S., BAILEY T., CHOI B., WEDLAKE M., MICHAELSON T., SREENIVASAN S.V., EKERDT J., WILLSON C.G., "Step and flash imprint lithography: A new approach to high-resolution patterning", *Proc. SPIE*, 3676, p. 379, 1999.

[COL 04] COLBURN M., CHOI B.J., SREENIVASAN S.V., BONNECAZE R.T., WILLSON C.G., "Ramifications of lubrication theory on imprint lithography", *Microelectronic Engineering*, 75, p. 331, 2004.

[COL 05] COLBURN M., CHOI B.J., SREENIVASAN S.V., BONNECAZE R.T., "Ramifications of lubrication theory on imprint lithography", in C.G. WILLSON (ed.), *Microelectron. Eng.*, 75, p. 321, 2004.

[COU 98] COULOMBE S.A., MINHAS B.K., RAYMOND C.J., SOHAIL S., NAQVI H., MCNEIL J.R., "Scatterometry measurement of sub-0.1 µm linewidth gratings", *J. Vac. Sci. Technol.*, B 16, p. 80, 1998.

[CRO 04] CROSS G.L.W., O'CONNELL B.S., LANGFORD R.M., PETHICA J.B.,"The mechanics of nanoimprint forming", *Mater. Res. Soc. Symp. Proc.*, 841 R1.6, 2004.

[CRO 05] CROSS G.L.W., O'CONNELL B.S., PETHICA J.B., "Influence of elastic strains on the mask ratio in glassy polymer nanoimprint", *Appl. Phys. Lett.*, 86, p. 081902, 2005.

[DAR 03] DARQUE-CERETTI E., FELDER E., *Adhésion et adhérence*, CNRS, Paris, 2003.

[DEV 04] DEVAPRAKASAM D., SAMPATH S., BISWAS S.K., "Thermal stability of perfluoroalkyl silane self-assembled on a polycrystalline aluminum surface", *Langmuir*, 20, p. 1329, 2004.

[FOW 64] FOWKES F.M., *Ind. Eng. Chem.*, 56, p. 40, 1964.

[FUA 05] FUARD D., PERRET C., FARYS V., GOURGON C., SCHIAVONE P., "Measurement of residual thickness using scatterometry", *J. Vac. Sci. Technol.*, B 23(6), p. 3069, 2005.

[FUC 04] FUCHS A., VRATZOV B., WAHLBRINK T., GEORGIEV Y., KURZ H., "Interferometric *in situ* alignment for UV-based nanoimprint", *J. Vac. Sci. Technol.*, B 22(6), p. 3242, 2004.

[GAR 07] GARIDEL S., ZELSMANN M., VOISIN P., ROCHAT N., MICHALLON P., "Structure and stability characterization of anti-adhesion selfassembled monolayers formed by vapour deposition for NIL use", *Proc. SPIE*, 6517, p. 65172C, 2007.

[GEN 89] DE GENNES P-G., BROCHARD-WYART F., QUÉRÉ D., *Gouttes*, *bulles*, *perles et ondes*, Belin, Paris, 1989.

[GEN 04] DE GENNES P-G., BROCHARD-WYART F., QUÉRÉ D., *Gouttes*, *bulles*, *perles et ondes*, Collection Echelles, Belin, Paris, 2004.

[GIL 60] GILMAN J.J., "Direct measurements of the surface energies of crystals", *J. Appl. Phys.*, 31, p. 2208, 1960.

[GIL 64] GILLIS PP., GILMAN J.J., "Double-cantilever cleavage mode of crack propagation", *J. Appl. Phys.*, 35, p. 647, 1964.

[GOO 60] GOOD R.J., GIRIFALCO L.A., "A theory for estimation of surface and interfacial energies. III. Estimation of surface energies of solids from contact angle data", *J. Phys. Chem.*, 64, p. 561, 1960.

[GOU 02] GOURGON C., PERRET C., MICOUIN G., "Electron beam photoresists for nanoimprint lithography", *Microelectronic Engineering*, 61–62, p. 385, 2002.

[GOU 03] GOURGON C., PERRET C., MICOUIN G., LAZZARINO F., TORTAI J.H., JOUBERT O., GROLLIER J.P.E., "Influence of pattern density in nanoimprint lithography", *J. Vac. Sci. Technol.*, B 21, p. 98, 2003.

[GOU 04] GOURGON C., TORTAI J.H., LAZZARINO F., PERRET C., MICOUIN G., JOUBERT O., LANDIS S., "Influence of residual solvent in polymers patterned by nanoimprint lithography", *J. Vac. Sci. Technol.*, B 22, p. 602, 2004.

[GOU 05] GOURGON C., PERRET C., TALLAL J., LAZZARINO F., LANDIS S., JOUBERT O., PELZER R., "Uniformity on 8" silicon wafers printed by nanoimprint lithography", *J. Phys. D: Appl. Phys.*, 38, p. 70, 2005.

[GOU 07] GOURGON C., CHAIX N., SCHIFT H., TORMEN M., LANDIS S., SOTOMAYOR TORRES C.M., KRISTENSEN A., PEDERSEN R.H., CHRISTIANSEN M.B., FERNANDEZ-CUESTA I., MENDELS D., MONTELIUS L., HAATAINEN T., "Benchmarking of 50 nm features in thermal nanoimprint", *J. Vac. Sci. Technol.*, B 25, p. 2373, 2007.

[GUO 07] GUO L.J., "Nanoimprint lithography: methods and material requirements", *Advanced Materials*, vol. 19, p. 495, 2007.

[HAA 00] HAATAINEN T., AHOPELTO J., GRUETZNER G., FINCK M., PFEIFFER K., "Step and stamp imprint lithography using a commercial flip chip bonder", *Proc. SPIE*, 3997, p. 874, 2000.

[HAI 96] HAISMA J., VERHEIJEN M., VAN DER HUEVEL K., VAN DEN BERG J., "Mold-assisted nanolithography: A process for reliable pattern replication", *J. Vac. Sci. Technol.*, B 14(6), p. 4124, 1996.

[HEY 00] L.J. HEYDERMAN, H. SCHIFT, C. DAVID, J. GOBRECHT, T. SCHWEIZER, "Flow behaviour of thin polymer films used for hot embossing lithography", *Microelectronic Engineering*., 54, p. 229, 2000.

[HIR 01] HIRAI Y., FUJIWARA M., OKUNO T., TANAKA Y., ENDO M., IRIE S., NAKAGAWA K., SASAGO M., "Study of the resist deformation in nanoimprint lithography", *J. Vac. Sci. Technol.*, B 19, p. 2811, 2001.

[HIR 03] HIRAI Y., YOSHIDA S., TAKAGI N., "Defect analysis in thermal nanoimprint lithography, *J. Vac. Sci. Technol.*, B 21, p. 2765, 2003.

[HIR 04] HIRAI Y., KONISHI T., YOSHIKAWA T., YOSHIDA S., "Simulation and experimental study of polymer deformation in nanoimprint lithography", *J. Vac. Sci. Technol.*, B 22, p. 3288, 2004.

[HOC 07] HOCHENG H., HSU W.H., "Effect of back mold grooves on improving uniformity in nanoimprint lithography", *Jpn. J. Appl. Phys.*, 46, p. 6370, 2007.

[HOU 07a] HOULE F.A., GUYER E., MILLER D.C., DAUSKARDT R., "Adhesion between template materials and UV-cured nanoimprint resists", *J. Vac. Sci. Technol.*, B 25, p. 1179, 2007.

[HOU 07b] HOULE F.A., RETTNER C.T., MILLER D.C., SOORIYAKUMARAN R., "Antiadhesion considerations for UV nanoimprint lithography", *Appl. Phys. Lett.*, 90, p. 213103, 2007.

[ICH 03] ICHIKAWA M., TANAKA Y., SUGANUMA N., KOYAMA T., TANIGUCHI Y., "Low-threshold photopumped distributed feedback plastic laser made by replica molding", *Jpn. J. Appl. Phys.*, 42, p. 5590, 2003.

[INS] http://web5.silverplatter.com.

[ISI] http://apps.isiknowledge.com.

[ITR] International Technology Roadmap for Semiconductors (ITRS), http://www.itrs.net.

[JAC 01] JACOBS H.O., WHITESIDES G.M., "Submicrometer Patterning of Charge in Thin-Film Electrets", *Science*, 291, p. 1763, 2001.

[JAS 97] JASZEWSKI R.W., SCHIFT H., GRÖNING P., MARGARITONDO G., "Properties of thin anti-adhesive films used for the replication of microstructures in polymers", *Microelectron. Eng.*, 35, p. 381, 1997.

[JAS 99] JASZEWSKI R.W., SCHIFT H., SCHNYDER B., SCHNEUWLY A, GRÖNING P., "The deposition of anti-adhesive ultra-thin teflon-like films and their interaction with polymers during hot embossing", *Applied Surface Science*, 143, p. 301,1999.

[JUC 04] JUCIUS D., GRIGALIUNAS V., GUOBIENE A., "Rapid evaluation of imprint quality using optical scatterometry", *Microelectronic Engineering*, 71, p. 190, 2004.

[JUN 05] JUNG G.Y., LI Z., WU W., CHEN Y., OLYNICK D.L., WANG S.Y., TONG W.M., WILLIAMS R.S., "Vapor-phase self-assembled monolayer for improved mold release in nanoimprint lithography", *Langmuir*, 21, p. 1158, 2005.

[JUN 06] JUNG G.Y., JOHNSTON-HALPERIN E., WU W., YU Z., WANG S.Y., TONG W.M., LI Z., GREEN J.E., SHERIFF B.A., BOUKAI A., BUNIMOVICH Y., HEATH J.R., WILLIAMS R.S., "Circuit fabrication at 17 nm half-pitch by nanoimprint lithography", *Nanoletters*, vol. 6, no. 3, p. 351–354, 2006.

[KAN 74] KANNINEN M.F., "A dynamic analysis of unstable crack propagation and arrest in the DCB test specimen", *Int. J. Fract.*, 10, p. 415, 1974.

[KEI 05] KEIL M., BECK M., LING T. G.I., GRACZYK M., MONTELIUS L., HEIDARI B., "Development and characterization of silane antisticking layers on nickel-based stamps designed for nanoimprint lithography", *J. Vac. Sci. Technol.*, B 23, p. 575, 2005.

[KIE 31] KIESSIG H., *Ann. Phys.*, 10, p. 715, 1931.

[KIM 95] KIM E., XIA Y.N., WHITESIDES G.M., "Polymer microstructures formed by molding in capillaries", *Nature*, 376, p. 581, 1995.

[KIM 97] KIM E., XIA Y., ZHAO X.M., WHITESIDES G.M., "Solvent-assisted microcontact Molding: A convenient method for fabricating three-dimensional structures on surfaces of polymers", *Adv. Mater.* 9, p. 651, 1997.

[KIM 03] KIM Y.S., LEE H.H., "Selective dewetting for general purpose patterning", *Adv. Mater.* 15 no. 4, p. 332, 2003.

[KIM 05] KIM E.K., STEWART M.D., WU K., PALMIERI F.L., DICKEY M.D., EKERDT J.G., WILLSON C.G., "Vinyl ether formulations for step and flash imprint lithography", *J. Vac. Sci. Technol.*, B 23, p. 2967, 2005.

[KIM 07] KIM M.S., KIM J.S., CHO J.C., M. SHTEIN, GUO L.J., KIM J., "Flexible conjugated polymer photovoltaic cells with controlled heterojunctions fabricated using nanoimprint lithography", *Appl. Phys. Lett.*, 90, p. 123113, 2007.

[KUM 94] KUMAR A., BIEBUYCK H.A., WHITESIDES G.M., "Patterning self-assembled monolayers: applications in material science", *Langmuir*, 10, p. 1498, 1994.

[LAN 06a] LANDIS S., CHAIX N., GOURGON C., PERRET C., LEVEDER T., "Stamp design effect on 100 nm feature size for 8 inch NanoImprint lithography", *Nanotechnology*, 17, no. 10, p. 2701–2709, 2006.

[LAN 06b] LANDIS S., LEVEDER T., CHAIX N., PERRET C., GOURGON C., "Nano-imprint of sub-100-nm dots and complex shape features on 8-inch wafer: influence of layout design", *Proc. SPIE*, 6151, p. 61512L, 2006.

[LAN 07] LANDIS S., CHAIX N., HERMELIN D., LEVEDER T., GOURGON C., "Investigation of capillary bridges growth in NIL process", *Microelectronic Engineering*, vol. 84, nos. 5–8, p. 940, 2007.

[LAN 08] LANDIS S., CHAIX N., GOURGON C., LEVEDER T., "Quantitative characterizations of a nanopatterned bonded wafer: force determination for nanoimprint lithography stamp removal", *Nanotechnology*, 19, p. 125305, 2008.

[LAN 10] LANDIS S. (Ed.), *Lithography*, ISTE, London, John Wiley & Sons, New York, 2010.

[LAZ 04] LAZZARINO F., GOURGON C., PERRET C., SCHIAVONE P., "Mold deformation in nanoimprint lithography", *J. Vac. Sci. Technol.*, B 22, p. 3318, 2004.

[LEE 03] LEE J.N., PARK, C., WHITESIDES G.M., "Solvent compatibility of poly(dimethylsiloxane)-based microfluidic devices", *Anal. Chem.*, 75, p. 6544, 2003.

[LEE 05a] LEE H., JUNG G.Y., "Wafer to wafer nano-imprinting lithography with monomer based thermally curable resin", *Microelectronic Engineering*, vol. 77, p. 168, 2005.

[LEE 05b] LEE H.J., RO H.W., SOLES C.L., JONES R.L., LIN E.K., WU W.L., HINES D.R., "Effect of initial resist thickness on residual layer thickness of nanoimprinted structures", *J. Vac. Sci. Technol.*, B 23, p. 3023, 2005.

[LEE 05c] LEE H.J., SOLES C.L., RO H.W., JONES R.L., LIN E.K., WU W., HINES D.R., "Nanoimprint pattern transfer quality from specular x-ray reflectivity", *Applied Physics Letters*, 87 (26) p. 263111, 2005.

[LEE 08] LEE J., PARK S., CHOI K., KIM G., "Nano-scale patterning using the roll typed UV-nanoimprint lithography tool", *Microelectronic Engineering*, vol. 85, p. 861, 2008.

[LEV 44] LEVENBERG K., "A method for the solution of certain problems in least squares", *Quart. Appl. Math.*, 2, p. 164, 1944.

[LEV 06] LEVEDER T., LANDIS S., DAVOUST L., CHAIX N., "Impact of planarization sheet addition on full wafer printing uniformity", *MRS Fall Proceedings*, 0961-O02-06, 2006.

[LEV 07] LEVEDER T., LANDIS S., DAVOUST L., CHAIX N., "Flow property measurements for nanoimprint simulation", *Microelectronic Engineering*, vol. 84, p. 928, 2007.

[LI 03] LI M., TAN H., CHEN L., WANG J., CHOU S.Y., "Large area direct nanoimprinting of SiO_2–TiO_2 gel gratings for optical applications", *J. Vac. Sci. Technol.*, B 21, p. 660, 2003.

[LIA 07a] LIANG X.G., TAN H., FU Z., CHOU S.Y., "Air bubble formation and dissolution in dispensing nanoimprint lithography", *Nanotechnology*, 18, p. 025303, 2007.

[LIA 07b] LIAO W.C., HSU S. L.C., "A novel liquid thermal polymerization resist for nanoimprint lithography with low shrinkage and high flowability", *Nanotechnology*, 18, p. 065303, 2007.

[LIN 08] LIN M., HELLEBUSCH D., WU K., KIM E., LU K., TAO L., LIECHTI K., EKERDT J., HO P., HU W., WILLSON C., "Interfacial adhesion studies for step and flash imprint lithography", *Proc. of SPIE*, Vol. 6921, p. 69210E, 2008.

[MAM 92] MAMIN H.J., RUGAR D., "Thermomechanical writing with an atomic force microscope tip", *Appl. Phys. Lett.*, 61, p. 1003, 1992.

[MAR 63] MARQUARDT D., "An algorithm for least-squares estimation of nonlinear parameters", *SIAM J. Appl. Math.*, 11 pp.43, 1963.

[MAS 88] MASZARA W.P., GOETZ G., CAVIGLIA A., MACKITTERICK J.B., "Bonding of silicon wafers for silicon-on-insulato", *J. Appl. Phys.*, 64, p. 4943, 1988.

[MAU 00] MAUGIS D., *Contact*, *Adhesion and Rupture of Elastic Solids*, Springer Verlag, Berlin, 2000.

[MCM 08] MCMACKIN I., PEREZ J., SELINIDIS K., MALTABES J., RESNICK D., SREENIVASSAN S.V., "High resolution defect inspection of step and flash imprint lithography for 32 nm half-pitch patterning", *Proc. SPIE*, 6921, p. 69211L, 2008 .

[MEL 03] MELOSH N.A., BOUKAI A., DIANA F., GERARDOT B., BADOLATO A., PETROFF, P.M., HEATH J.R., "Ultrahigh-density nanowire lattices and circuits", *Science*, 300, p. 112, 2003.

[MEN 84] MENAWAT A., HENRY J., SIRIWARDANE R.J., "Silanation of silica surfaces. A new method of constructing pure or mixed monolayers", *J. Colloid Interface Sci.*, 101, p. 110, 1984.

[MEN 06] MENDELS D.A., "Multi-scale modelling of nano-imprint lithography", *Proc. of SPIE*, Vol. 6151, p. 615113, 2006.

[MER 07] MERINO S., SCHIFT H., RETOLAZA A., HAATAINEN T., "The use of automatic demolding in nanoimprint lithography processes", *Microelectronic Engineering*, vol. 84 nos. 5–8, p. 958, 2007.

[MER 08] MERINO S., RETOLAZA A., SCHIFT H., TRABADELO V., "Stamp deformation and its influence on residual layer homogeneity in thermal nanoimprint lithography", *Microelectronic Engineering*, vol. 85, p. 877, 2008.

[MIC] www.micropat.com

[MIC 01] MICHEL B., BERNARD A., BIETSCH A., DELAMARCHE E., GEISSLER M., JUNCKER D., KIND H., RENAULT J.P., ROTHUIZEN H., SCHMID H., SCHMIDT-WINKEL P., STUTZ R., WOLF H., "Printing meets lithography: Soft approaches to high-resolution patterning", *IBM J. Res. Dev.*, 45, p. 697, 2001.

[MIT 03] MIT TECHNOLOGY REVIEW, *10 Emerging Technologies That Will Change the World*, p. 33, 2003.

[MOH 06] MOHAMED K., ALKAISI M.M., SMAILL J., "Resist deformation at low temperature in nanoimprint lithography", *Curr. Appl. Phys.*, 6, p. 486, 2006.

[MUR 06] MURALI R., BROWN D.K., MARTIN K.P., MEINDL J.D., "Process optimization and proximity effect correction for gray scale e-beam lithography", *J. Vac. Sci. Technol.*, B 24, p. 2936, 2006.

[NIS 99] NISHINO T., MEGURO M., NAKAMAE K., MATSUSHITA M., UEDA Y., "The lowest surface free energy based on –CF3 alignement", *Langmuir*, 15, p. 4321, 1999.

[OSS 90] VAN OSS C.J., GIESE R. F. JR., GOOD R.J., "Reevaluation of the surface tension components and parameters of polyacetylene from contact angles of liquids", *Langmuir*, 6, p. 1711, 1990.

[OWE 78] OWENS N.F., RICHMOND P., GREGORY D., MINGINS J., CHAN D., "Contact angles of pure liquids and surfactants on low-energy surfaces", in J.F. PADDAY (ed.), *Wetting, spreading and adhesion*, Academic Press, London, p. 127, 1978.

[PAR 54] PARRATT L.G., "Surface studies of solids by total reflection of X-rays", *Phys. Rev.*, 95, p. 359, 1954.

[PAR 04] PARK S., SCHIFT H., PADESTE C., SCHNYDER B., KÖTZ R., GOBRECHT J., "Anti-adhesive layers on nickel stamps for nanoimprint lithography", *Microelectron. Eng.*, 73-74, p. 196, 2004.

[PAR 09] PARK S., SONG Z., BRUMFIELD L., "Demolding temperature in thermal nanoimprint lithography", *Applied Physics A: Materials Science & Processing*, 2009.

[PED 08] PEDERSEN R.H., HANSEN O., KRISTENSEN A., "A compact system for large-area thermal nanoimprint lithography using smart stamps", *J. Micromech. Microeng.*, 18, p. 055018, 2008.

[PEN 93] PENADO F.E., "A closed form solution for the energy release rate of the double cantilever beam specimen with an adhesive layer", *J. Compos. Mater.*, 27, p. 383, 1993.

[PER 98] PERUTZ S., WANG J., KRAMER E.J., OBER C.K., ELLIS K., "Synthesis and surface energy measurement of semi-fluorinated low-energy surfaces", *Macromolecules*, 31, p. 4272, 1998.

[PER 04] PERRET C., GOURGON C., LAZZARINO F., TALLAL J., LANDIS S., PELZER R, "Characterization of 8-in. wafers printed by nanoimprint lithography", *Microelectronic Engineering*, 73–74, p. 172, 2004.

[PER 07] PEROZ C., HEITZ C., BARTHEL E., SØNDERGÅRD E., GOLETTO V., "Glass nanostructures fabricated by soft thermal nanoimprint", *J. Vac. Sci. Technol.*, B 25, p. L27, 2007.

[PHA 10] http://odysseus.culture.gr/.

[REB 07] REBOUD V., KEHAGIAS N., STRICCOLI M., PLACIDO T., PANNIELLO A., CURRI M.L., ZELSMANN M., REUTHER F., GRUETZNER G., SOTOMAYOR TORRES C.M., "Photoluminescence enhancement in metallic nanocomposite printable polymer", *J. Vac. Sci. Technol.*, B 25, p. 2642, 2007.

[RED 05a] REDDY S., BONNECAZE R.T., "Simulation of fluid flow in the step and flash imprint lithography process", *Proceedings of SPIE*, vol. 5751, p. 200, 2005.

[RED 05b] REDDY S., BONNECAZE R.T., "The dynamics of low capillary interfaces moving through sharp features", *Physics of Fluids*, 17, p. 122104, 2005.

[RED 06] REDDY S., Fluid and Solid Mechanics in the Step and Flash Imprint Lithography Process, Dissertation, Degree of Doctorate of Philosophy, University of Texas, Austin, May 2006.

[ROO 01] ROOS N., LUXBACHER T., GLINSNER T., PFEIFFER K., SCHULZ H., SCHEER H.C., "Nanoimprint lithography with a commercial 4-in. bond system for hot embossing", *Proc. SPIE*, 4343, p. 427, 2001.

[ROW 04] ROWLAND H. D. and KING W. P., "Polymer deformation and filling modes during microembossing", *J. Micromech. Microeng.*, 14, p. 1625, 2004.

[ROW 05] ROWLAND H.D., SUN A.M., SCHUNK P.R., KING W.P., "Impact of polymer film thickness and cavity size on polymer flow during embossing: toward process design rules for nanoimprint lithography", *J. Micromech. Microeng.*, 15, p. 2414, 2005.

[RUI 08] RUIZ R., KANG, H., DETCHEVERRY F.A., DOBISZ E., KERCHER D.S., ALBRECHT T.R., DE PABLO J.J., NEALEY P.F., "Density multiplication and improved lithography by directed block copolymer assembly", *Science*, 321, p. 936, 2008.

[STU 02] STUDER V., PÉPIN A., CHEN Y., *Appl. Phys. Lett.*, 80, 3614, 2002.

[SCH 01a] SCHEER H.C., SCHULZ H., "A contribution to the flow behaviour of thin polymer films during hot embossing lithography", *Microelectronic Engineering*, vol. 56, no. 3–4, p. 311–332, 2001.

[SCH 01b] SCHIFT H., HEYDERMAN L.J., AUF DER MAUR M., GOBRECHT J., "Pattern formation in hot embossing of thin polymer films", *Nanotechnology*, 12, no. 2, p. 173–177, 2001.

[SCH 03] SCHIFT H. , HEYDERMAN L., "Nanorheology – squeezed flow in hot embossing of thin films", in C. SOTOMAYOR TORRES (ed.), *Alternative Lithography – Unleashing the Potential of*, *Nanotechnology*, Nanostructure Science and Technology, p. 46–76, Kluwer Academic-Plenum Publishers, Dordrecht–New York, 2003.

[SCH 05a] SCHIFT H., SAXER S., PARK S., PADESTE C., PIELES U., GOBRECHT J., "Controlled coevaporation of silanes for nanoimprint stamps", *Nanotechnology*, 16, p. 171, 2005.

[SCH 00] SCHMID H, MICHEL B., "Siloxane polymers for high-resolution, high accuracy soft lithography", *Macromolecules*, 33, p. 3042, 2000.

[SCH 07] SCHMID G.M., THOMPSON E., STACEY N., RESNICK D.J., OLYNICK D.L., ANDERSON E.H., Toward 22 nm for unit process development using step and flash imprint lithography, *Proc. SPIE*, 6517, p. 651717, 2007.

[SCH 05b] SCHULZ H., WISSEN M., BOGDANSKI N., SCHEER H.C., MATTES K., FRIEDRICH C., "Choice of the molecular weight of an imprint polymer for hot embossing lithography", *Microelectronic Engineering*, Volumes 78–79, p. 625, 2005.

[SCHU 06] SCHULZ H., WISSEN M., BOGDANSKI N., SCHEER H.C., MATTES K., FRIEDRICH C., "Impact of molecular weight of polymers and shear rate effects for nanoimprint lithography", *Microelectronic Engineering*, vol. 83, p. 259, 2006.

[SCI] http://scitation.aip.org.

[SEG 08] SEGALMAN R.A., "Directing self-assembly toward perfection", *Science*, 321, p. 919, 2008.

[SHA 60] SHAFRIN E.G., ZISMAN W.A., "Constitutive relation in the wetting of low energy surfaces and the theory of the retraction method of preparing monolayers", *J. Phys. Chem.*, 64, p. 519, 1960.

[SIL 91] SILBERZAN P., LEGER L., AUSSERRE D., BENATTAR J.J., "Silanation of silica surfaces. A new method of constructing pure or mixed monolayers", *Langmuir*, 7, p. 1647, 1991.

[SIR 06] SIROTKIN V., SVINTSOV A., ZAITSEV S., SCHIFT H., "Viscous flow simulation in nanoimprint using coarse-grain method", *Microelectronic Engineering*, 83, p. 880–883, 2006.

[SIR 07] SIROTKIN V., SVINTSOV A., SCHIFT H., ZAITSEV S., "Coarse-grain method for modeling of stamp and substrate deformation in nanoimprint", *Microelectronic Engineering*, 84, p. 868, 2007.

[SIR 09] SIROTKIN V., SVINTSOV A., ZAITSEV S., "Optimization of droplets for UV-NIL using coarse-grain simulation of resist flow", *Proc. SPIE*, 7271, p. 72712I, 2009.

[SON 05] SONKUSALE S., AMSINCK C.J., NACKASHI D.P., DI SPIGNA N.H., BARLAGE D., JOHNSON M., FRANZON P.D., "Fabrication of wafer-scale, aligned Sub-25 nm nanowires and templates using Planar Edge Defined Alternate Layer (PEDAL) Process", *Physica E. Low Dimensional Systems and Nanostructures*, 28, p. 107–114, 2005.

[SUH 01] SUH K.Y., KIM Y.S., LEE H.H., "Capillary Force Lithography", *Adv. Mater.*, vol. 13, no. 18, p. 1386, 2001.

[TAN 98] TAN H., GILBERTSON A., CHOU S.Y., "Roller nanoimprint lithography", *J. Vac. Sci. Technol.*, B 16, p. 3926, 1998.

[TRA 08] TRABADELO V., SCHIFT H., MERINO S., BELLINI S., GOBRECHT J., "Measurement of demolding forces in full wafer thermal nanoimprint", *Microelectronic Engineering*, 85, p. 907, 2008.

[TOR 07] TORMEN M., CARPENTIERO A. FERRARI E., COJOC D., DI-FABRIZIO E., "Novel fabrication method for three-dimensional nanostructuring: an application to micro-optics", *Nanotechnology*, 18, p. 385301, 2007.

[VAL 05] VALLIN O., JONSSON K., LINDBERG U., "Adhesion quantification methods for wafer bonding", *Mat. Sci. Eng.*, R 50, p. 109, 2005.

[VOI 07] VOSIN P., Lithographie de nouvelle génération par nano-impression assistée par UV: étude et développement de matériaux et procédés pour l'application microélectronique, University thesis, Joseph Fourrier Grenoble I, 2007.

[WAN 99] WANG J., SCHABLITSKY S., YU Z., WU W., CHOU S.Y., "Fabrication of a new broadband waveguide polarizer with a double-layer 190 nm period metal-gratings using nanoimprint lithography", *J. Vac. Sci. Technol.*, B 17, p. 2957, 1999.

[WIE 99] WIEGEL D., KAUFMANN J., ARNOLD K., "Polar interactions of chondroitinsulfate: Surface free energy and molecular dynamics simulations", *Colloids and Surfaces*, *B: Biointerfaces*, 13, p. 143, 1999.

[WU 82] WU S. (Ed.), *Polymer Interface and Adhesion*, Marcel Dekker, New York, 1982.

[WU 98] WU W., CUI B., SUN X.Y., ZHANG W., ZHUANG L., KONG L., CHOU S.Y., "Large area high density quantized magnetic disks fabricated using nanoimprint lithography", *J. Vac. Sci. Technol.*, B 16, p. 3825, 1998.

[WU 07] WU K., WANG X., KIM E.K., WILLSON C.G., EKERDT J.G., "Experimental and Theoretical Investigation on Surfactant Segregation in Imprint Lithography", *Langmuir*, 23, p. 1166, 2007.

[XIA 98A] XIA Y., WHITESIDES G.M., "Soft Lithography", *Angew. Chem.*, 37, p. 550, 1998.

[XIA 98B] XIA Y., WHITESIDES G.M., "Unconventional Methods for Fabricating and Patterning Nanostructures", *Annu. Rev. Mater. Sci.*, 28, p. 153, 1998.

[XIA 06] XIA Q., YU Z., GAO H., CHOU S.Y., "In situ real time monitoring of nanosecond imprint process", *Appl. Phys. Lett.*, 89, p. 073107, 2006.

[YU 04] YU Z., GAO H., CHOU S.Y., "In situ real time process characterization in nanoimprint lithography using time-resolved diffractive scatterometry", *Appl. Phys. Lett.*, 85, p. 4166, 2004.

Chapter 3

Lithography Techniques Using Scanning Probe Microscopy

3.1. Introduction

About 20 years ago, a new category within the field of nano-lithography techniques was created by the introduction of local-probe microscopes [SAL 99, WIE 94], which take advantage of the local interaction that exist between a probe and the surface to be patterned. There is a whole family of such microscopes, the best known being scanning tunneling microscopes (STMs) [BIN 82], and atomic force microscopes (AFMs) [BIN 86] (Figure 3.1). Their fame is such that they are sometimes considered to be the workhorses of nanotechnology. We are going to show in this chapter that these microscopes, thanks to their ultimate resolution, can be viewed as the "end of the roadmap" of top-down techniques for nano-lithography. Indeed, their resolution makes it possible to not only resolve but also to provide precise imaging of the elementary constituents of matter (atoms, molecules), and they were soon recognized as valuable tools for patterning with atomic resolution.

Since their advent in the late 80s, their importance has grown rapidly, notably when used in combination with complementary techniques involving bottom-up approaches, such as self-assembly, guided growth, chemical reactions etc. They are at the crossroads of the two "top-down" and "bottom-up" approaches and are also compatible with a great number of analytical tools (optical, electrochemical etc.). Scanning probe techniques are therefore bound to play a central role in the nanofabrication evolution of the next decades.

Chapter written by Vincent BOUCHIAT.

3.2. Presentation of local-probe microscopes

Although each tool differs according to the detail of its mechanism, local probe microscopes all share the same principle: a local probe (referred to, for the rest of this chapter, as a "tip") is brought close to a sample, down to a nanometric distance from the surface, and the local physical properties (electrical, optical, mechanical, etc.) that result from the tip–sample interaction are measured in real-time. This measurement of this "near-field" interaction makes it possible to control the position of the tip in relation to the surface and to record information about its local properties (topography, conductance, chemical composition, etc.); see Figure 3.1.

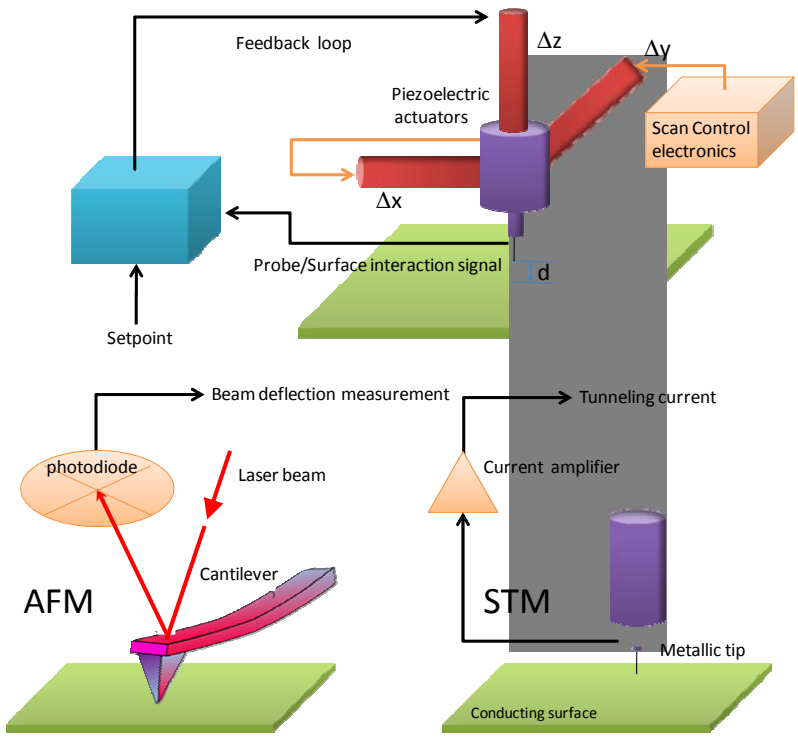

Figure 3.1. *General principle of operation of local-probe microscopes: the position of the tip is controlled in three directions by means of piezoelectric tubes. The continuous measurement of the probe/sample interaction signal allows the real-time control of the vertical position d of the probe while scanning in the X and Y directions The topographic image results from the recording of Z(X, Y). Bottom, left: AFM microscopy principle: the interaction signal is the deflection of a laser beam focused on a cantilever on which a tip is attached. Bottom, right: STM microscopy principal, the interaction signal is the measurement of the tunnel current between the tip and the surface of the conducting surface*

The relative position of the tip with respect to the surface is controlled by applying high voltages on piezoelectric ceramics (so-called 'scanners') that can move in three directions thanks to the application of an electronic voltage at their end. In this way, they ensure the accuracy of the distances Δx, Δy and Δz to better than one angström, meaning that they have the ability to resolve the inter-atomic distances when placed in a suitable environment (an ultra high vacuum).

In the case of atomic force microscopy (AFM), the interaction potential between the atoms of the end of the tip and those at the sample surface generates a local force which is either attractive or repulsive, the intensity of which varies greatly according to the tip/sample distance d. This force is measured thanks to the deflection of a laser beam focused on the reverse side of a mechanical cantilever on which the tip is attached. In the case of scanning tunneling microscopy (STM), the electronic current, resulting from electrons tunneling between the metallic tip and the surface, is amplified and then measured. The regulation of this current allows the electronic density to be recorded and imaged while the tip scans the surface.

In the case of Near-field Scanning Optical microscopes (NSOMs) [HEI 94], the evanescent electromagnetic wave generated at the tip–sample gap is collected at a distance shorter than the wavelength by means of an adapted optical system (fiber, etc.). To summarize, local-probe microscopes achieve the imaging of a surface by measuring a physical quantity in a non-propagative regime (hence the name "near-field" interaction). Depending on which microscope is used, this can be a tunnel effect current, an attractive or repulsive force, or an evanescent electromagnetic wave.

3.3. General principles of local-probe lithography techniques

The principles of scanning probe lithography techniques [AMP 05] are based on a simple idea: since these microscopes make it possible to achieve an image of the surface at the nanometric or even at the atomic scale, why not use them to modify a surface at the same scale?

The local interaction between the tip and the surface can indeed be used to modify a surface in a permanent way, according to a predefined lithographic pattern. The first applications [ALB 89, EIG 90] of these simple principles were demonstrated a few years after the invention of these microscopes. In the case of scanning tunneling microscopes, because the substrate needs to be conducting, the manipulation is most often achieved by changing the electrical conditions under which the tip is operated (the voltage pulse applied on the tip, modification of the regulation set point, etc.).

It is important to realize that scanning probe microscopes only provide surface imaging and cannot "see" below the surface. The absence of "lenses" (i.e. focusing elements) makes the tip–surface interaction diverge rapidly with depth. Consequently, they are not well adapted for in-depth structuring of a volume. The lithographic processes developed from these microscopes must take into account this issue. The structures readily produced after lithography will not have an aspect ratio (defined as the ratio of height/width of a pattern) above unity and only shallow nanostructuring can be envisioned. However, as seen in the following sections, specific physico-chemical methods can be used to "amplify" an ultra-thin lithographic pattern and allow that pattern to be transferred to the underlying layer without a significant increase of line width.

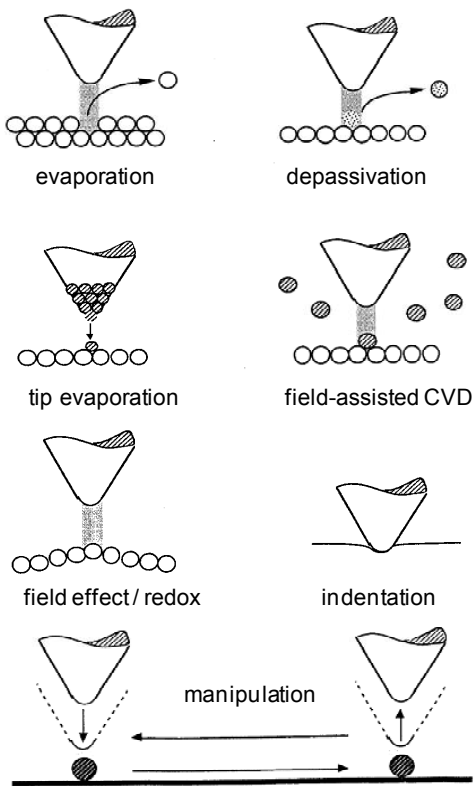

Figure 3.2. *Schematics of the different types of surface modification induced by local-probe microscope tips. Examples of the physical principles involved are described in the following sections of this chapter*

3.4. Classification of surface structuring techniques using local-probe microscopes

A peculiarity of scanning probe microscopes is that their resolution is of the same order of magnitude as that of matter's elementary constituents (atoms, molecules, etc.). Consequently, patterning can take into account its discontinuous and discrete nature and enable manipulation of the nano-objects one by one, leading to the direct fabrication of devices exhibiting features that provide direct evidence of quantum mechanical effects (Figure 3.3).

The ultimate challenge of the fabrication of a structure controlled atom by atom was taken up as early as 1990 by pioneering teams [ALB 89, EIG 90] specializing in scanning tunneling microscopy under ultra high vacuums. Their work culminated, in 1993, with the demonstration of artificially made structures such as "quantum corrals" [CRO 93] that show the confinement of electron waves (see Figure 3.3). Subsequently, a large number of different techniques have been suggested to nanometrically modify a surface (atom or molecule manipulation, controlled evaporation of atoms [LEB 97], indentation, resist insulation, local oxidation, etc.).

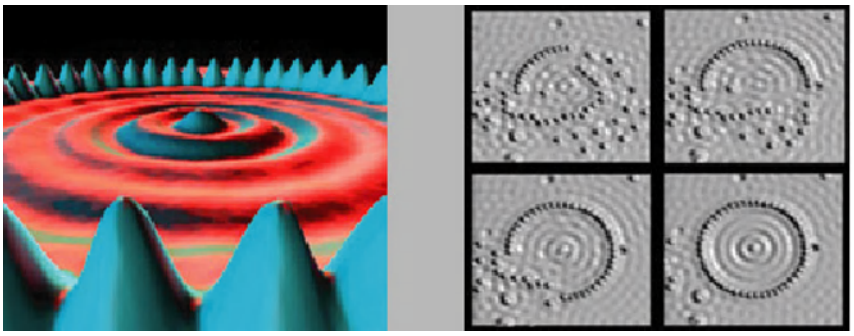

Figure 3.3. *Manipulation of adsorbed xenon atoms on a copper surface using a scanning tunneling microscope under high vacuum and at low temperature. The artificial structure is a 7nm wide Xenon ring created by atom-per-atom manipulation using the tip of the microscope as a grabbing tool. The standing waves within the ring correspond to electronic standing waves induced on the copper metallic surface by scattering of the Xenon atoms. The artificially produced ring, which has been called quantum corral, confines the electron wave. The resonance of the electronic waves imposed by the conditions at the limits is more significant at the center of the ring when it is closed. Adapted from [CRO 93]; Figure © IBM*

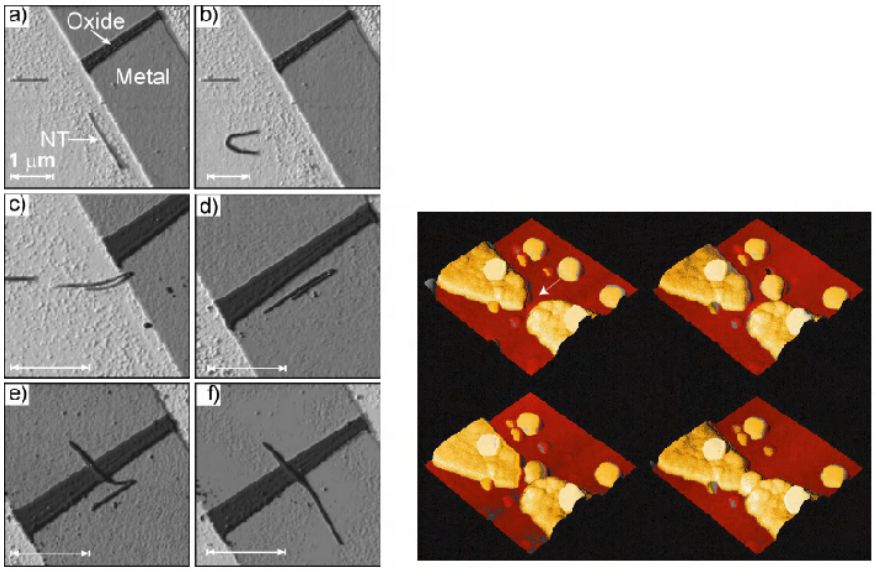

Figure 3.4. *Series of atomic force micrographs showing manipulation of carbon nanotubes (left, taken from [AVO 99]) and a gold particle (right, taken from [JUN 98]). In both cases, the nano-object (carbon nanotube left, gold nanoparticle right) is manipulated using an AFM tip. The nano-object eventually bridges the two electrodes, creating an active device which exhibits quantum properties*

3.4.1. *Classification according to the physical nature of the interaction*

Except for the two cases described in section 3.7 below, for which the tip plays a passive role in positioning, all the lithographies are based on the energetic interactions between the tip and the modified surface. The microscope's tip thus acts as a local energy source which can have having different physical actions: electrical, mechanical, optical or thermal.

It is then possible to classify most of the lithography techniques with respect to the physical origin of the interaction responsible for the surface modification (see Figure 3.5). Each type of interaction has led to several lithography techniques depending on the materials involved, thus creating a classification tree. Some of the applications have remained at the prototype stage, whereas others have reached an advanced pre-industrial state. One of the latter, for example, involves the high-speed thermo-mechanical indentation of resists [VET 00]. This technique, developed by IBM is a promising technique for information storage.

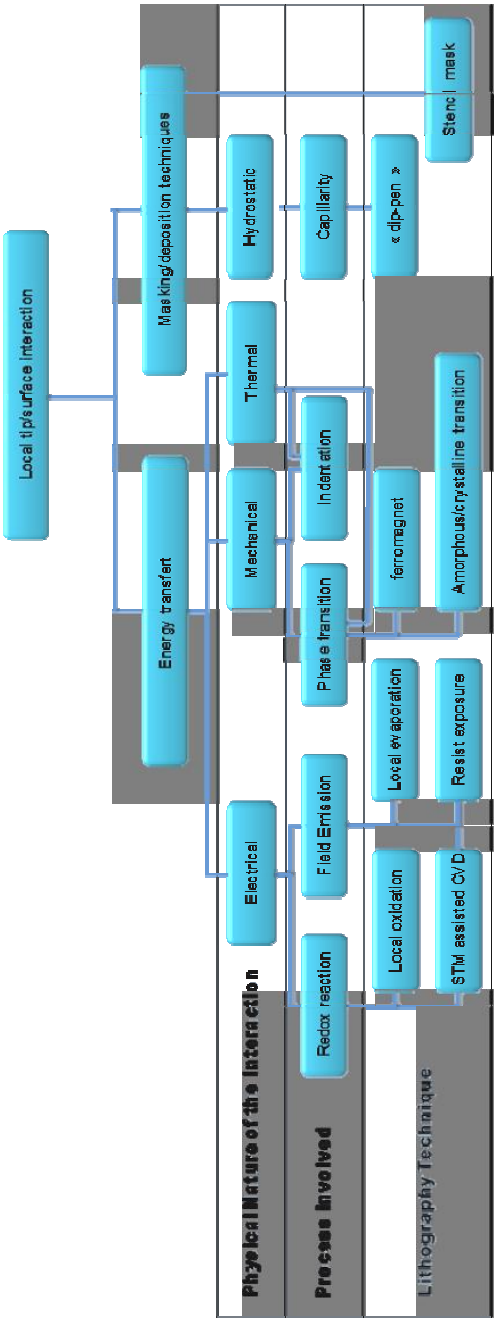

Figure 3.5. *Classification tree of scanning probe lithography techniques, classified according to the nature of the probe to surface interaction*

3.4.2. *Comparison with competing advanced lithography techniques*

Because of their originality, these techniques exhibit features that significantly differ from competing lithographies. Indeed, except in the case of nano-imprint [CHO 95, CHO 98] (described in Chapter 2) and the techniques based on local probes presented in this chapter, it can be seen (Figure 3.5) that the entire group of lithographies (including all those already at an industrial stage) operate at far-field, meaning that the distance between the patterning source and the patterned object is great compared to the size of the patterns obtained.

A "far-field" emission requires focalizing optical elements combined with high energy radiations (UV photons, X-rays, ions, electrons) [TOR 03]. Optical lithographies (see Chapter 1) and electron beam lithography (Chapter 2) must face diffusion limits and diffractions inherent to this far-field radiation. Their optimization imposes significant technical efforts in order to improve beam emission quality (electron gun, extreme UV sources, etc.) as well as to optimize the beam pathways (such as photonic or electronic lenses and phase shift engineering tools). These efforts have also led to extremely expensive tools.

By contrast, all local-probe microscopes operate only in near field and are not limited by difficulties of this kind. The absence of beam optics provides them with a high potential for reaching ultimate resolutions as well as limiting their integration costs.

Furthermore, the resolution limits are those imposed by technology and not by physics (such as diffraction or diffusion effects). In addition, the possible miniaturization of the writing devices make the tool much more affordable compared to the other techniques. It also has many interesting marketing prospects on a large scale, notably due to a good potential for upscaling and parallelization (for an application example involving information storage, see Figure 3.8 below).

The antagonism which exists between "near-field" techniques (which involve local interaction) and far-field techniques (which involve the focusing of a beam) makes possible a new classification of lithography (see Figure 3.6). This new classification differs significantly from the usual classification (partly shown in Figure 3.5) which only considers the nature of the emitted radiation.

It is also important to notice that the near-field lithographies (Figure 3.6, right) imply a comparatively smaller energy per pixel. By being "softer", their resolution is less prone to "proximity effects" [CHA 75]. This effect, associated with most far field techniques, is linked to the diffusion of incident radiation in the lithographic resist (see the description of basic lithography technologies in Chapter 6). This is an important factor limiting the resolution of far-field lithographies. However, the

apparent superiority of the scanning probe techniques does not come without a price to be paid, mainly in terms of throughput.

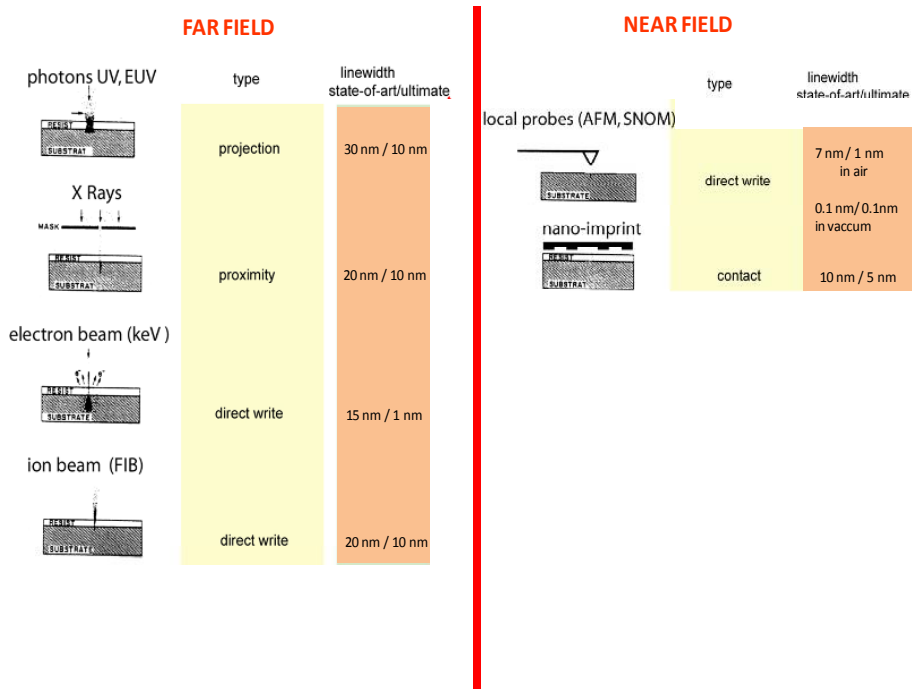

Figure 3.6. *Comparison of different techniques used to nanostructure surfaces with their associated resolutions. The dichotomy between far-field (left column) and near-field techniques (right column) can be observed*

3.4.3. *Industrial development perspectives*

A number of major disadvantages limit the application of local-probe lithography techniques on an industrial scale. On one hand, sequential techniques require a line to line surface scanning "in series" (in a different way to photolithography or nano-imprint which structure matter in a parallel way). On the other hand, the inertia of the piezoelectric scanning heads considerably limits the moving speed of the tip to a few microns per second, which ranks them as the slowest of the lithography techniques (Figure 3.7).

Many recent studies [PIC 07] based on the miniaturization of the piezoelectric heads tend to show that effective scanning speeds are expected to improve greatly in the near future. This will allow imaging (and lithography) using scanning probes to

be achieved at a rate higher than that of video images (25 images per second). Additionally, the technological pressure coming from disciplines related to nano-lithography, such as information storage [MAM 95], is an important motivation to improve microscope technology, mainly by placing the lithography tips in parallel [MIN 98].

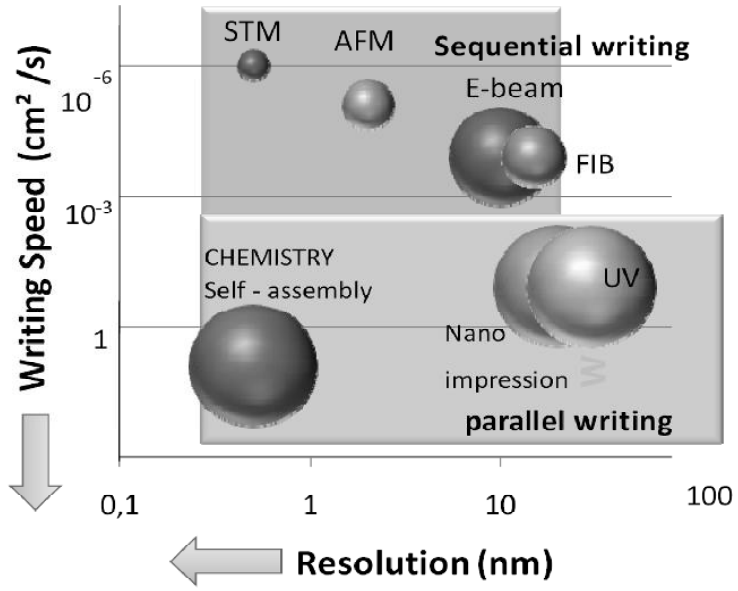

Figure 3.7. *Graph summarizing all the fabrication techniques including those methods said to be top-down or bottom-up. Methods are classified according to their resolution (X-axis), their writing speed (Y-axis) and their sequential or parallel assembling principle. The near-field techniques appear to be the most precise ones but also the slowest. The parallelization of AFM techniques (represented by a descendant arrow) compensates for their lack of speed*

The development of tip rows at Stanford University in 1997, and then of tip arrays at IBM-Zürich (Figure 3.8, left), are improvements that add up to compensate for the lack of speed by means of parallelization. Each tip scans a specific sector. Sophisticated electronic multiplexing allows each tip to be to independently addressed and an independent pattern to be created (Figure 3.8, right). It is then possible to reach cumulative scanning speeds in the cm^2/s range. This could therefore turn them into competing techniques compared to electron-beam lithography.

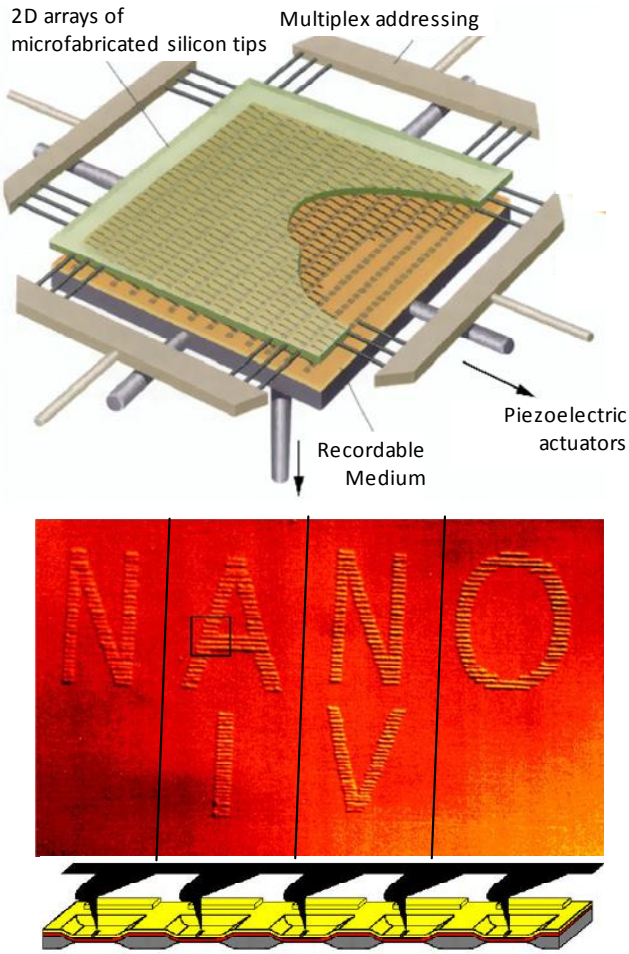

Figure 3.8. *Top:Fabrication principle of memory of very high density, using a 2D array of tips, each of them scanning a given sector. Writing is achieved using thermo-mechanical indentation on a polymer resist layer, while reading is done by thermoelectric measurements; storage density has been shown to exceed 100Gbit/in² (IBM). Bottom: lithography technique principle using bars of AFM tips. Each tip is addressed by an independent voltage and achieves patterns by scanning a given sector (Quate group, Stanford University)*

3.5. Lithographic techniques with polymer resist mask

Further than just demonstrating a controlled way of writing at the nanometric scale, a lithography technique must be introduced into the complete fabrication

process, that is to say, it needs to achieve its integration in relation with connectivity and lead to a functional electric prototype. One method to reassure oneself about a technique's compatibility with standard processes of microelectronics is to adapt some process steps (usually the writing step of a mask) while keeping the other steps unchanged (resist deposition, development, mask deposition). One example of this adaptability is the achievement of patterns using electron deposition in a polymer resist. This technique, described in the following section, is usually confined to lithography using scanning electron microscopy.

3.5.1. *Electron beam exposure of resists by scanning probe microscopes*

Electronic field emission occurs at much lower voltage for a sharp tip than that required for a planar electrode (typically a few tens of volts instead of kilovolts). It is easy to use an atomic force microscope's tip as a low energy electron source. The Calvin Quate group at Stanford University (USA) has conceived a hybrid AFM/STM microscope (see Figure 3.9) including two feedback control loops that allow an independent control of the interaction force and of the electron emission current due to the field-effect.

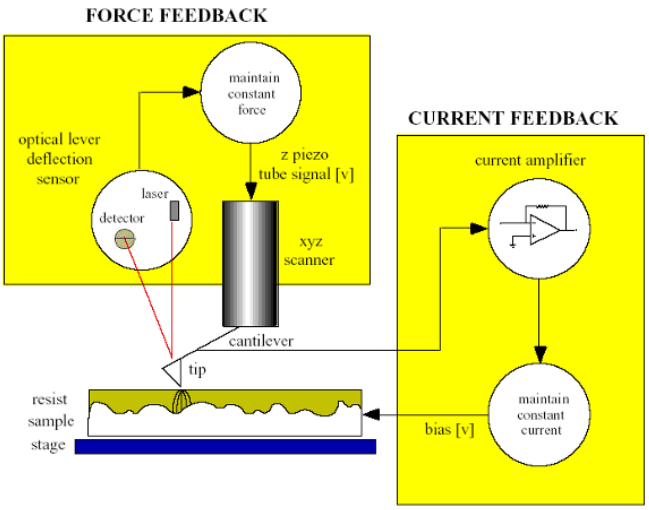

Figure 3.9. *A local-probe "Hybrid AFM/STM" microscope modified to allow near-field insulation of an electron-sensitive resist. The system includes two independently controlled regulation loops. The force regulation makes it possible to monitor the surface in the same way as for a standard AFM microscope, whereas the regulation of the emission current of the tip allows a given electron quantity per surface unit to be deposited. The emission current of the tip can be controlled in the range (1 pA – 1 nA) which corresponds to tip tensions around 40-60 V. (Figure inspired by [WIL 97])*

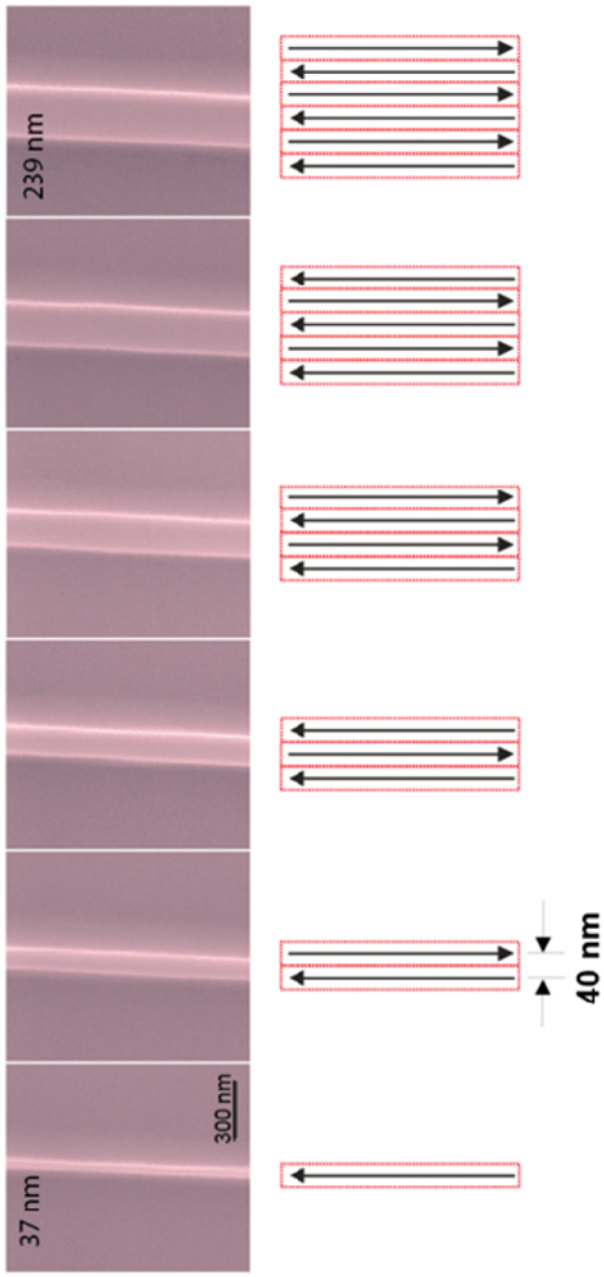

Figure 3.10. *Micrographies showing lithographed lines after resist development obtained by electronic insulation with an atomic force microscope with its current-polarized tip. The linear dose is 20 nC/cm. The electron energy is 20 eV. The resist profiles of the lithography pattern (obtained by tip scans with 40 nm line shifts) show the perfect linearity of the profile obtained thanks to the number of crossovers and consequently the total absence of proximity effect. © Quate Group, published in [WIL 98]*

When a tension is applied to a tip coated with a thin metallic layer making it completely conducting, an electron can be emitted towards the substrate by field emission. The resist layer on the substrate is exposed by the emission current and becomes locally soluble in a developer in a similar way as is done for electron beam lithography (EBL). It is important to notice that the energy of the electrons emitted by the tip (a few tens of electron volts) is much lower than that used in standard e-beam lithography techniques (from 30 to more than 100 kV).

Nonetheless, it is necessary to deposit a much greater quantity of electrons per surface unit. In order to obtain the same resist development, this amount can usually be 30 times higher. This looks like an inconvenience because it imposes a physical limit to the scanning speed. However, as already noted, the low electron energy limits their diffusion in the resist and cancels the proximity effect, thus ensuring a perfect linearity of the size and geometry of the lithographed patterns (see Figure 3.10).

3.5.2. *Development of a resist dedicated to AFM nano-lithography*

Recent researches have shown that one of the ways to take advantage of local-probe techniques is to develop lithographic resists dedicated to this method instead of using the resists developed for far-field lithography. During the writing process assisted by an electric field, a tension of a few volts between the tip and the surface induces an electric field that can exceed 10^9 V/m. Such an intense field decomposes the organic molecules into very reactive fragments which, in addition, induce reactions with the surrounding molecules in a way similar to chemically amplified resists.

For several years now, Jean Fréchet's group at Berkeley University has been developing new lithographic processes based on resists adapted to the specificities of local-probe lithography. Among the significant results, one can note the achievement of a fluorocarbon-based resist with which it is possible to form lithographic patterns 25 nm wide, traced with rates up to 1 cm/s [ROL 07]. Other resists, based on dendrimer compounds have also been developed [ROL 04]. Additional resists containing precursors enabling directed assembly of nano-objects for a nano-structure (for example, lines on which gold nanocrystals will be assembled [GER 08], Figure 3.11) have also been developed.

Another strategy consists of preparing molecules with a chemical bond more sensitive to the electric field, meaning a weak link. Under exposure from the AFM tip, the molecule will always break at this bond [SUE 03].

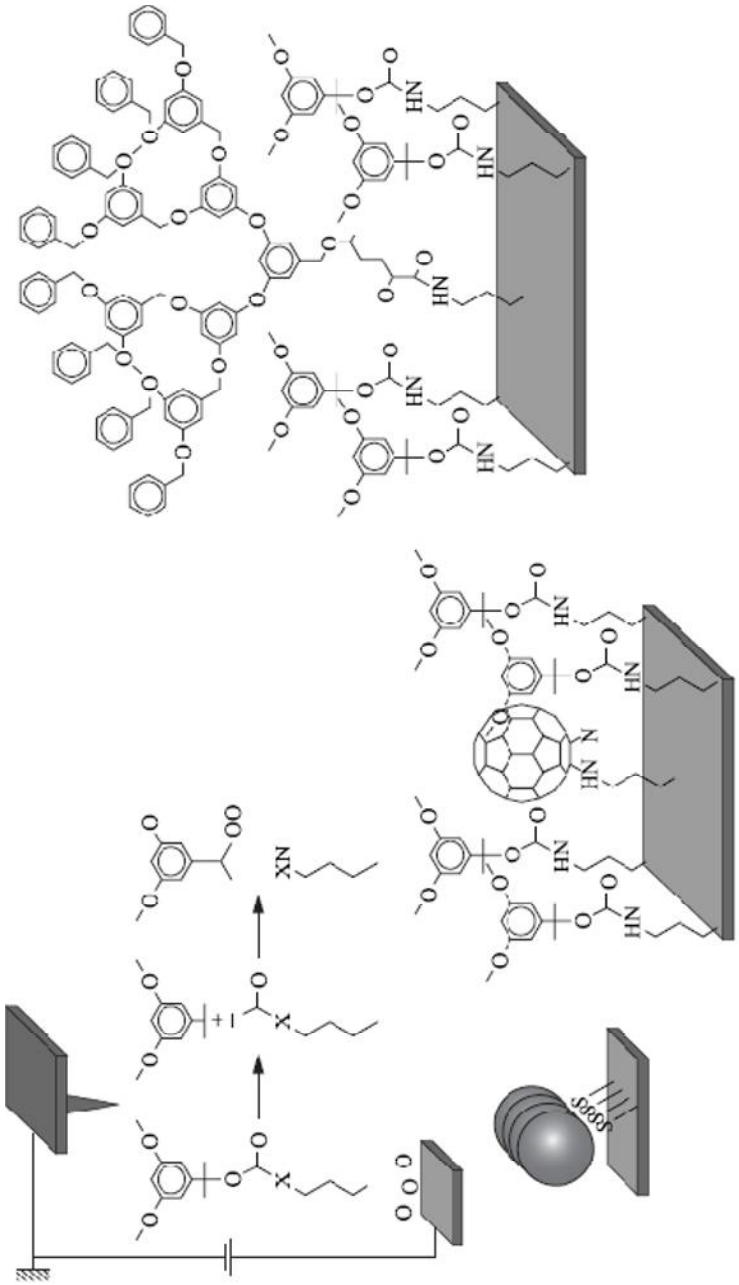

Figure 3.11. *Use principle of lithographic resist dedicated to local-probe microscopy: depending on the process used, it will allow localized deposition of defined nano-objects such as dendritic macromolecules, metallic nanoparticles or fullerenes. (© Jean Frechet group, U.C. Berkeley)*

3.5.3. *Lithography using mechanical indentation*

Another example of mask fabrication consists of using the mechanical properties of the atomic force microscope's tip in order to structure a resist [BOU 96, SOH 95]. Indeed, the sharp profile of AFM tips is well adapted to the achievement of trenches using mechanical indentation. In the image mode, this effect is usually avoided by limiting the interaction force in the nanonewton range. An increase of the control set point of the tip allows much greater interaction forces to be locally induced. The interaction force necessary to obtain indentation is generally in the range of a micronewton. Therefore, it reaches 100 to 1000 times the usual interaction value during imaging. This is equivalent to pressures under the tip in the range of gigapascals, thus being beyond the plastic limit of the polymeric layer for this range of size. In the example we describe, a trench of controlled position and size is achieved using mechanical indentation with an atomic force microscope's tip on a flexible resist. The viscosity of the resist used in this example has been first optimized for this technique (Figure 3.12). The pattern obtained is then transferred into a thin film of germanium by means of plasma etching. The trenches lead to slits which then form a mask after evaporation of the metal under vacuum (Figure 3.13).

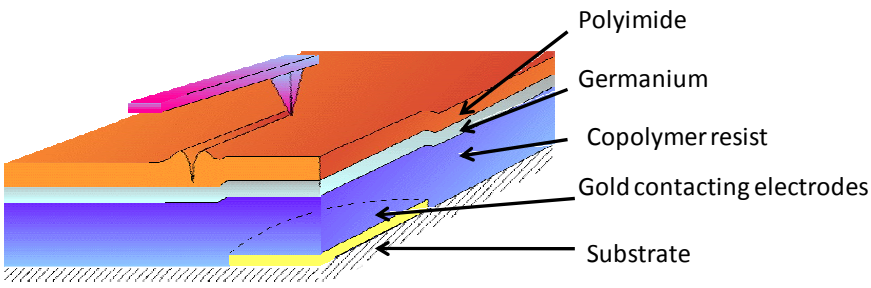

Figure 3.12. *Schematic of the principle describing the indentation technique of a polyimide resist by means of an atomic force microscope's tip*

In association with the oblique angle evaporation technique [DOL 88, ROM 88], it has been shown that this lithography allows us to obtain a functional nanodevice [BOU 96]. A single electron transistor operating at low temperature, with a line width of about 50 nm has been demonstrated. The resolution increase has helped to miniaturize the surface of tunnel junctions, thus improving the charge energy of the transistor island to a single electron and, as a result, its operating temperature. Similarly, mechanical interaction processes of the tip can also be used to modify the nanostructure of an existing device *in situ*. An AFM tip can indeed achieve local erosion on a great number of materials, including metallic thin films [IRM 98], gallium arsenide semi-conducting layers [REG 02], or even monomolecular auto-

assembled layers [WAD 01]. This has enabled the achievement of tridimensional structuring, useful for quantum nanoelectronics, in a way somewhat similar to that obtained by the interaction of a focused ion beam on a surface.

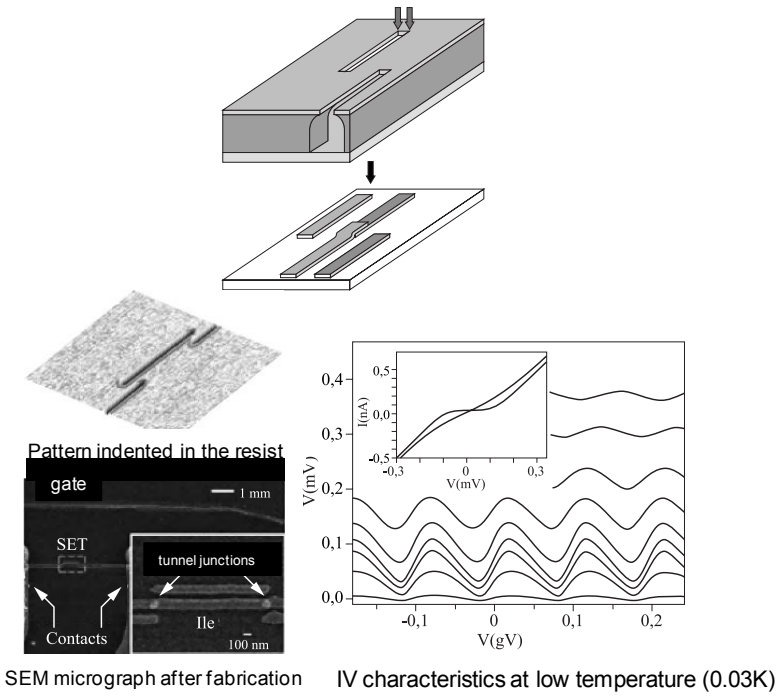

Figure 3.13. *Oblique angle evaporation principle through a free standing mask (adapted from [BOU 96]), thus allowing the fabrication of a tunnel junction made of aluminum oxide. The partial oxidation of the first layer is achieved before deposition of the second*

3.6. Lithography techniques using oxidation-reduction interactions

This is the family of local-probe lithography techniques that has led to the greatest number of technical developments and applications.

The principle is simple: it consists of inducing an oxidation-reduction reaction under the microscope's tip when it becomes electrically conducting, and is polarized above a given threshold. The reduced space between the tip and the sample becomes in some sense an electrochemical reactor locally inducing a deposition or modification of the material at the surface. A few examples achieved are given in the following sections.

3.6.1. *Direct fabrication by matter deposition induced by STM microscopy*

3.6.1.1. *Hydrogenated silicon depassivation by STM*

Hydrogenation is a chemical treatment that allows the very reactive dangling bonds that exist at the surface of depassivated single-crystal silicon (in which the native oxide has been stripped) to be neutralized. This hydrogenation consists of replacing them by Si-H bonds which are metastable and allow the surface to be to "passivated" with regards to oxidation. Application of a voltage on a local-probe microscope's tip (AFM or STM) makes it possible to break the Si-H bond and therefore locally depassivate the surface, thus revealing the dangling bonds once again. The patterned area will then be able to react with a contaminant present in the reactive chamber. This technique's advantage is the fact that it is generic and that it could be applied to different processes (see, for example, section 3.6.2.1). In addition, it is compatible with a step performed under an ultra high vacuum, thus allowing lithographic structures at the scale of a few atoms (Figure 3.14).

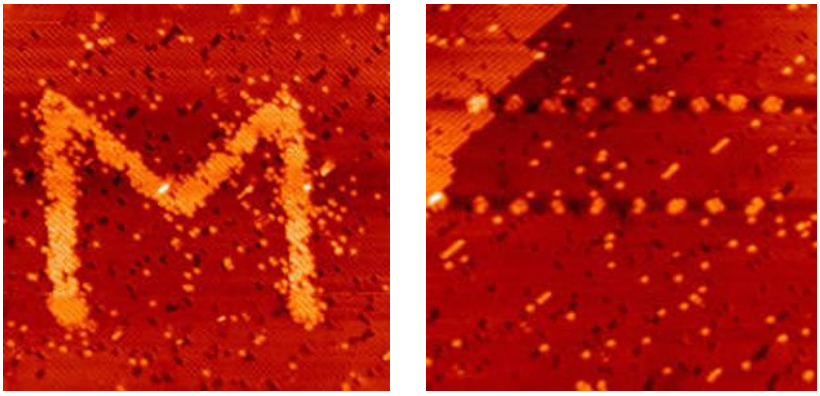

Figure 3.14. *Micrographs showing lithographic achievements by means of depassivation with an STM microscope on a hydrogenated silicon surface. Left: the letter "M" obtained has a width of approximately 23 nm, with a line width of around 3 nm. Each point on the image corresponds to a depassivated silicon atom. The presence here and there of isolated metastable atoms of hydrogenated silicon can be seen. Right: rows of dots of approximately 15-20 Angstroms in size created by voltage pulses on the tip. (Taken from IEMN Lille, adapted from [SYR 99])*

3.6.1.2. *Local chemical vapor deposition under STM*

The controlled local deposition of metallic particles by means of decomposition of a chemical vapor [THI 94] from organometallic compounds (Figure 3.15) is a technique that looks very much like chemical vapor deposition (CVD). Here, the decomposition of the precursor gas is achieved under the action of an intense

electric field that is established between the tip and the sample. This type of deposition is also achievable under a focused beam of gallium ions (FIB) (see Chapter 4). This technique coupled to STM has the advantage of having a nanometric precision specific to local-probe techniques. This process can be precisely controlled in position [MAR 00a, MAR 00b] (Figure 3.15) or, according to the desired volume of deposited material, and enables the simultaneous imaging of the object being lithographed. Moreover, it can be generalized to many different materials, including metals stable in air for nanometric volumes, such as rhodium, for example.

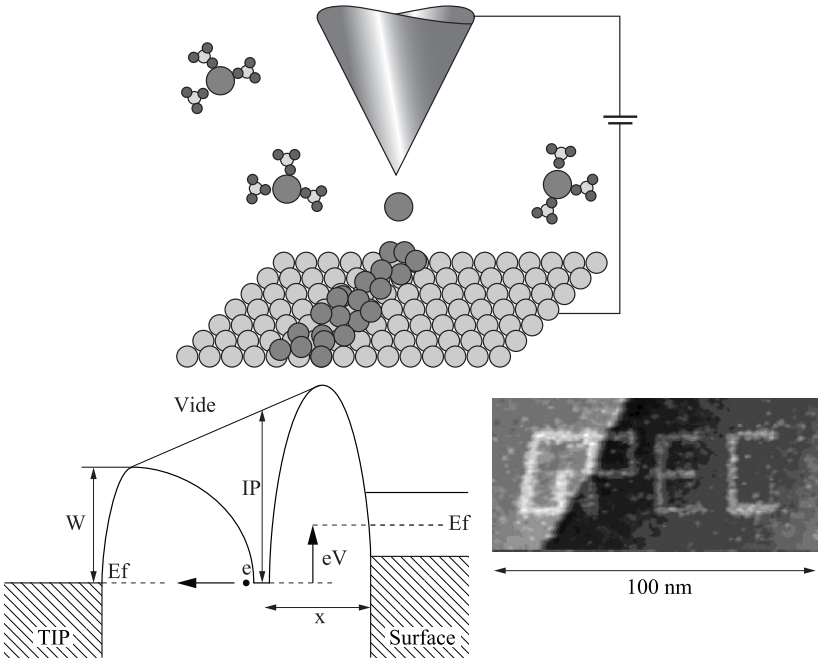

Figure 3.15. *Top: drawing showing the controlled deposition of a metal from the decomposition of an organo-metallic vapor under the tip of an STM. Bottom, left: energy band diagram showing the decomposition principle by means of the metallic precursor's reduction under the action of a tip–surface electric field and tunnel barriers existing between the tip and the surface (extract from [THI 94]). Bottom, right: STM micrograph of a pattern of metallic lines obtained by decomposition of organo-metallic vapor (taken from THI 94)*

The unsolved problem of this technique is the incompatibility that lies in the integration of the particles deposited with the measurement electrodes [MAR 00b]. It is a recurrent problem of all the advanced nanofabrication techniques but, in this case, there is an additional difficulty which lies in the impossibility of an STM tip to image an electrically insulated area. The use of a hybrid ATM/STM device

[KAT 97] similar to the one presented in section 3.5.1 and for which the regulation of the tip's position is obtained by measuring the tip/sample force interaction (like in the system presented in Figure 3.9) seems therefore essential if this type of technique is to be pursued further [AMP 05].

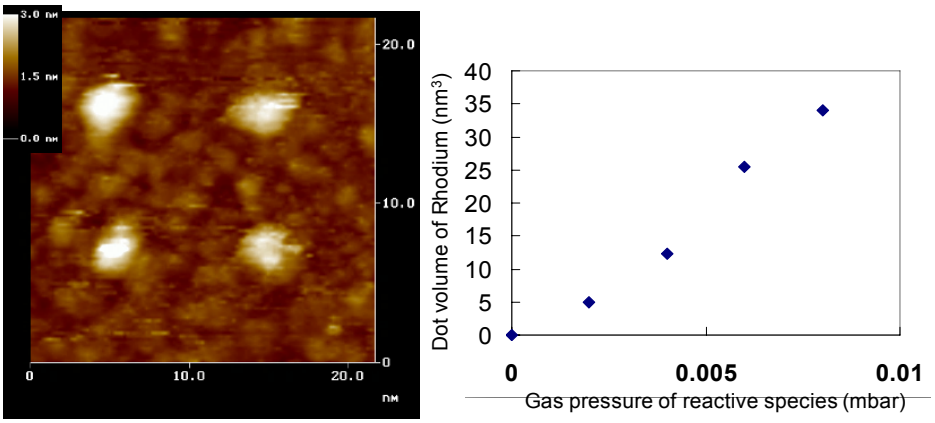

Figure 3.16. *Left: STM image of an ordered deposition of rhodium nanoparticles corresponding to 3 nm dots. Right: demonstration of the volume control for deposited particles versus precursor gas pressure (taken from [MAR 00B])*

3.6.2. *Local anodization under the AFM tip*

This technique is based on surface oxidation, intensified under the atomic force microscope's tip. The anodic oxidation, more widely known as "anodization", concerns an entire family of very diverse processes, of common use in industry, aiming at protecting metals from oxidation. The main idea consists of growing an oxide layer by electrochemical means, such that it becomes impermeable and stable for the material's future use. The local oxidation is in some way the miniaturization of the process in a reactive area between the AFM tip and the surface (Figure 3.17). Unlike previous techniques that require the microscope to be used in a controlled atmosphere, the present process can be used under ambient conditions. Indeed, the water contamination layer existing at the surface of the material leads to the formation of a stable meniscus that will play the role of an electrolyte, the tip being the cathode and the surface, the anode. The high electric field's gradient present in this gap will allow the localization of the reaction over an area of radius less than 10 nm. The mechanism intervening at this scale, described in [STI 97] is two-fold: on one hand, the field induces hydrolysis within the water meniscus leading to reactive ionic species and, on the other hand, it produces a diffusion of the charged oxidizing elements below the silicon surface.

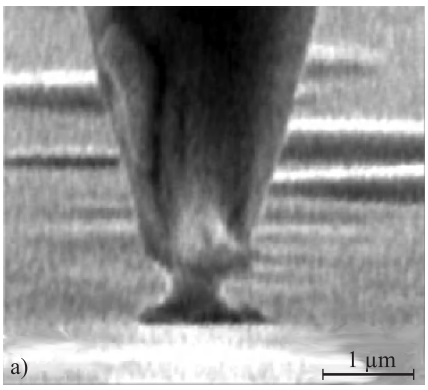

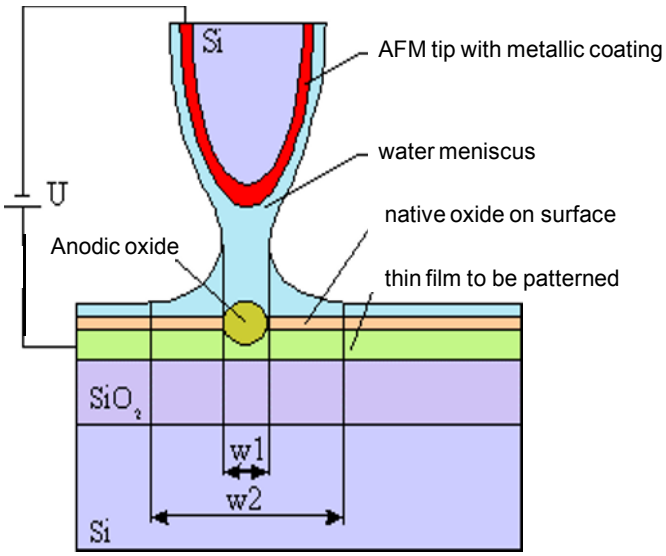

b)

Figure 3.17. *Top: Micrograph (taken by an environmental electron microscope) showing the existence of the water meniscus at the junction between the tip and the surface, which implements a miniaturized electrochemical medium, from [SCH 98]. Bottom: Principles of anodization under the atomic force microscope. Due to the potential threshold above which the reaction is activated, the pattern of anodic oxide has a width* w_1*, which is of the order of the tip curvature and is below the diameter of the water meniscus* w_2

The anodization technique induced by AFM was initially developed on an hydrogenated silicon substrate by J. Dagata (NIST, USA) in 1990 [DAG 90]. He was able to show that it was possible to grow, in a controlled manner, an oxide layer under the tip of an AFM on which a voltage is applied. Above a certain voltage

threshold from which the oxidation reaction starts, a layer of oxide a few nanometers thick and about 10 nm wide appears under the tip. The oxide quantity (in particular its thickness) can be precisely controlled by the tension applied to the tip as well as the speed rate of the tip. Figure 3.18 shows the precise control of the thickness of a lithographed line of a thin layer of niobium. Many different methods based on the permanent or intermittent contact of the tip as well as on an alternating tension in order to neutralize the space charge effects were subsequently developed.

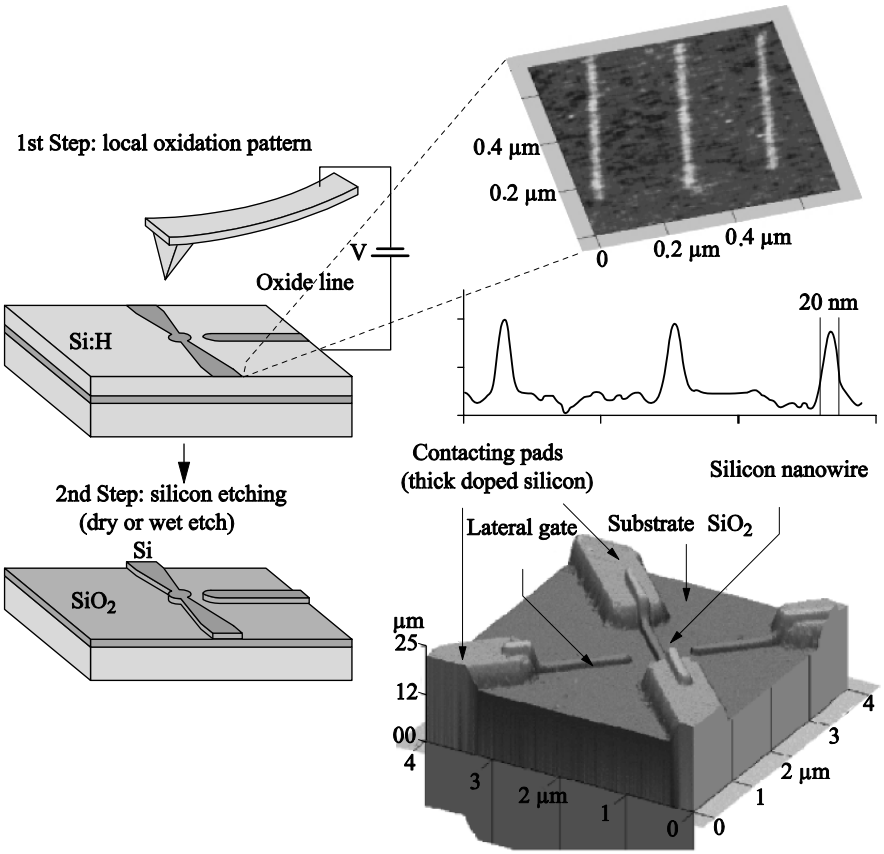

Figure 3.18. *Left: schematic of the fabrication process principle for silicon nanostructures by means of AFM nano-oxidation. The first step consists of the anodization by AFM of a silicon layer on an insulator previously hydrogenated on its surface. The local oxidation creates a contrast of a chemical nature between silicon and silicon oxide (height ~ 1 nm) which is developed during the wet etching of the silicon not protected by the oxide. This results in connected single-crystal nanostructures, on oxide*

This process has many advantages compared to other nanolithographic techniques: it is relatively inexpensive and versatile. It enables good dimensional control and a precise alignment because the tip – with no applied tension – allows the vicinity of the nanostructure to be visualized in a non-invasive way, in turn enabling easy alignment with respect to contacting electrodes. Finally, it allows *in situ* measurements during the lithography [SNO 95], allowing one to stop the process at an exact moment [SNO 96] no longer depending on the geometry but on the required electrical properties (device resistance, for example). This process can be applied on either silicon or ultra-thin metallic films and makes it possible to process quantum devices [SNO 96].

The fabrication of an oxide line on a hydrogenated silicon substrate (the substrate is similar to the one described in 3.6.1.1.) therefore enables silicon oxide lines to be achieved in precise spots on the sample. The key point consists of taking advantage of these oxide nanostructures by a process involving ultra-thin layers of a conducting material.

3.6.2.1. *Application to the fabrication of silicon nanostructures*

The first process described in this section concerns the application of AFM nano-oxidation to achieve nanostructures on thin layers of silicon-on-insulator [SNO 95]. Such a lithographed oxide wire behaves like a mask (Figure 3.18) capable of protecting the underlying material against a silicon attack by wet etching [TAB 92]. Therefore, the oxide wire protects the non-oxidized underlying material in a very efficient way (usually a fraction of a nanometer is enough to protect 20 nm of underlying silicon) and allows a structure in the silicon film to be freed (see Figure 3.18). This technique is completely adapted to the achievement of silicon-on-insulator (SOI) nanostructures [SNO 94]. The advantage of using SOI materials comes from the fact that the protected silicon is supported by an insulator substrate of buried oxide and allows electronic nanostructures supported on oxide to be produced (see Figure 3.18). The first studied structures were single-crystal silicon channels of connected nanometric diameter [CAM 95]. A lateral "finger" approaching this nanowire can be used as the gate and allows the fabrication of a field effect transistor for which the interaction between the electric field of the gate and the channel can be confined to distances of up to a few dozen nanometers (Figure 3.19). Such a device shows interesting electronic properties, more precisely for low temperatures where it can implement single electron devices [CLE 02].

This technique, which could in principle be included in a "standard" microelectronic process (implying other "standard" lithography processes like masking and etching) [BOU 02], offers a great flexibility towards the geometry of required structures (Figure 3.20). It is important to notice the low roughness of the nanostructures obtained (compared to similar structures obtained by means of

plasma etching) since all the processes are achieved in a liquid phase. Very recent results show that it is possible to push this technology up to achieving functional transistors of a channel width of about 4 nm [MAR 08]. This nano-oxidation process coupled to silicon-on-insulator also allows the fabrication of free standing electromechanical devices of very high resolution [VIL 04].

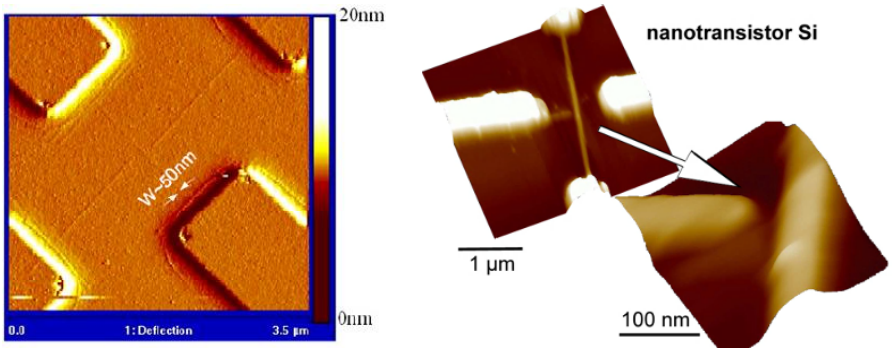

Figure 3.19. *Left: oxide lines before etching for the fabrication of a lateral gate transistor. Although their thickness is around 1 nm. the etching selectivity allows a reliable etching mask to be achieved. Right: device after the etching step, a simple silicon channel of diameter 50 × 15 (nm)*^{2}

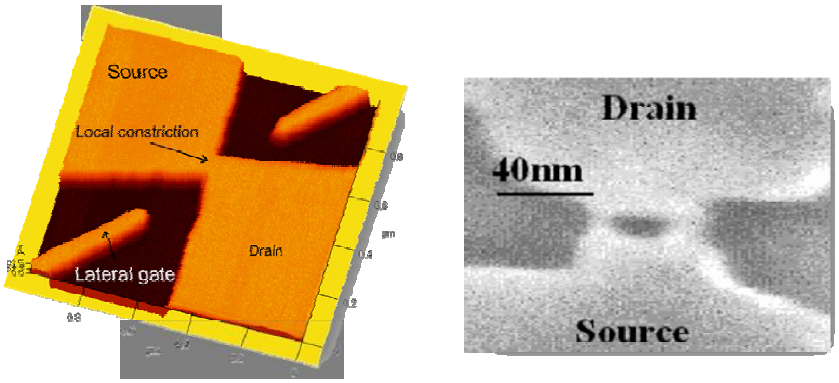

Figure 3.20. *AFM micrographs of silicon nanostructures obtained by local anodization technique. Left: device made of a point contact addressed by two lateral gates. Right: MEB micrograph of a nanostructure with two parallel channels; the width of the channels is around 15 nm. Notice the regularity and the weak roughness of the etched surfaces, characteristic of silicon wet etching [TAB 92]*

3.6.2.2. *Application to ultra-thin metallic film oxidation*

This oxidation technique is also very well adapted to superconducting and metallic layers. These layers of a thickness of a few nanometers (usually 3 to 10 nm) are thin enough to induce metal oxidation under the tip in the whole thickness, from which a controlled electrical separation [SNO 95] between the parts located on each side of the oxide line results (Figure 3.21). Nanostructures of relative complex shape can be made by limiting their shape and defining boundaries by AFM drawn insulating oxide lines (Figure 3.22), since the purpose of the lines is to limit or even interrupt the electronic conduction.

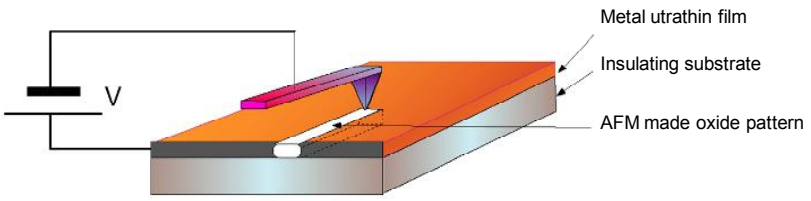

Figure 3.21. *Principle of local oxidation in AFM applied to ultra-thin metallic films. Unlike the nanooxidation on silicon described in the previous sections, for which the lithographic area corresponds to the conducting part after etching, this second process presents a "negative" direct writing where the insulating oxide pattern locally neutralizes the metal layer. The resolution obtained enables accurate control of the final metallic structure shape, in the range of 15 nm*

The dimensional control of a semi-conductor quantum dot obtained by lithography based on these techniques of nano-oxidation was demonstrated by the ENSSLIN team at ETH Zürich in 1997 [HEL 97]. The process is based on the nano-oxidation of an ultra-thin film of titanium which produces submicron local gates on a 2D electron gas. Next, it was shown by the same team [HEL 98], that the titanium film could be removed and that the oxidation could be induced in the heterostructure. This technique proved to be successful by revealing new interference processes in quantum rings [FUH 01] obtained by lithographic techniques.

At the same time, semi-conducting heterostructures were studied. Matsumoto's team in Japan (Electrotech Lab, Tsukuba) focused on the nanostructuring of titanium and niobium ultra-thin films [MAT 96]. In 1998, they demonstrated a single-electron transistor operating at ambient temperature [SHI 98]. The success of this technique is the result of mastering a lithography allowing metals to be structured at a sub-50 nm scale, combined with the realization of ultra-thin niobium layers (less than 10 nm thick) which have specific electrical characteristics.

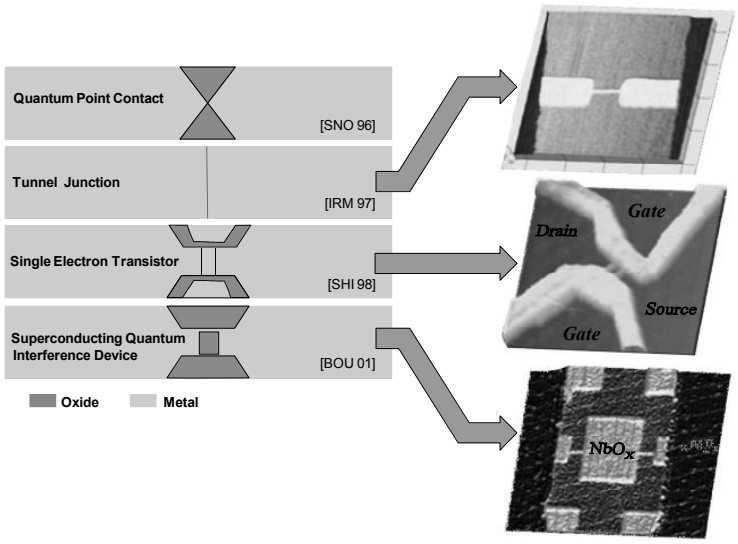

Figure 3.22. *Left: Diagrams presenting different functional quantum devices achieved by AFM lithography on metallic ultra-thin layers. The AFM patterned insulating areas are in gray. The thinner lines are semi-transparent barriers that let the current through and implement in-trench tunnel barriers. Right: AFM micrographies of standard samples*

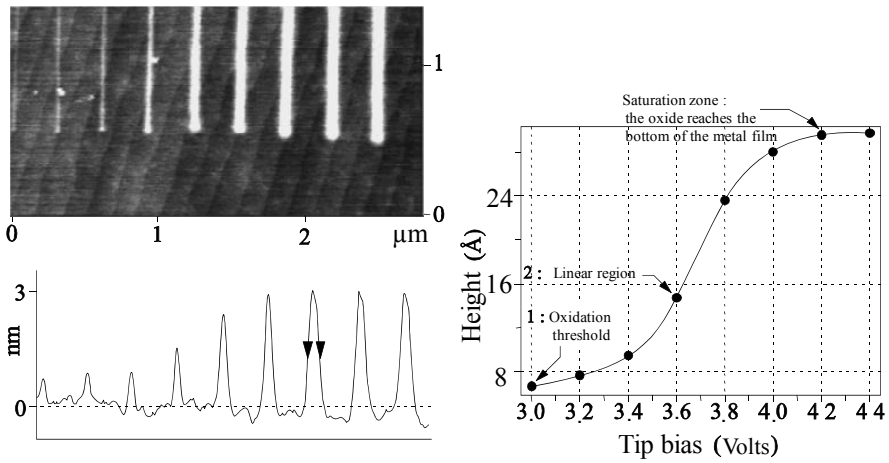

Figure 3.23. *Series of oxide lines patterned on an epitaxial niobium layer grown on a sapphire substrate for increasing tip tensions. The 3 anodic oxidation regimes used, under AFM for an ultra-thin layer, were: 1.oxidation threshold (here 3 V); 2. linear regime; 3. Saturation regime for which the entire layer was oxidized, pushing the oxide towards the side and increasing the line width*

Single-electron electronic developments [GRA 92] over the last 20 years and, more recently, superconducting technologies applied to quantum information (Superconducting Qubits) rely almost entirely on a unique technology, that is to say the aluminum/aluminum oxide-type tunnel junctions obtained by electron beam lithography, and then oblique angle evaporation through a free standing mask (as is shown in Figure 3.13, top).

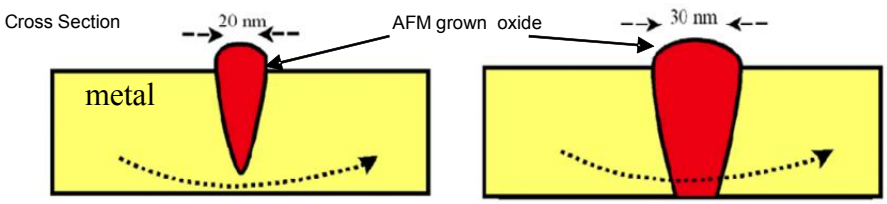

Figure 3.24. *Cross sections perpendicular to an AFM grown oxide single pixel line (image adapted from [IRM 97]). Left: Incomplete oxidation in the thickness showing a variable thickness constriction leading to a remaining metallic neck around the substrate. Right: complete oxidation realized at higher tip bias, realizing an in-trench tunnel junction*

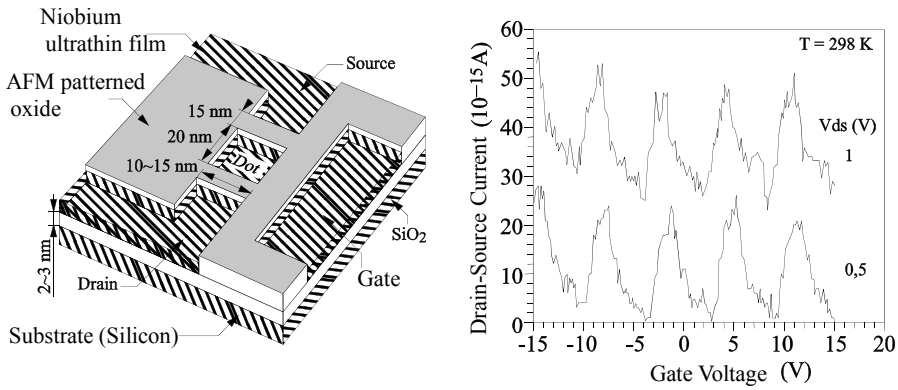

Figure 3.25. *Fabrication, by means of oxidation under AFM, of the first single electron transistor (SET) operating at ambient temperature. Left: Structure schematics, the light grey areas are the insulating parts achieved by AFM. Right: drain-source current oscillations as a function of gate tension. Each period corresponds to a polarized electron at the gate. (Figure adapted from [SHI 98])*

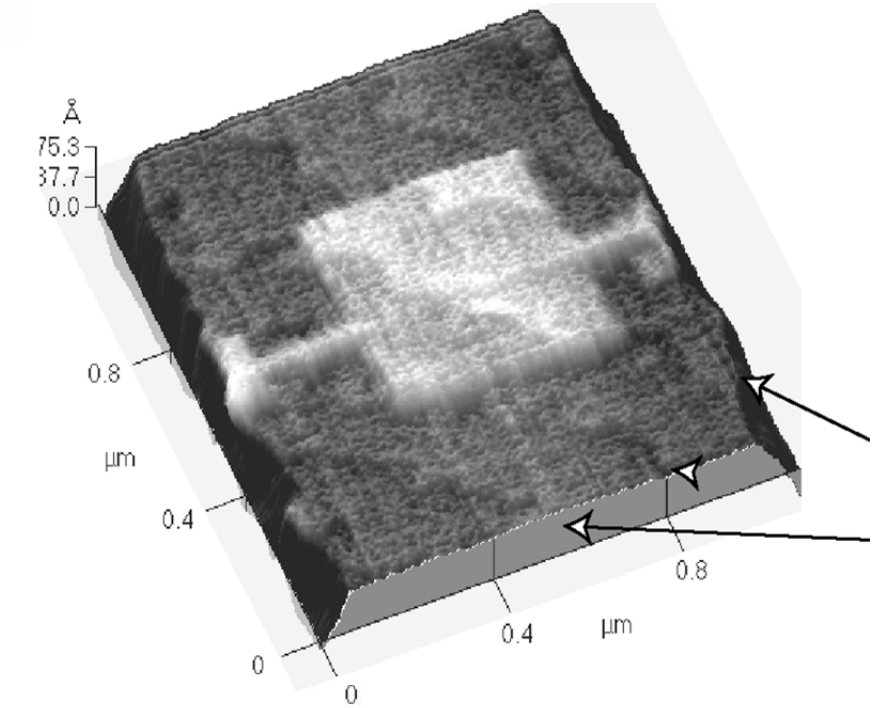

Figure 3.26. *Interferometer device achieved by means of AFM oxidation of a niobium layer. The light colored surfaces correspond to the areas oxidized by AFM scanning. The arrows show the replication of the atomic steps of the sapphire at the surface. They are also present at the surface of the anodic oxide traced by AFM (central surface, light colored). The atomic step height is equal to the distance between to niobium atoms, meaning 0.3 nm. The precise control of the oxidation quantity is a guarantee of the quality and of the reproducibility of the nanostructures obtained*

With the help of these new anodic oxidation techniques, original techniques have been elaborated to try to make them free from successive evaporations. By precisely controlling the oxidation parameters of the AFM tip, it is possible to reduce the width of the oxide barrier up to the point where it allows a tunnel coupling to be established between the two lateral electrodes. However, the oxide nature and the homogeneity of its thickness are decisive for the tunnel barrier quality [IRM 97]. This tends to prove that the tunnel transport mainly takes place through the defects of the oxide barriers (pin-holes). Additional applications of these techniques have been obtained by the observation of superconductivity properties of the lithographed objects [BOU 01].

By optimizing the lithography parameters to only oxidize part of the thickness of these films, it is possible to reduce the diameter of the superconducting nanowires. This is illustrated by the fabrication of a miniaturized superconducting quantum interferometer (Figure 3.26) for which the size of the active elements allows the magnetometric detection of nanometric magnets [FAU 09].

3.6.2.3. *Advantage of tips grafted by carbon nanotubes*

AFM tips with carbon nanotubes at their end have been used in order to improve the performances of local-probe anodization techniques [DAI 98]. Nanotubes were already known [DAI 96] for their remarkable properties for AFM imaging when grafted on a tip's end: their high rigidity compared to their size, as well as their small diameter allows the resolution and stability of the acquired images in the intermittent contact mode to be improved in a noticeable way.

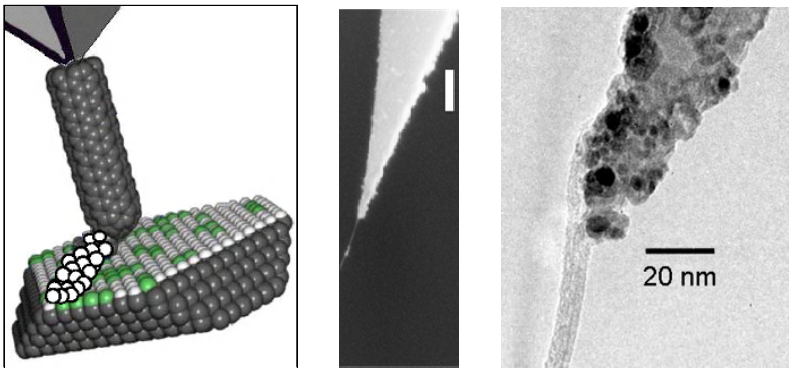

Figure 3.27. *Left: principle schematic showing oxide growth at the end of an AFM tip grafted by a carbon nanotube. The hydrophobicity of the nanotube considerably reduces the extension of the water meniscus. Center and right: electronic micrographs (center: scanning microscopy, right: transmission microscopy) showing controlled grafting obtained by* in situ *growth of a carbon nanotube by a chemical vapor deposition technique [MAR 06]*

Furthermore, there are two additional interesting properties when these tips are used for AFM nano-oxidation: on one hand, the electric field is focused by the nanotube and on the other hand, the hydrophobic characteristic of the nanotube surface [KUR 07] reduces the lateral extension of the water meniscus (Figure 3.28). These two effects contribute to improve the stability of the lithography as well as the lateral resolution of the obtained oxide lines for which the current record is 7 nm [COO 99]. In addition, the remarkable mechanical properties of nanotubes enable very high writing speeds of around 100 µm/s while keeping good tip durability.

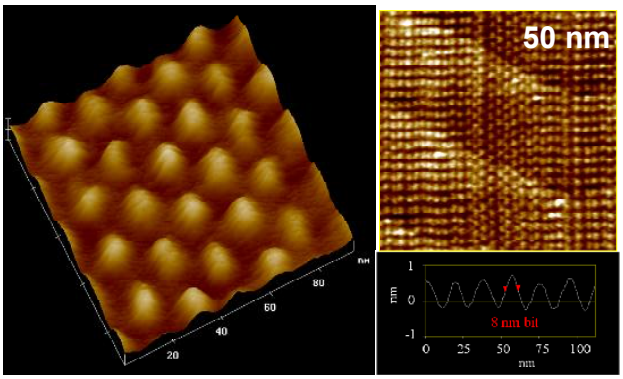

Figure 3.28. *Demonstration of anodization of a niobium layer by means of a nanotube grafted tip. The AFM micrography shows that the point density obtained by this technique is 15 terabytes/inch^2. Adapted from [COO 99]*

3.7. "Passive" lithography techniques

This sub-family of near-field lithography techniques groups together the most recent lithography techniques for which the tip does not behave as a local energy source (thus the name of passive techniques). The localization possibilities of the tip are used to achieve a precise alignment on the surface and produce a local deposition by means of capillarity (dip-pen lithography) or of masking (stencil mask).

3.7.1. *Dip-pen lithography*

In 1998, a team directed by Chad Mirkin at Northwestern University, Illinois, elaborated a new technique called dip-pen lithography for which the microscope's tip is coated beforehand with a liquid that is able to deliver, at a given point, a controlled quantity of matter. This technique makes the most out of the capillarity forces that successively collect a small liquid quantity from the tip's surface to release it in a controlled way.

The principle of dip-pen lithography is very similar to the dipping of a pen into an inkwell. The tip is coated beforehand with a small quantity of liquid by soaking it in a humid zone (the inkwell) which wets the tip's surface by capillarity. The tip is then moved and put in contact with the surface according to a predetermined pattern of points. The time during which the tip remains on a specific surface precisely determines the liquid quantity deposited at each point. Diffusion principles show that the size increase of the deposited objects vary with the square root of the time that the tip stays on the surface. It is important to notice that the controlled

deposition of very small quantities (controlled deposition of dip-pen lithography fluids [PIN 99]) has relevant applications for molecular biology [LEE 02].

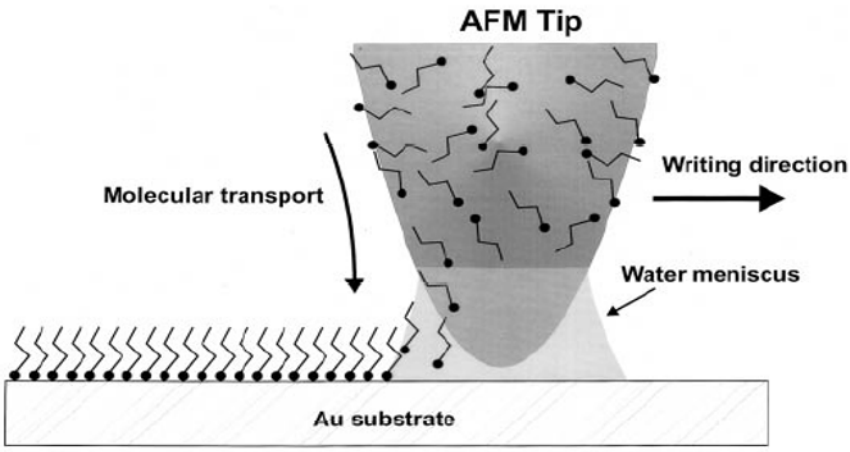

Figure 3.29. *Principle of dip-pen lithography*

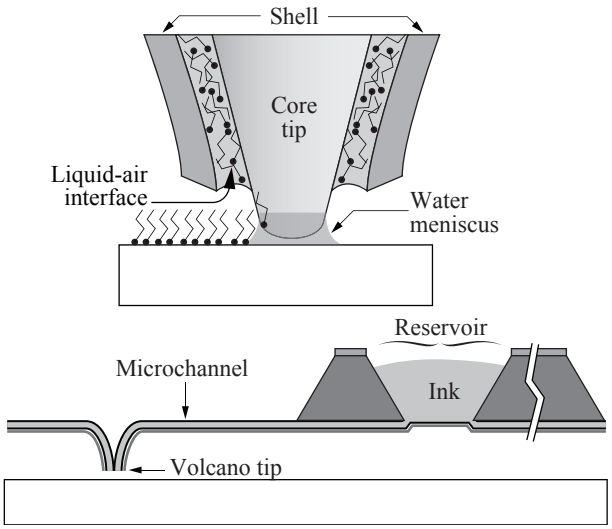

Figure 3.30. *Schematic cross-section of a second generation dip-pen stylograph's tip, with an ink reservoir, thanks to the integration of a micro-fluidic technology at the tip. This recent improvement makes it possible to remove the backward and forwards movements towards the position of the ink reservoir (no further need for an inkwell) and also improves the deposition speed and precision. © C. Mirkin*

3.7.2. *Alignment technique by means of a mechanical masking (stencil mask)*

This technique is the adaptation to local-probe lithography techniques of the possibilities of making material deposition in the presence of mechanical masks (called stencil masks) [DES 99]. The added value here is linked to the alignment properties of the mechanical masks thanks to atomic force microscopy [PER 04]. Unfortunately, these masking techniques with the tip are still not well known. This technique is roughly using the AFM tip as a stencil during the vacuum evaporation of a thin metallic layer, or during ion irradiation of the surface [MEI 06, PER 04]. The shadowing of the tip, correctly positioned in relation to a nanostructure, allows, for example, that nanostructure to be connected to metallic electrodes. The fabrication of dedicated tips (for example with a central channel driven by focused ion beam techniques, Figure 3.31) enables the optimization of the stencil's shape.

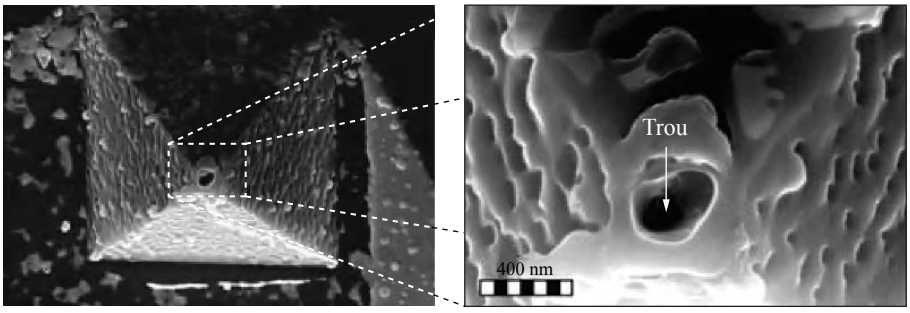

Figure 3.31. *Micrography by scanning electron microscopy of an AFM silicon nitride tip, the symmetry axis of which has been drilled by a focused ion beam. Such a tip makes it possible to geometrically confine matter deposition by means of shadowing and enables the achievement of lines by moving the tip during deposition. From [MEI 06]*

The on-going applications of this technique concern the possibility of delivering doping impurities or even a single dopant at precise points [SCH 06]. If applied to controled doping of a silicon channel, it is expected that the realization of a "qubit" (the elementary component of a quantum computer) will be achieved. This is done by using the electron spin of the ion impurity [SCH 03] inside the silicon matrix as the quantum information medium. Similar research concerning "diamond crystal implantation", for quantum information, is in progress [MEI 06].

3.8. Conclusions and perspectives

Through the presentation of this brief overview we intend to show the remarkable application potential of local-probe microscopy techniques for

nano-lithography. Beyond their ultimate resolution (1 to 10 nm, depending on the process chosen), what must be remembered is the extreme versatility of these techniques, a guarantee of still further innovation.

It is interesting to notice that these techniques are at the convergence of the complementary *top-down* (matter structuring – considered as a homogeneous continuum – by thinner and thinner lines) and *bottom-up* (built from elementary components: atoms, molecules) approaches. They are aimed at niche applications and their low industrial impact is a result of the fact that the fine-tuning of the lithographic parameters remains a traditional and time-consuming task. Unlike the competing techniques based on microscopes developed 50 years ago, local probes are still young and their maturity is far from being reached. They are also financially attractive because of their possible miniaturization, thanks to the developments of embedded electronics. Unfortunately an essential aspect is often forgotten: the need to accompany these new lithographic processes with the development of bespoke materials (new resists, single-crystal ultra-thin layers) in order to benefit from all the potential of these surface microscopy techniques.

3.9. Bibliography

[ALB 89] ALBRECHT T.R., DOVEK M.M., KIRK M.D., LANG C.A., QUATE C.F., SMITH D.P.E., "Nanometer-scale hole formation on graphite using a scanning tunneling microscope", *Applied Physics Letters*, 55, p. 1727–9, 1989.

[AMP 05] AMPERE A.T., ANDREA N., CHEN T.P., "Nanofabrication by scanning probe microscope lithography: A review", *Journal of Vacuum Science & Technology B: Microelectronics and Nanometer Structures*, 23, p. 877–894, 2005.

[AVO 99] AVOURIS P., HERTEL T., MARTEL R., SCHMIDT T., SHEA H.R., & WALKUP R.E., "Carbon nanotubes: Nanomechanics, manipulation, and electronic devices", *Appl. Surf. Science*, 141, p. 201, 1999.

[BIN 86] BINNIG G., QUATE C.F., GERBER C., "Atomic force microscope", *Physical Review Letters*, 56, p. 930, 1986.

[BIN 82] BINNING G., ROHRER H., GERBER C., WEIBEL E., "Surface studies by scanning tunneling microscopy", *Physical Review Letters*, 49, p. 57, 1982.

[BOU 96] BOUCHIAT V., ESTEVE D., "Lift-off lithography using an atomic force microscope", *Appl. Phys. Lett.*, 69, p. 3098, 1996.

[BOU 01] BOUCHIAT V., FAUCHER M., THIRION C, WERNSDORFER W., FOURNIER T., PANNETIER B., "Josephson Junctions and Superconducting Interferences devices made by local anodisation of niobium ultra-thin films", *Applied Physics Letters*, vol.79, p. 123, 2001.

[BOU 02] BOUCHIAT V., FAUCHER M., FOURNIER T., PANNETIER B., THIRION C., WERNSDORFER W., CLÉMENT N., TONNEAU D., DALLAPORTA H., SAFAROV S., VILLEGIER J.C., FRABOULET D., MARIOLLE D., GAUTIER J., "Resist-less patterning of quantum nanostructures using an atomic force microscope", *Microelectronic Engineering*, 61–62, p. 517–22, 2002.

[CAM 95] CAMPBELL P.M., SNOW E.S., MCMARR P.J., "Fabrication of nanometer-scale side-gated silicon field effect transistors with an atomic force microscope", *Appl. Phys. Lett.*, vol. 66, p. 1388–90, 1995.

[CHA 75] CHANG T.H.P., "Proximity effect", *J. Vac. Sci. Technol.*, 12, p. 1271, 1975.

[CHO 95] CHOU S.Y., KRAUSS P.R., Renstrom, P.J., "Imprint of sub-25 nm vias and trenches in polymers", *Applied Physics Letters*, vol. 67 p. 3114, 1995.

[CHO 98] CHOU S.Y., Nanoimprint lithography US Patent 5,772,905, USA,1998.

[CLE 02] CLEMENT N., BOUCHIAT V., TONNEAU D., DALLAPORTA H., FRABOULET D., MARIOLE D., GAUTIER J. & SAFAROV V., "Electronic transport properties of single crystal silicon nanowires fabricated using an Atomic Force Microscope", *Physica E: Low-dimensional Systems and Nanostructures*, 13, p. 999–1002, 2002.

[COO 99] COOPER E.B., MANALIS S.R., FANG H., DAI H., MATSUMOTO K., MINNE S.C., HUNT T., QUATE C.F., "Terabit-per-square-inch data storage with the atomic force microscope", *Applied Physics Letters*, 75, p. 3566–8, 1999.

[CRO 93] CROMMIE M. F., LUTZ C. P., & EIGLER D. M., "Confinement of electrons to quantum corrals on a metal surface", *Science* Vol. 262, p.218 – 220, 1993.

[DAG 90] DAGATA J.A., SCHNEIR J., HARARY H.H., EVANS C.J., POSTEK M.T., BENNETT J., "Modification of hydrogen-passivated silicon by a scanning tunneling microscope operating in air", *Applied Physics Letters*, 56, p. 2001–3, 1990.

[DAI 96] DAI H., HAFNER J.H., RINZLER A.G., COLBERT D.T., SMALLEY R.E., "Nanotubes as nanoprobes in scanning probe microscopy", *Nature*, 384, p. 147–50, 1996.

[DAI 98] DAI H., FRANKLIN N., HAN J., "Exploiting the properties of carbon nanotubes for nanolithography", *Applied Physics Letters*, 73, p. 1508–1510, 1998.

[DES 99] DESHMUKH, M., RALPH D.C., THOMAS M., SILCOX J., "Nanofabrication using a stencil mask", *Appl. Phys. Lett.*, 75, 1631 (1999)

[DOL 88] DOLAN G.J., DUNSMUIR J.H., "Very small (20 nm) lithographic wires, dots, rings, and tunnel junctions", *Physica*, B 152, p. 7, 1988.

[EIG 90] EIGLER D.M., SCHWEIZER E.K., "Positioning single atoms with a scanning tunnelling microscope", *Nature*, 344, p. 524, 1990.

[FAU 09] FAUCHER M., JUBERT P.O., FRUCHART O., WERNSDORFER W. & BOUCHIAT V., "Optimizing the flux coupling between a nanoSQUID and a magnetic particle using atomic force microscope nanolithography", *Supercond. Sci. Technol.*, vol. 22, p. 064010, 2009.

[FUH 01] FUHRER A., LÜSCHER S., IHN T., HEINZEL T., ENSSLIN K., WEGSCHEIDER W., BICHLER M., "Energy spectra of quantum rings", *Nature*, 413, p. 822, 2001.

[GER 08] GERMAIN J., ROLANDI M., BACKER S.A. & FRÉCHET J.M.J., "Sulfur as a novel nanopatterning material: An ultrathin resist and a chemically addressable template for nanocrystal self-assembly", *Adv. Mater*. 20(23), 4526–4529, 2008.

[GRA 92] GRABERT H., DEVORET M.H. *Single charge tunneling coulomb blockade phenomena in nanostructures*, Plenum Press, New York, 1992.

[HEI 94] HEINZELMANN H., POHL D.W., "Scanning near-field microscopy" *Applied Physics A: Materials Science & Processing*, 59, p. 89, 1994.

[HEL 97] HELD R., HEINZEL T., STUDERUS P., ENSSLIN K., HOLLAND M., "Semiconductor quantum point contact fabricated by lithography with an atomic force microscope" *Appl. Phys. Lett.*, 71, 2689, 1997.

[HEL 98] HELD R., VANCURA T., HEINZEL T., ENSSLIN K., HOLLAND M., WEGSCHEIDER W., "In-plane gates and nanostructures fabricated by direct oxidation of semiconductor heterostructures with an atomic force microscope", *Appl. Phys. Lett.*, 73, 262, 1998.

[IRM 97] IRMER B., KEHRLE M., LORENZ H., KOTTHAUS J.P., "Fabrication of Ti/Tiox tunneling barriers by tapping mode atomic force microscopy induced local oxidation", *Applied Physics Letters*, 71, p. 1733–1735, 1997.

[IRM 98] IRMER B., *et al.*, "Josephson junctions defined by a nanoplough", *Applied Physics Letters*, 73 (14), p. 2051–2053, 1998.

[KAT 97] KATHRYN W., HYONGSOK T.S., ABDULLAH A., CALVIN F.Q., "Hybrid atomic force/scanning tunneling lithography", *Journal of Vacuum Science & Technology B: Microelectronics and Nanometer Structures*, 15, p. 1811–7, 1997.

[JUN 98] JUNNO T., CARLSSON S.-B., XU HONGQI, MONTELIUS L., & SAMUELSON L., "Fabrication of quantum devices by Ångström-level manipulation of nanoparticles with an atomic force microscope" , *Applied Physics Letters*, 72 (5): p. 548, 1998.

[KUR 07] KURAMOCHI H., TOKIZAKI T., YOKOYAMA H., DAGATA J.A., "Why nano-oxidation with carbon nanotube probes is so stable: I. Linkage between hydrophobicity and stability", *Nanotechnology*, 18, p. 135703, 2007.

[LEB 97] LEBRETON C., WANG Z.Z., "Nano-hole formation on gold surface using scanning tunnelling microscope", *Appl. Phys.*, A 66, S777–S782, 1998.

[LEE 02] LEE K.B., PARK S.J., SMITH C.A.M.C., MRKSICH M., "Protein nanoarrays generated by dip-pen nanolithography" *Science*, 295, p. 1702, 2002.

[MAM 95] MAMIN H.J., TERRIS B.D., FAN L.S., HOEN S., BARRETT R.C., RUGAR D., "High-density data storage using proximal probe techniques", *IBM Journal of Research and Development*, 39, p. 681, 1995.

[MAR 00A] MARCHI F., TONNEAU D., DALLAPORTA H., PIERRISNARD R., BOUCHIAT V., SAFOROV V., DOPPELT P., EVEN R., "Nanometer scale patterning by scanning tunneling microscope assisted chemical vapour deposition", *Microelectronic Engineering*, 50, p. 59, 2000.

[MAR 00B] MARCHI F., TONNEAU D., BOUCHIAT V., DALLAPORTA H., SAFAROV V., DOPPELT P., EVEN R., BEITONE L., "Direct patterning of noble metal nanostructures with a scanning tunneling microscope", *Journal of Vacuum Science & Technology*, B 18, p. 1171, 2000.

[MAR 06] MARTY L., IAIA A., FAUCHER M., BOUCHIAT V., NAUD C., CHAUMONT M., FOURNIER T., BONNOT A.M., "Self-assembled single wall carbon nanotube field effect transistors and AFM tips prepared by hot filament assisted CVD", *Thin Solid Films*, 453, p. 1024–1027, 2006.

[MAR 08] MARTINEZ J., MARTINEZ R.V., GARCIA R., "Silicon nanowire transistors with a channel width of 4 nm fabricated with atomic force nanolithography", *Nano Letter*, vol. 8, p. 3636–39, 2008.

[MAT 96] MATSUMOTO K., ISHII M., SEGAWA K., OKA Y., VARTANIAN B.J., HARRIS J.S., "Room T Set Par Stm", *Appl. Phys. Lett.*, 68, p. 34, 1996.

[MEI 06] MEIJER J., VOGEL T., BURCHARD B., RANGELOW I., "Concept of deterministic single ion doping with sub-nm spatial resolution" *Appl. Phys.*, A, vol. 83, 2006.

[MIN 98] MINNE S.C., YARALIOGLU G., MANALIS S.R., ADAMS J.D., ZESCH J., ATALAR A., QUATE C.F., "Automated parallel high-speed atomic force microscopy", *Appl. Phys. Lett.*, 72, p. 2340, 1998.

[PER 04] PERSAUD A., ALLEN F., GICQUEL F., PARK S.J., LIDDLE J.A., SCHENKEL T., IVANOV T., IVANOVA K., RANGELOW I.W., BOKOR J., "Single ion implantation with scanning probe alignment", *J. Vac. Sci. Tech.*, B 22, p. 3115–3118, 2004.

[PIC 07] PICCO L.M., BOZEC L., ULCINAS A., ENGLEDEW D.J., ANTOGNOZZI M., HORTON M.A., MILES M.J., "Breaking the speed limit with atomic force microscopy", *Nanotechnology*, 18, p. 044030, 2007.

[PIN 99] PINER R.D., ZHU J., XU F., HONG S., MIRKIN C.A., "Dip-pen nanolithography", *Science*, 283, p. 661–3, 1999.

[REG 02] REGUL J., KEYSER U.F., PAESLER M., HOHLS F., ZEITLER U., HAUG R., MALAVE J.A., OESTERSCHULZE E., REUTER D., WIECK A.D., "Fabrication of quantum point contacts by engraving GaAs/AlGaAs heterostructures with a diamond tip", *Appl. Phys. Lett.*, 81, p. 2023, 2002.

[ROL 04] ROLANDI M., SUEZ I., DA, H., FRÉCHET J.M.J., "Dendrimer monolayers as negative and positive tone resists for scanning probe lithography", *Nanolett.*, 4, 889–893, 2004.

[ROL 07] ROLANDI M., SUEZ I., SCHOLL A., FRÉCHET J.M.J., "Fluorocarbon resist for high speed scanning probe lithography", *Angew. Chem.*, 2007, 46 (39), p. 7477–7480, 2007.

[ROM 88] ROMIJN J., VAN DER DRIFT E., "Nanometer-scale lithography for large lateral structures", *Physica*, B 152, p. 14, 1988.

[SAL 99] SALVAN F., THIBAUDAU F., "Microscopie à sonde locale", *Techniques de l'ingénieur, traité Analyse et caractérisation*, article no. P895, 1999.

[SCH 98] SCHENK M., FUTING M., REICHELT R., "Direct visualization of the dynamic behavior of a water meniscus by scanning electron microscopy", *J. App. Phys.*, 84, p. 4880–4884, 1998.

[SCH 03] SCHENKEL T., *et al.*, "Solid state quantum computer development in silicon with single ion implantation" *J. Appl. Phys.*, 94, p.7017, 2003.

[SCH 06] SCHENKEL, A TYRYSHKIN,M. DE SOUSA R., WHALEY K.B., BOKOR J., LIDDLE J.A., PERSAUD A., SHANGKUAN J., CHAKAROV I., LYON S. A., "Electrical activation and spin coherence of ultra low dose antimony implants in silicon", *Applied Physics Letters*, 88, p. 112101, 2006.

[SHI 98] SHIRAKASHI J.I., MATSUMOTO K., MIURA N., KONAGAI M., "Single-electron charging effects in Nb/Nb oxide-based single-electron transistors at room temperature", *Appl. Phys. Lett.*, 72, p. 1893, 1998.

[SOH 95] SOHN L.L., WILLETT R.L., "Fabrication of nanostructures using atomic-force-microscope-based lithography", *Appl. Phys. Lett.*, 67, p. 1552, 1995.

[SNO 94] SNOW E.S., CAMPBELL P.M., "Fabrication of Si nanostructures with an atomic force microscope", *Applied Physics Letters*, 64, p. 1932–1934, 1994.

[SNO 95] SNOW E.S., CAMPBELL P.M., "Afm fabrication of sub-10-nanometer metal-oxide devices with in situ control of electrical properties", *Science*, 270, p. 1639, 1995.

[SNO 96] SNOW E.S., PARK D., CAMPBELL P.M., "Single-atom point contact devices fabricated with an atomic force microscope", *Appl. Phys. Lett.*, 69, p. 269, 1996.

[STI 97] STIEVENARD D., FONTAINE P.A., DUBOIS E., "Nanooxidation using a scanning probe microscope: An analytical model based on field induced oxidation", *Applied Physics Letters*, 70, p. 3272–3274, 1997.

[SYR 99] Syrykh C., Nys J. P., Legrand B., Stiévenard D., "Nanoscale desorption of H-passivated Si(100)–2×1 surfaces using an ultrahigh vacuum scanning tunneling microscope", *J. Appl. Phys.*, 85, p. 3887, 1999.

[TAB 92] TABATA O., ASAHI R., FUNABASHI H., SHIMAOKA K., SUGIYAMA S., "Anisotropic etching of silicon in Tmah solutions", *Sens. and Actuat.*, A 1, p. 51, 1992.

[THI 94] THIBAUDAU F., ROCHE J.R., SALVAN F., "Nanometer-scale lithography on Si surface by decomposition of ferrocene molecules using a scanning tunneling microscope", *Applied Physics Letters*, 64, p. 523–5, 1994.

[TOR 03] TORRES C.M.S. (ED.), *Alternative lithography, unleashing the potentials of nanotechnology*, Springer Technology & Industrial Arts, Berlin, 2003.

[VET 00] P. VETTIGER, M. DESPONT, U. DRECHSLER, U. DÜRIG, W. HÄBERLE, M.I. LUTWYCHE, H.E. ROTHUIZEN, R. STUTZ, R. WIDMER & BINNIG G.K., "The 'millipede': More than one thousand tips for future AFM storage", *IBM J. of Research and Development*, 44, p. 323, 2000.

[VIL 04] VILLARROYA M., PEREZ-MURANO F., MARTIN C., DAVIS Z., BOISEN A., ESTEVE J., FIGUERAS E., MONTSERRAT J., BARNIOL N., "AFM lithography for the definition of nanometre scale gaps: application to the fabrication of a cantilever-based sensor with electrochemical current detection", *Nanotechnology*, 15, p. 771–776, 2004.

[WAD 01] WADU-MESTHRIGE K., AMRO N.A., GARNO J.C., XU S., LIU G.Y., "Fabrication of nanometer-sized protein patterns using atomic force microscopy and selective immobilization", *Biophys. J.*, vol. 80, p. 1891–1899, 2001.

[WIE 94] WIESENDANGER R., *Scanning probe microscopy and spectroscopy*, *methods and applications*, Cambridge University Press, Cambridge, USA, 1994.

[WIL 97] WILDER K., SOH HYONGSOK T., ATALAR A., QUATE C.F., "Hybrid atomic force/scanning tunneling lithography", *J. Vac. Sci. Technol.*, B 15, n° 5, p. 1811–1817, 1997.

[WIL 98] WILDE K., QUATE C. F., SINGH B., KYSER D.F., "Electron beam and scanning probe lithography: A comparison", *J. Vac. Sci. Technol.*, B 6, p. 3864, 1998.

Chapter 4

Lithography and Manipulation Based on the Optical Properties of Metal Nanostructures

4.1. Introduction

Among lithography techniques that use an electromagnetic wave (of wavelength λ) to insulate a resist, optical lithography is undoubtedly the most attractive, for cost and simplicity reasons. Its main weak point is its resolution, limited for dense features at a value of $\lambda/2n$ set by diffraction, n being the refraction index of the medium into which the electromagnetic field propagates. In practice, this value corresponds to about a hundred nanometers in UV lithography. With the aim of improving this resolution, for several years the main approach has been the reduction of λ (extreme UV lithography) and the increase of n (immersion lithography) [LIN 06]. However, these approaches are expensive and require the expending of considerable mid- and long-term economic and technological efforts.

An alternative solution consists of using the optical near-field, where evanescent and propagating waves coexist [COU 01]. While propagating waves are associated with the diffraction limit $\lambda/2n$ by propagation of light and summing of the fields (the Huygens-Fresnel principle of far-field diffraction), evanescent waves (which result from the diffraction of light by the high spatial frequencies of an object [GOO 96]) can be associated with nanometric optical confinements.

Chapter written by Renaud BACHELOT and Marianne CONSONNI.

Within the framework of the appearance of near-field optics techniques, several approaches to optical nano-sources have been developed over the last 20 years [COU 01]. One of the most famous relies on the diffraction of a plane wave by a nano-aperture in a metallic screen [BET 44, BOU 50]. These sources, which have dimensions well under sub-wavelength, can be used in near-field optical spectroscopy/microscopy as well as for high-resolution optical lithography. The latest practices about the different near-field optical lithography approaches can be found in recent review articles [ROY 04, TSE 07].

In this chapter, attention is drawn to the use of particular evanescent optical fields in optical nano-lithography: the fields associated with surface plasmons carried by metallic structures. This type of field, which has a nanometric confinement in at least one spatial direction, has aroused growing interest in the near-field optics community. This interest is illustrated by the recent release of a dedicated journal (*Plasmonics*) and the opening of a biannual conference, dedicated to the physics and applications of surface plasmons[1]. With the help of several relevant examples (sections 4.3 and 4.4), we will see that surface plasmons, the remarkable physical properties of which will be described in section 4.2, have allowed the implementing of a nanometric optical lithography, and more generally the manipulation and control of various types of materials photosensitive at a molecular scale.

4.2. Surface plasmons

This section provides a few definitions and general points about plasmons and their properties, and introduces the characteristics related to their use in lithography.

4.2.1. *Definition of a volume plasmon*

In a metal described by the Drude model (that is to say, for which only the electrons from the conduction band and the intraband transitions are taken into account), the free electrons are considered to be an electron gas. This gas is likely to undergo longitudinal charge-density oscillations (plasma oscillations), of which the associated quantum is called a volume plasmon [KIT 96].

1 Surface Plasmon Photonics (SPP) conferences. The last (SPP4) was held in Amsterdam (21–25 June 2009). SPP5 will take place in South Korea (15 May–20 May 2011).

4.2.2. *Delocalized surface plasmons*

4.2.2.1. *Definition*

The expression of Maxwell's equations at a metal–dielectric interface shows that surface electromagnetic waves can propagate along metallic films. These waves, associated with local oscillations of the electron density of the metal, are called delocalized surface plasmons. This last name comes from the fact that they propagate along the whole metallic surface, in a non-local way.

4.2.2.2. *Dispersion equation*

The dispersion equation of surface plasmons propagating along a metal–dielectric interface can be obtained by solving the wave equation along this interface:

$$\Delta \vec{E} + \frac{\omega^2}{c^2} \varepsilon \vec{E} = 0 \qquad [4.1]$$

E being the electric field and ω and ε being, respectively, the frequency and the dielectric permittivity of the medium considered. Given that the plasmons are waves that are confined and propagate along the interface (x axis), the considered solutions are the following:

$$\vec{E}(r)\exp(-i\omega t) = \vec{E}(z)\exp(ik_{sp}x)\exp(-i\omega t) \qquad [4.2]$$

where k_{sp} is the wave vector component along the interface and $E(z)$ stands for the field evanescent decay along the z-axis perpendicular to the metallic surface.

Boundary conditions on field components at the metal–dielectric interface lead to the dispersion equation:

$$k_{sp} = k_0 \sqrt{\frac{\varepsilon_m(\omega)\varepsilon_d}{\varepsilon_m(\omega) + \varepsilon_d}} = k'_{sp} + ik''_{sp} \qquad [4.3]$$

where $\varepsilon_m = \varepsilon'_m + i\varepsilon''_m$ and ε_d are, respectively, the permittivity of the metal at the considered frequency ω, and the dielectric's permittivity, and $k_0 = \omega/c$.

In the case of the Drude model [KIT 96], for optical frequencies significantly higher than electron collision frequency, the permittivity of the metal is described by the relation:

$$\varepsilon_m(\omega) = 1 - \frac{\omega_p^2}{\omega^2} \qquad [4.4]$$

where ω_p is the plasma pulsation. The substitution of this expression in equation [4.3] then leads to the dispersion relation, represented in a qualitative manner in Figure 4.1.

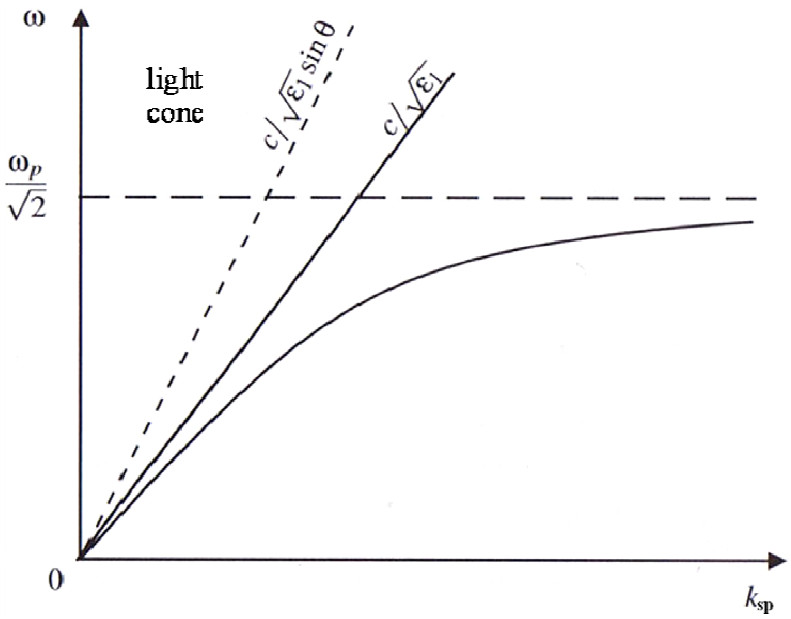

Figure 4.1. *Qualitative plotting of the dispersion relation of a surface plasmon mode on a metal–dielectric interface (full line curve). For a comparison, the straight lines represent the dispersion relation for propagating waves at grazing incidence (slope $c\varepsilon_1^{-1/2}$) and at θ incidence (slope $c\varepsilon_1^{-1/2}/\sin\theta$); ε_1 here corresponds to the permittivity of the dielectric medium. Figure taken from [COU 01]*

The curves obtained indicate that for a given metal–dielectric interface, the plasmon modes only exist below a certain frequency, the component along the interface of the wave vector of the plasmons k_{sp} being always greater than that of the

progressive light wave at the same frequency. This property of plasmons is one of the reasons why they are used in lithography: plasmons excited at a wavelength λ_0 have an actual wavelength λ_{sp} smaller than λ_0, which potentially enables a better resolution than with the initial light wave. This also implies that plasmons cannot be excited by sending a light wave directly onto a metallic film. Indeed, there is no coupling between this incident wave and the plasmons unless the components of the wave vectors of these two entities are equal. The generation of plasmons by coupling with an incident light wave thus requires the components of the wave vector of the light wave which are parallel to the surface of the metallic film to be increased.

As shown in Figure 4.2(a), the first possibility consists of illuminating the metallic film with an evanescent wave generated by a total reflection in a high index prism (Kretschman–Raether or Otto configuration). The second possibility, described in Figure 4.2(b), consists of adding a diffractive element in the system (a grating or sub-wavelength aperture) such that:

$$k_{//incident} + / - k_{//element} = k_{sp} \qquad [4.5]$$

where k//incident is the in-plane projection of the incident wave vector and k//element is the in-plane wave vector generated by the diffractive element.

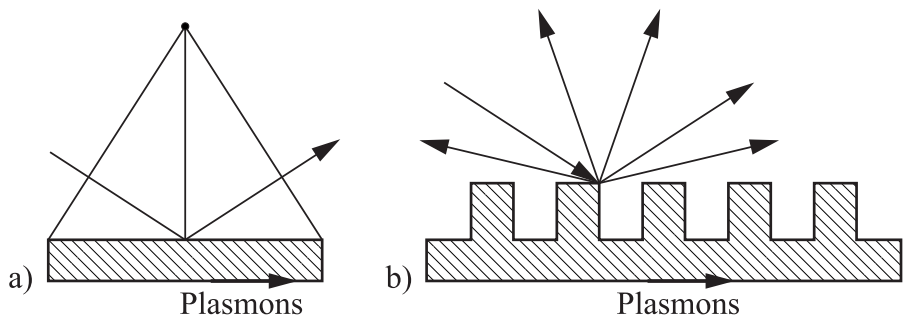

Figure 4.2. *Diagrams of different systems achieving surface plasmon excitation: (a) illumination of a metallic film by an evanescent wave obtained by total reflection on a high index prism; (b) addition of a diffractive element (here a grating) allowing the component of the wave vector parallel to the surface of the metallic film to be increased*

In each case, the properties of the achieved devices (materials, geometries) are highly dependent on the plasmon mode considered, that is to say the index of the metal and the dielectric at the illumination wavelength.

4.2.2.3. *Attenuation distances*

Determining the wave vector of the plasmons with dispersion equation [4.3] also gives access to other plasmon properties, amongst which is their propagating distances in different directions. Indeed, along the metal–dielectric interface, the propagation distance of the plasmons is given by $1/2k''_{sp}$, where:

$$k''_{sp} = k_0 \left(\frac{\varepsilon_m(\omega)\varepsilon_d}{\varepsilon_m(\omega)+\varepsilon_d} \right)^{3/2} \frac{\varepsilon''_m(\omega)}{2(\varepsilon'_m(\omega))^2} \qquad [4.6]$$

Perpendicular to the interface, the attenuation distances of the plasmon correspond to the distance from the interface where the wave amplitude is divided by *e*. In the metal, this length is given by the expression:

$$d_{metal} = k_0 \left(\frac{\varepsilon'_m(\omega)+\varepsilon_d}{\varepsilon'_m(\omega)^2} \right)^{1/2} \qquad [4.7]$$

In the dielectric, the attenuation distance of the plasmon equals:

$$d_{diel} = k_0 \left(\frac{\varepsilon'_m(\omega)+\varepsilon_d}{\varepsilon'_d} \right)^{1/2} \qquad [4.8]$$

As for plasmon excitation in the visible spectrum at a silver–photosensitive resist interface, the order of magnitude of these propagation distances is around a few microns along the interface and several dozens of nanometers perpendicular to it. In section 4.4, we will see that the value of these parameters plays a crucial role in the design of some devices, as the scale of the lithographed structures directly depends on the "scope of action" of the plasmons considered.

4.2.3. *Localized surface plasmons*

4.2.3.1. *Definition*

The Fourier theory of diffraction [GOO 96] predicts that a wave is evanescent in a direction if the object has spatial frequencies greater than $2n/\lambda$ in the plane perpendicular to that direction. Therefore, the $k_{//}$ component of the wave vector in

the plane is great (greater than the total wave vector's module k) and is settled by the spatial frequencies. Thus, we have $k = k^2_{//} + k^2_{\perp}$ where $k_{//} > k$. The $k_{\perp}$ component of the wave vector perpendicular to the plane is therefore purely imaginary and the wave is evanescent along that direction. This reasoning can be generalized in 3D: if the object is confined in all directions (nanosphere, nanorod, etc.), it can be associated with a wave evanescent in all directions. This is the case for a metallic nano-object, of which surface plasmon is evanescent in all directions (unlike delocalized surface Plasmon – see section 4.2.2 – where k_{sp} has a non-zero real part). The object then forms an optical nanosource, and these are called localized surface plasmons.

4.2.3.2. *Plasmon resonance*

The electronic resonance of metallic bulk materials only depends on the physical properties of that material. In particular, the plasma frequency ω_p becomes:

$$\omega_p = \sqrt{ne^2 / \varepsilon_0 m^*} \qquad [4.9]$$

where n is the charge density, ε_0 the vacuum permittivity and m^* the effective electron mass. Unlike bulk materials, metallic nanoparticles show plasmon resonances that not only depend on the material under consideration but also on the geometry and the environment of the particles. For simple geometries (spheroids, oblate spheroids, prolate spheroids), the plasmonic properties of the nanoparticles can be described by analytical models issued from Mie theory [VAN 81]. For example, the polarizability α of a spheroid has the following form [BOH 83], which perfectly illustrates the dependence on geometry and environment:

$$\alpha(\omega)_i = \varepsilon_0 V \left(\frac{\varepsilon_m(\omega) - \varepsilon_d}{\varepsilon_d + (\varepsilon_m(\omega) - \varepsilon_d) L_i} \right) \qquad [4.10]$$

where $\varepsilon_m(\omega)$ and ε_d represent the dielectric constant of the nanoparticles and the surrounding medium. V is the particle's volume and L_i is a geometrical parameter associated with the space direction i ($i = x$, y or z). For example, for a sphere, $L_x = L_y = L_z = 1/3$.

The resonance of the particle thus corresponds to a minimization of the denominator of expression [4.10] and results in a local field enhancement (compared to the incident field) that can be used for a high-resolution optical lithography, as studied later in this chapter.

The resonance plasmon modes of a nanoparticle are discrete and their number depends on the particle's geometry. For instance, a stretched out spheroidal gold nano-rod shows two dipolar plasmon modes: one along the short axis, close to that of a sphere of the same diameter, and one along the long axis, shifted towards red by the coherence loss effects of the plasmons, which induce attenuation [MUL 06].

When a particle has a more complex geometry, the analytical description then becomes difficult and numerical models are therefore preferred for predicting the optical properties of the particles. An example of a calculation is given in Figure 4.3 which shows the intensity distribution around a 27 nm wide silver nanotriangle, illuminated at two wavelengths: 600 nm (Figure 4.3(a)) and 385 nm (Figure 4.3(b)).

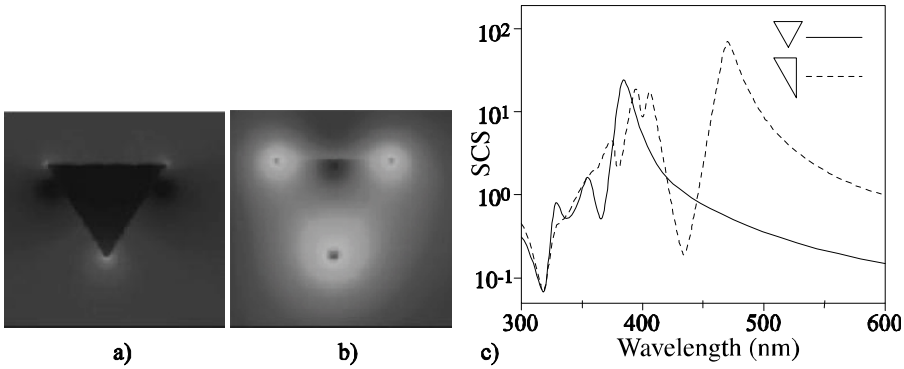

Figure 4.3. *Example of complex metallic structures (silver triangles) showing a main plasmon resonance in blue (numerical analysis). (a) Intensity mapping of the near-field with an illumination at λ = 600 nm (out of resonance); (b) intensity mapping of the near-field with an illumination at λ = 385 nm (resonance); (c) resonance plot for two types of triangles with different shapes (SCS: scattering cross section). Taken from [KOT 01]*

In this second case, the plasmon resonance is excited and the optical field is locally amplified. Figure 4.3(c) also shows the resonance curves obtained for two different nanotriangle shapes. The spectrum variations observed here illustrate well the influence of the particles' geometry on the resonance properties.

.In Figures 4.3(a) and 4.3(b), it is also interesting to notice that the field is confined at the triangle's corners. This effect is not a resonance effect (it occurs for both considered wavelengths) but corresponds to the excitation of an electromagnetic singularity [VAN 95]. This effect is comparable to edge effects, well-known in electrostatics where a field is greatest at the small radius of curvature

of an isopotential metallic surface. The use of this effect in electromagnetism and in near-field optics in particular has aroused growing interest over the last 15 years, as it can excite an optical nanosource without having to satisfy electronic resonance conditions, by exploiting the field component perpendicular to the metallic surface. Indeed, this component shows a discontinuity: it equals zero inside the metal but it can be very high at the surface, as a function of the surface density of charge. This also makes this effect very dependent on polarization: for a tip of small radius of curvature at its end, the optical edge effect can only be efficiently excited if the incident electromagnetic field has a component along the tip's axis (see Figure 4.4).

As will be studied in section 4.3, the local optical sources shown in Figures 4.3 and 4.4 were successfully used to implement near-field nanophotolithography.

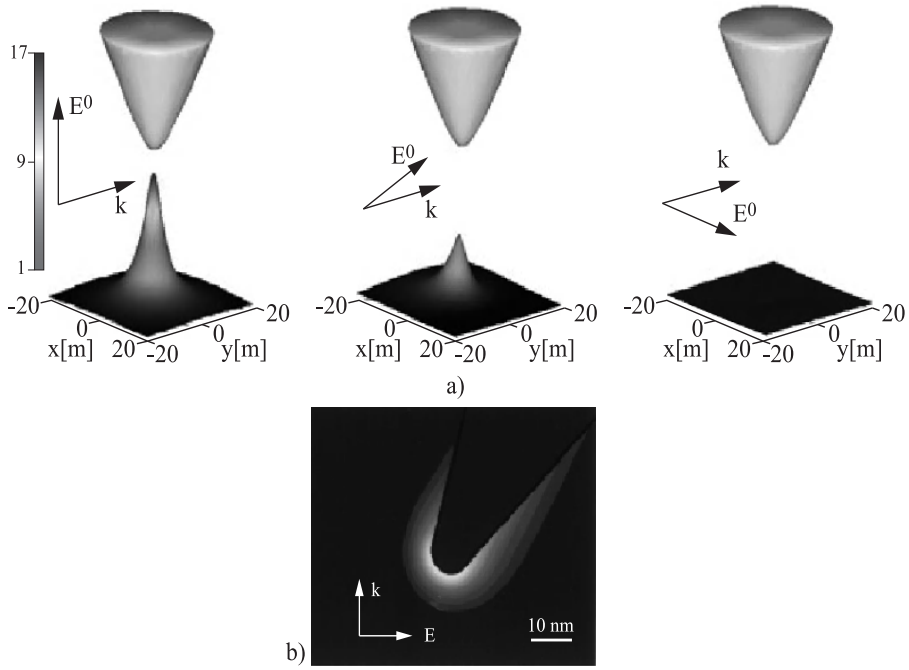

Figure 4.4. *Illustration of the optical edge effect and its dependence on polarization. (a) End of a tungsten tip, with intensity distribution under the tip as a function of the polarization of a grazing incident wave [KOT 01]; (b) intensity distribution at the end of a gold tip out of plasmon resonance [SAN 99]*

4.2.4. *Application to lithography*

The surface plasmon lithography technique consists of using the plasmon field to insulate a photosensitive resist layer. As previously indicated, this technique, based on the use of surface waves, is a near-field type technique, which means that it requires a strong proximity between the structures producing the plasmons and the photosensitive resist layer. It also implies being capable of efficiently exciting the plasmons at a metal–photosensitive resist interface at wavelengths that correspond to the sensitivity range of these polymers.

The application of plasmons to lithography is therefore possible under the following conditions:

– by maintaining close contact (distances typically inferior to 10 nm) between the structures that generate the plasmons and the photosensitive resist layer, the environment being under vacuum, with the application of strong pressure on both elements, with resist deposition directly onto the nanostructures, distance control by regulation techniques, and with the use of a spacer, etc.;

– by excitation of the plasmons in the UV or visible light range. This condition, added to a high refraction index for the photosensitive resists, considerably narrows the range of usable metals as well as the excitation mode. In visible light, the best metal is silver but the strong reactivity of this material with air makes gold another good candidate. Aluminum, on the other hand, is one of the only metals that has plasmon resonance at UV wavelengths currently used in standard optical lithography (193 nm). As for plasmon excitation, the index of refraction of the photosensitive resist layer of about 1.7 often makes it hard to find prisms with a high enough index for excitation with an evanescent wave. Most of the time, the excitation is performed with the help of intermediate diffractive elements, such as gratings or sub-wavelength apertures.

4.3. Localized plasmon optical lithography

Many experiments have shown that is possible to use localized surface plasmons (resonant or not) for controlled matter nanophotostructuring. A quite detailed description of these experiments was produced by Bachelot [BAC 07]. Some relevant examples are presented here, showing that this approach not only enables nanophotostructuring of different types of materials but also enables us to improve our knowledge of optical nanosources and the optical response of matter at a molecular level.

4.3.1. *Near-field optical lithography by optical edge effect*

4.3.1.1. *Polymer nanophotostructuring*

Figures 4.5(a) and 4.5(b) show examples of positive (photo-degradable) or negative (photo-polymerizable) photosensitive polymer nanophotostructuring. These were achieved by scanning different photosensitive resists with a metallic tip illuminated with *p*-polarized visible light (polarization in the incidence plane, as in the left example in Figure 4.4(a)). In Figure 4.5(a), this metallic tip was placed at the center of a Gaussian beam strongly focused by an immersion objective (numerical aperture greater than 1). For such strong focuses, some longitudinal components can appear in the focal plane (here the plane of the positive resist), which promotes the excitation of an electromagnetic singularity. Figure 4.5(a) is an atomic force microscope (AFM) image, performed after scanning the sample with the irradiated tip and developing the resist. Despite quite a modest pattern resolution (~ 200 nm), an interesting observation was made: the incident intensity and the exposure time were such that the incident dose (expressed in surface energy density) was under the photolysis threshold of the material. Only local stimulation under the tip made it possible to go below this threshold, to locally trigger a photochemical process and thus to fabricate patterns by scanning without being sensitive to far-field "background noise". Figure 4.5(b) also shows the result of an experiment carried out under similar conditions to Figure 4.5(a), but on a negative resist. A two-photon controlled photo-polymerization at a $\lambda/10$ scale is demonstrated here..

Figure 4.5(c) shows localized surface plasmon nanophotolithography results obtained on an alternative photosensitive resist particularly well-suited for the use of evanescent optical nanosources. It is made of azobenzene molecules of chemical formula [4-(N-(2-hydroxyethyl)-N-ethyl-) amino-4'-nitroazobenzene] grafted (i.e. linked by covalent bonds) onto a PMMA matrix (poly-methyl-methacrylate). It is usually called "PMMA-DR1" (DR1= *dispersed red one*, in reference to its red color).

PMMA-DR1 has many assets in the context of nanophotolithography: sensitivity toward visible light (absorption spectrum centered around 500 nm); flexibility of use (PMMA is a standard resist in electron beam lithography); and self-development properties. Indeed, under the action of light, this material spontaneously develops a surface topography, directly related to the spatial intensity distribution of the actinic light, which is easily observable, for example, by atomic force microscopy. This topography, which is strongest when the intensity of the actinic light is great, is due to the migration of DR1 azobenzene in the presence of a light wave. This process, which also depends on polarization [GIL 06], has been interpreted as a consequence of a sequence of isomerization cycles of the azobenzene molecules, associated with the seeking of a maximum energy state [NAT 02], thus leading to an optical self-assembly of these molecules.

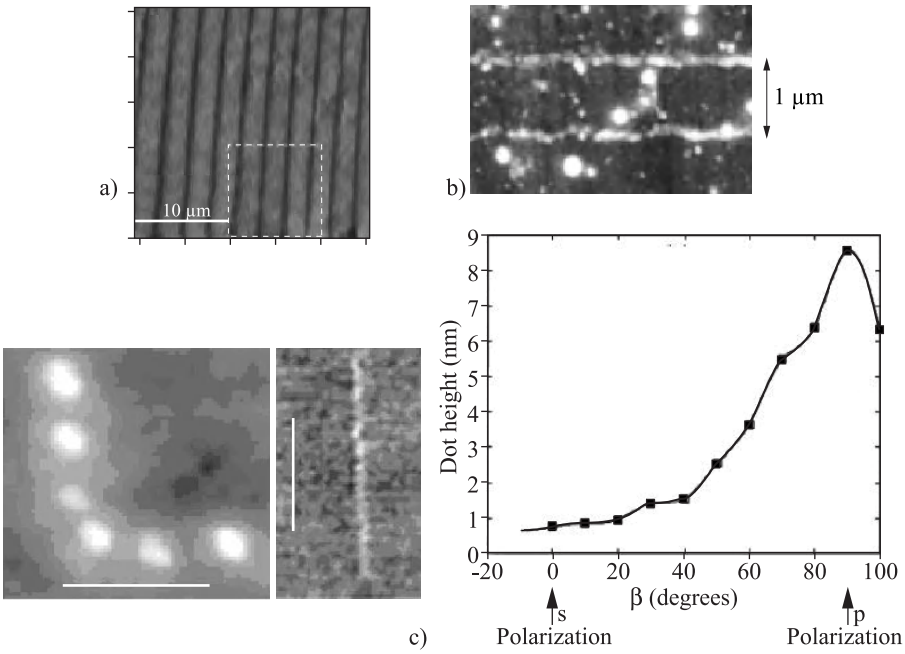

Figure 4.5. *Nanophotolithography on photopolymers. AFM images obtained after illumination of a metallic tip scanning over a resist: (a) positive [TAR 02]; (b) negative [YIN 02]; or (c) self-developing: PMMA-DR1 [BAC 03]. For this last example, the white bars represent the wavelength of the incident light, 514 nm. The right curve also shows the height of the PMMA-DR1 dot obtained as function of the polarization angle of the incident laser beam*

Figure 4.5(c) shows some results of the nanostructuring of a PMMA-DR1 surface under a metallic tip illuminated in *p*-polarization. The two figures on the left show a photolithography with a resolution of about twenty nanometers (λ/25). The figure on the right gives a measurement of the height of the dot obtained as a function of the angle of polarization. This height is maximal for a *p*-polarization, which confirms the importance of polarization in the excitation of optical edge effects and the fact that these effects are greatest when the incident polarization is in the optical axis of the metallic tip.

4.3.1.2. *Structuring of inorganic layers*

Many other types of materials can be nanostructured by near-field optical techniques [ROY 04], which demonstrates the richness of this domain and in particular the possibilities for studying and considering mastering the surface

physico-chemistry of metallic tips. As an example, the enhanced optical field at the end of scanning tunneling microscopy (STM) metallic tips has been used for nanostructuring gold surfaces (Figure 4.6). A remarkable resolution of 10 nm has been achieved by illuminating the tips in *p*-polarization with 5 ns pulses at a 532 nm wavelength. In addition, several interesting observations have been made:

– when using silver-coated tungsten tips, it is first observed that islands appear (Figure 4.6(a)). This effect has been interpreted as the consequence of the plasmon resonance of silver aggregates at the end of the tip, inducing heat, partial fusion and re-deposition on the surface. As a result, this is a controlled and photo-assisted deposition of metallic aggregates;

– by contrast, when bare tungsten tips are used, scanning the surface leads to the formation of furrows (Figure 4.6(b)). This second phenomenon is the result of a repulsive interaction between two dipoles: one being of the light-generated tip and the other being of the grains of gold on the surface, leading to the displacement of the gold atoms under the tip.

This nanophotolithography process (which was also demonstrated with silicon tips: Figure 4.6(c)) also gives rise to interesting discussions and studies. In particular, local photothermal effects (heating of the tip up to 850°C and consequent expansion of more than 5 nm) were put forward to explain the processes involved [HUA 02]. This temperature increase related to plasmon surface excitation is also at the heart of new photothermal plasmonic lithographies, based on the local thermal modification of polymers. This type of effect is usually obtained by heating an atomic force microscope tip with an electric current [HUA 07]. However, a theoretical plasmonic lithography model based on the heating (at more than 430 K) of gold particles excited at their plasmon resonance by a pulsed beam was recently proposed, the main challenge of this approach being how to achieve a high spatial resolution by minimization of heat diffusion [COR 07].

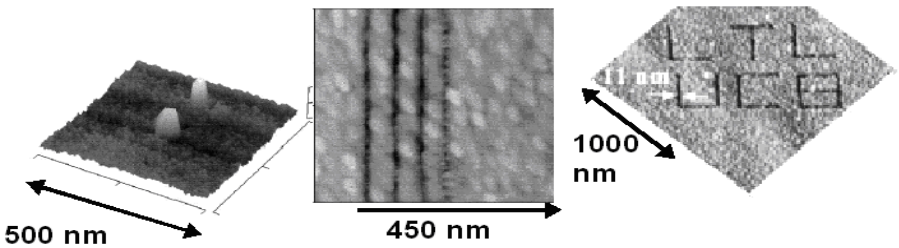

(a) b) (c)

Figure 4.6. *Nanophotostructuring of metallic layers (gold layers): (a) with a silver tip; (b) with a tungsten tip; (c) with a silicon tip. From [DIC 97] and [CHI 05]*

To conclude, one last very promising approach can be cited, despite the few concrete studies engaged on the subject. It consists of using near-field optical lithography with a metallic tip in order to locally photo-oxidize a semiconductor surface, previously hydrogen-passivated: in this situation, the enhanced local field induces desorption of the hydrogen atoms, leading to a local oxidation of the material's surface [LU 99]. This last example illustrates the possibility of structuring a silicon surface directly, without using any photosensitive polymer.

4.3.2. *Use of nanoparticle resonances*

Figures 4.7(a) and 4.7(b) show examples of lithography results obtained at the proximity of resonant metal nanoparticles.

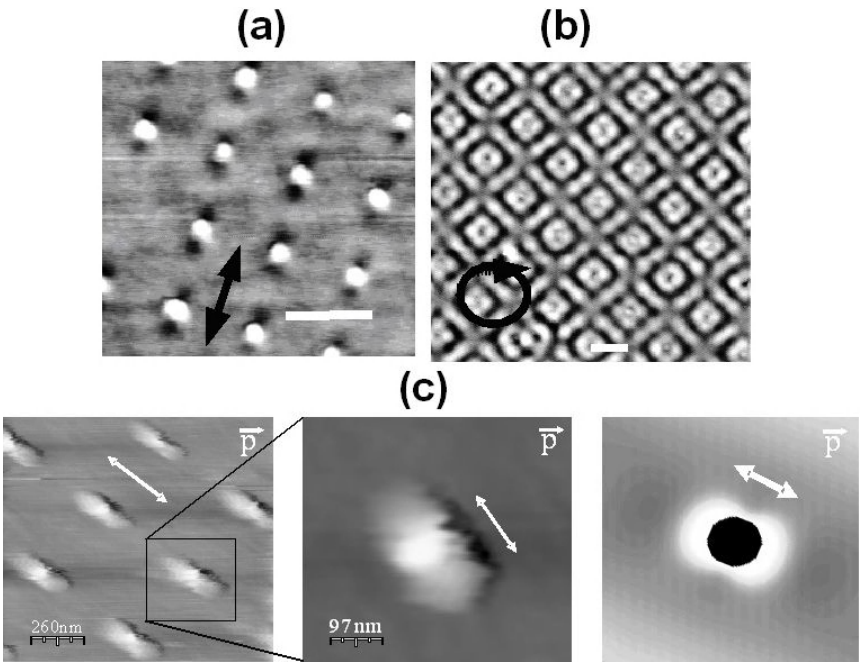

Figure 4.7. *Localized surface plasmon optical lithography (AFM images after exposure). PMMA-DR1 deposited on silver particles illuminated with linear (a) or circular (b) polarization [HUB 05]. The white bar represents the wavelength of the incident light (514 nm). (c) Nanophoto-polymerization of a negative resist near silver nanostructures excited at their dipolar plasmon resonance. The theoretical light intensity distribution is shown on the right [IBN 07]*

In Figure 4.7 a PMMA-DR1 layer was directly deposited on silver nanostructures and the result was characterized by AFM after exposure at a 514 nm wavelength, with an incident field of different polarization states and directions (represented by the black arrows). The white bar represents a distance equal to the light's wavelength.

Thanks to these images, it is possible to see how the optical near-field of such nanofeatures can structure matter at a scale much smaller than the wavelength, thus overcoming the $\lambda/2n$ limit imposed by the diffraction of light. In particular, these observations bring to light the dipolar plasmon resonance of silver nanoparticles (Figure 4.7(a)) and the optical self-assembly of the azobenzene molecules from the PMMA-DR1 in the near-field of a square array of particles illuminated in a circular polarization (Figure 4.7(b)).

However, it should be underlined that any interpretation of these images has to take into account the migration process of these molecules under an electromagnetic field, and in particular their sensitivity to polarization (see section 4.3.1).

Figure 4.7(c) shows that it is also possible to perform nanophotopolymerization near metallic nanoparticles excited at their plasmon resonance, which allows their optical properties to be controlled by nanophotostructuring their direct environment. Silver nanoparticles were here coated with a radical photopolymerizable formulation. The system was illuminated in normal incidence by a 514 nm wavelength close to the dipolar plasmon resonance of the particles and located in the absorption spectrum of the photochemical system. After rinsing, AFM imaging reveals an anisotropic photopolymerization, corresponding to a 3D molding of the field distribution associated with the dipolar plasmon resonance of the particle (the calculated field intensity is shown on the right of the image).

In the near-field, this dipole is oriented along the incident polarization (whereas its radiation diagram in far-field is perpendicular to the incident field). The hybrid metal–polymer particles thus obtained show specific optical properties. It was indeed demonstrated that an index nano-ellipsoid has been fabricated around the particles, introducing a new lower degree of symmetry and inducing spectrum energy level splitting of the particles. In particular, the extinction spectrum of the particles (and consequently their color) became dependent on the incident polarization [IBN 07]. This type of hybrid nanoparticles could represent a new generation of artificial materials, the color of which varies as a function of the incident polarization. These examples illustrate how, through near-field photolithography, studying and characterizing local optical fields and manipulating matter at a molecular scale can be done simultaneously.

Polarization dependence is a specific feature of plasmonic lithography, which enables a great flexibility of use and can be exploited in a new conception of lithography. As an example, Figure 4.8 shows a recent programmable nanophotolithography set-up [KOE 07]. This method consists of addressing the metallic particles of an array in a controlled manner by selectively exciting them thanks to the tuning of simple parameters related to the incident field (direction of the incident wave vector, polarization state). This approach consists mainly of locally controlling the interferences (thus the phase) in order to make certain particles bright and certain others dark. The numerical analyses of Figure 4.8 indicate that a sole square array of silver particles illuminated with a polarized plane wave can enable a great number of nanometric lighting combinations, just by modifying the wave vector and the direction of the incident polarization.

Eventually, this device could enable various patterns to be sequentially photo-fabricated, by placing a photosensitive resist layer in contact with the array.

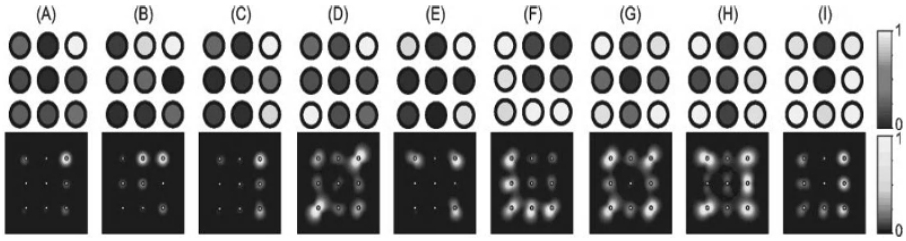

Figure 4.8. *Programmable plasmonic lithography. Different combinations of silver particles are excited by changing the propagation and polarization directions of an incident plane wave. Top row: particles addressed. Bottom row: calculation of the corresponding intensity distribution of light [KOE 07]*

4.4. Delocalized surface plasmon optical lithography

Two types of approaches were initiated during the use of delocalized plasmons for optical lithography. The first consists of coupling these plasmons with metallic nanostructures present on a mask, so that its sub-wavelength patterns are duplicated in the photosensitive resist layer. The second uses these nanostructures to generate counter-propagative surface plasmons. In this case, the patterns printed correspond to the interference fields resulting from the propagation and the superimposition of the different excited plasmons.

4.4.1. *Coupling between nanostructures and delocalized surface plasmons*

It has been mentioned that the near-field characteristic of plasmons makes these waves insensitive to the Rayleigh diffraction limit. The aim of this first approach is to put this property to good use in order to efficiently transfer sub-wavelength patterns present on a mask in a photosensitive resist layer. The technique consists of making a metallic mask that contains the nanostructures to be printed and to illuminate it so that plasmons are excited. In this configuration, the resolution achieved in the resist depends mainly on the size of the nanostructures present on the mask.

Many masks can be used, according to the patterns to be lithographed and on the illumination wavelength. For instance, a gold mask containing a single dot illuminated with visible light enables an isolated hole to be made [MAR 03]. This same pattern can also be achieved well below sub-wavelength dimensions by illumination with UV in an aluminum film that has an optimized bowtie-shaped nano-aperture [WAN 06].

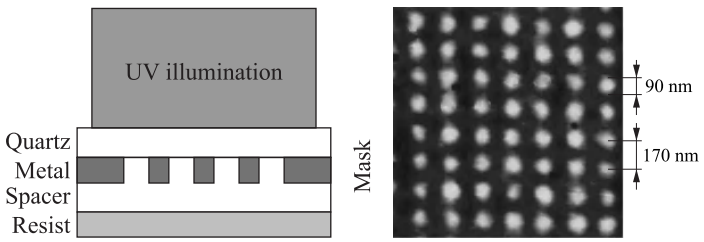

Figure 4.9. *Example of a plasmonic lithography device [SRI 04]. Right: AFM image of the patterns printed into a photosensitive resist layer. The initial mask pattern is an array of 40 nm diameter and 170 nm-period holes*

Figure 4.9 shows some results obtained from a perforated aluminum layer [SRI 04]. In this case, thanks to the extraordinary transmission phenomenon of this structure [EBB 98], UV illumination of an array of holes of sub-wavelength dimensions makes it possible to transfer an array of dots of the same step size in the resist layer. The efficiency of this type of system can also be improved by the addition of a metallic layer between the substrate and the photosensitive resist layer [SHA 05]. Indeed, this layer allows an additional excitation of plasmons on the substrate, the coupling between these surface plasmons and the mask leads to an increase of the total intensity as well as the confinement of the field in the photosensitive resist layer.

4.4.2. *Surface plasmon launch and interferences*

It was mentioned in section 4.2.2 (in particular, thanks to the plotting of the dispersion relation in Figure 4.1) that plasmons have an effective wavelength λ_{sp} smaller than that of the incident light by which they are excited. This second approach of plasmonic lithography uses this property in order to increase the potential resolution of the patterns printed in the photosensitive resist layer.

The principle consists of making a nanostructured metallic mask, the illumination of which will induce the excitation of counter-propagative plasmons. In this set-up, the patterns printed in the photosensitive resist layer correspond to the interference pattern that results from the propagation and the superimposition of those plasmons. The resolution achieved is set by the period of the fringes generated, which depends on the effective wavelength of the excited plasmons; the maximum dimensions of the insulated area are given by the propagation distances of the plasmons considered (see equations [4.6] to [4.8]).

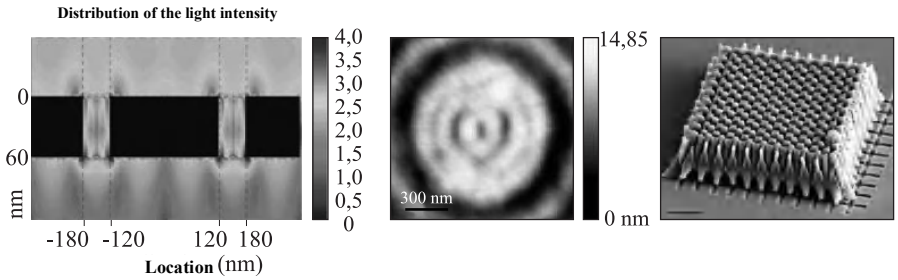

Figure 4.10. *Examples of optical lithography based on surface plasmon interference. Left: FDTD simulation of a field at the exit of a metallic slit grating [LUO 04]; middle: AFM image of a pattern printed at the center of a circular excitation grating [DER 07]; right: SEM image of a 3D pattern achieved from a mask made out of two gratings. The black bar = 2 µm [SHA 06]*

One of the major challenges of this technique is the conception of a mask that enables the generation of the desired interference field. For example, a grating of sub-wavelength slits induces the excitation of two counter-propagative plasmon waves, of which the interference between each slit leads to the printing of lines in the photosensitive resist [LUO 04]. Even more complex patterns such as dots or rings can also be achieved by using several separate excitation gratings with different orientations [DER 07, LIU 05]. Figure 4.10 shows some of the results obtained for each of these configurations. In particular, Figure 4.10 (right) shows

that this technique can also be adapted for printing 3D patterns when the interference field generated spreads intensely enough in the three directions of space [SHA 06].

4.5. Conclusions, discussions and perspectives

Through many examples, we have seen that, thanks to surface plasmons, it is possible to photostructure matter at a nanometric scale without being limited by light's wavelength. On these scales, the interaction process between light and matter are numerous and often imply local thermal effects.

This very recent field of research (most references quoted in this chapter are less than ten years' old) has also allowed the knowledge of materials and the implementing of high-performance optical plasmonic nanosources to be considerably improved. Reciprocally, the rapid progress of nano-optics has enabled nanosources suited for nanophotolithography to be developed. However, the objectives of near-field plasmonic nanophotolithography should not be seen as competing with those defined in the International Technology Roadmap for Semiconductors [ITR], which has preferred wavelength reduction up until now. This is more a complementary approach, appreciated for its low cost and ease of implementation, in particular thanks to the use of visible light and the control of its polarization state. In addition, the targeted applications go far beyond the domain of microelectronics, since they also concern high-density optical storage and manipulation of molecules. Plasmonic lithography could also be used as a link in a complex nanostructuring chain. For example, the mold, or "template" used in NanoImprint lithography could be fabricated with a near-field optical lithography technique.

Nonetheless, one of the handicaps of this technique remains the near-field and the necessity of a close proximity between the mask and the substrate to be insulated. The choice of photosensitive resist is also critical, as it must allow the resolution provided by the plasmons. Furthermore, the integration and the development of plasmonic lithography in the current fields are still conditioned by the solving of the various contamination issues for tools as well as for the photosensitive resist, induced by the metals present on the masks.

Furthermore, the performances of surface plasmon-assisted lithography will be improved by the addition of new concepts in the existing techniques, making the future of this method undoubtedly promising. As for the "tip" approach, it is known that the simultaneous work of hundreds of matrix-arranged tips can be controlled [DES 07], which makes the concept of high-density fast multi-tip optical storage credible. As for the "mask" approach, controlling the distance between the mask and

the photosensitive material will soon allow the inclusion of the concept of a "superlens", which consists of performing sub-wavelength imagery via a stack achieving a negative refraction [PEN 00]. However, the addition of this type of stack into lithography devices will allow sub-wavelength patterns to be transferred in a photosensitive resist layer [FAN 05] and, on the other hand, project the image far from the mask, which should limit the contamination issues of the mask and the photosensitive material.

Finally, this approach to lithography will undoubtedly benefit from new physical effects associated with metallic nanostructures, which are currently the subject of intense research. These effects include second-harmonic generation [HUB 07], photoluminescence [BOU 05], strong near-field coupling [ATA 04] and multipolar resonance excitation [KRE 00]. These effects will allow a better resolution, and a better control of the intensity and the wavelength of nanosources in relation to photosensitive materials.

4.6. Bibliography

[ATA 04] ATAY T., SONG J.H., NURMIKKO A.V., "Strongly Interacting Plasmon Nanoparticle Pairs: From Dipole-Dipole Interaction to Conductively Coupled Regime", *Nano Lett.*, 4, 1627–1631, 2004.

[BAC 03] BACHELOT R., H'DHILI F., BARCHIESI D., LERONDEL G., FIKRI R., ROYER P., LANDRAUD N., PERETTI J., CHAPUT F., LAMPEL G., BOILOT J.-P., LAHLIL K., "Apertureless near-field optical microscopy: A study of the local tip field enhancement using photosensitive azobenzene-containing films", *J. Appl. Phys.*, 94, 2060–2072, 2003.

[BAC 07] BACHELOT R., "Near-field optical structuring and manipulation based on local field enhancement in the vicinity of metal nanostructures", Chapter 7 in S. KAWATA, V.M. SHALAEV (eds), *Tip Enhancement Advances in Nano-Optics and Nano-Photonics*, Elsevier, Amsterdam, 2007.

[BET 44] BETHE H.A., "Theory of diffraction by small holes", *Phys. Rev.*, 66, 163–182, 1944.

[BOH 83] BOHREN C.F., HOFFMANN D.R., *Absorption and Scattering of Light by Small Particles*, Wiley, New York, 1983.

[BOU 50] BOUWKAMP C.J., "On the diffraction of electromagnetic waves by small circular disks and holes", *Philips Res. Rep.*, 5, p. 401–422, 1950.

[BOU 05] BOUHELIER A., BACHELOT R., LERONDEL G., KOSTCHEEV S., ROYER P., WIEDERRECHT G.P., "Surface plasmon characteristics of tunable photoluminescence in single gold nanorods", *Phys. Rev. Lett.*, 95, 1–4, 2005.

[CHI 05] CHIMMALGI A., GRIGOROPOULOS C. P., KOMVOPOULOS K., "Surface nanostructuring by nano-/femtosecond laser assisted scanning force microscopy", *J. Appl. Phys.*, 97, p. 104319-1-12, 2005.

[COR 07] CORTIE M.B., HARRIS N, FORD M.J., "Plasmonic heating and its possible exploitation in nanolithography", *Physica B: Condensed Matter*, 394, p. 188–192, 2007.

[COU 01] COURJON D., BAINIER C., *Le champ proche optique*, *Théorie et applications*, Springer, Berlin, 2001.

[DER 07] DEROUARD M., HAZART J., LÉRONDEL G., BACHELOT R., ADAM P.M., ROYER P., "Polarization-sensitive printing of surface plasmon interferences", *Opt. Expr.*, 15, p. 4238–4246, 2007.

[DES 07] DESPONT M., "Millipede probe-based storage", *SPIE advanced lithography*, IBM Corp., Feb. 25th.–March 2nd 2007.

[DIC 97] DICKMANN K., JERSH J., DEMMING F., "Focusing of laser radiation in nanostructures", *Surface and Interface Analysis*, 25, p. 500–504, 1997.

[EBB 98] EBBESEN T.W., LEZEC H.J., GHAEMI H.F., THIO T., WOLFF P.A., "Extraordinary optical transmission through sub-wavelength hole arrays", *Nature*, 391, p. 667–669, 1998.

[FAN 05] FANG N., LEE H., SUN C., ZHANG X., "Sub-diffraction-limited optical imaging with a silver superlens", *Science*, 308, p. 534–537, 2005.

[GIL 06] GILBERT Y., BACHELOT R., ROYER P., BOUHELIER A., WIEDERRECHT G.P., NOVOTNY L., "Longitudinal anisotropy of the photoinduced molecular migration in azobenzene polymer films", *Opt. Lett.*, 31, p. 613–615, 2006.

[GOO 96] GOODMAN J., *Introduction to Fourier Optics*, McGraw-Hill, New York, 2nd edition, 1996.

[HUA 02] HUANG S.M., HONG M.H., LU Y.F., LUKYANCHUK B.S., SONG W.D., CHONG T.C., "Pulsed-laser assisted nanopatterning of metallic layers combined with atomic force microscopy", *J. Appl. Phys.*, 91, p. 3268–3274, 2002.

[HUA 07] HUA Y., SAXENA S., HENDERSON C.L., KING W.P., "Nanoscale thermal lithography by local polymer decomposition using a heated atomic force microscope cantilever tip", *Journal of Micro/Nanolithography*, *MEMS and MOEMS*, 6, p. 023012–023017, 2007.

[HUB 05] HUBERT C., RUMYANTSEVA A., LÉRONDEL G., GRAND J., KOSTCHEEV S., BILLOT L., VIAL A., BACHELOT R., ROYER P., CHANG S.-H., GRAY S.K., WIEDERRECHT G.P., SCHATZ G.C., "Near-field photochemical imaging of noble metal nanostructures", *Nano Letters*, 5, p. 615–619, 2005.

[HUB 07] HUBERT C., BILLOT L., ADAM P.-M., BACHELOT R., ROYER, P., GRAND J., GINDRE D., DORKENOO K.D., FORT A., "Role of surface plasmon in second harmonic generation from gold nanorods", *Appl. Phys. Lett.*, 90, p. 181105–07, 2007.

[IBN 07] IBN EL AHRACH H., BACHELOT R., VIAL A., LÉRONDEL G., PLAIN J., ROYER P., SOPPERA O., "Spectral degeneracy breaking of the plasmon resonance of single metal nanoparticles by nanoscale near-field photopolymerization", *Phys. Rev. Lett.*, 98, p. 107402-107405, 2007.

[ITR] International Technology Roadmap for Semiconductors (ITRS). www.itrs.net.

[KIT 96] KITTEL C., *Introduction to Solid States Physics*, John Wiley & Sons, New York, 7th edition, 1996.

[KOE 07] KOENDERINK A.F., HERNANDEZ J.V., ROBICHEAUX F., NOORDAM L. D., POLMAN A., "Programmable nanolithography with plasmon nanoparticles", *Nano Letters*, 7, p. 745–749, 2007.

[KOT 01] KOTTMANN J.P., MARTIN O.J.F., SMITH D.R., SHULTZ S., "Non-regularly shaped plasmon resonant nanoparticle as localized light source for near-field microscopy", *Microsc*., 202, 60–65, 2001.

[KRE 00] KRENN J.R., SCHIDER G., RECHBERGER W., LAMPRECHT B., LEITNER A., AUSSENEGG F.R., WEEBER J.C., "Design of multipolar plasmon excitations in silver nanoparticles", *Appl. Phys. Lett.*, 77, 3379–3381, 2000.

[LIN 06] LIN B.J., "The ending of optical lithography and the prospects of its successors", *Microelectron. Eng.*, 83, 604–613, 2006.

[LIU 05] LIU Z.W., WEI Q.H., ZHANG X., "Surface plasmon interference nanolithography", *Nano Lett.*, 5, 957–961, 2005.

[LU 99] LU Y.F, MAI Z.H., QIU G., CHIM W.K., "Laser-induced nano-oxidation on hydrogen-passivated Ge (100) surfaces under a scanning tunneling microscope tip", *Appl. Phys. Lett.*, 75, p. 2359–2361, 1999.

[LUO 04] LUO X., ISHIHARA T., "Surface plasmon resonant interference nanolithography technique", *Appl. Phys. Lett.*, 84, p. 4780–4782, 2004.

[MAR 03] MARTIN O.J.F., "Surface plasmon illumination scheme for contact lithography beyond the diffraction limit", *Microelectron. Eng.*, 67–68, p. 24–30, 2003.

[MUL 06] MULVANEY P., PEREZ-JUSTE J., GIERSIG L., LIZ-MARZAN L.M., PECHARROMAN C., "Drastic surface plasmon mode shifts in gold nanorods due to electron charging", *Plasmonics*, 1, p. 61–66, 2006.

[NAT 02] NATANSOHN A., ROCHON P., "Photo-induced motions in azo-containing polymers", *Chem. Rev.*, 102, 4139–4175, 2002.

[PEN 00] PENDRY J.B., "Negative refraction makes a perfect lens", *Phys. Rev. Lett.*, 85, p. 3966–3969, 2000.

[ROY 04] ROYER P., BARCHIESI D., LÉRONDEL G., BACHELOT R., "Near-field optical patterning and structuring based on local-field enhancement at the extremity of a metal tip", *Philos. Trans. R. Soc. Lond.*, series A, 362, p. 821–842, 2004.

[SAN 99] SÁNCHEZ E.J., NOVOTNY L., XIE X.S., "Near-field fluorescence microscopy based on two-photon excitation with metal tips", *Phys. Rev. Lett.*, 82, p. 4014–4017, 1999.

[SHA 05] SHAO D.B., CHEN S.C., "Surface-plasmon-assisted nanoscale photolithography by polarized light", *Appl. Phys. Lett.*, 86, p. 253107, 2005.

[SHA 06] SHAO D.B., CHEN S.C., "Direct patterning of three-dimensional periodic nanostructures by surface-plasmon-assisted nanolithography", *Nano Lett.*, 6, p. 2279–2283, 2006.

[SRI 04] SRITURAVANICH W., FANG N., SUN C., LUO Q., ZHANG X, "Plasmonic Nanolithography", *Nano Lett.*, 4, p. 1085–1088, 2004.

[TAR 02] TARUN A., DAZA M.R.H., HAYAZAWA N., INOUYE Y., KAWATA S., "Apertureless optical near-field fabrication using an atomic force microscope on photoresist", *Appl. Phys. Lett.*, 80, p. 3400–3402, 2002.

[TSE 07] TSENG A., "Recent developments in nanofabrication using scanning near-field optical microscope lithography", *Optics and Laser Technology*, 39, p. 514–526, 2007.

[VAN 81] VAN DE HULST H. C., *Light Scattering by Small Particles*, Dover, New York, 1981.

[VAN 95] VAN BLADEL J., *Singular Electromagnetic Field and Sources*, IEEE, Oxford, 1995.

[WAN 06] WANG L., UPPULURI S.M., JIN E.X., XU X., "Nanolithography using high transmission nanoscale bowtie apertures", *Nano. Lett.*, 6, p. 361–364, 2006.

[YIN 02] YIN X., FANG N., ZHANG X., MARTINI I. B., SCHWARTZ B. J., "Near-field two-photon nanolithography using an apertureless optical probe", *Appl. Phys. Lett.*, 81, p. 3663–3665, 2002.

Chapter 5

Patterning with Self-Assembling Block Copolymers

5.1. Block copolymers: a nano-lithography technique for tomorrow?

Since 1960, the microelectronics industry has witnessed enormous progress focused essentially on the development and application of Metal Oxide Semiconductor (MOS) transistor technologies. Indeed, whereas in 1962 the first integrated circuit included two transistors, today the most powerful microprocessors are composed of several tens of millions of MOS transistors per chip (e.g. 42 million for Intel's Pentium 4). This rapid expansion of microelectronics is driven by the perpetual requirement to manage and store larger quantities of data on increasingly smaller supports, with less energy consumption. This incessant reduction of device dimensions will soon reach the limits of conventional fabrication processes and traditional technologies, such as optical lithography and etching, and will probably not be able to create high density objects of a size c.18 nm, the length predicted for transistors in 2018 [ITR 01]. In this context, the use of block copolymer (BCP) thin films seems to be a powerful alternative for quite specific applications to overcome the intrinsic limitations of traditional lithographic techniques. This technology, based on the self-organization of polymeric chains similar to conventional polymer photoresist chains used in semiconductor fabrication, allows the realization of regular patterns whose dimensions cannot be achieved by optical lithography processes. After decades of being of only secondary importance, as reflected by an almost negligible number of publications on the subject, the capacity of BCPs to

---

Chapter written by Karim AISSOU, Martin KOGELSCHATZ, Claire AGRAFFEIL, Alina PASCALE and Thierry BARON.

self-assemble into periodic morphologies is likely to play a key role in nanotechnological applications in the future. The utilization of the BCP technique to obtain lithographic masks was first proposed in 1995 by Mansky [MAN 95], and appears today as one of the technological solutions to generate localized uniform objects with low dimension (~20 nm) and high density (~10^{11}/cm^2).

Block copolymers are a specific type of polymer and can be classified as soft matter. They are composed of at least two chemically different polymer fragments ("blocks") which are covalently linked. Generally, copolymers are flexible and can bend at monomer junctions, leading to a great architectural diversity, examples of which include linear copolymers, graft copolymers and star copolymers [OHT 86]. When only two subchains of different monomers, *A* and *B*, are bound covalently to each other, a diblock copolymer is formed. A simple linear *AB* diblock copolymer chain (called: PA-*b*-PB) is composed of fN polymer *A* segments and $(1-f)N$ polymer *B* segments, linked at one end together by a covalent bond, where N denotes the degree of polymerization and f the fraction of block *A* in the chain. The product χN controls the tendency of the *A* and *B* blocks to separate, where χ is the Flory-Huggins segmental interaction parameter. At sufficiently large values (i.e. $\chi N > 10.5$), the A and B blocks become immiscible and form periodically separated nanodomains [OHT 86]. Depending on the composition, f, diblock copolymers can organize into several equilibrium structures: lamellae, hexagonally ordered nanodomains, bicontinuous cubic gyroids, or a body-centered-cubic lattice of spheres (see Figure 5.1) [MAT 94]. The periodicity of these structures is determined by a competition between the interfacial tension and the entropic penalty for stretching different blocks in order to maintain a uniform segment density [MAT 96].

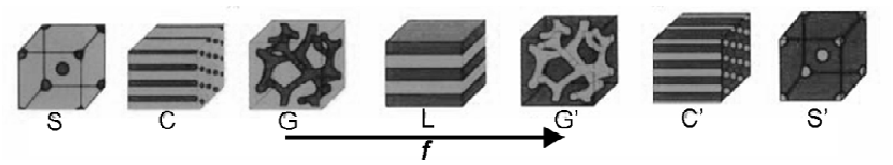

Figure 5.1. *Schematic representation of diblock copolymer phases as a function of f: (S) spherical; (C) cylindrical; (G) gyroid; (L) lamellar; (G') inverse-gyroid; (C') inverse-cylindrical; (S') inverse-spherical phases [LI 05]*

BCP thin films only allow two pattern geometries to be obtained which can be used as lithographic masks: line/space or circular nanodomain patterns. The gyroid structure (Figure 5.1) is not adapted for lithographic applications. In practical terms, block copolymer templates presenting a monolayer of cylindrical nanodomains which are parallel to the substrate, or a lamellar phase oriented perpendicularly to

the substrate, could be used to obtain masks allowing the transfer of striped line/space patterns. Alternatively, thin films presenting cylindrical nanodomains perpendicular to the substrate, or a monolayer of spherical nanodomains, can be used to fabricate circular nanopatterns.

Although only line/space or circular nanodomain patterns could be achieved by using BCP as a lithographic mask, this technique will be able, in the long run, to supplant conventional lithography for the realization of several technological applications, such as for:

– the realization of increasingly small Dynamic Random Access Memory (DRAM) cells presenting shallow trench array capacitors with a higher capacitance than planar capacitors with the same dimensions [BLA 04a],

– the elaboration of nanocrystal floating-gate memories which offer greater robustness than conventional Flash memory devices when dimensions are reduced, as imposed by the demand of an ever higher integration density [BLA 07].

The utilization of diblock copolymer masks could be interesting for other applications where dense patterns of discrete objects are needed. Examples include quantum dots or nanopillars [PAR 97, AIS 08], the fabrication of high density magnetic recording devices [CHE 01] and the fabrication of nanowires [THU 00a].

Unfortunately, the organization of patterns in BCP films is often accompanied by the presence of isolated defects or an array of defects which can be prejudicial to the applications cited above. Thus, block copolymer self-assembly and its defect formation and diffusion have to be understood and perfectly controlled.

5.2. Controlling self-assembled block copolymer films

Many thin film studies performed during the last years have focused on asymmetric diblock copolymers as nanolithographic templates. As already mentioned, two pattern types can be generated by a self-assembling diblock copolymer film: striped line/space patterns and circular patterns, depending on the morphology of the self-assembling BCP film. Below, we describe the formation of periodical circular patterns, knowing that striped line/space patterns globally present a similar behavior.

Remember that these circular 2D-periodic hexagonally organized patterns can be obtained either (1) from a monolayer film organized into close-packed spheres, or (2) from a thin film containing an array of cylindrical nanodomains oriented vertically to the substrate. Segalman *et al.* [SEG 03] studied the organization of films formed by a monolayer of spheres and found that hexagonal block copolymer

patterns consist of well-organized areas (grains) separated by boundaries (arrays of topological defects) and discrete defects. In these lattices, isolated defects are called "disclinations" or orientational defects since they affect the orientational 2D lattice order. If the defective nanodomain is pentacoordinated the defect is called "negative disclination", and it is called "positive disclination" if the nanodomain is heptacoordinated. If two disclinations of different sign are paired (7-5) a defect called a "dislocation" is formed.

These defects will now be illustrated using a hexagonal lattice obtained by using a thin diblock copolymer film composed of polystyrene (PS) and polymethylmethacrylate (PMMA), referred to as PS-*b*-PMMA. Figure 5.2(a) is a Scanning Electron Microscopy (SEM) image of a typical 2D hexagonally organized array of holes in a PS matrix that Aissou *et al*. [AIS 07a] obtained after annealing a PS-*b*-PMMA layer at 200°C under vacuum (10^{-2} mbar) for 72 h and removing the PMMA blocks using a deep UV light treatment. The porous PS template is composed of different grains whose nanodomains (dark on the image) are oriented vertically to the surface and have a diameter of about 20 nm and a periodicity of about 40 nm. Figure 5.2(b) shows the associated Delaunay triangulation of the SEM image presented in Figure 5.2(a).

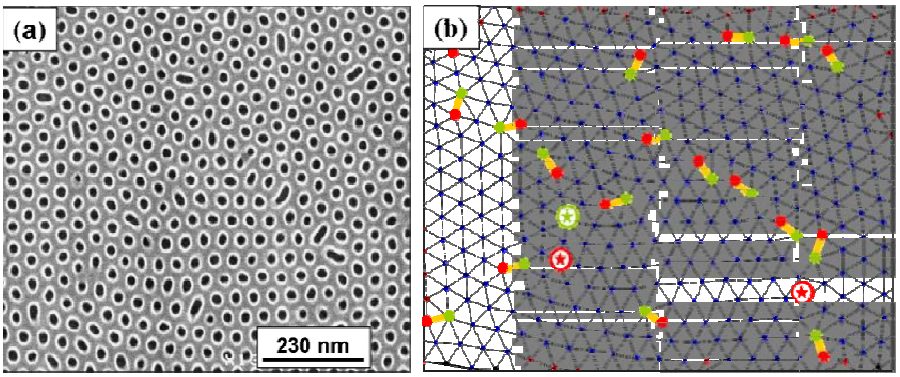

Figure 5.2. (*a) Typical SEM image of a porous PS film obtained after annealing at 200°C under vacuum for 72 h, and removal of PMMA cylinders. (b) The associated Delaunay triangulation of the porous PS film presented in (a). Cylinders with seven and five neighbors are indicated by light and dark grey dots, respectively. Dislocations formed by a pair of 5-7 disclinations are indicated by connecting bars. Disclinations consisting of a hepta- or pentacoordinated nanodomain are indicated by a light or dark grey encircled star, respectively. Reproduced and adapted with permission from Macramolecules [AIS 07a]*

In Figure 5.2(b), we can observe well-organized grains corresponding to regions where all cylinders are 6-fold coordinated; these grains are delimited by defects. Heptacoordinated and pentacoordinated nanodomains (light and dark grey dots,

respectively) correspond to defects which separate grains presenting an anisotropic shape and a specific orientation. Disclinations consisting of a penta- or heptacoordinated nanodomain are indicated by a dark or light grey encircled star, respectively (Figure 5.2(b)), and dislocations are indicated by a connecting bar. Vega *et al*. [VEG 05] noted that disclinations present in hexagonal patterns, correlate to high angle grain boundaries i.e. with an angle disorientation between two adjacent grains higher than 15°. Hammond *et al.* [HAM 03] studied topological defects in films forming cylindrical nanodomains oriented vertically to the surface, and their study revealed that the local stress field of the lattice influences the pore dimensions and that the mean nanodomain area varies as a function of the degree of coordination of the pore. In the PS-*b*-PMMA diblock copolymer case described above, a disparity of pore areas between 5-fold, 6-fold and 7-fold coordinated nanodomains was evidenced [AIS 07a], a disparity which is higher among the 7-fold sites than among the 5-fold or 6-fold sites. This strong variation is induced by a deformation of the unit cell (a pore plus its PS corona) from an isotropic shape to an anisotropic shape (see Figure 5.2(a)). This phenomenon induces a variation in the object dimensions fabricated with block copolymer patterns. An example is shown in Figure 5.6(b).

The presence of defects delimiting well-organized areas and the variation of the diameter of the nanodomains, attributed to a local constraint of the array [OHT 95], are prejudicial limitations for nanotechnological applications of these films. The nucleation-growth mechanism of macroscopic grains has been extensively debated over the last decade in order to improve the 2D order of the film [SEG 03, VEG 05, PIG 07, HAR 04]. Theoretical [YOK 02] and experimental [VEG 05, HAR 04, HAR 00] studies have focused on the evolution of these topological defects as a function of time, and have reported that the number of dislocations and disclinations decreases when the annealing time increases. In the case of lattices containing a monolayer of spheres, Vega *et al.* [VEG 05] concluded that this diminution is due either to a mechanism of grain rotation or to a mechanism of annihilation of low angle grain boundaries.

Agreeing with these models, Aissou *et al.* [AIS 07a] proposed a microscopic mechanism, which explains the diffusion of the dislocations during annealing for cylindrical nanodomains organized in a hexagonal lattice. This mechanism, which is based on the division of deformed heptacoordinated cylinders into two distinct cylinders, allows the displacement and the new orientation of the dislocations (which are at the origin of the reduction of the density of the topological defects) to be explained.

Even if the number of topological defects decreases during the annealing time and their disappearance allows a homogenization of the size of the nanodomains, the mechanisms at the origin of this diminution are generally slow. For example, an

annealing time of several weeks would theoretically be necessary to obtain a perfect organization of the domains on a surface of 1 cm^2. Although several methods, such as solvent annealing [KIM 04], allow a better organization of nanodomains to be obtained locally than by thermal annealing, so far only thermally processable materials have a good chance of becoming adopted technology.

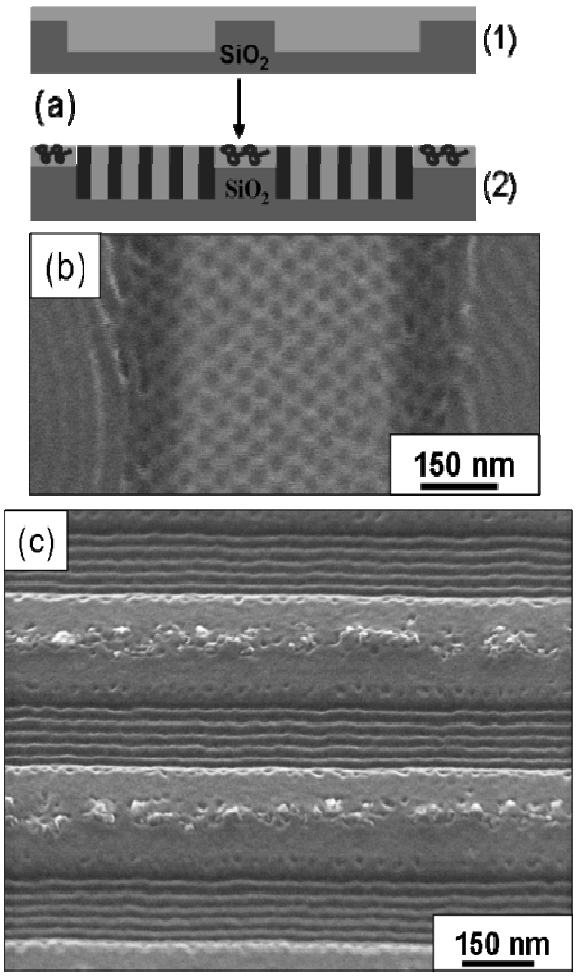

Figure 5.3. *(a) Schematic representation of a BCP thin film deposited on a patterned substrate: (a) before (1) and after (2) annealing; (b) Plan-view SEM images of a PS template presenting vertically oriented cylinders in a groove obtained after removal of the PMMA; (c) Plan-view SEM image of a PS template presenting horizontally oriented parallel cylinders in grooves obtained after removal of the PMMA*

In order to increase the kinetics of defect elimination, several studies have shown that partial or total confinement of the film would allow this problem to be solved. Among these techniques one can cite nanoimprint lithography [LI 04], surface nanopatterning by local chemical modification [STO 06, EDW 06] or graphoepitaxy [SEG 01, XIA 05] which consists of creating trenches in the substrate with conventional photolithography/etching processes. The idea of this last technique is that the confinement of the film in the trench induces a strong constraint on the nanodomains formed which are then forced to organize in an optimal way (without defects). It has been shown, in the case of spherical nanodomains, that they first form close to the sidewalls and then form inwards so that the film is well ordered across the width of the grooves and along their axes [CHE 02, CHE 06, SEG 03]. Graphoepitaxy has also been shown to be an effective strategy for ordering cylinder-forming block copolymers with domains oriented either perpendicular [XIA 05, LI 04] (e.g. Figure 5.3(b)) or parallel [SUN 04] (e.g. Figure 5.3(c)) to the substrate, and in geometries more complex than parallel grooves such as circles [BLA 04b] and bends [SUN 04].

These techniques allow an improvement in the order of the nanodomains formed in thin films which have to be integrated in fabrication processes for nanotechnological applications whose feasibility has already been demonstrated and which have the potential to be commercialized. It has already been demonstrated that diblock copolymer thin films organized using graphoepitaxy can be used for the fabrication of magnetic storage media [NAI 02, XIA 05] or nanowire field effect transistors (FETs) [BLA 05].

5.3. Technological applications of block copolymer films

The realization of etching masks with a high BCP film thickness h is essential because of the low selectivity of organic films with respect to the inorganic material (SiO_2, SiN, etc.) to be etched. This is why films presenting an array of vertically oriented block copolymer cylinders seem to be more advantageous for the realization of discrete circular nanopatterns compared to films presenting an array of spheres, because they present, *a priori*, no thickness limitation.

Indeed, a film composed of spherical nanodomains must have an initial thickness of roughly the natural monolayer thickness h_0 due to the fact that the spheres of a second layer would be shifted with respect to the spheres of the lower one (phase S and S', Figure 5.1) which would prevent the use of the film as a mask. This can cause an absence of objects on 200 mm devices in zones where the film is thicker than h_0, since thickness variations of some nanometers always occur in an uncontrolled way at this scale. For this reason, the following discussion concerns pattern transfer using cylindrical nanodomains.

For lithography applications of films presenting a cylinder or lamella array of nanodomains, oriented perpendicular to the surface, it is essential that the substrate surface develops similar interaction energies with the various blocks constituting the polymer chains. In other words, it is crucial that the interaction energies between the surface and each copolymer block are modified, e.g. by using a chemical treatment, so that surface energies become equivalent.

BCP films composed of spherical nanodomains do not require a particular surface treatment if they are used as a lithographic mask, because only one of the phases is in contact with the substrate.

Before diblock copolymer films can be used to transfer a structure, one of the phases has to be selectively removed. Details of some of the physical and/or chemical processes which allow this to be done, in order to obtain a nanolithographic mask, are detailed below.

Thurn-Albrecht *et al.* demonstrated that it is possible to remove the polymethylmethacrylate (PMMA) block from a PS-*b*-PMMA system by using UV light [THU 00b]. The UV radiation induces a preferential PMMA phase degradation via chain scission, whereas PS is crosslinked and becomes insoluble leaving a porous PS template. Using an ozone treatment, Park *et al.* [PAR 97] showed that polyisoprene (PI) and polybutadiene (PB) blocks in PS-*b*-PI and PS-*b*-PB systems could be selectively removed. This is due to the ability of ozone to cleave carbon-carbon double bonds (C=C) which are contained in polydienes. For these same systems, Park *et al.* noted that it is possible to reverse the mask, i.e. to selectively etch the PS block by staining the carbon-carbon double bonds with OsO_4. Recently, for a poly(styrene-*b*-dimethylsiloxane) system (PS-*b*-PDMS), a selective degradation of the PS block was observed by using a two step plasma etching process: (i) a CF_4 plasma followed by (ii) a O_2 plasma [JUN 07]. First, the fluorinated chemistry allows the removal of the air/polymer PDMS contact layer while the O_2 plasma selectively etches the carbon skeleton of the PS block copolymer. Finally, we can quote the use of systems containing polyferrocenyldimethylsilane (PFS). These systems presenting a Si and Fe based skeleton have a strong resistance to O_2 etching. Generally, in the literature, this type of polymeric chains is found associated to a PS block or to a PI block, i.e. blocks which can be easily removed by O_2 plasma etching [LAM 00, CHE 03].

In other words, the choice of the diblock chains is very important to allow the selective removal of one block with respect to the other. We will now illustrate some of the objects obtained using diblock copolymer films presenting vertical nanodomains.

BCP films can be used either as etching masks to transfer a pattern directly to the underlying substrate, or as deposition masks to organize dots or lines of different materials on the substrate surface. It is also possible to combine etching and deposition by first transferring the pattern to the substrate by etching and then depositing material dots or lines in the etched holes or trenches. The polymer template can also be reversed by using it for the deposition of dots followed by lift-off. These dots can then be used as a hard-mask to generate substrate nanopillars by plasma etching.

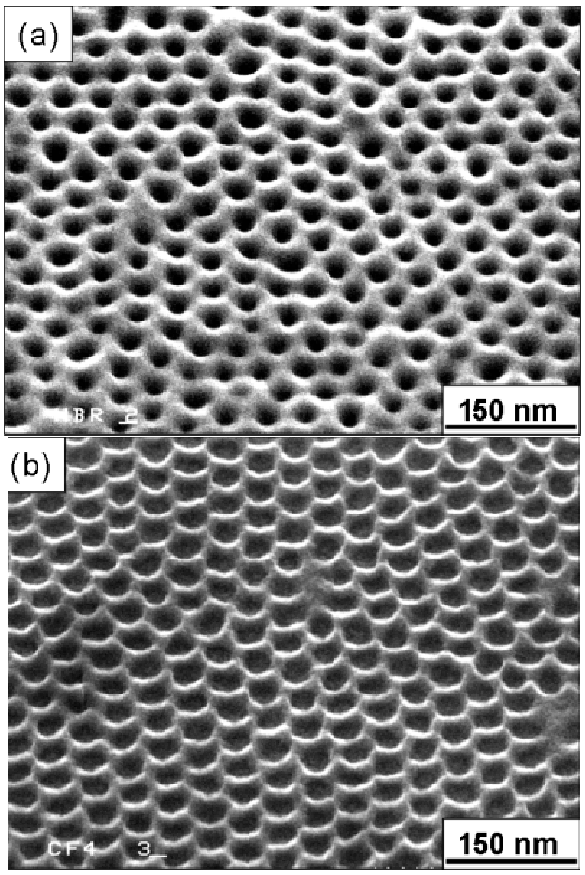

Figure 5.4. *SEM images of an array of organized holes in a silicon oxide layer obtained by using a PS mask for plasma etching with different chemistries: (a) an HBr plasma allows a mean hole diameter of about 20 nm to be achieved, and (b) a CF_4 plasma allows a mean hole diameter of about 30 nm to be achieved. Reproduced and adapted with permission from Surface Science [AIS 07b]*

If a diblock copolymer template is used as deposition mask, a low temperature process, such as physical vapor deposition (PVD), has to be used because the polymer template is not resistant to the high temperature of a Chemical Vapor Deposition (CVD) process.

The first pattern transfers using a BCP mask were carried out by Park *et al.* [PAR 97] by depositing various PS-*b*-PB films, whose compositions were adjusted to obtain a monolayer of spheres or lying cylinders, onto silicon nitride substrates (Si_3N_4). Park *et al.* have shown that it is possible to transfer holes, trenches or pillars to the Si_3N_4 substrate. Similar results were reported for the PS-*b*-PI system. Proceeding in the same way, Harrison *et al*. [HAR 97] presented evidence of the possibility to create holes in a germanium layer. For example, Figure 5.4 presents an array of organized holes in a 10 nm SiO_2 layer obtained using a PS porous template as an etching mask. The mean hole diameter can be tuned by adapting the chemistry of the etching plasma [AIS 07b].

The utilization of a monolayer of spheres or horizontal cylinders as a mask for metal deposition has not been successful, due to the low depth of holes or trenches in the mask, which makes the liftoff very difficult. In order to overcome this problem, Park *et al.* [PAR 01] intercalated a polyimide layer between the substrate and the Si_3N_4 layer. The use of this trilayer (PS/Si_3N_4/polyimide) allows the realization of a mask with deep holes, thus facilitating the liftoff step after the metal deposition. Eventually, Park *et al.* obtained an organized pattern of Ti/Au dots. Nevertheless, this spectacular result requires a huge number of process steps.

A real revolution for BCP lithography was marked by the realization of vertical cylinders in a controlled manner. Film thickness is no longer limited to a monolayer of spheres, and there is no residual PS layer between the substrate and the nanodomains of the mask, as in the case of the spherical nanodomain phase. However, it is necessary to prevent the preferential adsorption of one of the two blocks constituting the copolymer film. Mansky *et al.* [MAN 97] showed that it is possible to control interfacial energies and wetting behavior of polymers by grafting random copolymer brushes on the silicon surface. In order to obtain cylinders oriented perpendicular to the substrate, Thurn-Albrecht *et al.* [THU 00b] used this method to obtain the same surface behavior for PS and PMMA. By using the random PS-*r*-PMMA copolymer, Thurn-Albrecht *et al*. obtained PS-*b*-PMMA films with vertically-oriented PMMA cylinders after annealing. Then, after exposure to UV light and immersion in an acetic acid developer, an array of holes in a PS template was obtained. Guarini *et al.* [GUA 01, BLA 01] were the first to transfer this type of mask to a SiO_2 layer by CHF_3 Reactive Ion Etching (RIE), and then to an Si substrate by SF_6 RIE. The hole pattern obtained can be used to enhance the charge storage capacity of a metal-oxide-semiconductor (MOS) capacitor without increasing the lateral dimensions. This could allow DRAM memory cells to be

manufactured with a higher capacity than that obtained with planar technology. Guarini *et al.* [GUA 02] also realized a pattern reversal by depositing a silicon nitride layer by rapid thermal chemical vapor deposition onto a porous SiO_2 mask obtained using diblock copolymer technology. Then, the SiO_2 template and the silicon nitride on top of it were removed leaving a mask of silicon nitride dots on the substrate. This mask was then used to obtain silicon nanopillars by etching.

Guarini *et al.* [GUA 03] also demonstrated the possibility of fabricating a nanocrystal flash memory by using a diblock copolymer mask for the deposition of Si dots, capping them with a 7 to 12 nm thick control oxide layer, and then depositing a polysilicon gate.

In order to illustrate the use of a PS porous template as a deposition mask, Figure 5.5 presents an organized metal dot array obtained by a lift-off technique.

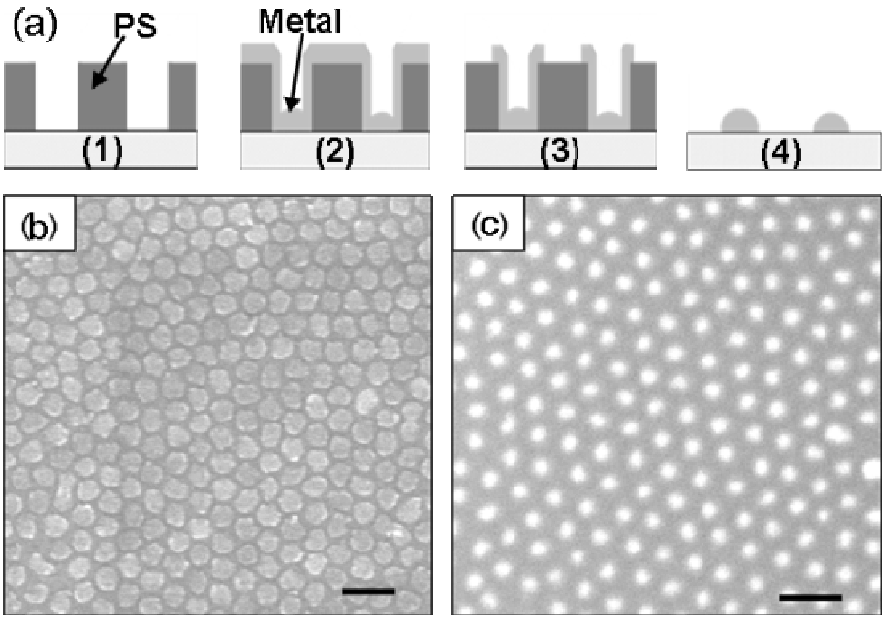

Figure 5.5. *(a) Schematic process flow diagram for metal dot fabrication by lift-off technique: (1) Ps porous template,(2) after metal deposition onto the mask, (3) after an Ar plasma to selectively remove the excess metal on the top PS layer and (4) after an O_2 plasma to remove the residual polymer and side-walls of metal-coated PS. (b) SEM image of a 5 nm thick Pt dot array on SiO_2.(c) SEM image of a 5 nm thick Au dot array on SiO_2. The black bars correspond to 80 nm*

These metal dot arrays have been used as hard-masks to generate (i) organized Si nanopillars by HBr/Cl_2 plasma etching (see Figure 5.6) [AIS 07a] or (ii) to fabricate organized $Si_{0.8}Ge_{0.2}$ quantum dots in Si nanopillars by using a Cl_2/O_2 plasma to etch an Si/SiGe multilayer (see Figure 5.7) [AIS 08]. These kinds of quantum dots could serve as building blocks for future optoelectronic applications.

In order to obtain perfectly organized metallic dots, other studies were carried out simultaneously by using macromolecules containing a PFS block. In particular, the PI-*b*-PFS system was used to obtain Si-Fe oxide dots by O_2 RIE, after the organization of PFS spheres in a PI matrix [LAM 00]. Indeed, the O_2 RIE process allowing the removal of the PI phase induces a partial oxidation of the PFS. Taking the etching robustness of the oxidized spheres into account, these spheres were used to etch multi-layers (PFS/ SiO_2/W/Co/Si) in order to obtain W dots on a Co layer or magnetic Co dots on a Si layer [CHE 01].

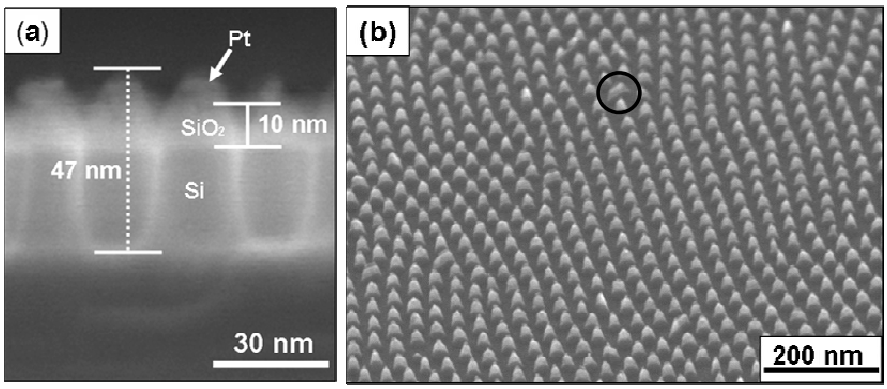

Figure 5.6. *SEM images of nanopillars obtained after transfer of a Pt dot mask to a substrate by etching with an HBr/Cl_2 plasma: (a) Profile image showing the different layers of the pillars (5nm Pt/10 nm SiO_2/ Si) and (b) enlarged image view showing a hexagonal array. The black circle shows a deformed nanopillar due to the presence of a defect in the PS mask. Reproduced and adapted with permission from Macramolecules [AIS 07a]*

To conclude, it has been shown throughout this chapter that it is possible to use thin diblock copolymer films as etching or deposition mask to fabricate discrete objects (holes, dots and pillars) with small dimensions and high density which cannot be obtained by conventional optical lithography and plasma etching. These objects are building blocks for more complex applications (flash memories, DRAM, LED, nanowire FET, etc.). It is preferable to use films with vertically organized nanodomains (cylinders and lamellae) because they present no thickness limitation. This is important for etching processes where the selectivity with respect to the substrate is low. Furthermore, they allow the critical lift-off step to be performed if

the template is used as a deposition mask. The choice of the blocks constituting the block copolymer chains is also very important and is guided by the fact that one block has to be removed (chemical and/or physical etching) selectively with respect to the other, in order to obtain a nanolithographic mask.

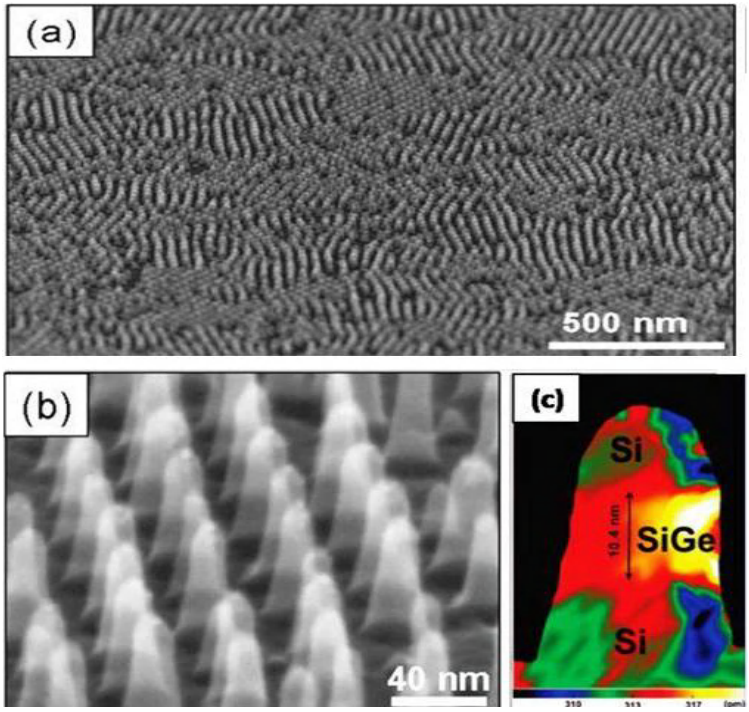

Figure 5.7. (*a) and (b) SEM images of Si nanopillars containing SiGe at different magnifications obtained after a Pt dot mask transfer to the substrate having an alternation of 10 nm thick Si and $Si_{0.8}Ge_{0.2}$ layers by using a Cl_2/O_2 etching plasma. (c) (111) interplanar distance map in pm obtained from a single nanopillar by using Geometrical Phase Analysis. Reproduced and adapted with permission from Chemistry of Materials [AIS 08]*

The presence of defects in the films has also been discussed. It is imperative that defects are limited or suppressed to be able to use these films as a technological solution for future microelectronics. Topological defects (dislocations and disclinations) are difficult to control and curing mechanisms have very slow kinetics. A solution to overcome this problem is to partially or totally confine the BCP film by using nanoimprint lithography, local chemical modification or graphoepitaxy techniques in order to accelerate the kinetics of defect elimination.

5.4. Bibliography

[AIS 07a] AISSOU K., BARON T., KOGELSCHATZ M., PASCALE A., "Phase behavior in thin films of cylinder-forming diblock copolymer: Deformation and division of heptacoordinated microdomains", *Macromolecules*, 40, 5054, 2007.

[AIS 07b] AISSOU K., BARON T., KOGELSCHATZ M., GENTILE P., "Self-assembled block polymer templates as high resolution lithographic masks", *Surf; Sci*., 601(13), 2611, 2007.

[AIS 08] AISSOU K., BARON T., KOGELSCHATZ M., DEN HERTOG M., ROUVIERE J. L. HARTMANN J. M., PELISSIER B., "Fabrication of well-organized and densely packed Si nanopillars containing SiGe nanodots by using block copolymer templates", *Chem. Mater*., 20, 6183, 2008.

[BLA 01] BLACK C. T., GUARINI K. W., MILKOVE K. R., BAKER S. M., RUSSELL T. P., TUOMINEN M. T., "Integration of self-assembled diblock copolymers for semiconductor capacitor fabrication", *Appl. Phys. Lett*., 79, 409, 2001.

[BLA 04a] BLACK C. T., GUARINI K. W., ZHANG Y., KIM H. J., BENEDICT J., SIKORSKI E., BABICH I. V., MILKOVE K. R., "High-capacity, self-assembled metal–oxide–semiconductor decoupling capacitors", *IEEE Electron Device lett.*, 25(9), 622, 2004.

[BLA 04b] BLACK C. T., BEZENCENET O., "Nanometer-scale pattern registration and alignment by directed diblock copolymer self-assembly", *IEEE Trans. Nanotech.*, 3(3), 412, 2004.

[BLA 05] BLACK C. T., "Self-aligned self assembly of multi-nanowire silicon field effect transistors", *Appl. Phys. Lett*., 87, 163116, 2005.

[BLA 07] BLACK C. T., RUIZ R., BREYTA G., CHENG J. Y., COLBURN M. E., GUARINI K. W., KIM H.-C., ZHANG Y., "Polymer self assembly in semiconductor microelectronics", *IBM J. Res. & Dev*., 51 (5), 605, 2007.

[CHE 01] CHENG J. Y., ROSS C. A., CHAN V. Z., THOMAS E. L., LAMMERTINK G. H., VANSCO G. J., "Formation of a cobalt magnetic dot array via block copolymer lithography", *Adv. Mater.*, 13(15), 1174, 2001.

[CHE 02] CHENG J. Y., ROSS C. A., THOMAS E. L., SMITH H. I., VANCSO G. J., "Fabrication of nanostructures with long-range order using block copolymer lithography", *Appl. Phys. Lett.*, 81, 3657, 2002.

[CHE 03] CHENG J. Y., ROSS C. A., THOMAS E. L., SMITH H. I., VANSCO G. J., "Templated self-assembly of block copolymers: effect of substrate topography", *Adv. Mater.*, 15(19), 1599, 2003.

[CHE 06] CHENG J. Y., ZHANG F., SMITH H. I., VANCSO G. J., "Pattern registration between spherical block-copolymer domains and topographical templates", *Adv. Mater.*, 18, 597, 2006.

[EDW 06] EDWARDS E. W., STOYKOVICH M. P., NEALEY P. F., SOLAK H. H., "Binary blends of diblock copolymers as an effective route to multiple length scales in perfect directed self-assembly of diblock copolymer thin films", *J. Vac. Sci. Technol. B*, 24(1), 340, 2006.

[GUA 01] GUARINI K. W., BLACK C. T., MILKOVE K. R., SANDSTROM R. L., "Nanoscale patterning using self-assembled polymers for semiconductor Applications", *J. Vac. Technol. B*, 19, 2784, 2001.

[GUA 02] GUARINI K. W., BLACK C. T., ZHANG Y., KIM H., SIKORSKI E. M., BABICH I. V., "Process integration of self-assembled polymer templates into silicon Nanofabrication", *J. Vac. Technol. B*, 20, 2788, 2002.

[GUA 03] GUARINI K. W., BLACK C. T., ZHANG Y, BABICH I. V., SIKORSKI E. M., GIGNAC L. M., "Low voltage, scalable nanocrystal FLASH memory fabricated by templated self assembly", *IEEE*, IEDM 03-541, 22.2.1, 2003.

[HAM 03] HAMMOND M. R., SIDES S. W., FREDRICKSON G. H., KRAMER E. J., RUOKOLAINEN J., HAHN S. F., "Adjustment of block copolymer nanodomain sizes at lattice defect sites", *Macromolecules*, 36, 8712, 2003.

[HAR 97] HARRISON C., PARK M., CHAIKIN P. M., REGISTER R. A., ADAMSON D. H., "Lithography with a mask of block copolymer microstructures", *J. Vac. Technol. B*, 16(2), 544, 1997.

[HAR 00] HARRISON C. K., ADAMSON D. H., CHENG Z., SEBATIAN J. M., SETHURAMAN S., HUSE D. A., REGISTER R. A., CHAIKIN P. M., "Mechanisms of ordering in striped patterns", *Science*, 290, 1558, 2000.

[HAR 04] HARRISON C. K., ANGELESCU D. E., TRAWICK M. L., CHENG Z., HUSE D. A., CHAIKIN P. M., VEGA D. A., SEBASTIAN J. M., REGISTER A., ADAMSON D. H., "Pattern coarsening in a 2D hexagonal system", *Europhys. Lett.*, 67(5), 800, 2004.

[ITR 01] International Technology Roadmap for Semiconductors, http://www.itrs.net /links/2001itrs/Home.htm, 2001.

[JUN 07] JUNG Y. S., ROSS C. A., "Orientation-controlled self-assembled nanolithography using a polystyrene-polydimethylsiloxane block copolymer", *Nano Lett.*, 7(7), 2046, 2007.

[KIM 04] KIM S. H., MISNER M. J., XU T., KIMURA M., RUSSELL T. P., "Highly oriented and ordered arrays from block copolymers via solvent evaporation", *Adv. Mater.*, 16(3), 226, 2004.

[LAM 00] LAMMERTINK G. H., HEMPENIUS M. A., VAN DEN ENK J. E., CHAN V. Z., THOMAS E. L., VANSCO G. J., "Nanostructured thin films of organic-organometallic block copolymers: One-step lithography with poly(ferrocenylsilanes) by reactive ion etching", *Adv. Mater.*, 12(2), 98, 2000.

[LI 04] LI H. W., HUCK W. T. S., "Ordered block-copolymer assembly using nanoimprint lithography", *Nano Lett.*, 4(9), 1633, 2004.

[LI 05] LI M., COENJAERTS C. A., OBER C. K., "Patternable block copolymers", *Adv. Polym. Sci*., 190, 183, 2005.

[MAN 95] MANSKY P., CHAIKIN B., THOMAS E. L., *J. Mater. Sci*. 30, 1987, 1995.

[MAN 97] MANSKY P., LIU Y., HUANG E., RUSSELL T.P., HAWKER C., "Controlling polymer-surface interactions with random copolymer brushes", *Science*, 275, 1458, 1997.

[MAT 94] MATSEN M. W., SCHICK M., "Stable and unstable phases of a diblock copolymer melt", *Phys. Rev. Lett*., 72(16), 2660, 1994.

[MAT 96] MATSEN M. W., BATES F. W., "Origins of complex self-assembly in block copolymers", *Macromolecules*, 29(23), 7641, 1996.

[NAI 02] NAITO K., HIEDA H., SAKURAI M., KAMATA Y., ASAKAWA K., "2.5-inch disk patterned media prepared by an artificially assisted self-assembling method", *IEEE Trans. Magn.*, 38(5), 1949, 2002.

[OHT 86] OHTA T., KAWASAKI K., "Equilibrium morphology of block copolymer melts", *Macromolecules*, 19(10), 2621, 1986.

[OHT 95] OHTA T., IWAY Y., ITO A.., GUNTON J. D., *Physica B*, 213, 672, 1995.

[PAR 97] PARK M., HARRISON C., CHAIKIN P. M., REGISTER R. A., ADAMSON D. H., "Block copolymer lithography: Periodic arrays of ~10^{11} holes in 1 square centimeter", *Science*, 276, 1401, 1997.

[PAR 01] PARK M., CHAIKIN P. M., REGISTER R. A., ADAMSON D. H., "Large area dense nanoscale patterning of arbitrary surfaces", *Appl. Phys. Lett*., 79(2), 257, 2001.

[PIG 07] PIGNOL R. J., GOMEZ L. R., BAST W., VEGA D. A., "Grain rotation in 2d-hexagonal systems with competing interactions", *Physica B*, 389(1), 94, 2007.

[SEG 01] SEGALMAN R. A., YOKOYAMA H., KRAMER E. J., "Graphoepitaxy of Spherical Domain Block Copolymer Films", *Adv. Mater*., 13(15), 1152, 2001.

[SEG 03] SEGALMAN R. A., HEXEMER A., HAYWARD R. C., KRAMER E. J., "Ordering and melting of block copolymer spherical domains in 2 and 3 Dimensions", *Macromolecules*, 36(9), 3272, 2003.

[STO 06] STOYKOVICH M. P., NEALEY P. F., "Block copolymers and conventional lithography", *Materials Today*, 9(9), 20, 2006.

[SUN 04] SUNDRANI D., DARLING S. B., SIBENER S. J., "Guiding polymers to perfection: Macroscopic alignment of nanoscale domains", *Nano Lett.*, 4(2), 273, 2004.

[THU 00a] THURN-ALBRECHT T., SCHOTTER J., KÄSTLE A., EMLEY N., SHIBAUCHI T., KRUSIN-ELBAUM T., GUARINI K., BLACK C. T., TUOMINEN M., RUSSELL T. P., "Ultrahigh-density nanowire arrays grown in self-assembled diblock copolymer templates", *Science*, 290, 2126, 2000.

[THU 00b] THURN-ALBRECHT T., STEINER R., DEROUCHEY J., STAFFORD C. M., HUANG E., BAL M., TUOMINEN M., HAWKER C. J., RUSSELL T. P., "Nanoscopic templates from oriented block copolymer films", *Adv. Mater.*, 12(11), 787, 2000.

[VEG 05] VEGA D. A., HARRISON C., ANGELESCU D. E., TRAWICK M. L., HUSE D. A., CHAIKIN P. M., REGISTER R. A., "Ordering mechanisms in two-dimensional sphere-forming block copolymers", *Phys. Rev.*, E 71, 061803, 2005.

[XIA 05] XIAO S. G., YANG X. M., EDWARDS E. W., LA Y-H., NEALEY P. F., "Graphoepitaxy of cylinder-forming block copolymers for use as templates to pattern magnetic metal dot arrays", *Nanotechnology*, 16(7), S324, 2005.

[YOK 02] YOKOJIMA Y., SHIWA Y., "Hydrodynamic interactions in ordering process of two-dimensional quenched block copolymers", *Phys. Rev.*, E 65, 056308, 2002.

Chapter 6

Metrology for Lithography

6.1. Introduction

This chapter is intended to present the implications, problems and existing or potential solutions relating to the critical dimension (CD) measurement stage of lithography, for either R&D or industrial processes.

During the fabrication of electronic devices, CD measurement occurs after each technological step that may induce a topological change to the surface. As the dimensions of electronic devices get smaller, the metrological steps get more critical and accuracy of measurement is all the more necessary. Consequently, the intrinsic limits of each metrological technique, likely to provide dimensional information for manufactured patterns, must be known.

First, the needs of lithography (in terms of dimensional characterization and what is at stake with these needs in the short/long term future) are defined. Secondly, each of the traditional measurement techniques commonly used after lithography, to measure fabricated patterns and guarantee the dimensions initially desired, will be presented. Hence three categories of characterization techniques are presented: scanning electron microscopy (SEM), 3D atomic force microscopy (AFM 3D) and scatterometry.

Chapter written by Johann FOUCHER and Jérôme HAZART.

6.2. The concept of CD in metrology

6.2.1. *CD measurement after a lithography stage: definitions*

CD is the *Critical Dimension* of an object made on a given substrate (a silicon wafer, for example). As shown in Figure 6.1, theoretical CD corresponds to the dimensions of a pattern measured at the interface between it and the layer underneath. We talk of CD1 for object no. 1, CD2 for object no. 2, etc.

Readers should be careful not to extrapolate the remarks above to other kinds of dimensional control specific to other technological steps (such as gate, or interconnect plasma etching, etc.). Indeed, one must keep in mind that the performances of each characterization technique presented here strongly depend on the type of equipment, the kind of material used as a substrate, and on the environment (hygrometry, temperature, vibrations, etc.).

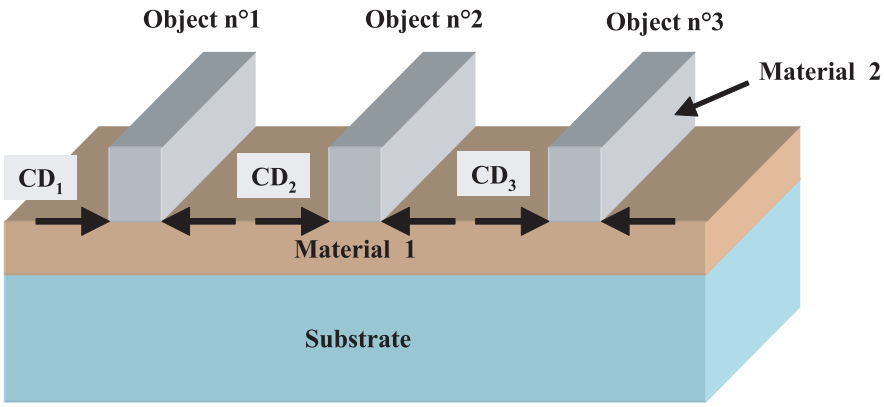

Figure 6.1. *CD term definition*

Too often, metrology equipment users regard the figures obtained after a characterization step as true. Yet the "true" value is very difficult to obtain in a standard environment (such as a research lab or industrial site) compared to a metrology center where the entire environment and the metrological chain are known and totally under control. Nevertheless, with a few precautions and by always keeping in mind the measurement's purpose, it is still possible to get close to the "true" or "absolute" values so desired by technologists every day.

In addition to traditional CD measurement, it may be very useful to have access to the following data: pattern height, pattern sidewall angle (SWA) and also sidewall roughness along resist lines (measuring line edge roughness (LER) and line width

roughness (LWR); see Figure 6.2). The last two parameters are critical, because they directly affect the electrical performance of CMOS transistors, for example when gate width is no more negligible than LER/LWR values.

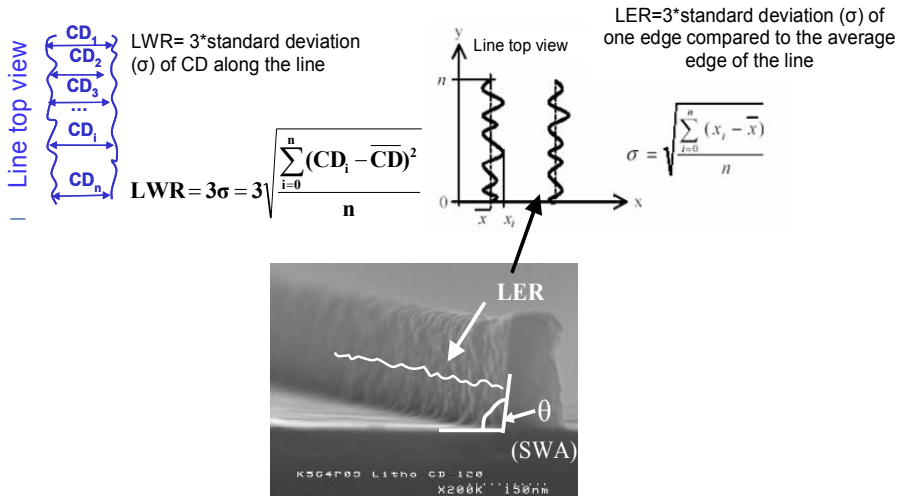

Figure 6.2. *LER and LWR definition, representing sidewall roughness along patterns*

6.2.2. *What are the metrological needs during a lithography step?*

6.2.2.1. *Notions of accuracy and reproducibility during measurement*

Depending on the working environment (R&D or production), the person working with a given CD metrological technique will have different expectations. Indeed, for R&D needs, a predictive technique is required, that is to say one which gives "true" measures. The notion of accuracy is thus introduced.

6.2.2.1.1. Measurement accuracy

Accuracy error is the global error resulting from all the possible causes for each measurement result taken separately. Consequently, it is the ability of the tool to give error-free results.

Conversely, from a production point of view, the fabrication process or the technological step are supposed to be perfectly under control, and the CD metrology step is only there to regularly control the process. A very reproducible technique would then be favored; thus, the notion of measurement reproducibility is introduced.

6.2.2.1.2. Measure reproducibility

Reproducibility is the ability of a measurement tool to give measurements free from accidental error. Accuracy defines result dispersion. If only one measurement is made, accuracy represents the probability that this measure represents the average result ("probability" from the latin word "probare" meaning "to prove or to test", and referring to "something that may happen"); the latter (the average result) being obtained after an infinity of measurements. As shown in Figure 6.3, if one considers measurement repartition as a dartboard, accuracy is the ability to hit the middle and reproducibility is the spread of the results.

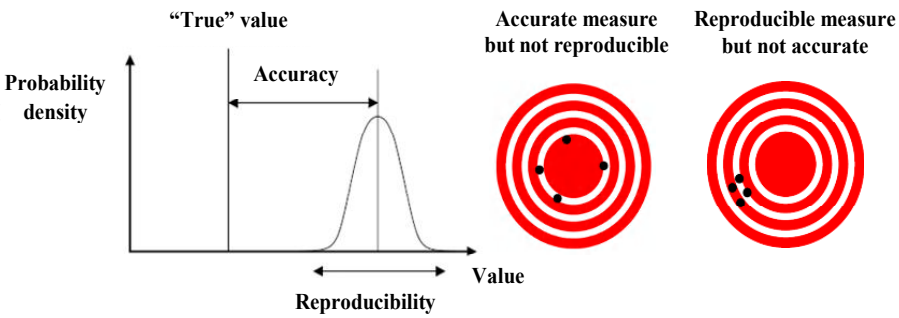

Figure 6.3. *Schematic view of measure reproducibility and accuracy*

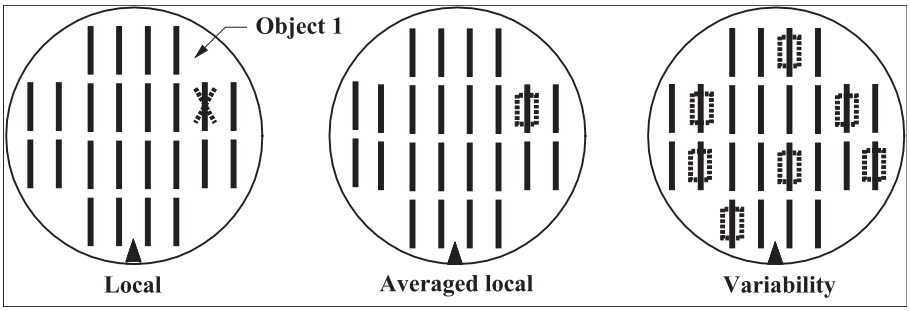

Figure 6.4. *Schematic view of local measurement, averaged local measurement and variability*

6.2.2.2. *Notions of local measurement, average local measurement and variability*

Depending on the technological needs and requirements of the process to be developed, a metrologist may only be interested in a local measurement, an average

measurement or several measurements local and/or averaged, so as to know the variability of a process across a given surface (see Figure 6.4).

6.2.2.2.1. Local measurement

A local measurement gives access to the CD value for a given couple of coordinates (X,Y). There is no notion of integration of the measurement over a certain length of the structure (local variability).

6.2.2.2.2. Averaged local measurement

An averaged local measurement is a CD measurement for a given couple of coordinates (X,Y) taking into account the local variability of the structure dimensions (e.g. sidewall roughness).

6.2.2.2.3. Variability

The notion of variability must be introduced when looking at the homogeneity or uniformity of a fabrication process across a given surface (for example a 300 mm wafer for the semiconductor industry). The term CDU (CD uniformity) is employed and always refers to 3σ (three times the standard deviation of the measured values).

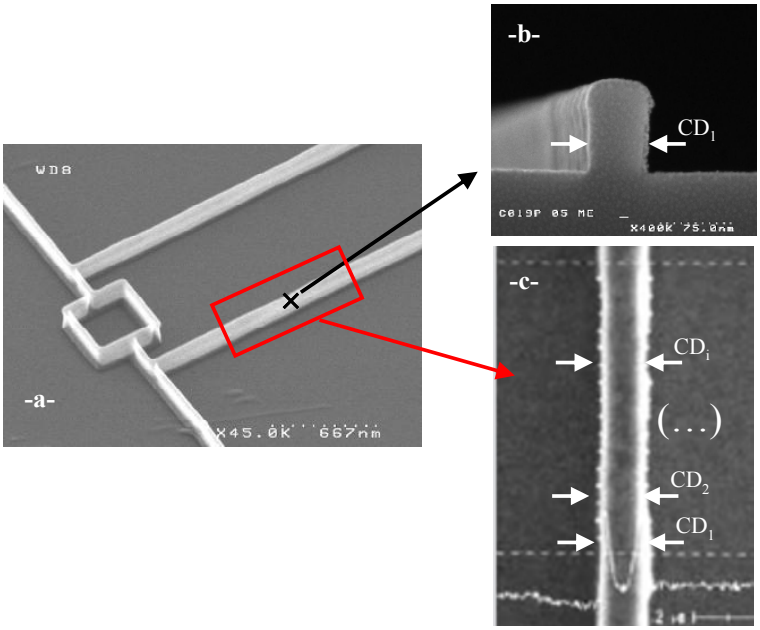

Figure 6.5. *SEM images of a resist pattern: a) overall SEM image; b) side view; (c) top view*

To illustrate the subject, consider Figure 6.5(a) representing a resist pattern obtained after a lithography step. For a local (cross) measurement, the substrate has to be cut, then characterized from the cross section (Figure 6.5(b), local information in two dimensions (CD and height of the structure) is obtained. Considering an averaged local measurement (rectangle), the line will only be imaged from above but the measurement will be integrated over a given length (Figure 6.5(c)). Information is averaged but only in one dimension. We have access to the variability of the average CD along the line but there is no information on the height. Images were obtained by Scanning Electron Microscopy (SEM); this technique is detailed in section 6.3. By repeating these measurements over a whole wafer, we can easily deduce the uniformity of a given lithography process.

6.3. Scanning electron microscopy (SEM)

Scanning electron microscopy is a powerful technique to observe surface topography. It is mainly based on detection of secondary electrons emerging from the surface being studied when a very narrow beam of primary electrons scans it. Images with resolution usually smaller than 3 nm and a large depth of field may be obtained [PAQ 06, REI 93].

6.3.1. *SEM principle*

In a lithography context, SEMs are tools dedicated to observation and/or measurement of patterns resulting from lithography processes. A focused electron beam scans a sample surface step by step. Primary electrons are accelerated from the source to the sample thanks to an accelerating voltage ranging from 0.2 kV to 30 kV, depending on the sample material and the SEM tool.

As the beam goes down in the vacuum column, it is focused and the beam diameter is reduced from several micrometers down to a few nanometers, thanks to condensing lenses. According to applications and the required magnification and resolution, the manipulator adjusts the accelerating voltage and the beam diameter to improve the image. A detector collects the emitted secondary electrons coming from the sample and records the signal as an (x,y) function. The general scheme of such a tool is presented in Figure 6.6.

A scanning electron microscope usually comprises the following elements:

– an electronic column comprising an electron gun, several electromagnetic lenses (“condensers”), some alignment and adjustment electric coils, and a electronic beam scanning system. This column is kept under vacuum, at least 10^{-3} Pa. In standard microscopes, the vacuum required is obtained thanks to a rotary vane pump

coupled with a secondary pumping device, such as an oil diffusion pump (sometimes with two of them in series), or a turbomolecular pump;

– an "object room" where the sample is introduced (either via an airlock or not);

– a detector to detect secondary electrons (in our specific case). It must be said that for other kind of applications (not detailed here), detectors sensitive to other kind of electronic or electromagnetic emissions can be implemented;

– an image visualization system and a data exploitation system to process information coming from the sample.

Two kinds of tools are encountered. In a microelectronic industry production environment, CD-SEM are usually used, whereas X-SEM (or cross-section SEM, because the sample is cleaved) is used for R&D purposes.

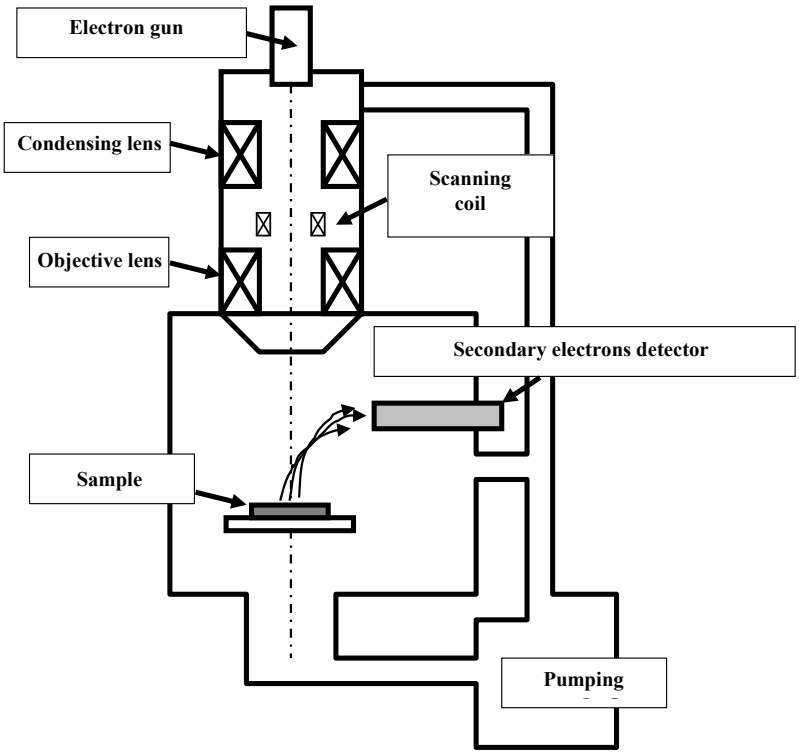

Figure 6.6. *General layout of a scanning electron microscope*

6.3.1.1. *X-SEM imaging (cross-section)*

X-SEM imaging is totally manually operated. First, the sample must be cleaved precisely at the place where the measurement is to be made. Cleaving can be done manually thanks to a diamond scribe and a dedicated clip, or automated thanks to a tool comprising a cleaving machine coupled with a microscope. In both cases, the sample is ruined and the measurement location is not as precise as the one obtained with CD-SEM. In the best cases, precision is to a few hundred micrometers with an X-SEM whereas measurement can be made as close as 50 nm of the desired spot with a CD-SEM.

Working voltage is usually between 5 keV and 30 keV.

The main asset of X-SEM is its ability to observe patterns in 3D (see Figure 6.7) and to measure patterns in two dimensions (height and CD). Indeed, even if observation is in 3D, we can only get 2D measurements and only in a single spot (there is no possible integration of measurements along the line and, hence, no possibility to quantify dimension variability along it).

6.3.1.2. *CD-SEM imaging*

The CD-SEM principle is to automatically introduce a wafer in the vacuum chamber and to observe patterns only from the top (there is no wafer cleaving; see Figure 6.8). Due to this non-destructive method, CD-SEM is compatible with the production environment and with an in-line fabrication process control. Automated measurements coupled with powerful signal processing algorithms (detailed below) contribute to make CD-SEM a robust, fast (< (s/measurement) and very reproducible technique.

In a microelectronic production environment, CD-SEM usually works between 300 V and 1000 V. For lithography applications, depending on the operator skill, working voltage is between 300 V and 500 V.

With CD-SEM, measurement is fully automated, hence reducing operator errors. It uses specific recognition patterns to locate the patterns to be measured and to position the system precisely and repeatedly. It also has automated autofocus. Its beam controlling system is very stable so as to reduce measurement errors.

The electromagnetic field created has a lower energy hence reducing pattern deterioration and limiting charging phenomenon. Image distortion is then often reduced and better quality images are obtained, especially with low atomic number elements and when working with silicon or photosensitive resists.

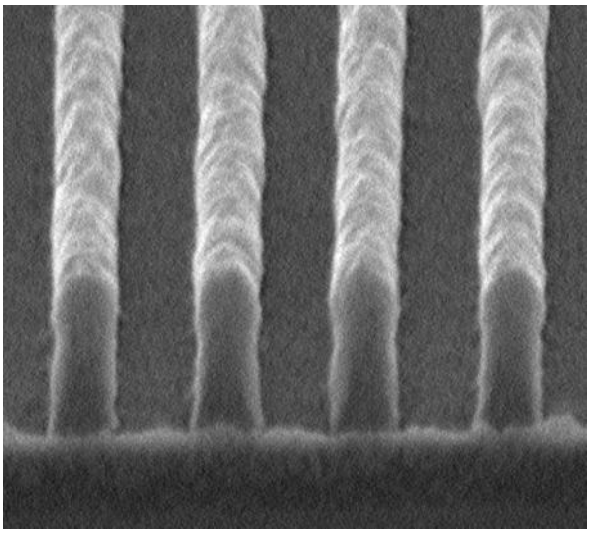

Figure 6.7. *Typical X-SEM image of resist lines*

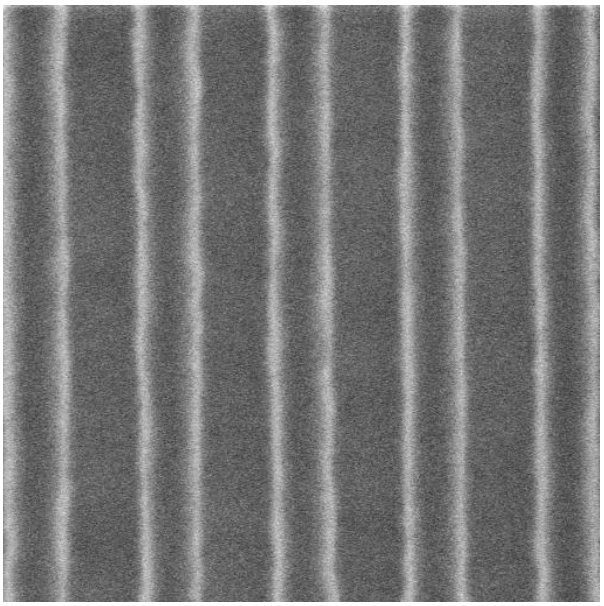

Figure 6.8. *Typical CD-SEM image of resist lines*

Limited 1D vision of the fabricated structures is the main drawback of this technique. Consequently, it is impossible to get information on resist height, sidewall angle, and possible presence of footing, etc.

6.3.2. *Matter–electron interaction*

When an electronic beam with an energy level Eo penetrates inside a solid material, elastic and inelastic interactions with the material occur. During inelastic interactions, electrons gradually lose their energy, which is mostly transferred to electrons of the atomic orbital. To a lesser extent this energy can vanish through radiative emissions, during interaction with nuclei. These radiations compose the so-called bremsstrahlung emissions.

Elastic interactions, mostly with nuclei, modify incident electrons' trajectories, hence leading to their scattering. These interactions may induce the following phenomena (see Figure 6.9):

– backscattered electronic emission, made of primary electrons coming back out of the surface after (almost) elastic shock and leaving the target with an energy more or less close to E_0;

– secondary electron emission, with low energy (usually around 10 eV) resulting either from primary electrons strongly slowed down by inelastic shocks, or more often by primary electron ejection (mainly valence electrons) snatched from the atoms by ionization;

– Auger electron (element specific) emission, coming from the target atom deexitation process after ionization;

– absorbed electron current, mainly composed of primary electrons that did not manage to get away and that are usually evacuated towards the mass, and also induced current in semi-conductors. This absorbed current triggers charge phenomena in insulation materials;

– visible (or near visible) electromagnetic radiation emission;

– highly energetic photons (X-ray) emission. On the one hand they form the continuous spectrum coming from the slowing motion of incident electrons in the magnetic field of the nuclei and, on the other hand, a specific emission of each atom species, resulting from their ionization by incident electrons.

Broadly speaking, the level of each emission depends on the incident beam energy E0, on the nature of the scanned atoms (their atomic number Z), and on the incident angle of the beam at the surface.

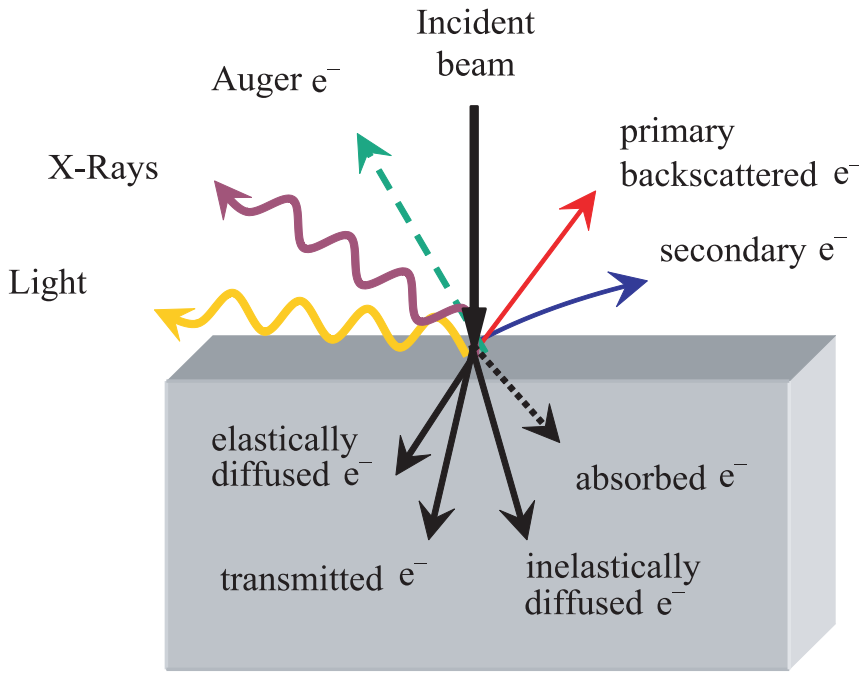

Figure 6.9. *Main electronic and electromagnetic emissions resulting from interaction between sample and electron beam*

6.3.2.1. *Emission and spatial resolution*

The more the electrons are accelerated and the less dense the matter, the deeper they penetrate within the material. Average penetration depth z may be approximated considering the energy E_0 and the specific mass ρ of the target impact area, by a simplified law such as [CAZ 01a, CAZ 01b, FIT 74, REI 85]:

$$z_M = k\frac{E_0^n}{\rho^p}$$

where z_M (m) is penetration depth, E_0 (keV) the electrons' energy, and ρ (g/cm^3) the specific mass.

Various electronic and electromagnetic emissions come from interaction zones, more or less deep and more or less wide, depending on the incident beam impact (see Figure 6.10). Secondary electronic emission comes from a narrow zone of a few nm^3 around the electronic beam impact. Back scattered emission comes from a deeper zone of few hundred nanometers (10^4 to 10^6 nm^3).

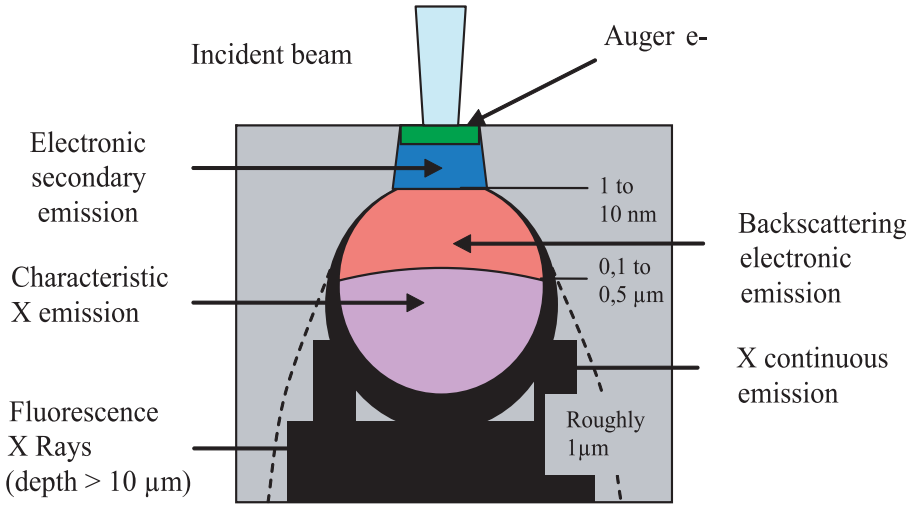

Figure 6.10. *Electronic and electromagnetic emission zones*

6.3.2.2. *Secondary electrons*

Here we focus on secondary electrons which are the basis of SEM imaging for lithography applications. They result from inelastic interactions between primary electrons and valence electrons. They have energy of a few electron-volts (typically between 5 and 10 eV).

Some electrons resulting from interactions with deeper electrons may have a higher energy but, as a rule, the secondary electron domain is restricted to those below 50 eV.

Considering this low energy, only the electrons emitted close to the surface may escape (they come from a zone of several nanometers' depth). Secondary electrons are hence sensitive to surface irregularity, to topography. An electric field can easily deviate them and then a detector may catch them (see Figure 6.6).

In addition, different types of secondary emission may be distinguished:

– "true" secondary emission (also called "type I"), caused by primary incident electrons;

– emissions induced by backscattering electrons, either inside the sample itself (type II), or at level of the polar pieces in the object chamber (type III).

Secondary electronic emission is characterized by its yield, δ (the ratio between primary and secondary electron numbers). Contributions due to secondary electrons coming from primary electrons is narrow, whereas the contribution due to backscattered electrons is spatially wider (see Figure 6.11).

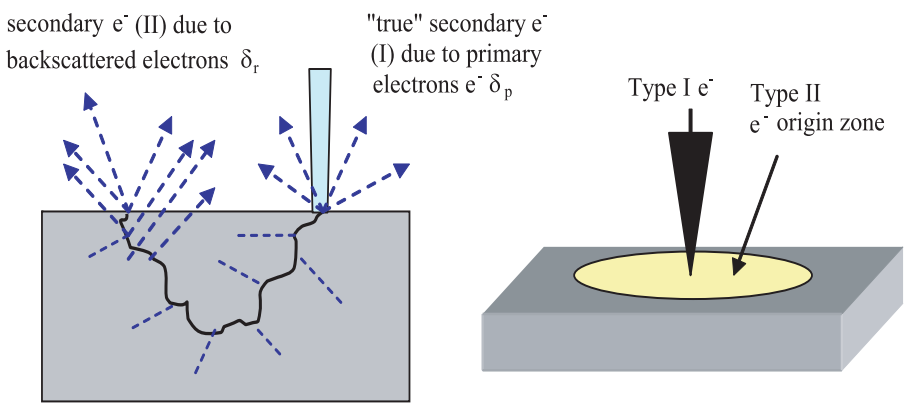

Figure 6.11. *Secondary electron emissions areas*

Several parameters impact on secondary electronic emission:

– E_0 value (or E_{PE}): δ reach a maximum when E_0 is close to 300 eV in the case of carbon (main component of photosensitive resists) and then decreases as E_0 increases, to finally reach a threshold $\delta_s = 0{,}58$ (see Figure 6.12) [FAR 93, SEI 83];

– the incident angle α: if the beam hits a sloping surface, more secondary electrons may come out of the material (see Figure 6.13). δ strongly changes depending on α, approximately as 1/cos α;

– topography: if the beam is directed towards a trench or a hole, less electrons manage to escape, several of them being reabsorbed by the material.

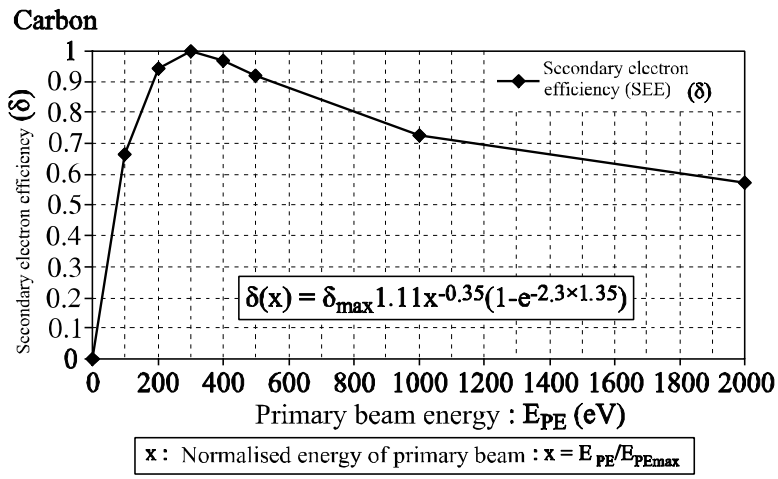

Figure 6.12. *Surface electronic yield variation (δ secondary) according to incident electron energy in the case of carbon, the major component of photosensitive resists*

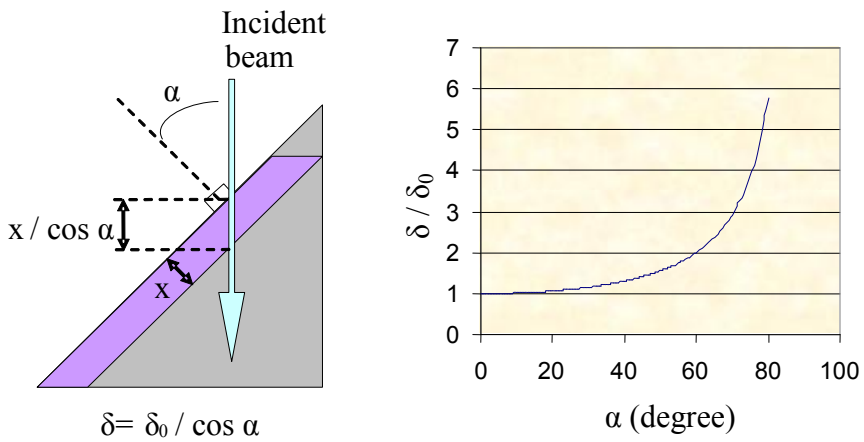

Figure 6.13. *Beam incident angle influence on secondary electron yield. When the slope increases, the trajectory length where the generated secondary electrons may escape from the material increases*

6.3.3. *From signal to quantified measurement*

Pattern dimensional measurement with CD-SEM is based on this dependence of secondary electron yield on incident angle between beam and surface. If the beam is perpendicular to the surface, steep areas (typically pattern sidewalls) where

generated secondary electrons are more numerous appear clear, whereas horizontal areas appear darker (see Figures 6.14(a) and 6.14(b). Based on these contrasts, algorithms lead to dimensional characteristics of the lithographed patterns (average line width, sidewall roughness, etc.). However, images are only in two dimensions and cannot lead to pattern height measurement.

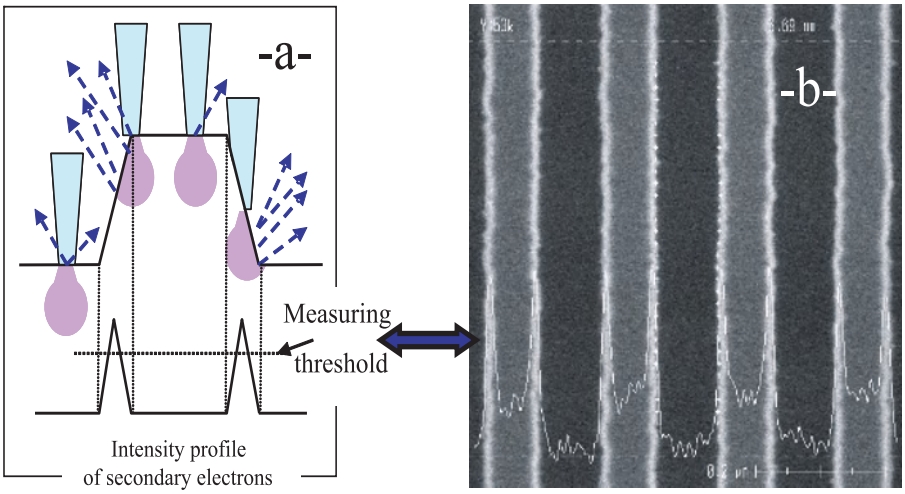

Figure 6.14. *Origin of the observed contrast on SEM images of a lithographed pattern*

By filtering the intensity profile of secondary electrons so as to reduce signal noise and by applying a threshold algorithm [DAV 95, LOW 96], a characteristic measurement of the line can be obtained, such as in Figure 6.14(b). However, optimization of the threshold level so as to obtain the true pattern CD is very difficult. Indeed there is no physical relation between threshold level and pattern height [DAV 99, VIL 01] as illustrated in Figure 6.15. This is an intrinsic limit for accuracy and consequently a non-negligible drawback of the method for fundamental applications. Indeed, measurement error does not only depend on the chosen threshold but, above all else, on the material composition, and on the profile and height of the measured pattern.

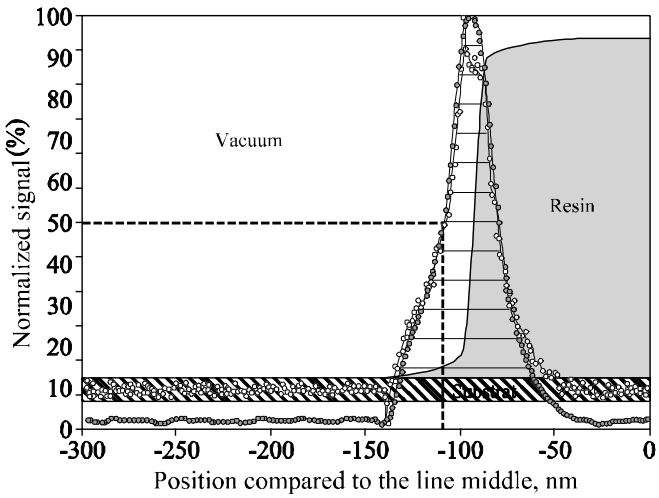

Figure 6.15. *Origin of the observed contrast on SEM images of a lithographed pattern*

As also shown in Figure 6.16, the top-view imaging of lines leads to dark area when dealing with a negative pattern. Indeed, electrons from the primary beam cannot scan the matter corresponding to the negative profile; hence all the real topographic information is lost. We are here facing the second strong limitation of this technique concerning measurement accuracy. And yet, negative profiles are frequently encountered in lithography, for example when studying a Focus Exposure Matrix (FEM) where height and profile strongly vary.

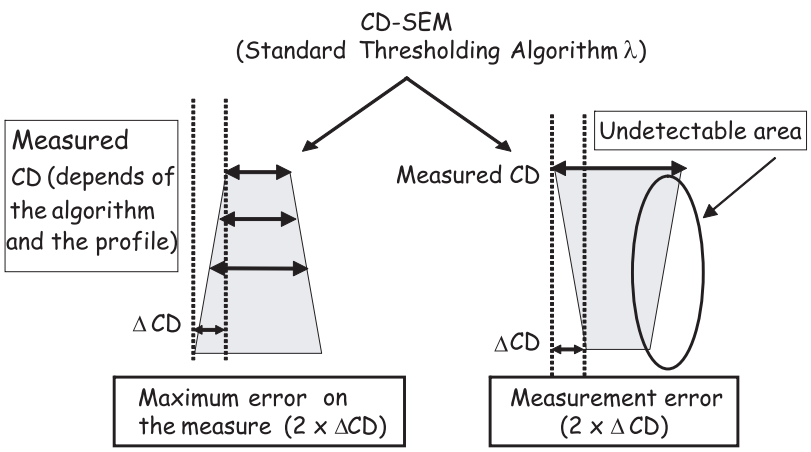

Figure 6.16. *Intrinsic limitation of CD-SEM measurement accuracy*

These two intrinsic limitations of the CD-SEM technique may cause important problems when working for upstream R&D in advanced microelectronics. Indeed dimensional constraints governed by Moore's Law set a tolerance on dimensions of 10%. For example, if a lithography process has to be developed today for R&D, targeting a 30 nm pattern (at the bottom of the pattern), dimensions must be guaranteed under ± 3 nm. With a simple trigonometric law (see Figure 6.17), and a typical pattern of 130 nm height and sidewall angle θ = 88°, we should realize that if the algorithm leads to a measure of the top of the pattern, errors on CD will reach 9 nm. CD-SEM measurement has a major difficulty: bright zones, representing the sides of the pattern are not precisely defined at the nanometric scale and can't be defined because all the information on the profile is integrated into the two bright zones along the lines (for example), or more precisely at the edge of any pattern measured.

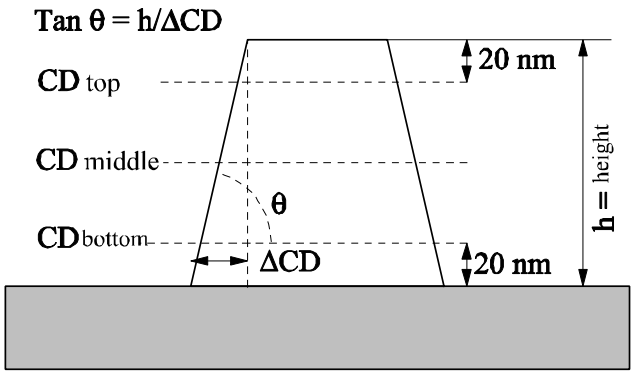

Figure 6.17. *Trigonometric definition of measurement uncertainty, ΔCD*

This means that, without an optimum preliminary calibration step for these threshold algorithms, it is nearly impossible to get an accurate measurement with a CD-SEM. Nevertheless, the first two advantages remain: speed of measurement and reproducibility.

Bright or uncertain zones are all the more likely with X-SEM since the tool is manually adjusted and the sample is never precisely facing the beam (see Figure 6.18). However, its main asset lies in the versatility of the sample orientation, which allows observation of lithographed patterns from every angle. CD-SEM and X-SEM are very complementary for R&D and production needs.

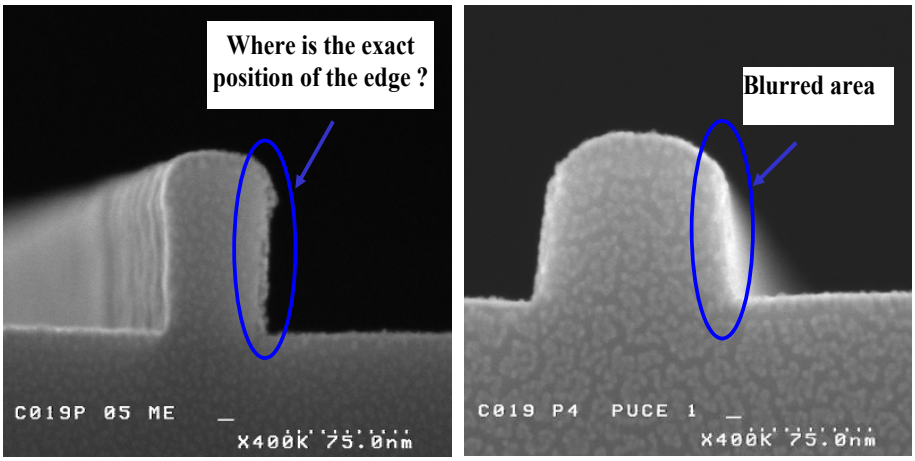

Figure 6.18. *Significant areas of measurement uncertainty using X-SEM*

6.3.4. *Provisional conclusion on scanning electron microscopy*

The SEM technique is a very powerful and useful technique to assist lithography process development. It allows observation of a pattern (to check the quality of a fabricated pattern) and has very reproducible measurement (in the case of CD-SEM). Nevertheless, for both techniques, measurement accuracy is not guaranteed for two main reasons:

1. CD-SEM gives a 1D integrated imaging of a pattern, suppressing information on height and profile;

2. X-SEM's approximate sample positioning, combined with the need to cleave the sample, leads to large areas of uncertainty.

6.4. 3D atomic force microscopy (AFM 3D)

Atomic Force Microscopy (AFM) was presented in 1986 by G. Binnig, C.F. Quate and C. Gerber, as an application of the scanning tunneling microscope (STM) concept dedicated to atomic scale analysis of isolating materials. Since then, this technique has been adapted to various environments such as vacuum, liquids, low temperatures, and magnetic fields and also for chemical and biological applications. This chapter is not intended to present AFM theory but just its fundamental characteristics and, furthermore, how to benefit from a derivative technique called AFM 3D to very precisely measure the CD of lithographed patterns.

6.4.1. *AFM principle*

The basic principles of atomic force microscopy are probably the easiest to understand among microscopy techniques [BIN 85, MAR 87]. An interesting analogy is the ability of a blind person to mentally construct an image of surrounding objects thanks to their sense of touch. Like the fingers of this person, an AFM is able to give a very detailed picture of the analyzed object, not only in terms of the topography of its surface but also concerning its texture, whether hard or soft, smooth or rough, sticky or slippery.

The AFM tip is mounted on a cantilever, and this is the main element of the system (see Figure 6.19). Thanks to interaction forces, it can produce an image of the analyzed surface. This cantilever is fixed onto a support.

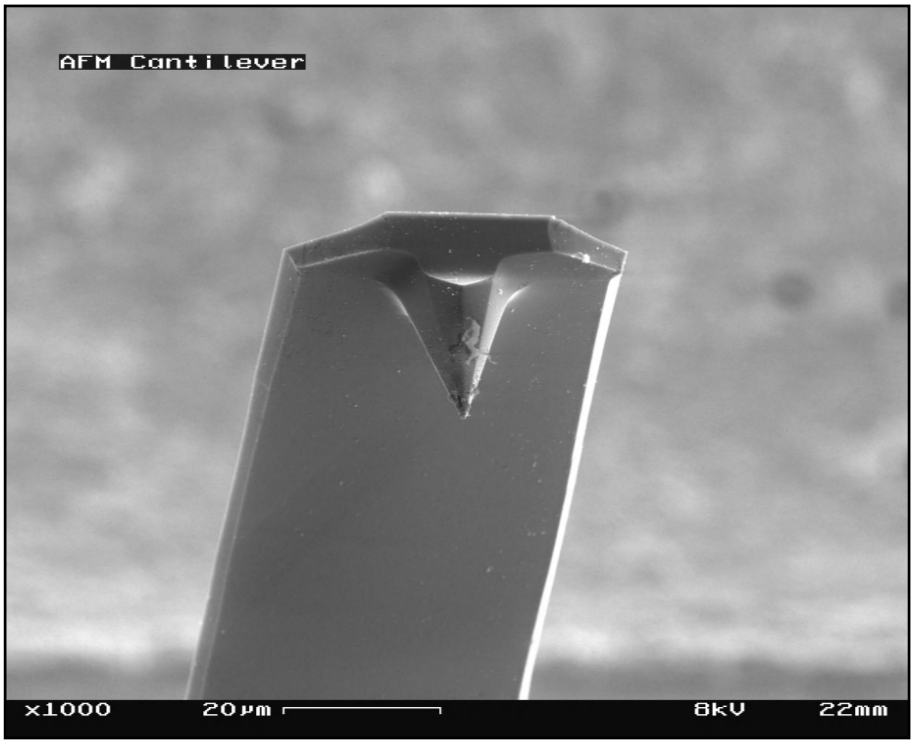

Figure 6.19. *SEM image of an AFM tip (zoom × 1000)*

The cantilver lets the tip oscillate while it scans the surface. It has a very low stiffness constant thus enabling the AFM to control very precisely the force between the tip and the sample. When the first AFM was first built, a tiny diamond shard was meticulously glued onto a tiny strip of gold foil. Today, the tip–cantilever unit is usually made of silicon or silicon nitride, both hard and wear resistant materials. The cantilevers are mainly classified according to their stiffness constant and resonant frequency. The essential parameters for the tip are its thinness (measured by its curvature radius) and its aspect ratio. Tip thinness determines tool resolution power. To get an order of magnitude, a typical standard tip is a 3 µm long conical tip with a radius of curvature of about 30 nm.

The motion of the tip–cantiler group is performed by piezoelectric transducers. For a piezo-electric gas lighter, stretching of the piezoelectric crystal causes a sufficiently high voltage gap to produce a spark. The opposite effect is used in the AFM: applying a voltage to the piezoelectric ceramic induces a stretching of the latter. This motion is very reproducible with atomic precision, given that the electric pulses are precise enough. There are several possible configurations for the placing of the piezoelectric ceramics. However, a generic configuration is described in Figure 6.20 where the transducer is placed under the probed sample. Sample motion is controlled in the three directions x, y and z, each being assigned to a specific channel of the electronic driver. During measurement, the sample is placed very close to the tip thanks to the z channel, then its surface is scanned line-by-line using the x and y channels.

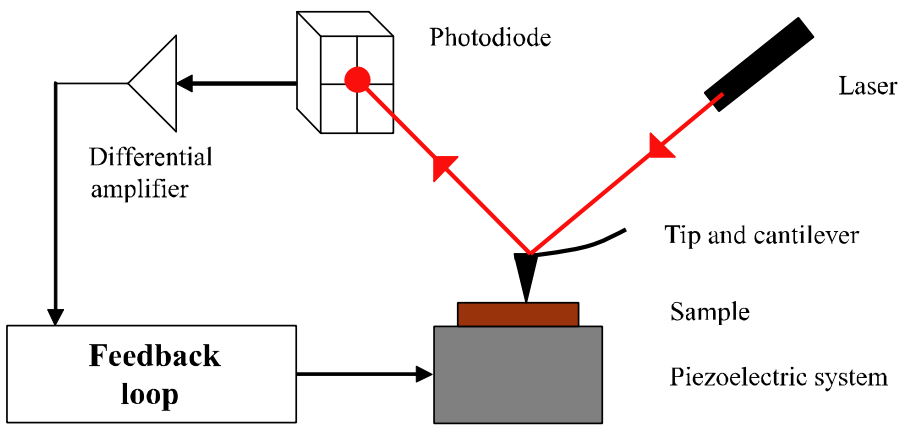

Figure 6.20. *Schematic view of an atomic force microscope*

Tip motion must be controlled while scanning the surface. Several systems may perform this control, the one based on a laser beam deflection being the most common (see Figure 6.20). Usually, the back of the cantilever is coated with a thin metal layer to become reflective. A laser beam is directed toward the edge of the cantilever, preferably right above the tip, then reflected toward a detection photodiode. In modern tools, the photodiode consists of four quadrants. As the tip moves, according to the sample topography, the reflected beam angle changes and consequently the laser spot on the photodiode also moves, inducing intensity changes for the four quadrants. Since the cantilever–detector distance is three orders higher than the cantilever length (micrometers compared to millimeters) this detection system greatly amplifies movements and is hence very sensitive. Any intensity difference between the two top quadrants and the two bottom ones accounts for a vertical displacement of the tip. Intensity differences between the right and left pairs accounts for a lateral displacement or torsion of the tip. Consequently, friction phenomena between the tip and the surface may be distinguished from mere topographical information.

Recording effects of interaction forces between the tip and the sample as the probe scans the surface produces images of those effects resulting in cantilever deflection. In the easiest operating mode, cantilever deflection is kept to a given fixed value for each point to be analyzed, thanks to a closed loop control. This closed loop control is the key difference between AFM and former systems using a stylus [BRA 04].

6.4.1.1. *Piezoelectric ceramics*

The tube's inner surface (see Figure 6.21) is made of a thin layer of radially polarized piezoelectric ceramic. Electrodes are stuck to the inner and outer wall of the tube. The outer face is divided into segments parallel to the axis.

By applying a voltage difference between the inner electrode and the four outer electrodes, the tube extends or contracts, i.e. moves in the z direction (see Figure 6.21). If the voltage difference is only applied to one of the outer electrodes, the tube bends, i.e. moves in the x or y direction. To accentuate this bending and hence increase the scanning range, outer electrodes are placed opposite each other. Consequently when a $+n$ voltage is applied on one electrode and $-n$ on its opposite, the tube bending is twice as much as if only one electrode had been submitted to a voltage difference.

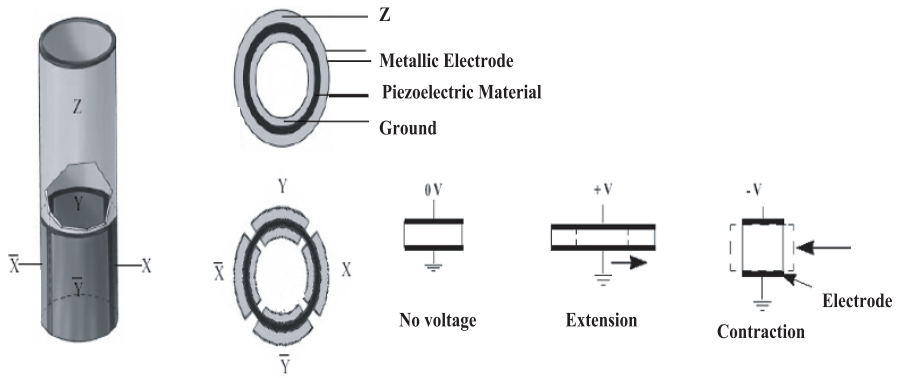

Figure 6.21. *Schematic view of a piezoelectric tube and of a reverse piezoelectric effect on a PZT tube*

In spite of the incredible precision of motion of piezoelectric materials, they are not deprived of non-linearity, in all possible geometries. Non-linearity can be neglected for small displacements but becomes critical when scans grow longer. In a tube configuration, the system suffers from hysteresis, as shown in Figure 6.22.

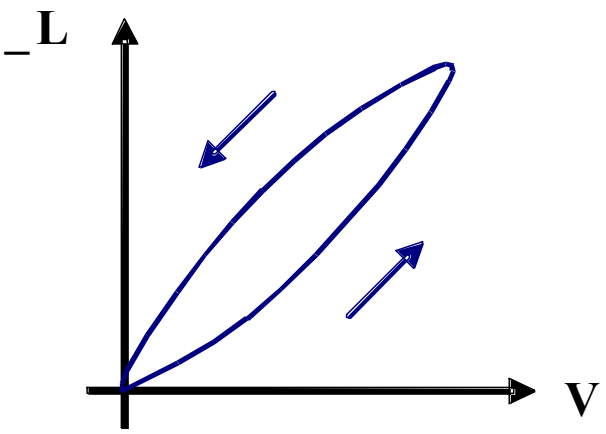

Figure 6.22. *Hysteresis loop of a piezoelectric tube*

6.4.1.2. *Tips*

The tip is AFM's critical element. Bad quality tips, even mounted on the most sophisticated tools, will only lead to results at best disappointing and, at worse, wrong. Since the beginning of AFM, dedicated, specially fabricated tips were required and "homemade" fabrication was quickly given up [MOR 99].

Techniques, similar to those employed for integrated circuits fabrication, such as optical lithography with a mask, chemical etching or chemical vapor deposition, are used to microfabricate modern tips and cantilevers. Tips and cantilevers are almost always made of silicon, silicon nitride or diamond. They can be conducting or not, and they are often coated with a different element to prevent problems such as wear. When using optical detection, the cantilever is usually coated with a thin layer of gold to improve its reflectivity. If magnetic sensitivity is required, ferromagnetic coating may be applied.

There are two main possible designs for the cantilever on which the tip is mounted (see Figure 6.23). A triangular shape or a V shape is used to minimize torsion and is adapted to purely topographic measurements. The more familiar cantilever with a simple rectangular shape is the best for measuring the friction properties of a sample, since it has a rotational degree of freedom enabling sensitivity to lateral forces.

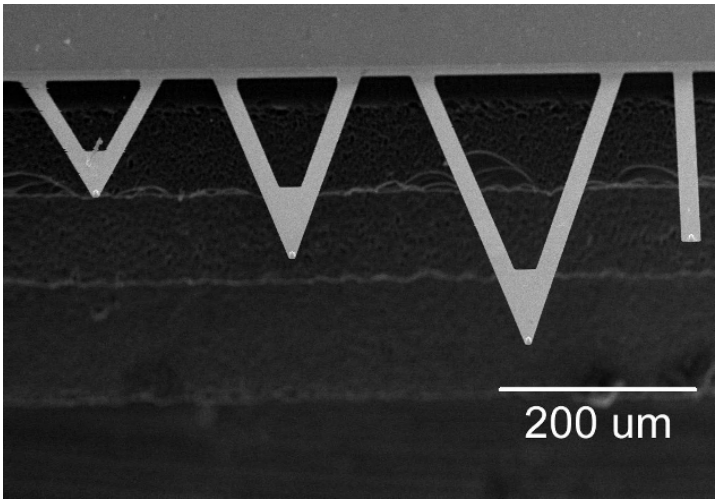

Figure 6.23. *SEM image of AFM cantilevers*

6.4.1.3. *Tip shape*

Tip shape choice is very important and must be tightly related to the properties of the sample being analyzed.

Standard tips can be classified into two categories: low or high aspect ratio (AR). As illustrated in Figure 6.24, choice depends on the sample and the ratio CD/height of the pattern (when considering the limited case of lithographied patterns to be analyzed with an AFM).

Figure 6.25 presents some images of typical cylindrical tip shapes with different AR according to the desired applications.

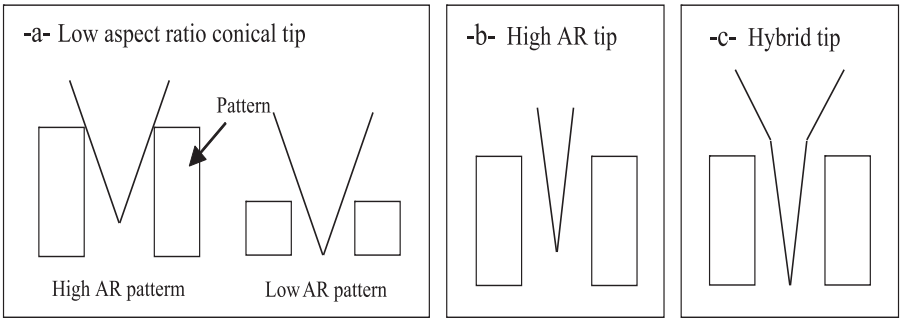

Figure 6.24. *Conical tip choice according to pattern and tip aspect ratio*

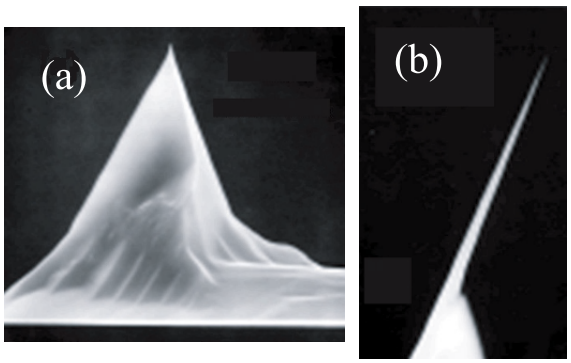

Figure 6.25. *(a) Low AR cylindrical tip; (b) high AR cylindrical tip*

6.4.1.4. *Detection methods*

With regards to AFM technique, optical detection thanks to laser beam deflection is the most used. Mechanical amplification principle lies in the fact that very small movements of the reflective surface generate large movements of the light spot on the photodiode quadrants. Amplification depends on cantilever size: the shorter the cantilever, the larger the angular change. This technique is particularly efficient and allows atomic scale displacement detection.

In some cases, interferometry is used as a detection method to follow the tip motion more accurately. This deals more easily with large tip movements and leads to a better signal to noise ratio. However, from a practical point of view, this technique requires a much more rigorous insulation from vibrations.

6.4.1.5. *Van der Waals forces and distance–force curves*

Even if a material appears neutral for a short period of time, electron distribution over extremely short times may not necessarily be perfectly symmetrical. At a given time, each molecule shows a distinctive charge distribution, and, eventually a different number of electrons; consequently they may interact electrically according to Van der Waals forces existing inside every kind of materials. These interactions also happen between the AFM tip edge and the nearby substrate. Their behavior can be modeled by the Lennard–Jones potential (see Figure 6.26) which allows expression of potential energy variation of an atom of the tip apex (edge of the tip) interacting with an atom of the surface, as a function of distance (r):

$$E = 4\varepsilon\left[\left(\frac{\sigma}{r}\right)^{12} - \left(\frac{\sigma}{r}\right)^{6}\right]$$

for which ε and σ are material dependant constants. σ is approximately equal to the diameter of the atoms involved. The term $1/r^{12}$ is responsible for abrupt variations at short distances, that is to say when $r < \sigma$. It expresses a strong repulsion at short distance, predicted by the Pauli exclusion principle. The term $1/r^{6}$ is responsible for slower variations for larges distances when attractive Van der Waals forces dominate.

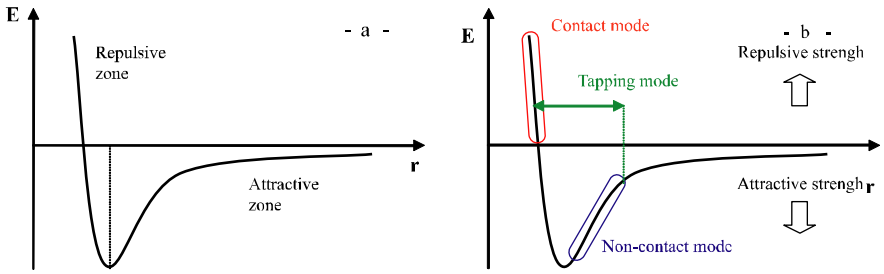

Figure 6.26. *(a) Schematic representation of Lennard–Jones potential with (E) being the potential energy of a pair of atoms and (r) being the distance between them; (b) three basic AFM modes associated with the previous diagram*

6.4.1.6. *AFM working modes*

An AFM has different working modes, differentiated by implied interaction forces. Each mode has drawbacks and advantages. It is more judicious to focus on the complementary nature of the modes, instead of always using the same one as a universal standard, usually leading to measurement aberrations. A standard AFM has three main modes represented in Figure 6.26. These three techniques are located on the Lennard–Jones potential according to their implied forces. These modes work with a tip–surface interaction kept constant, that is to say, the operator has to assign a setting parameter corresponding to a given interaction and hence a given tip height. Each time this setting parameter is not fulfilled, a feedback loop is set off in real time to get back to the initial setting.

6.4.1.6.1. DC or contact mode

This was the first mode to be developed, in which the tip directly "touches" the surface in a feeler tool way. Interactions are then repulsive. This mode is the easiest to use by far, and can be coupled with simultaneous measurements of adhesion, friction, or contact stiffness. However, wear and deformations generated by the tip may deteriorate image quality for some samples.

In this mode, the operator has to fix a setting force called "setpoint" corresponding to a given cantilever deflection. When the system detects a deflection different from the defined setting, feedback is launched to return the tip to the z position where the setting is respected. Tip altitude z is hence adjusted for each point so as to keep the tip–surface interaction constant. Hence, the iso-force image obtained may be assimilated directly to the surface topography.

6.4.1.6.2. AC or non-contact modes

Two non-contact modes can be distinguished. The first, a resonant mode, generally considered as the "true" non-contact mode, consists of placing the cantilever quite far away from the surface (from several tens to hundreds of nanometers) and scanning attractive interactions. In this mode, the tip never touches the surface and oscillates close to its resonant frequency with low amplitude. In this case, regulation acts either on the cantilever oscillation frequency or its amplitude. For example, when working at a given excitation frequency, oscillation amplitudes vary and give information on local force gradients. This amplitude is represented by a vertical displacement of the spot on the photodiode. Consequently the operator can define settings amplitudes that will be the reference for the regulation. Displacements made to keep this amplitude constant are recorded to form an iso-gradiant force image. The tip oscillating quite far from the surface, this mode loses some of the advantages of local probe and is usually not used for topographical study. However, it allows analysis of long range, electrical or magnetic forces using conducting or magnetic tips.

The second mode, called a "tapping" mode, or intermittent contact mode, is a non-linear resonant mode where amplitude of oscillations is larger and the average tip position closer to the surface. At each cycle, the tip hits the "wall" made by the surface repulsive forces. This operating mode is harder to analyze than the previous. Here again, the cantilever is excited around its resonant frequency and amplitude variations of the cantilever are monitored.

This mode is frequently employed to study a samples' topography. Forces involved on the sample can be really soft and the very short contact time hardly induces friction forces on the sample. This prevents deformations on some samples and wear (which is always possible when using a contact mode). The contact area is reduced, even on very deformable samples, hence conferring a very good lateral resolution to this mode.

6.4.2. *3D AFM (AFM 3D) special features*

Standard AFM as described above is quite limited if used to measure lithographied patterns. Indeed, the tapping mode would be the most suitable for this kind of measurement, yet two reasons limit its use. First, when using conical tips (see Figure 6.27(a)) it is impossible to measure re-entrant profiles, for example. Consequently CD tips or flared tips have to be used (see Figure 6.27(b)). Second, even with a flared tip in tapping mode, it would be impossible to get enough point density on pattern sidewalls (see Figure 6.28).

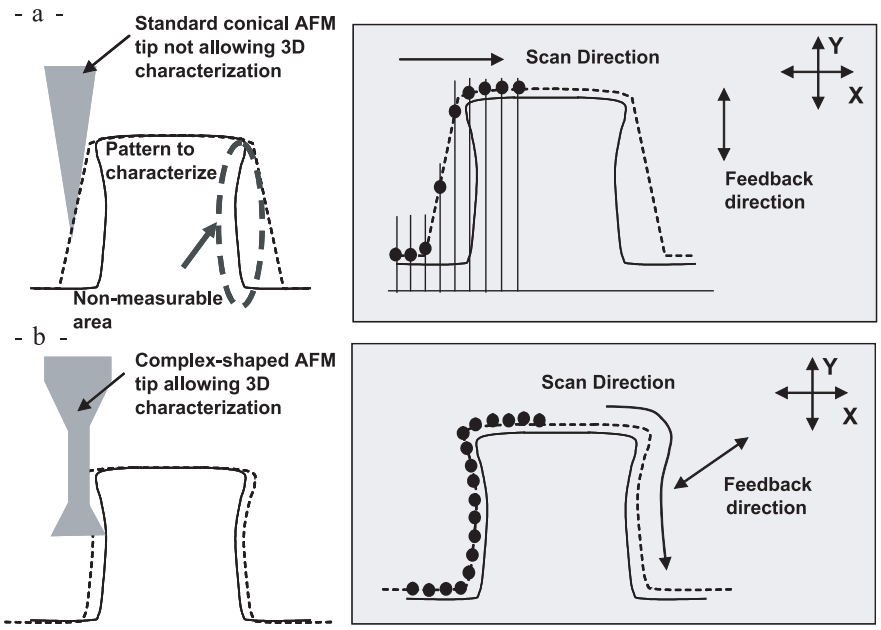

Figure 6.27. *Illustration of the phenomenon of AFM tip convolution: (a) typical tip shape convolution issue using a conical tip; (b) the problem is solved by using a flared tip*

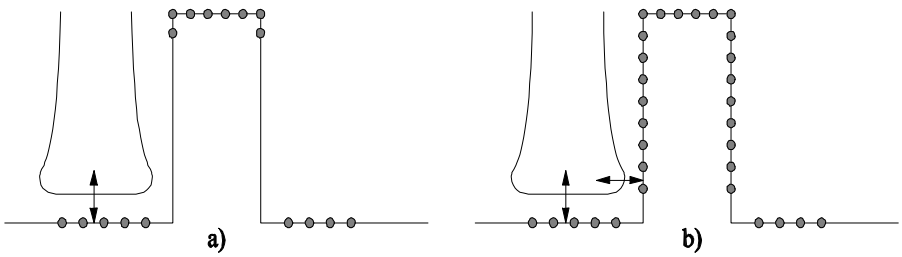

Figure 6.28. *(a) Combining tapping mode and flared tip does not allow access to sidewall information; (b) combining CD-mode and flared tip allows access to accurate sidewall information*

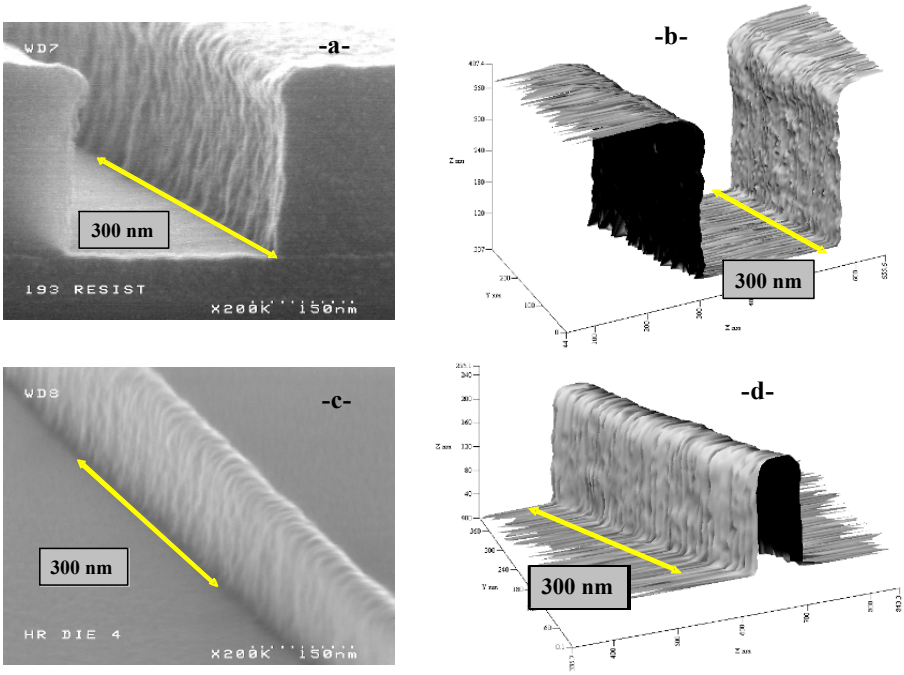

Figure 6.29. *X-SEM images of (a) lithographied pattern with 193 resist and (c) E-Beam resist (c); corresponding AFM 3D profiles are shown in (b) and (d), respectively*

Indeed, data recording on pattern sidewalls is almost impossible (except if the sidewall has quite a gentle slope) because the tip feedback loop only works for the *y* direction. When working with *CD mode* there is a feedback loop on both *x* and *y* directions (see Figure 6.27). Note that the feedback works permanently on the cantilever amplitude for either *x* or *y* directions. By combining this CD mode with a CD tip, it is then possible to measure every kind of structure in the 3D, even with re-enterant profiles (see Figure 6.29(b)). Then, every kind of lithographied pattern can be imaged very faithfully (see Figure 6.29).

6.4.2.1. *Measuring time*

Contrary to received wisdom (an inheritance from classic AFM, with which getting one image could last hours), image acquiring time with 3D AFM is quite fast, between 20s and 1 min according to the precision and accuracy required for the measurement.

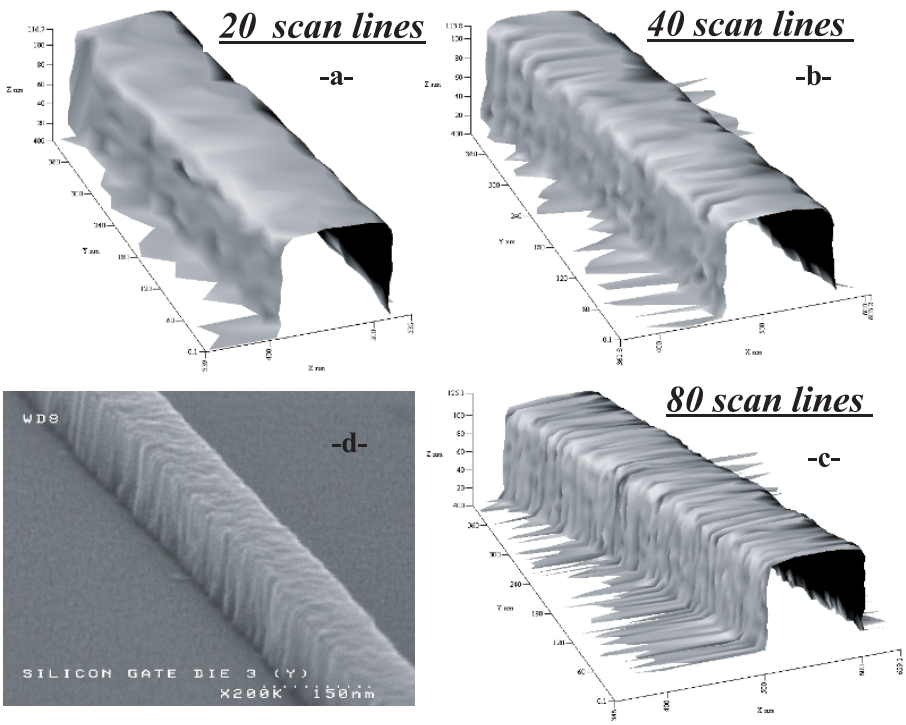

Figure 6.30. *Resolution can be drastically impacted as a function of the number of scan lines*

As shown in Figure 6.30, according to the number of scan lines, three-dimensional resolution will be different. If the operator wants general information on profile and an average CD over a given line length, then they could make an image comprising of in the order of 20 scan lines (typical imaging time: 20s; see Figure 6.30(a)).

On the other hand, if one wants information on line variability (LER and LWR), 80 to 100 scan lines are required for the image (typical imaging time: 1min). In this latter case, the resulting image (see Figure 6.30(c) will have the same qualities as an X-SEM image (Figure 6.30(d)) with the advantage of giving an image plus LER/LWR measurements, which is impossible with X-SEM.

6.4.2.2. *CD tips*

The introduction of CD tips in 1994 by Martin and Wickramasinghe [MAR 94] triggered a revolution among reference metrological techniques. Tips dedicated to

the CD mode have a flared shape, enabling measurement of re-entrant profiles. Typical CD tips and their basic characteristics are represented in Figures 6.31 and 6.32. The five main parameters are:

1) tip diameter (D_0), which determines the smallest measurable hole;

2) tip useful length (L_1), which sets the highest measurable pattern;

3) tip re-entrant maximum profile (O_1), which conditions tip limits to measure re-entrant profiles;

4) tip left and right radius of curvature (R_c), which set the dark area at the bottom of the pattern where no measurement can be made. Typical R_c values are between 10–20 nm, depending on tip model; and

5) re-entrant profile maximum height (H_1), which gives access to the maximum height corresponding to the maximum re-entrant profile (O_1) of the tip.

These last two parameters are tightly linked and determine the measurement quality of patterns comprising negative profiles.

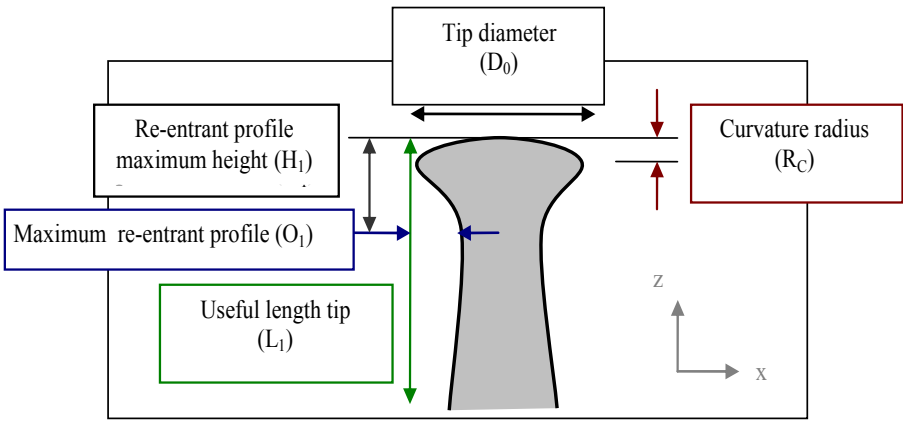

Figure 6.31. *Characteristic dimensions of CDR tips (critical dimension re-entrant profile)*

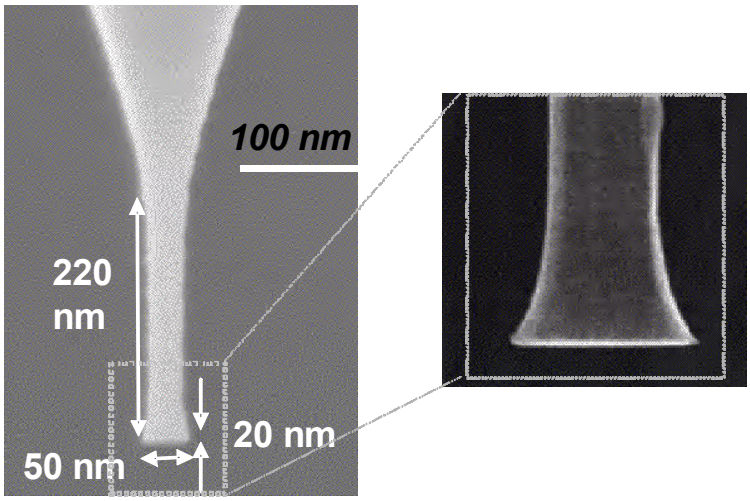

Figure 6.32. *SEM images of a typical 3D AFM flared tip*

6.4.2.3. *CD tip characterization*

To guarantee measurement accuracy with nanometer precision, tips must be characterized before and after each measurement. Indeed, while imaging with AFM, the rough image is always a convolution of the tip (radius and shape) and the real structure (see Figure 6.33). To have access to real dimensions, one has to deconvolute the size and the shape of the tip via mathematical algorithms which process the deconvolution, step by step [DAH 05]. Measurement uncertainty will be all the more important if this deconvolution is not undertaken. Indeed, during the measurements, the tip may wear off or increase in size by collecting particles. If this size change is not taken into account, it is impossible to guarantee measurements with nanometer precision. Ideally, tip size should not vary more than a few angströms before and after a measurement. In that case, reproducibility and accuracy can be guaranteed better than 1 nm.

To this end, two structures of known shape and dimension are used. The first structure (Figure 6.34) enables measurement of tip size. This structure is made of a silicon line with vertical and quite smooth sidewalls, obtained by a plasma etch. This structure's horizontal dimension (L_1) (see Figure 6.34(a)) has first been calibrated thanks to a standard isolated line, which then helps in determining tip width. Indeed, measuring this known L_1 line width with a flared tip leads to measurement of an L-width line (see Figure 6.34(b)) which is the sum of the structure width (L_1) and the tip real size (L_2). One can then derive the absolute tip size: $L_2 = L - L_1$.

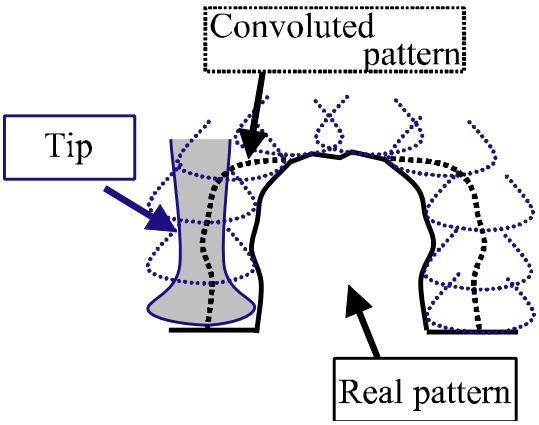

Figure 6.33. *SEM image of typical CD tip for AFM 3D*

Indeed, if we consider the contact point (p_1) between the tip and the structure at z_1 height (see Figure 6.34(c)), the x coordinate is the x_1 coordinate corresponding to a half-diameter shift compared to the structure edge (the benchmark origin being the tip center). Symmetrically, it is the same on the other side of the structure at the same height z_1. By scanning all the calibration structure along x and z directions, one gets at the end of the measurement the convolution of the tip with the structure (see Figure 6.34(d)). The final dimension obtained is $L = L_1 + L_2$. Tip size is then deduced: $L_2 = L - L_1$.

The second structure (see Figures 6.35(a) and 6.35(b)) has a re-entrant profile allowing imaging and characterization of right and left sides of tips with complex shape, and one can hence get access to qualitative information on tip shape thanks to the basic characteristics mentioned before. This structure can either be a line or a trench. To obtain a very precise reconstruction of tip shape, it is very important that all the regions of the tip make contact with the characterization structure. Ideally, this contact point is unique for each side of the tip. The critical step is consequently the realization of these two contact points between the structure and the tip, which allows full characterization of the tip geometry. To get almost two pinpoints as contact points, the edges of the structure are slightly turned upward and thinned to finally obtain curvature radii smaller than 10 nm (see Figure 6.35(b)).

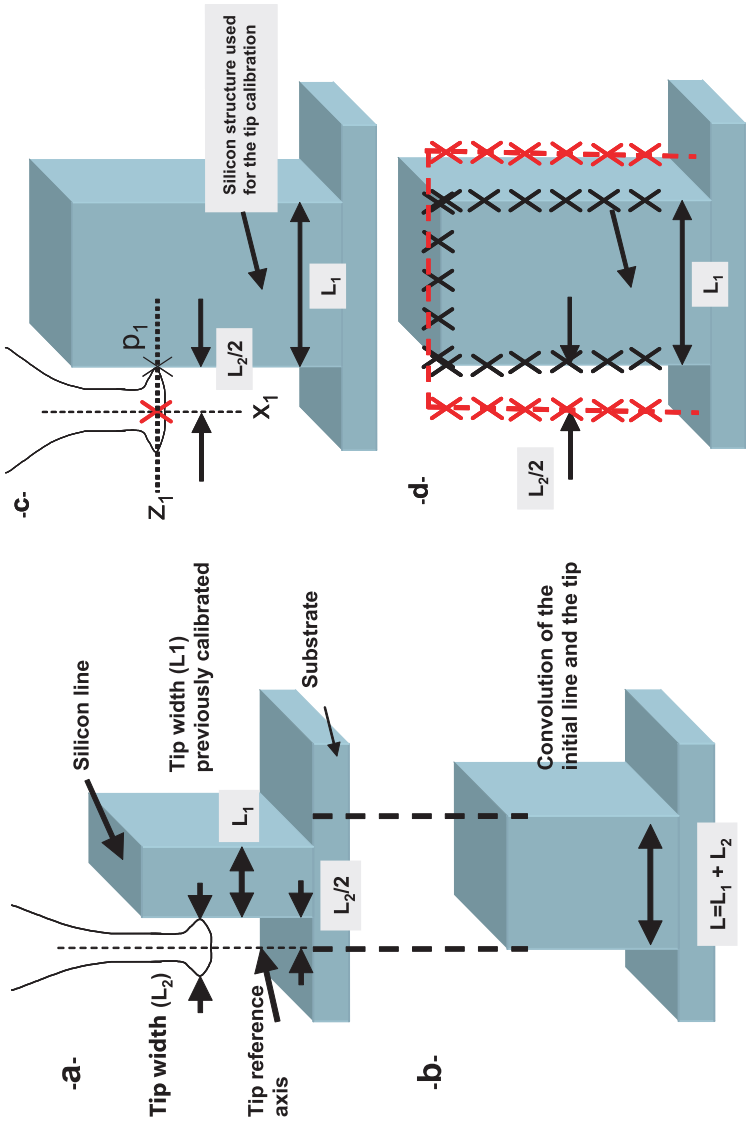

Figure 6.34. *Vertical structure for tip width characterization*

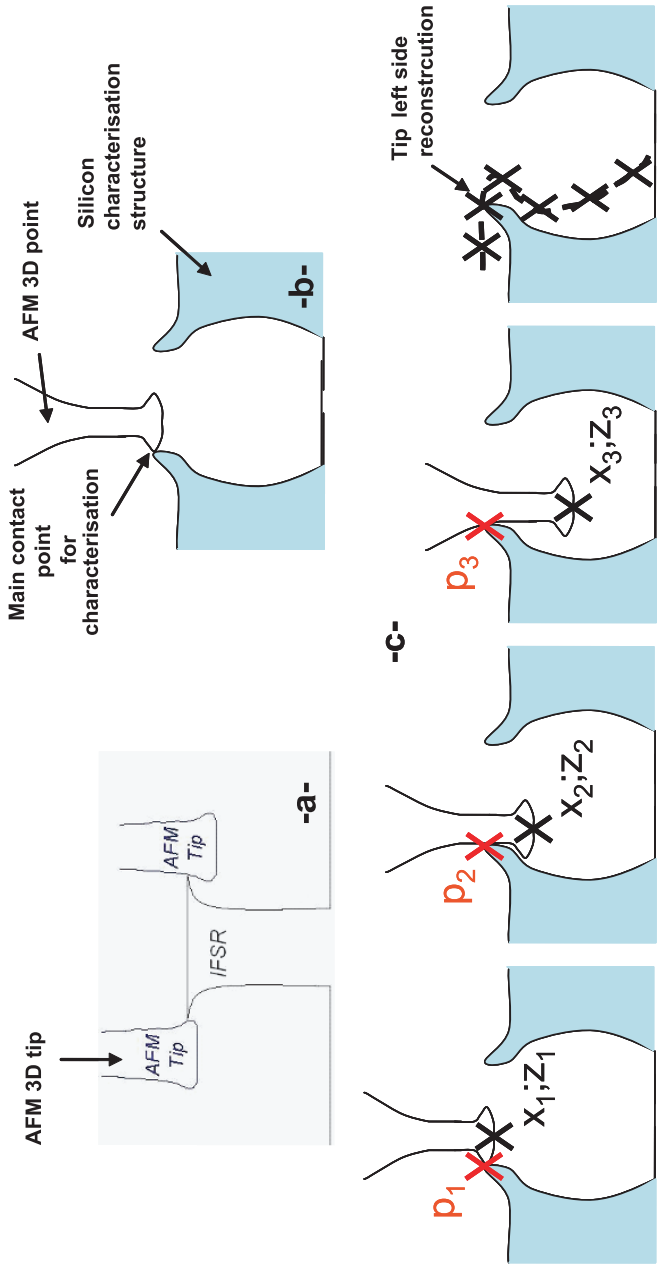

Figure 6.35. *Characterization structure for CD tip shape determination: (a) and (b) re-entrant and ascending structure scheme; (c) tip shape reconstruction principle*

Figure 6.35(c) explains the principle of tip shape reconstruction. Considering a contact point p_i between the tip and the edge of the characterization structure, this precise point corresponds to the (x_i, z_i) coordinates. By representing all the coordinate couples obtained by scanning the whole characterization structure with the tip, it is possible to deduce the shape of the left and right side of the tip (see Figure 6.35(c), final drawing).

The edge of the ascending part of the characterization structure, which provides the contact point between the tip and the structure, must be ultra thin so as to get a contact point close to pinpoint, otherwise the quality of the measurement accuracy and the reproducibility will not be good.

For both characterization structures, measurements have to be made with enough sampling (typically one measurement point every 5 Å) to guarantee best measurement accuracy and best measurement reproducibility.

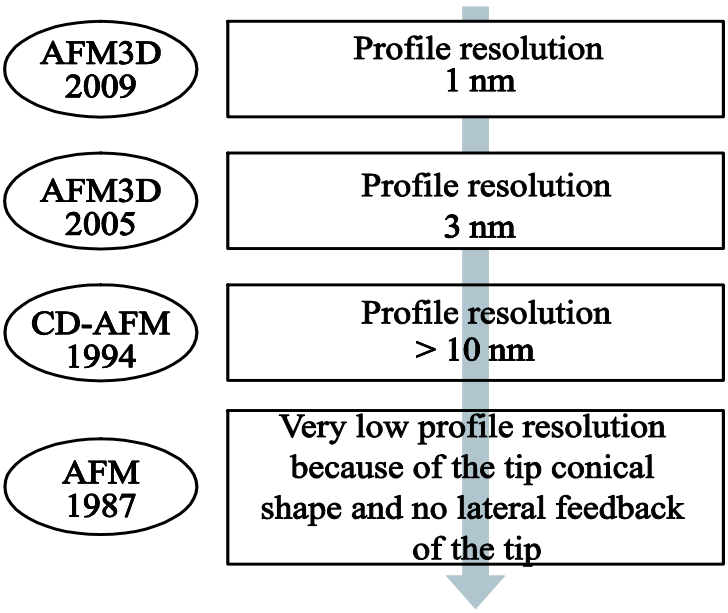

Figure 6.36. *Improvements in AFM 3D lateral resolution since its first use*

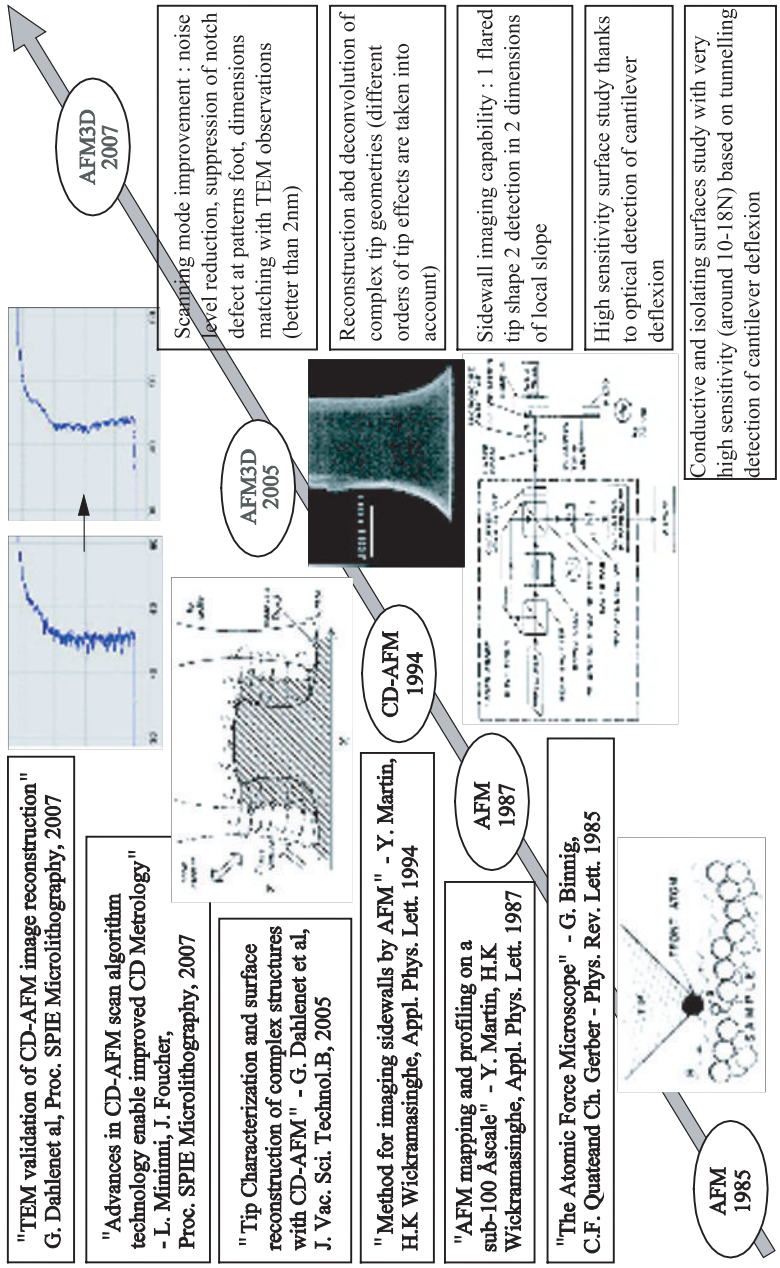

Figure 6.37. *Technological evolution of AFM 3D since invention of AFM in 1985*

6.4.3. *Provisional conclusion on AFM 3D*

AFM 3D is considered a reference metrological tool [DIX 07, UKR 05]. It excels in calibrating CD metrological techniques, but also in the development and follow–up of lithography process, thanks to its measurement versatility and its ability to perform in-line measurements, hence being compatible with the most stringent requirements of the semi-conductor industry. It is a recent technique (1994) now offering a 1nm measurement accuracy [DAH 07, MIN 07] (instead of more than 10 nm at the outset; see Figure 6.36) and a measurement reproducibility of around 0.8 nm. Figures 6.36 and 6.37 present basic references and technological progress associated with AFM 3D, which confer this tool with a promising future in the nanotechnology world. In particular, the possibilities of improvement are still very great, notably with new tip development (for example based on carbon nanotubes) or with new scan modes, for example, dedicated to outline metrology to be used in OPC applications.

6.5. Grating optical diffractometry (or scatterometry)

Scatterometry is an indirect optical method to measure geometrical parameters of diffraction gratings. It analyzes their optical reflectivity and compares it to the theoretical reflectivity computed out of modeled gratings. By identifying theoretical and measured reflectivities, parameters of the modeled gratings are regarded as measures of the real parameters.

This technique has been used since the eighties [KLE 80]. Yet, as the usual tools such as optical microscopes and scanning electron microscopes became outdated and unable to answer the always more stringent requirements of metrology (ever more parameters to measure with ever more precision and accuracy) [ITR 07, UKR 07], the development of this technique accelerated. Compared to CD-SEM, scatterometry enables 2D characterization of gratings (height, CD, SWA) faster and more reproducibly than CD-SEM. Consequently, thanks to its precision, reproducibility and the non-destructive nature of its measurement [MIN 98], this technique was met with quite a favorable welcome in the microelectronics industry.

In this chapter, we will see that this technique is very generic and has several execution modalities, not only for the conception of measuring tools but also for methodology of measurement analysis. This is why we would rather focus on methodologies and examples instead of giving an exhaustive view of the subject. For more practical aspects of scatterometry for metrology, readers should refer, for example, to the SEMATECH report [AZO 07].

Finally, after reading this chapter, we would like readers to have the keys to not only understanding scatterometry and determining whether it can be useful for them, but also that they have acquired an objective and critical point of view of this technique. That is why we have focused on the method's limitations, counterbalancing the extensive and optimistic bibliography already available on the subject.

6.5.1. *Principle*

Scatterometry is an optical measurement technique of object dimensions (usually sub-micron) repeated periodically on a plane substrate. The technique is based on theoretical analysis of the light diffracted by the measured objects.

6.5.1.1. *Object lightning*

Usually, the light source falling on the object is several microns wide, whereas the periodic objects are about one hundred nanometers. Consequently, the spot illuminates several identical objects (see Figure 6.38).

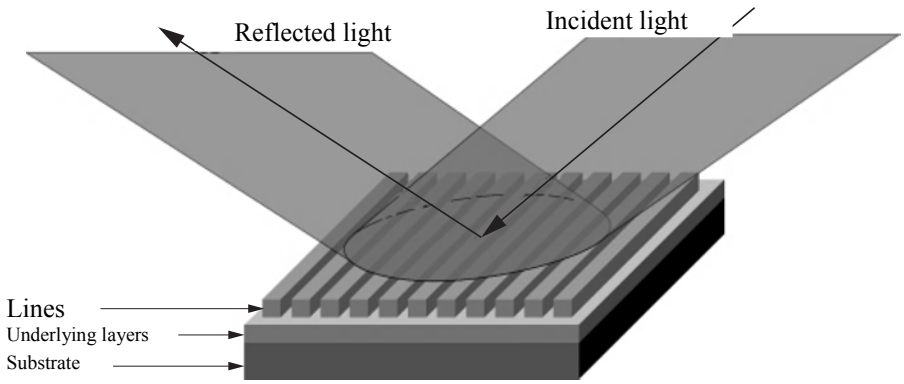

Figure 6.38. *Scatterometry measurement: line lighting scheme. The analysis spot is usually bigger than the measured lines*

Since objects are periodical, light rays are diffracted into preferred directions given by diffraction grating law [PET 80]:

$$\sin\theta_p^d = \sin\theta^{inc} + p\frac{\lambda}{\Lambda}$$

with p the diffraction order (relative integer), θ^{inc} the ray incident angle compared to surface normal, θ_p^d the diffraction angle for p order.

The number of diffracted orders is the number of relative integers p for which $\sin\theta_p^d \in [-1,1]$. The number of diffracted orders is all the more important when the wavelength is short or the period Λ is great. Generally, only the order p=0 is analyzed during scatterometric measurement. Furthermore, light may be polychromatic (several wavelengths λ) or with several incidences (several θ^{inc}).

6.5.1.2. *Making the optical signature*

The electromagnetic waves fall on hundreds of objects which should be arranged in a periodic pattern. Each object contributes to the incident light wave's diffraction; the impact on the global reflected signal is multiplied by the number of objects. Moreover, some phenomena of electromagnetic couplings between objects, and of interferences of reflected beams, strengthen or cancel some of the characteristics of the single object diffracted fields. Consequently, if one assumes that all the objects are identical, variation in one detail will noticeably modify the reflected signal. In classical imaging, the numerical aperture (NA) of the optical system and the working wavelength (λ), both set the resolution limit [BOR 99]. Rayleigh criteria give an evaluation of this resolution limit, as $\Delta x = \lambda/(2NA)$. In the visible range, resolution is limited to a few hundred nanometers, which is far below the requirements of metrology for microelectronics.

In scatterometry, the reflected signal comprises information on object details; even those whose dimensions are below the Rayleigh criteria. So, the difference with imaging lies in signal processing. With imaging, the image is built without an *a priori* knowledge and is consequently limited. By contrast, scatterometry may reach resolutions below one nanometer provided that *a priori* information on the geometric model of the objects are given to the reconstruction algorithms.

6.5.1.3. *Modeling*

Usually, an object's fabrication process is known. Not only are the material refractive indexes known, but also the objects shape and rough dimensions. Consequently the object is represented by a shape, the dimensions of which are parameters to be determined, and with materials which are known. A theoretical answer is computed thanks to electromagnetic computation programs for several sets of parameters (usually several thousand), and the answer which is the closest to the observed optical signature is chosen. The parameters values corresponding to the chosen signature are an estimate of the object shape dimensions. Figure 6.39 presents the general principle of scatterometry measurement.

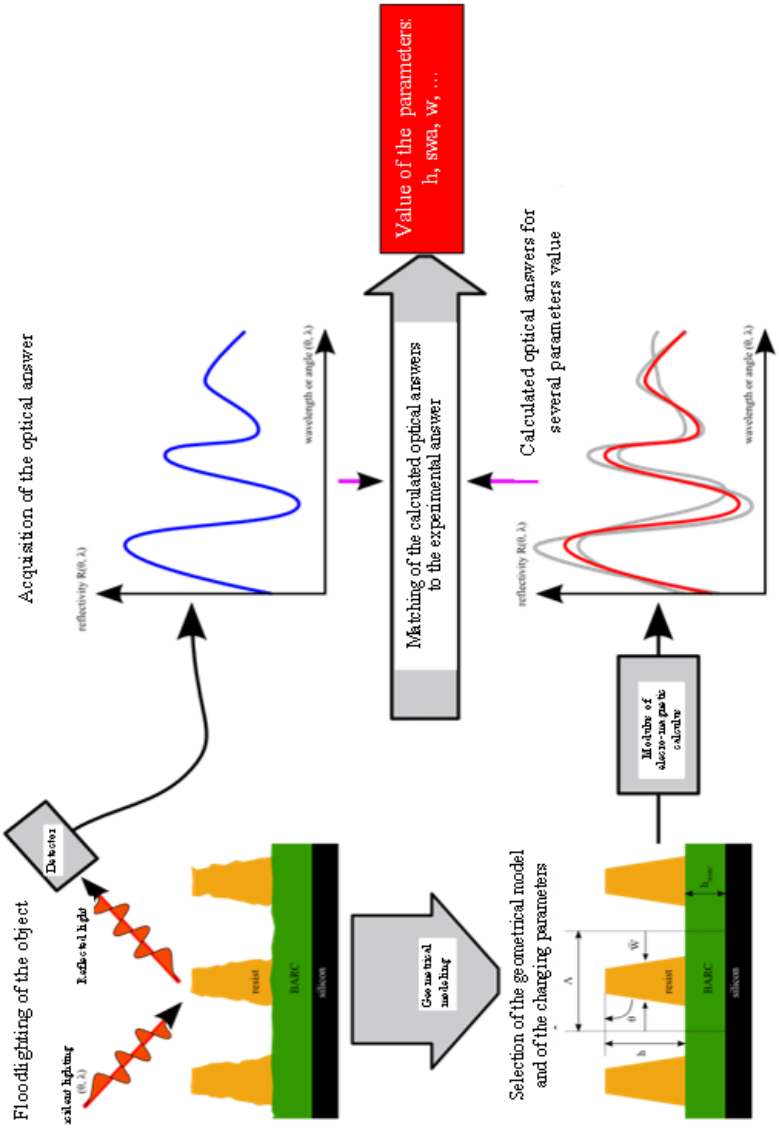

Figure 6.39. *General principle of scatterometric measurement. The optical response of the object is measured by an optical system. The object is modeled and its parameters are optimized so as to minimize the difference between the measurement and the electromagnetic simulation of the model*

In a nutshell, a theoretical object is modeled and its parameters are adjusted to best match theory and experiment. The best parameters are then called "measurements" (of height, width, sidewall angle, etc.).

6.5.2. *Example: ellipsometry characterization of post development lithography*

Scatterometry is often used to measure resist line width after lithography and development, and, eventually, after etching. Line patterns periodically repeated are drawn inside squares roughly 50 microns wide (usually in the cutting path of the silicon wafer, that is to say between the useable chips).

Here, in the first place, the simplest geometrical model usually used is a trapezoid line model placed on a Bottom Anti-Reflective Coating (BARC) on top of silicon. Figure 6.40 shows the generally-used geometrical model and the corresponding parameters.

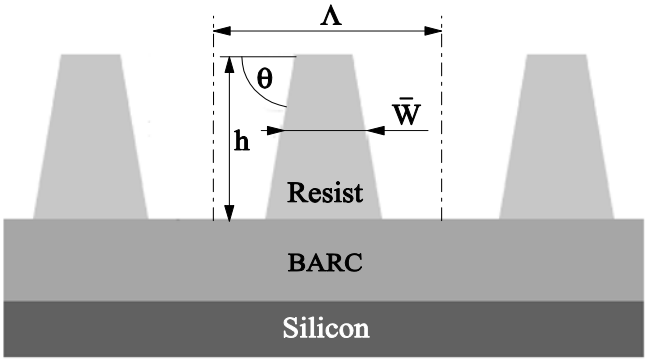

Figure 6.40. *Example of modeling: resist lines set into grating on an anti reflective substrate (BARC) on silicon. In this example, the model is determined by five parameters (h, h_{barc}, $\overline{w}$, θ, Λ)*

A distinction must be made between "free" geometrical parameters and "fixed" ones, according to the information level for each. Generally, the pitch parameter Λ (pattern period) is known precisely, the h_{barc} variable (anti-reflective coating thickness) is usually characterized before resist deposition. These two variables are hence fixed because they are known. By contrast, variables concerning the trapezoid dimensions are unknown. They characterize the lithography process quality. Consequently h (pattern height), $\overline{w}$ (half-height critical dimension), and θ (sidewall angle) are all free variables.

6.5.2.1. *Ellispsometry measurements*

The optical measuring tool is usually an ellipsometer working at a fixed angle and with variable wavelength (between 20–800 nm, that is to say, between 1.5–5.0 eV). This tool is usually used to measure thicknesses of deposited coatings on a given substrate. The ellipsometer enables the measurement of the complex variable related to the ratio of reflectivity amplitude for "*p*" polarization (r_p, perpendicular to the lines) and "*s*" (r_s, parallel to the lines):

$$\rho = \frac{r_p}{r_s} \overset{def}{\equiv} \tan\Psi \exp(j\Delta), \text{ with } j = \sqrt{-1}, \quad \Psi, \Delta \in [0, 2\pi]$$

Generally, this complex variable is measured thanks to two real variables α and β comprised between -1 and +1:

$$\begin{cases} \alpha = \dfrac{\tan^2\Psi - \tan^2 A}{\tan^2\Psi + \tan^2 A} \\ \beta = \dfrac{2\cos\Delta \tan\Psi \tan A}{\tan^2\Psi + \tan^2 A} \end{cases}$$

with *A* standing for a parameter of the measurement system (position of the ellipsometer analyzer).

Figure 6.41 shows the (α, β) curves fit for a grating of resist lines of 100 nm width, 240 nm period, on an anti-reflective layer of 90 nm on top of silicon.

6.5.2.2. *Sensitivity to parameter variations*

Ellipsometry has already demonstrated its extreme sensitivity to thickness and refractive index variations of the layers of a given stack. This property is also true when considering variations of a grating's main parameters (lines height and width).

Figure 6.42 shows the variations of the measured signals α and β when one of the parameters $\overline{w}$, *h* or θ varies, that is to say:

$$S_k(\lambda) = \frac{\partial\alpha(\lambda, p)}{\partial p_k} \times \Delta p_k$$

with $p = (\overline{w}, h, \theta)$, $k \in \{1, 2, 3\}$ and Δp = (1 nm, 1 nm, 1°).

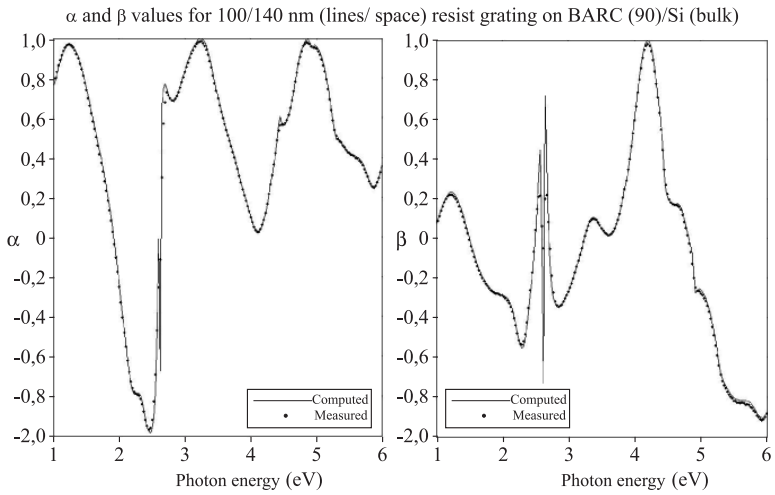

Figure 6.41. *Curves fitting between theory and experiment for the ellipsometric answers a and b in the case of a dense resist line pattern on 90nm of BARC on top of silicon (line width $\overline{w}$ = 100 nm, period Λ=240 nm, sidewall angle θ =90°), according to photon energy (eV)*

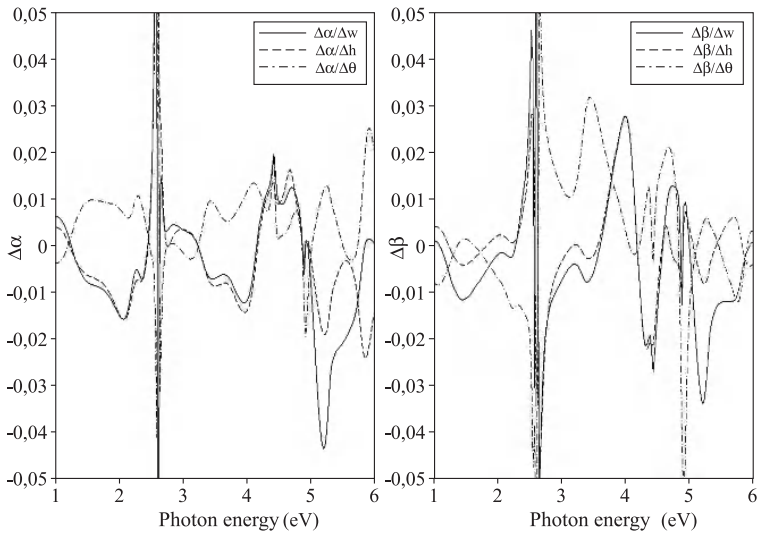

Figure 6.42. *Variations of α and β measurements when grating parameters vary. The modelised grating is the same as in Figure 6.41. The modelised variations are 1 nm for the $\overline{w}$ parameter, 1nm for the height h and 1° for the sidewall angle θ The signal variation associated with a parameter variation is strongly linked to the nominal grating parameters*

In this example variations are of the order of some 10^{-3}. Generally this value is above the noise level of usual tools; consequently it allows measurement of very small variations (around 1 nm), provided that the chosen geometric model is close enough to the real structure.

Note that the curves in Figure 6.42 are specific to a given structure and to given experimental conditions. Indeed, signal variations depend on parameter values (and not only on parameter variations). Consequently these sensitivity curves are different from one structure to another. In particular, as line dimensions decrease, sensitivity quickly decreases, particularly for the sidewall angle θ.

Sensitivity analysis of an optical configuration for a given object and a given tool is a very complex problem. Section 6.5.4 gives some additional information.

6.5.2.3. *Signatures analysis*

In this example, signature analysis consists of finding the parameters $p^* = (\bar{w}^*, h^*, \theta^*)$ such that the difference between the measured (α^{exp}, β^{exp}) and the theoretical (α^{theo}(p*), β^{exp}(p*)) signatures is as small as possible. In most cases, the criteria to minimize is χ_2 which, in this case, may be written as:

$$\chi^2(p) = \frac{1}{2N}\left\{\sum_{i=1}^{N}\left(\frac{\alpha^{theo}(p,\lambda_i) - \alpha^{\exp}(\lambda_i)}{\sigma_{\alpha,i}}\right)^2 + \sum_{i=1}^{N}\left(\frac{\beta^{theo}(p,\lambda_i) - \beta^{\exp}(\lambda_i)}{\sigma_{\beta,i}}\right)^2\right\}$$

with σ_α and σ_β representing the noise (or uncertainty) levels for the variables α and β. The χ_2 criteria may be understood as an euclidian distance between the theoretical and experimental signals in the wavelength space, weighted by the given confidence level σ.

For this stage, an electromagnetic computation program evaluates the theoretical signatures corresponding to the various parameters, and another module chooses among the tested parameters those producing the lowest χ_2. The practical details of these computations are numerous and are partially presented in section 6.5.4.

6.5.2.4. *The different optical configurations*

As previously mentioned, scatterometry's generic principle may be applied to a great variety of optical configurations. The treatment of the measurements differs because the configuration specificities have to be integrated into any modeling. Instead of making a difference between industrial scatterometers (proposed by major suppliers for microelectronics) and more academic tools, we instead emphasize the different principles involved, their advantages and drawbacks.

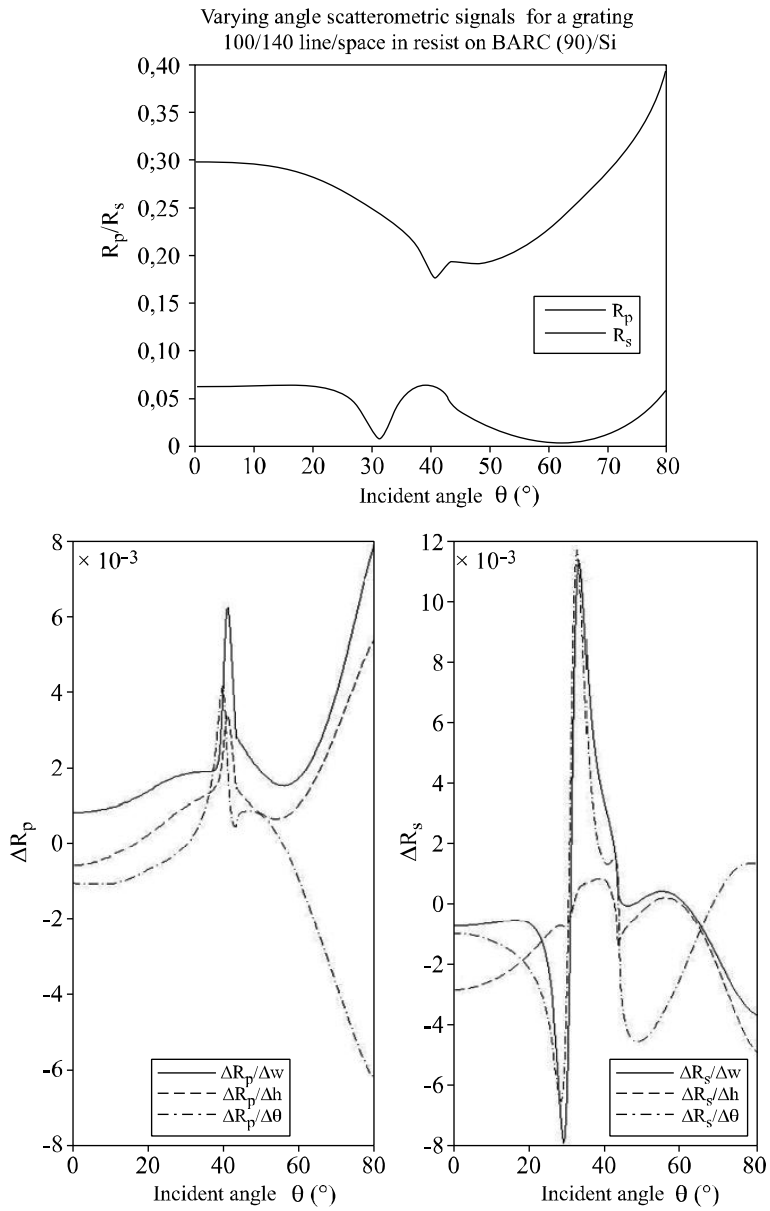

Figure 6.43. *Left: s and p polarization reflectivities for variable incident angles when observing the grating described in Figure 6.41. Right: variations of these reflectivities when one of the grating parameters varies (line width $\overline{w}$, height h, sidewall angle θ). Reflectivity is normalized compared to 1*

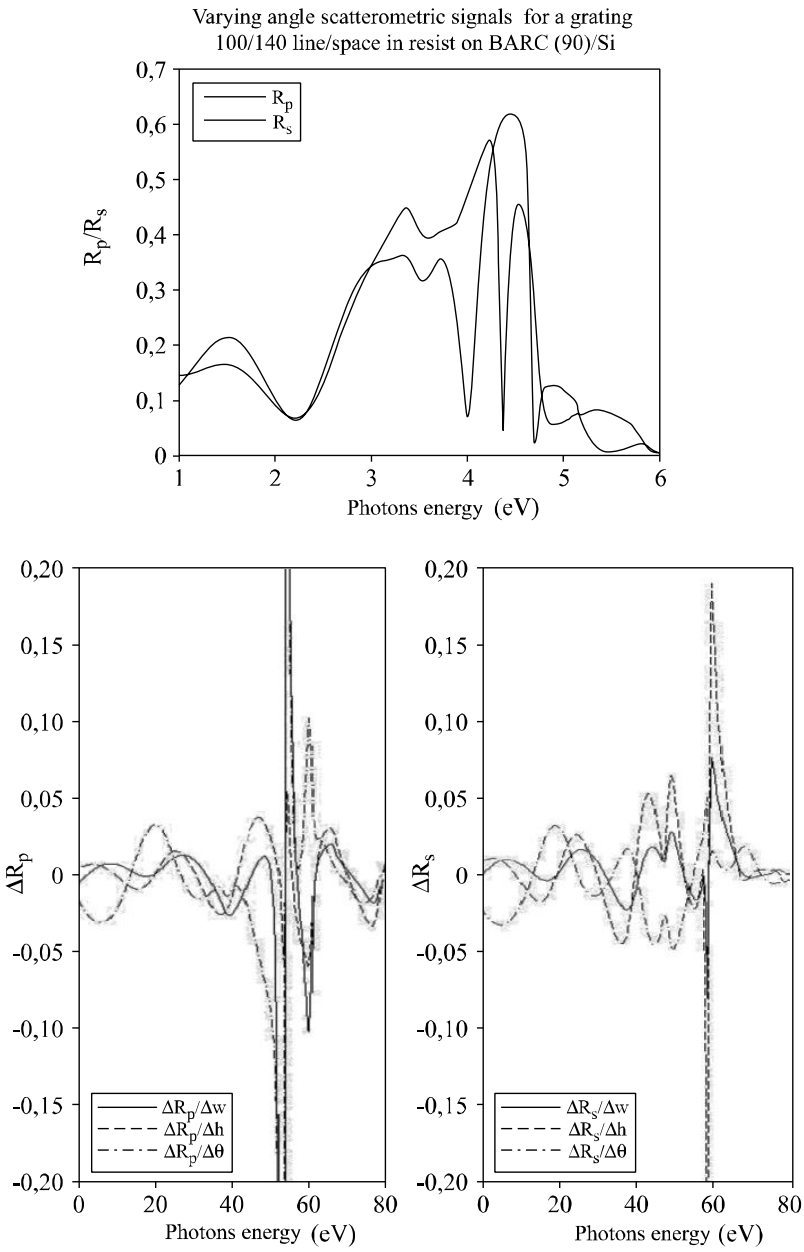

Figure 6.44. *Left: s and p reflectivity spectrum for the grating of Figure 6.40. Right: variations of these reflectivities when one of the grating parameters varies (line width $\overline{w}$, height h, sidewall angle θ). Reflectivity is normalized compared to 1*

6.5.2.5. *Spectroscopic and angular configurations*

Scatterometers can be classified into two groups: spectroscopic tools and those with angular resolution. At the time of writing, no tool combines the two approaches.

Spectroscopic configurations offer to measure the optical response of the patterns when illuminated by a polychromatic light (usually in the visible-UV range: 250–750 nm) with only one value of incident angle. The optical response may be an ellipsometric signal [$\alpha(\lambda)$, $\beta(\lambda)$], a reflectometric signal [$R_p(\lambda)$, $R_s(\lambda)$] (R_p and R_s being the reflectivity coefficients for *p* and *s* polarizations) or a polarimetric signal $M(\lambda)$, with M being the Müller matrix of the object illuminated.

On the other side, angular configurations offer to measure the optical response of a pattern for several incident angles. The most frequent tools measure reflectivity for p and s polarizations, that is to say [$R_p(\theta,\phi)$, $R_s(\theta,\phi)$], θ and ϕ respectively standing for the polar and azimuthal angles of the incident waves. Note that some polarimetric tools measure the Müller matrix $M(\theta,\phi)$ according to the incident angles.

Figure 6.43 shows a signature example, concerning a grating with lithography and developed resist and lit with a variable incident angle. Figure 6.44 presents the same variables for a changing wavelength.

In the microelectronics industry, the most widespread techniques are spectroscopic ellipsometry (KLA Tencor, Nanometric) spectroscopic reflectometry (Nanometrics, Nova) and goniometry (variable angle) with a single wavelength (KLA Tencor).

6.5.3. *Pros and cons*

Performances of the tools, either spectroscopic or angularly resolved, strongly depend on several configuration parameters such as signal to noise ratio, angular or spectral range, etc. They also depend on the targeted application and the optical and geometrical characteristics of the analyzed objects. That is why classification of the existing equipment according to their performances and general criteria is very difficult. Nevertheless, it is still relevant to quote some advantages and drawbacks inherent to each tool category.

Spectroscopic tools have the advantage of being able to distinguish a material difference between two geometrical elements. Indeed, two materials will never have

the same refractive index over a large wavelength range. This is not the same when only one wavelength is used.

Nevertheless refractive index characterization for materials is a complex indirect problem and brings its own uncertainties. An imprecise index measurement may have an impact and significant effects on the precision of spectrometric scatterometry (which use refractive index tables). Consequently one-wavelength methods such as angularly resolved scatterometry are easier to implement.

6.5.4. *Optical measurements analysis*

Scatterometry associates measurements of an optical response to a measurement-computing algorithm. Optical measurement has to be sensitive to the variations of the parameters one wants to measure, and these variations must be distinct for each parameter. The computing algorithm is a compulsory tool. It withdraws information on parameter values out of the optical measurements and provides usable dimensional results.

Today, there is no direct non-iterative algorithm that enables this processing. Generally, the strategy consists of calculating the optical signal (see section 6.5.4.1) for a set of parameters defined by either a sequence (a set of iterations) of fixed parameter values (tabulation of the optical responses; the so-called "library" method) or an adaptative sequence (see section 6.5.4.3). For each iteration, the electromagnetic response is computed and a statistic analysis enables a decision to be taken: either to continue or to stop the sequence (see section 6.5.4.2). In the next sections, we give a quick overview of the techniques of measurements analysis.

6.5.4.1. *Electromagnetic modeling*

Electromagnetic modeling of patterns illuminated by the tool optical system, consist of calculating the electromagnetic properties of light diffracted by the pattern (the ideal object described by a set of parameters). More precisely, it consists of resolving, with an acceptable computing time, Maxwell's equations (electromagnetic laws) for an incident ray on the considered pattern, hence producing a theoretical signature $R^{theo}(\mathrm{x}_i,\mathrm{p})$, with $x_{i=1\ldots N}$ standing for the illumination conditions (incident angle, wavelength, etc.) and p representing the parameter vector of the studied object.

There is not one single computation technique and its choice will not be discussed in this chapter. Nevertheless, "the coupled wave" technique is preferably chosen for mono-periodic patterns. In the literature, it is often referred to as the

"RCWA method" (rigorous coupled wave analysis) or as the "MMFE" (modal method by Fourier expansion).

The RCWA method uses the periodicity of a structure to develop the field and index distribution into Fourier's series. When the structure is not invariant compared to an axis perpendicular to the periodicity axis (which is the case of resist line patterns showed in Figure 6.45, when the sidewall angle is not equal to 90°), the structure is sliced into small rectangular layers (see Figure 6.45).

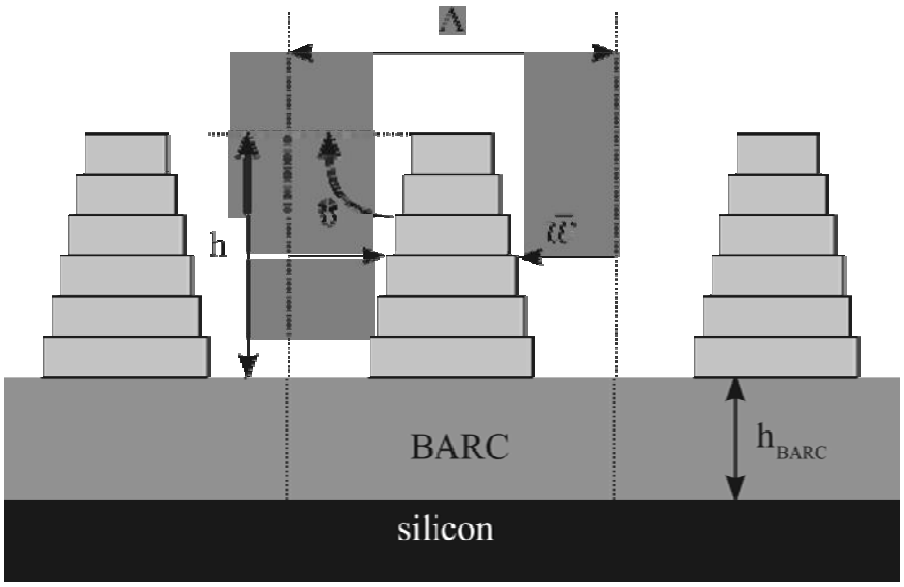

Figure 6.45. *Electromagnetic modeling of the structure from Figure 6.40. When the profile presents non-vertical sidewalls, it is cut into rectangular slices. Computation precision is linked to the number of slices*

For each slice, the normal modes of the electromagnetic field are developed into Fourier's series. Then the electromagnetic field is decomposed on the basis of the normal modes. Finally, continuity equations from one slice to another (which define the modes coupling between slices) are applied, hence establishing a complex relation between incident and reflected fields.

The incident field is given by the optical configuration; it is then easy to determinate the field reflected by the structure, which is the result sought.

Computation precision is mainly determined by two criteria: the finite number of Fourier coefficients used for the computation and the number of slices used for

structure cutting, which must be as great as possible. Computation time generally varies according to the cubic power of the number of harmonics and linearly with the number of slices. Surprisingly, the computation is all the more precise if the period is short, because less harmonics are required for a good electromagnetic field representation. An empirical formula helps determine the required number of harmonics:

$$M_\eta = A(\eta) f(1-f)\Delta\varepsilon \frac{\Lambda}{\lambda}$$

where A(η) is a constant which depends on the required precision η, f is the ratio between the line width and the period Λ, Δε is the permittivity contrast between the top and bottom indexes of the grating (air and resist in the case of Figure 6.45).

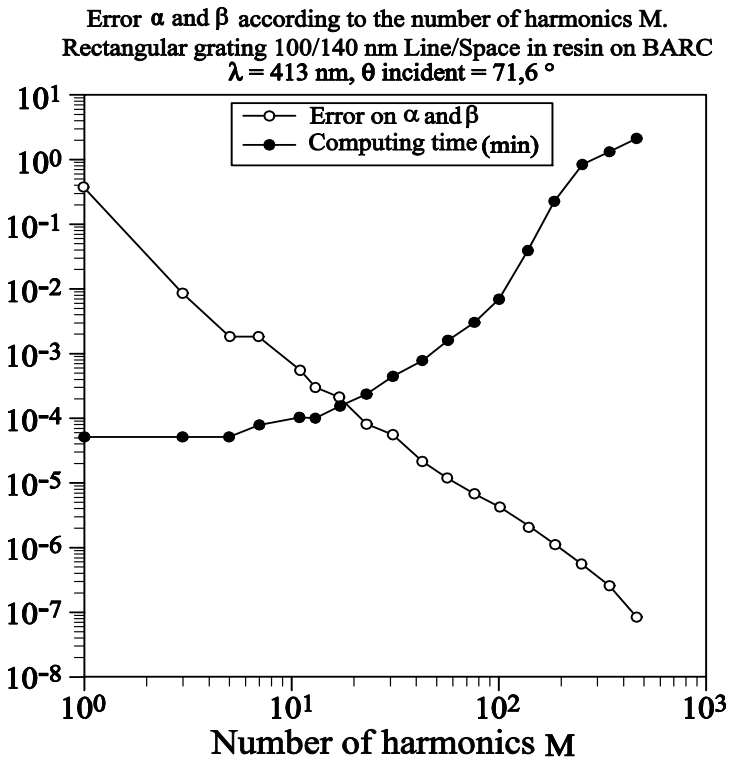

Figure 6.46. *RCWA method convergence plot according to the number of harmonics describing the electromagnetic field in the structure (grating described in Figure 6.40). The curve is only plotted for one incident angle (θ^{inc} = 71.6°) and one wavelength (λ = 413 nm)*

Figure 6.46 presents the RCWA method's convergence, according to the number of harmonics used to describe the electromagnetic field of the structure. Computing time is also given (in minutes).

Remember that in almost all cases, the electromagnetic field is poly-chromatic or multi-angle (respectively spectroscopic or angularly resolved scatterometers). Consequently the incident field is decomposed into elementary monochromatic and mono-angle ("plane wave") fields. So, computation of a spectroscopic or angular signal requires several computation rounds and computation time is multiplied by the number of analyzed plane waves. Typically, computations take into account one hundred waves.

Other modeling techniques are being studied for monoperiodic and biperiodic cases. One could quote the effective index method for structures whose dimensions are small compared to wavelength [ABD 07], the integral methods based on the development of electromagnetic solutions into Green functions [MAC 02, YEU 01], or the curvilinear coordinates method [CHA 80].

6.5.4.2. *Statistic modeling*

Once the electromagnetic computation for one or several ideal pattern is over, the problem consists of comparing it to the measured signals. In most cases, χ_2 measures the distance between two signals [WAS 04]:

$$\chi_2(p) = \frac{1}{N}\sum_{i=1}^{i=N}\left(\frac{R^{\exp}(\theta_i,\lambda_i) - R^{theo}(\theta_i,\lambda_i,p)}{\sigma_i}\right)^2$$

where N represents the number of points where the signal is recorded, (θ_i, λ_i) represent the incident light conditions (incident angle and wavelength) for the experimental point i, R^{exp} and R^{exp} are the experimental and theoretical signal vectors, σ_i is the noise level corresponding to the experimental condition I, and $\boldsymbol{p}$ is the parameters vector for which the χ_2 criterion is evaluated.

This criterion choice has consequences because it implies underlying hypotheses concerning the statistical state of the distances between R^{exp} and R^{theo}, indeed their probability density must be Gaussian and uncorrelated. Actually, these hypotheses may be questionable because they are not checked. Nevertheless the χ_2 criterion remains the most popular because of its simplicity.

6.5.4.3. *Parameters determination*

Parameter determination consists of finding the parameters vector $\boldsymbol{p}^*$ such that the statistical criterion (usually χ_2) is minimal.

This parametric optimization can be extremely difficult because there are usually several parameter sets, p, which are local χ_2 minima. The solution sought corresponds to the minimum of these local minima.

These local minima are due to non-linearity of the signals $R^{theo}(\theta i, \lambda i, p)$ considered as a function of the parameter p. Consequently, the number of local minima depends not only on the number of parameters but also on the optical configuration. As an example, ellipsometric signatures have a more pronounced non-linear behavior than goniometric signatures: generally, for ellipsometric measurements, χ_2 function will have more local minima.

This distinctive feature has consequences for the numerical methods because non-linear optimization is much more complex and requires much more computation time than linear (or convex) optimization.

When faced with this difficulty, several strategies may be adopted, depending on the application and the complexity of the geometry studied. The first solution consists of finding the global minimum of the χ_2 function over the whole space of parameters, thus costing long computation time. The second solution assumes that the zone containing the global minimum is quite precisely known, so that it contains only one local minimum. This local minimum will be found thanks to a local optimization algorithm.

Practically, these two approaches are used complementarily. The first one is used to detect the zone where the global minimum is also local, and the second is used to precisely find the global minimum.

Parametric optimization is an extremely broad subject which will not be dealt with here. Some scatterometric results treated by heuristic and deterministic algorithms are given in [RAY 04]. We will only mention library search (section 6.5.4.4) and Levenberg-Marquardt non-linear regression [PRE 92].

6.5.4.4. *Library search*

This method consists of first calculating the theoretical response $R^{theo}(\theta, \lambda, p)$ for a great number N_L of parameters $\{p\}$ and then choosing the parameter set $\boldsymbol{p}^*$ for which $\chi_2(p)$ is minimum. All the calculated signatures are called "library" and stocked on a file server. When a measurement is realized, it is compared to the

library. The advantage is that once the library is set up, the searching time for $\boldsymbol{p}^*$ is very fast.

Regression search consists of finding a sequence of parameter sets $\boldsymbol{p}_n$ for n = 1, 2, 3, etc., such that $\chi_2(p_{n+1}) < \chi_2(p_n)$. When n is great enough, we find p^* such that $\chi_2(p^*)$ is minimum. Compared to the library search, theoretical response $R^{\text{theo}}(\theta, \lambda, p_n)$ computation is made during the solution search, which slows the searching time down but does not require long pre-computations.

In a production environment, the first approach is preferred. Yet the generally accepted solution is a mix of both techniques.

6.5.4.5. *Limits*

Scatterometry limits are given by statistical criteria and by analysis of the scatterometer parameters and their informative environment.

6.5.4.5.1. Statistical limits

Supposedly, a chosen geometric model is perfect and the measurement noise is strictly Gaussian (its standard deviation is constant; in the homoskedastic case $\sigma_i = \sigma$). Consequently parameters follow a Gaussian law with a variance–covariance matrix expressed by:

$$[V] = Var(p) = \frac{\sigma^2}{N}[S]^{-1}$$

where the sensitivity matrix [$\boldsymbol{S}$] is given by:

$$S_{kl} = \frac{1}{N}\sum_{i=1}^{i=N} \frac{\partial R^{theo}(\theta_i, \lambda_i, p)}{\partial p_k} \times \frac{\partial R^{theo}(\theta_i, \lambda_i, p)}{\partial p_i}$$

A geometrical interpretation of the variance–covariance matrix can be found in [UKR 07]. V diagonal contains the squared standard deviation (uncertainty) of the various parameters ($\sigma^2_{pk} = V_{kk}$) and the correlation between two parameters is easily obtained with the relation:

$$R_{kl} = \frac{V_{kl}}{\sqrt{V_{kk}V_{ll}}} \quad R_{kl} \in \left]-1,1\right[$$

These simple relations enable us to propose some practical rules on parameter uncertainty:

– it is proportional to the measurement noise level σ;

– it is inversely proportional to the square root of the number of measurement points $\sqrt{N}$;

– it is inversely proportional to the measurement sensitivity, that is to say the signal variation for a given parameter;

– for two variables, we can establish that it is proportional to $1\Big/\sqrt{1-R_{12}^2}$.

Consequently, tools are intrinsically limited by measurement noise, the number of points, the measurement sensitivity to parameters variations, and by the correlation of measurements.

Considering this statistical point of view, it is all the more possible to compare different tools and optical configurations, provided that noise and the number of experimental points are given, and the sensitivity calculated [HAZ 07].

Nevertheless, even if this analysis is necessary, it is not satisfactory from many points of view. Indeed, theoretically, parameter uncertainty ([V]) tends toward zero when noise tends towards zero or the number of points tends towards infinity. In practice, this is not observed and parameter variance is always two to ten times (and sometimes more, according to the case) greater than the theoretical variance. Besides, biases are observed, that is to say that the mean value of parameters doesn't tend towards the true value. It comes from the fact that this analysis assumes that the model chosen to represent the measurement is perfect.

6.5.4.5.2. Practical limits

Of course, the perfect model hypothesis, which is common to all data analysis methods, is, in essence, wrong [HAZ 03]. However, it plays a crucial role in scatterometry for several reasons, which may be linked to the above statistical analysis. On the one hand, measurement noise is usually low; consequently modeling errors are more visible. On the other hand, considering today's microelectronics metrology requirements, measuring tools are at the edge of their sensitivity and, coupled with the increasing number of parameters to determine,

sensitivity ([***S***]) becomes very low. As a consequence, the impact of modeling errors becomes greater and greater.

Modeling error takes several forms and can be split into several terms:

$R^{exp} = R^{theo}$

$+ \varepsilon$ experimental signal noise

$+ \varepsilon_M$ geometric modeling error

$+ \varepsilon_I$ error related to optical indexes uncertainty

$+ \varepsilon_T$ experimental setup modelling error

$+ \varepsilon_P$ sample position and alignment error

The geometric modeling error ε_M corresponds to the error made when some details of a pattern are not parametered, or when the object is not homogenous, that is to say not identical from one period to another [PUN 07, QUI 05].

Index modeling error happens when the refractive index tables involved are not exact. Generally, indexes are also determined by data inversion techniques and the problems are the same as for scatterometry ("statistical" error, modeling error, etc.).

These two kind of errors concern the characteristics of the object we want to characterize and hence, the *a priori* knowledge of it. However, partial knowledge of the measuring tool may also induce modeling errors ε_T: incident beam quality (aperture angle, wavelength), polarizer alignment, beam alignment, calibration files, all being functions of imperfections from fabrication, mechanical element precision, or even knowledge of all the phenomena implied in a measurement.

Positioning error ε_P concerns the place of a sample compared to the beam. It depends on the alignment precision of the moving stage holding the sample, the sample attitude correction, and also the precision of the polar orientation (compared to the main axes of the optical system) of the diffraction gratings.

Unlike measurement noise, ε_M, ε_I and ε_T errors are systematic (constant). Indeed, the model is generally fixed for a measurement session and the tool remains still during a measurement. By contrast, the ε_P samples positioning error may be considered to be semi-statistic because it is systematic for one measurement but varies from one plate loading to another.

Practically, variance of the sum of the modeling errors is greater than the measuring noise variance. Consequently, measurement reproducibility is very good but there is a non-negligible measuring bias.

6.5.5. *Specificities of scatterometry for CD metrology*

As already mentioned, scatterometry is an indirect optical measuring technique and has several differences compared to other more classical metrological techniques.

6.5.5.1. *Nondestructive measurement*

It has been demonstrated that SEM measurements, which imply an electron flow often quite energetic, may noticeably modify the geometry of exposed elements such as resist lines. By contrast, light involved in scatterometric tools is in the visible and near UV range, that is to say between 250 nm and 750 nm. For wavelengths in this range, photons have low energy and, if the flow remains low (which is the case for common tools), do not noticeably modify a material's properties. Nevertheless, studies are ongoing to extend the spectral range towards shorter wavelengths (for example 150 nm); in these conditions, some materials such as resists may be fatally modified, hence limiting the applications of UV scatterometry.

6.5.5.2. *Unlocalization*

Scatterometry performs a global measurement of a pattern. Indeed the incident optical beam falling on a grating is usually much larger than the space between lines (typically 25–250 microns). Consequently the measured optical signature corresponds to the diffraction of some hundred to some thousand of lines. The geometrical data retrieved describe an "average" line, a typical sample of a great number of lines. By contrast, atomic force microscopy (AFM) or scanning electron microscopy (SEM), produce a local measurement, providing an individual line width. Scatterometry calibration through AFM or SEM measurement consists first in evaluating, across a large area, the size of lines for a great number of samples and, second, in comparing their mean value to the one given by scatterometry. This calibration process is very difficult because tools may not be measuring the same data (definition problem of line width when the sidewall angle is not a right angle) and a great number of reference measurements are required to obtain good precision on the mean value of lines characteristic.

6.5.5.3. *Indirect measurement*

Scatterometric measurement is totally indirect, contrary to AFM or SEM, for which this peculiarity is less pronounced. Measurement processing is complex since

it implies electromagnetic computation algorithms along with parametric optimization processes. Consequently, measuring time comprises a non-negligible part of computer treatment. Moreover, the relationship between the measured data (α and β optical responses in the case of ellipsometry) and the measured parameters (width, eight, etc.) is strongly non-linear, and this has several consequences:

– it is very difficult to obtain a rough estimate for the parameters through a quick visual inspection;

– solutions may be multiple, that is to say that sometimes the distinction between two solutions (sets of parameters) may be ambiguous.

Remember that, considering the precision required today in microelectronics, AFM and SEM are also indirect metrologic methods given that in both cases, a signal processing algorithm is necessary to obtain the geometrical characteristics of the objects (deconvolution, thresholding, averaging, and, eventually, Monte Carlo computation). However, rough data are still readable, at least at first sight.

6.5.5.4. *Background effects*

Spectrometric scatterometry is an optical technique that usually uses visible and near UV light (between 250 nm and 750 nm). For some of these wavelengths, materials employed in microelectronics are either transparent (or semi-transparent) or absorbing, but deposited in thin layers of a few tens of nanometers. Consequently, when an object is lithographed on top of a multilayer stack or on top of another pattern, all the elements of the illuminated structure bring their contribution to the measured signal.

Consequently, during scatterometric measurement, we should take into account all the parameters from the geometry and from the refractive indexes of all the elements implied. For example, in the case of a resist line on top of a BARC, even if this later material is absorbing, it cannot be considered as a semi-infinite medium and the BARC thickness and the silicium index must be integrated in the model.

On the other hand, given the wavelength of the working light, which is often smaller than the characteristic dimensions of the objects or the spaces between objects, the optical response cannot be considered as the sum of uncorrelated contributions coming from isolated objects, and the proximity effects must be integrated in the modeling. For example 100 nm lines with a 200 nm spacing between them will not have the same signature as the same lines with a 700 nm spacing. In the case of periodic structures (usually treated by scatterometry) this can easily be understood by considering the average matter density argument. These proximity effecrs are automatically taken into account in the electromagnetic computation models.

Finally, note that the lighting spot size is usually of a few tens of microns. For a simplified treatment, the measured pattern has to be homogenous across the whole surface of the measuring spot to prevent diffraction phenomena at the edges of the pattern.

6.5.6. *Scatterometry implementation: R&D versus production*

Today scatterometry is in widespread use over the semi-conductor industry for advanced microelectronic applications. This technique particularly excels in production thanks to two main qualities: its measurement speed (roughly 2s per measurement) and is reproducibility (Sub 0.5 nm at 3σ); for several technological steps, included lithography, scatterometry is unrivalled with regards to these two qualities.

Unfortunately for this technique, the correlation between measured parameters (height, CD, SWA) may sometimes be so important that it involves measurement non-accuracy. This is unacceptable for R&D and potentially for production when working with peculiar materials stacks [UKR 06]. Moreover, the result obtained is a mean value that does not take into account the process variability at the grating scale, and hence generates an additional uncertainty for the final result [GER 07].

6.5.6.1. *R&D*

As regards lithography, scatterometry may be a metrological means to define the process windows when working on a focus exposure matrix (FEM) thanks to its measurement speed and its ability to measure steep or re-entrant profiles (which is impossible with CD-SEM).

Unfortunately, this technique presents a main drawback for R&D. When working on a lithography step with varying focus conditions, if comparing measurements from scatterometry (made with fixed-angle ellipsometry) with reference measurements made with AFM 3D, as illustrated in Figure 6.47, correlation between the output parameters of scatterometry generates non-accuracy on the measurement that may involve a wrong choice concerning the optimum process window (see Figures 6.48 and 6.49).

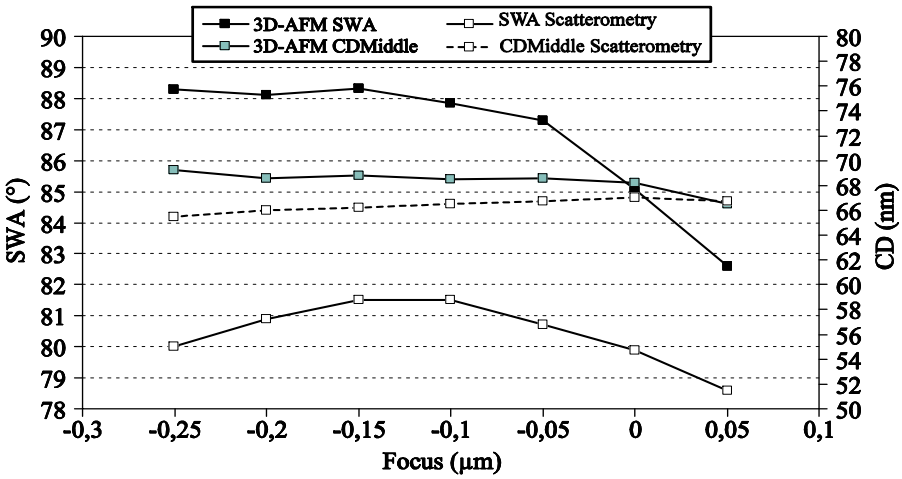

Figure 6.47. *Scatterometric and AFM 3D measurements (SWA and CD Middle) for various focus values (193 lithography process)*

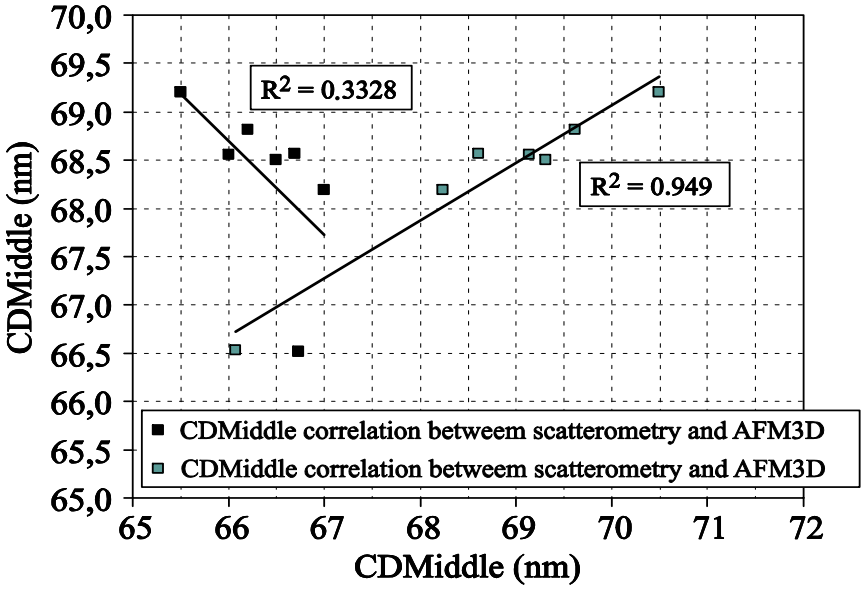

Figure 6.48. *Correlation on measured CD Middle (see Figure 6.47) between scatterometry and AFM 3D*

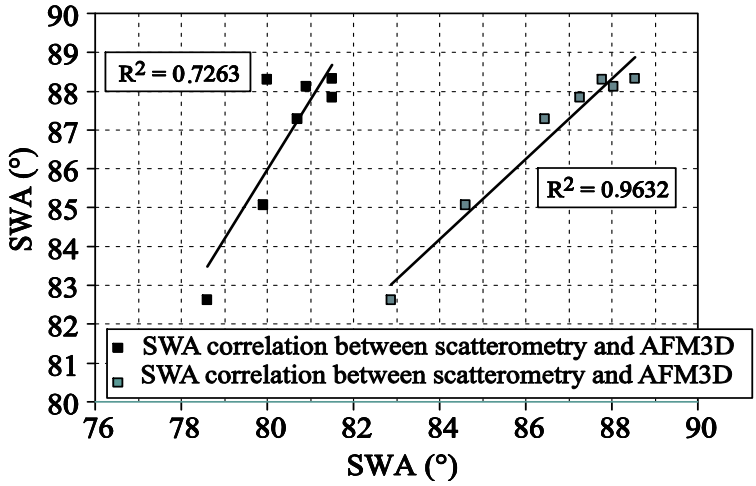

Figure 6.49. *Correlation between scatterometry and AFM 3D for the SWA measured in Figure 6.47*

In this precise case, focus variation generates, at the same time, sidewall angle (SWA) variations combined with height variation (Figure 6.50) (visible with AFM data). These parameters being correlated by scatterometry, it is then impossible to get measurement accuracy. The tighter the dimensional constraints are, the more this correlation between parameters will have a harmful impact on the process definition. This is one of the most extreme limitations of scatterometry for R&D applications today.

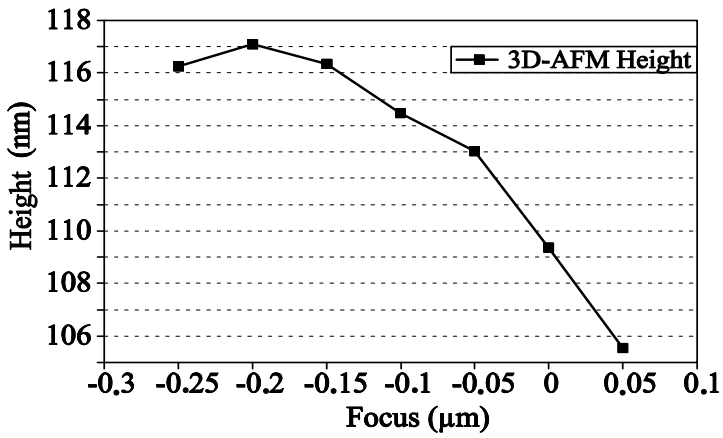

Figure 6.50. *AFM 3D height measurements according to focus values*

6.5.6.2. *Production*

Despite these drawbacks of correlation between output parameters, scatterometry is a very powerful technique in production because of the qualities already mentioned. With stack evolution, in particular the introduction of metals in the gate levels of transistors, scatterometry is again challenged. Indeed, metals' high reflectivity generates rough measurement signals that are more difficult to analyze, and which consequently disturb measurement quality. Generally, today's trend in the semi-conductor sector consists of complexifying stacks by introducing multiple layers of more or less exotic materials. Eventually, scatterometry has problems in measuring these products. For this kind of application, scatterometry will have to be replaced by other techniques. On the other hand, its easy implementation for simple stacks guarantees good prospects for scatterometry with, today at least, no challengers.

6.5.7. *New fields for scatterometry*

Given its working principle and its "easy" implementation, scatterometry has multiple prospects for various applications: focus control of optical projection systems for lithography tools [INA 07, LEN 07, SAR 07], real time scatterometry for etching control [SOU 07], mask control [GAL 07], and LER roughness analysis [SHY 07].

6.6. What is the most suitable technique for lithography?

The most judicious answer is non-committal: it depends… In fact, despite what a lot of people wish, there is not and there will never be a universal technique for CD metrology for lithography. Four to five years ago, CD-SEM was the only technique present in the production environment in the semi-conductor field, plus, for R&D, there was X-SEM. Next, due to the technological constraints requiring more morphological parameters such as SWA, and height, scatterometry was introduced in production to complement CD-SEM. Today, technological requirements ask for an exact 3D characterization of the fabricated patterns. AFM 3D is being introduced either in production or R&D, so as to complement the tools already mentioned.

Depending on the needs identified, it is recommended that a hybrid metrological concept (or complementary metrological concept) be followed that takes advantage of each technique's best points, and takes into account each technique's limitations (see Figure 6.51). AFM 3D equipment fulfills theses requirements for CD measurements for lithography.

In the following section we present some typical application examples.

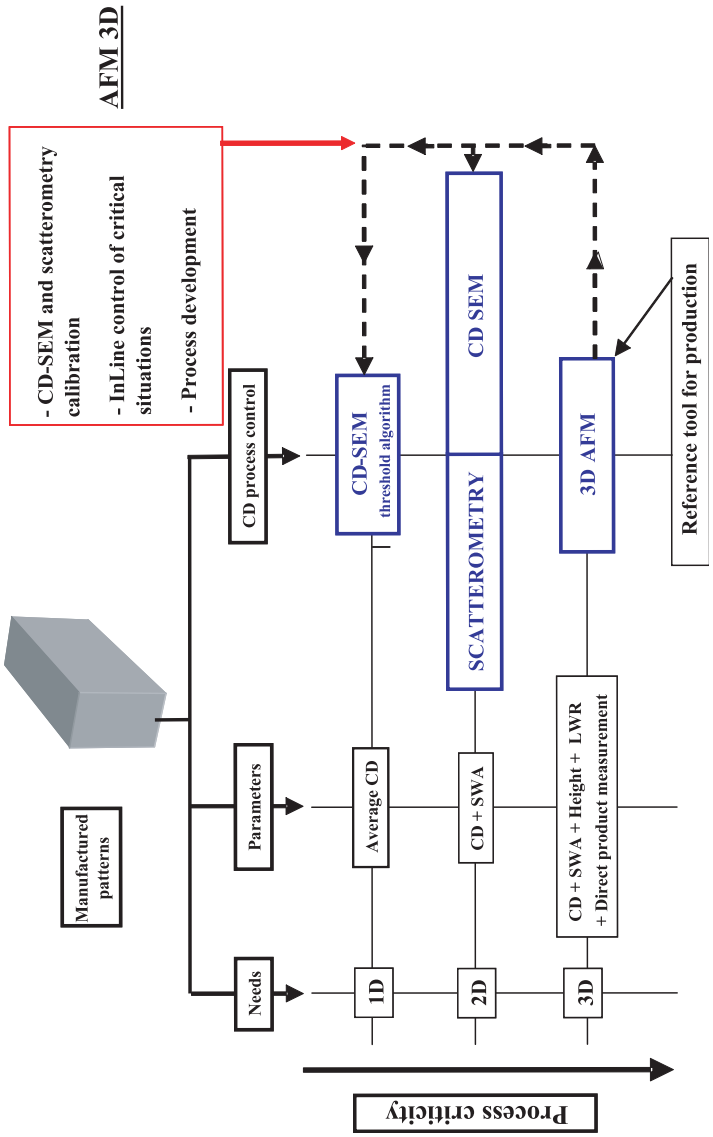

Figure 6.51. *Hybrid metrology concept (or complementary metrology) based on metrology reference tool: AFM 3D*

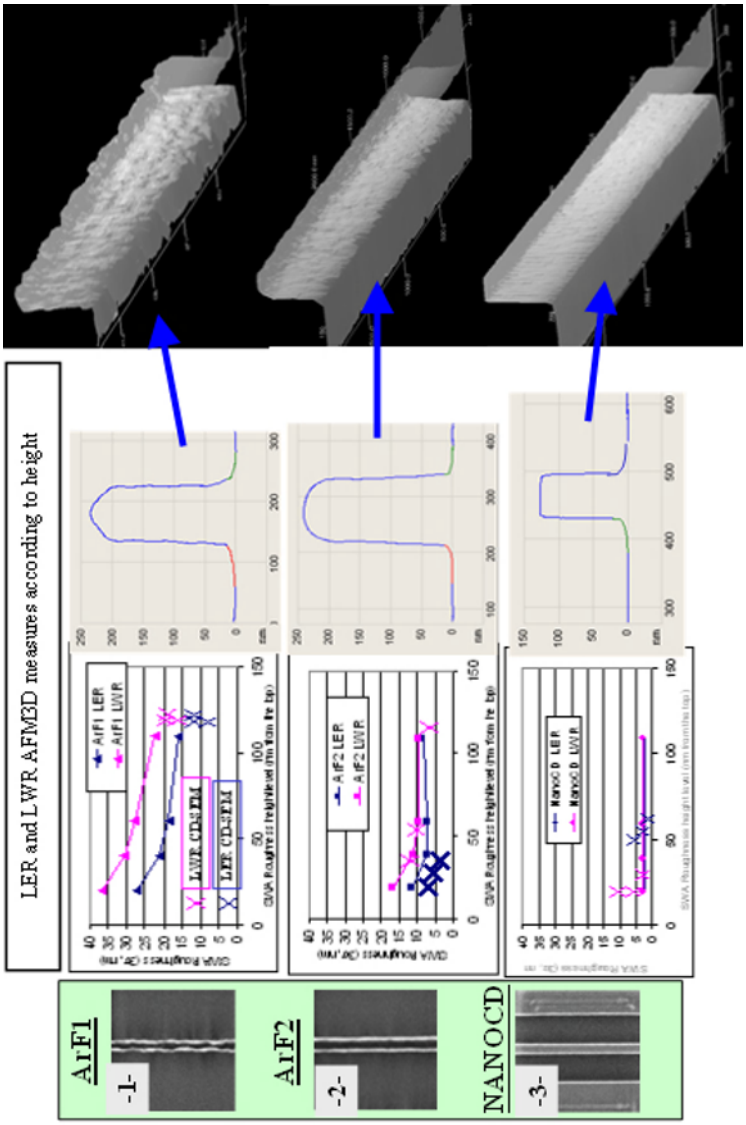

Figure 6.52. *LER and LWR evaluation with AFM 3D for two resists 193 (1 and 2) according to pattern height. Comparison with CD-SEM images and with a reference silicon sample (3)*

6.6.1. *Technique correlation*

In lithography, R&D studies can be greatly accelerated for example by combining CD-SEM and AFM 3D to reduce resist LER and LWR [FOU 06] (see Figure 6.52). Correlation between two techniques for LER and LWR studies enables a more accurate analysis thanks to AFM 3D, as well as the evolution of these parameters according to pattern height. Variations on LER and LWR values are also decorrelated from the height and profile of the measured features (which is not possible with CD-SEM).

6.6.2. *Technique calibration*

In order to optimize production techniques such as scatterometry or CD-SEM , it is really easy to take advantages of AFM 3D versatility so as to calibrate or develop the measurement algorithms used by these two techniques [FOU 05]. As shown in Figure 6.53, it is for example possible to optimize CD-SEM measuring thresholds so that they perfectly match the reference measurements obtained with AFM 3D. Once calibration is performed, CD-SEM (which is faster than AFM 3D) can advantageously be used in a production step, for example, and guarantee true measurements, with prospects for better yields. Very importantly, this calibration step is adapted to given material and profile (height and SWA), consequently there are no universal calibration rules.

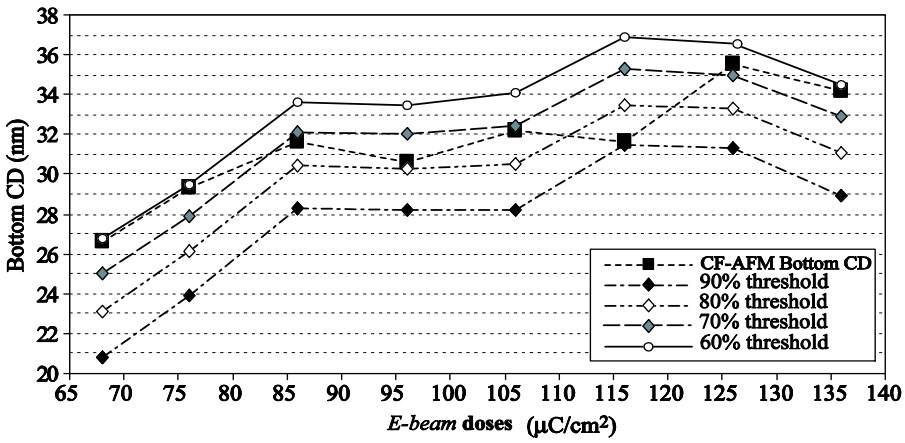

Figure 6.53. *CD measurements on an E-Beam resist. CD increases as the E-Beam dose increases. Only one CD-SEM threshold corresponds to each pattern dimension*

6.6.3. *Process development*

For some lithography needs, instead of using X-SEM which is time consuming, AFM 3D can sometimes be used to totally replace X-SEM, thanks to its measurement accuracy and automization qualities. For example, in the case described by Figure 6.54, AFM 3D enables studies of PEB impact on an E-Beam resist profile. Typically, whereas an X-SEM measurement will last roughly 1 hour for a sample, the same sample can be measured in less than 15 minutes, including mounting and tip characterization. Then, once the first measurement is made, each additional measurement take only 30 seconds because there is no tip-mounting step. The huge time gain is clearly visible compared to X-SEM.

6.6.4. *Evaluation of morphological damage generated by the primary electron beam from CD-SEM*

Electron–matter interaction is quite important when measuring resist patterns with CD-SEM. It generates morphological damages on the pattern which depend on the measuring conditions (incident energy, intensity, number of integration windows, etc.). AFM 3D can measure these degradations very accurately and quantify them in nanometers. Consequently it is all the more possible to correct the CD-SEM algorithms with these offset values [FOU 05]. Typically, CD-SEM or X-SEM generate several nanometers shrinking in 3D for 193 resist patterns. If the measuring offset is not taken into account, these pattern dimensions are systematically underestimated by several nanometers (see Figure 6.55).

In this precise case, focus was put on the potential degradation on a 193 resist pattern and a silicon pattern. We selected a precise spot on these patterns. First a line portion was measured with AFM 3D (average profile in black), then at the same place, a standard measurement in R&D and in production conditions was made (typically 300eV for resist and 500eV for silicon). Finally a second measurement was made at the same place with AFM 3D (average profile in grey). We observe that the CD-SEM measurement has no impact on the morphology of the silicon pattern whereas the 193 resist pattern has shrunk by 8 nm (4 nm on each side). This is the well-known phenomenon called shrinkage. Given the values at stake, this phenomenon is absolutely not negligible and must be taken into account, for example, in the frame of OPC studies [FOU 09].

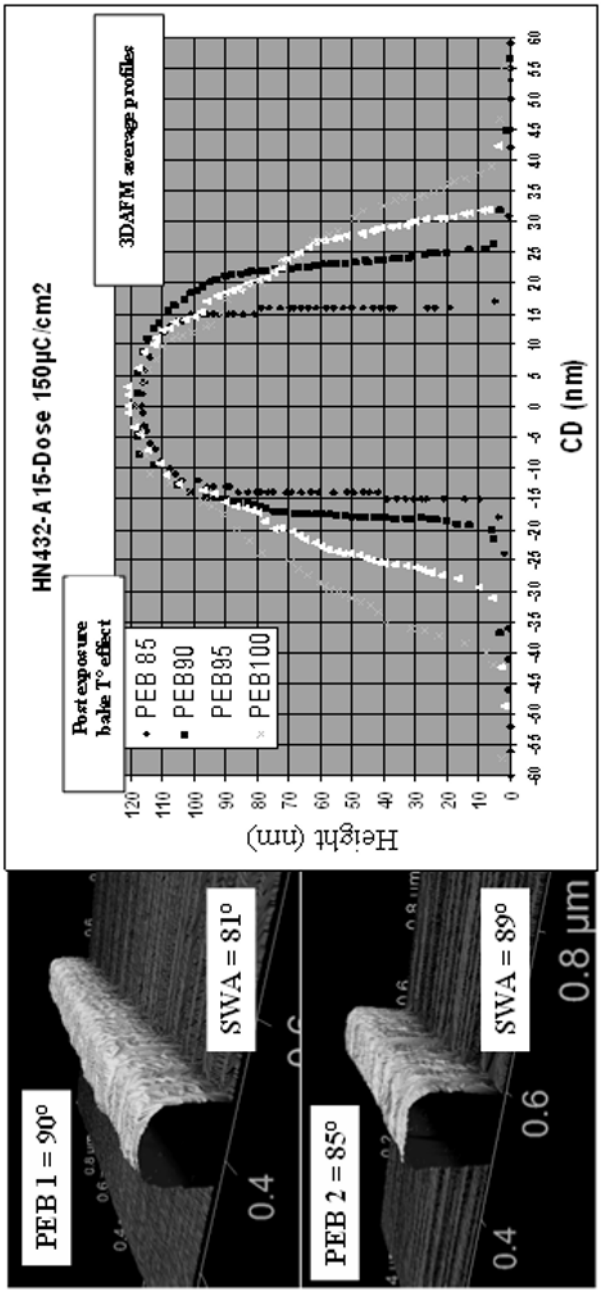

Figure 6.54. *AFM 3D study of PEB impact on the average profile of a pattern realized with an E-Beam resist exposed with a dose of 150 µC/cm²*

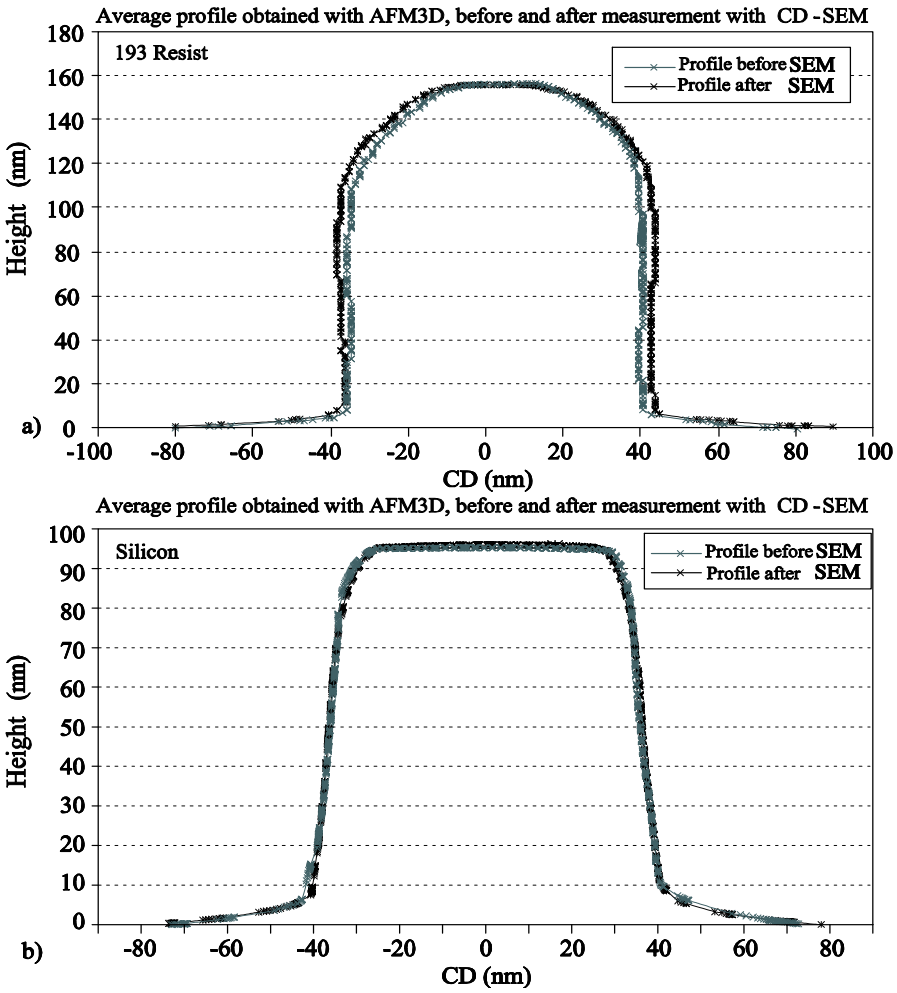

Figure 6.55. *AFM 3D study of interaction between CD-SEM electron beam and (a) a resist pattern, and with (b) a silicon pattern*

6.7. Bibliography

[ABD 07] ABDULHALIM I., "Optical scatterometry with analytic approaches applied to periodic nano-arrays including anisotropic layers", *Modeling Aspects in Optical Metrology*, 6617(1), p. 661714, 2007.

[AZO 07] AZORDEGAN A., BUNDAY B., BANKE B., ARCHIE C., SOLECKY E., ALLGAIR J., SILVER R., Unified advanced optical critical dimension (ocd) scatterometry specification for sub-65 nm technology, Technical report, SEMATECH, inc., January 2007.

[BIN 85] BINNIG G., QUATE C.F., GERBER C., "The Atomic Force Microscope", *Phys. Rev. Lett.*, vol. 56, p. 930–933, 1985.

[BOR 99] BORN M., WOLF E., *Principles of Optics: Electromagnetic Theory of Propagation, Interference and Diffraction of Light*, Cambridge University Press, Cambridge, 7th edition, october 1999.

[BRA 04] BRAGA P.C., RICCI D., *Atomic Force Microscopy: Biomedical Methods and Applications*, Humana Press, Totowa, USA, 2004.

[CAZ 01A] CAZAUX J., "Correlation between the X-ray induced and the electron-induced electron emission yields of insulators", *J. Appl. Phys.*, 89, p. 8265, 2001.

[CAZ 01B] CAZAUX J., "About the secondary electron yield and the sign of charging of electron irradiated insulators", *Eur. Phys. J. Appl. Phys.*, 15, p. 167, 2001.

[CHA 80] CHANDEZON J., RAOULT G., MAYSTRE D., "A new theoretical method for diffraction gratings and its numerical application", *Journal of Optics*, 11(4), p. 235–241, 1980.

[DAH 05] DAHLEN G., OSBORN M., OKULAN N., FOREMANN W., CHAND A., FOUCHER J., "Tip characterization and surface reconstruction of complex structures with critical dimension atomic force microscopy", *J. Vac. Sci. Technol.*, B 23, vol. 6, p. 2297–2303, 2005.

[DAH 07] DAHLEN G., MININNI L., OSBOM M., LIU H.C., OSBOME J.R., TRACY B., DEL ROSARIO A., "TEM validation of CD-AFM image reconstruction", *Proc. SPIE, Microlithography*, vol. 6518 (3), p. 651818.1–651818.12, 2007.

[DAV 95] DAVIDSON M.P., SULLIVAN N.T., "Monte Carlo simulation for CD SEM calibration and algorithm development", *Proc. SPIE*, 2439, p. 334–344, 1995.

[DAV 99] DAVIDSON M.P., VLADAR A.E., "An inverse scattering approach to SEM line width measurements", *Proc. SPIE*, 3677, p. 640–649, 1999.

[DIX 07] DIXSON R., ORJI N.G., "Comparison and uncertainties of standards for critical dimension atomic force microscope tip width calibration", *Proc. SPIE*, vol. 6518, p. 651816, 2007.

[FAR 93] FARHANG H., NAPCHAN E., BLOTT B.H., "Electron backscattering and secondary electron emission from carbon targets: comparison of experimental results with Monte Carlo simulations", *J. Phys. D: Appl. Phys.*, no. 26, p. 2266–2271, 1993.

[FIT 74] FITTING H.J., "Transmission, energy distribution, and SE excitation of fast electrons in thin solid films", *Physica Status Solidi*, A 26, p. 525, 1974.

[FOU 05] FOUCHER J., SUNDARAM G., GORELIKOV D.V., "The application of critical shape metrology toward CD-SEM measurement accuracy on sub-60 nm features", *Proc. SPIE*, 5752, p. 489, 2005.

[FOU 06] FOUCHER J., FABRE A.L., GAUTIER P., "CD-AFM versus CD-SEM for resist LER and LWR measurements", *Proc. SPIE*, 6152, p. 61520V, 2006.

[FOU 09] FOUCHER J., FAURIE P., FOUCHER A.L., CORDEAU M., FARYS V., "The measurement uncertainty challenge for the future technological nodes production and development", *Proc. SPIE*, 7272, p. 72721K, 2009.

[GAL 07] GALLAGHER E., BENSON C., HIGUCHI M., OKUMOTO Y., KWON M., YEDUR S., LI S., LEE S., TABET M., "Scatterometry on pelliclized masks: an option for wafer fabs", *Metrology*, *Inspection*, *and Process Control for Microlithography*, 21, 6518(1), p. 65181T, 2007.

[GER 07] GERMER T.A., "Simulations of optical microscope images of line gratings", *Proc. SPIE*, vol. 6518, p. 65180U, 2007.

[HAZ 03] HAZART J., GRAND G., THONY P., HERISSON D., GARCIA S., LARTIGUE O., "Spectroscopic ellipsometric scatterometry: sources of errors in critical dimension control", *Process and Materials Characterization and Diagnostics in IC Manufacturing*, 5041(1), p. 9–20, 2003.

[HAZ 07] HAZART J., BARRITAULT P., GARCIA S., LEROUX T., BOHER P., TSUJINO K., "Robust sub-50-nm cd control by a fast-goniometric scatterometry technique", *Metrology*, *Inspection*, *and Process Control for Microlithography*, 21, 6518(1), p. 65183A, 2007.

[INA 07] INA H., SENTOKU K., OISHI S., MIYASHITA T., MATSUMOTO T., "Focus and dose controls, and their application in lithography", *Metrology, Inspection, and Process Control for Microlithography*, 21, 6518(1), p. 651807, 2007.

[ITR 07] International technology roadmap for semiconductors – metrology, Technical report, 2007.

[KLE 80] KLEINKNECHT H.P., MEIER H., "Linewidth measurement on ic masks and wafers by grating test patterns", *Appl. Opt.*, 19(4), p. 525, 1980.

[LEN 07] LENSING K., CAIN J., PRABHU A., VAID A., CHONG R., GOOD R., LAFONTAINE B., KRITSUN O., "Lithography process control using scatterometry metrology and semi-physical modelling", *Metrology*, *Inspection*, *and Process Control for Microlithography*, 21, 6518(1), p. 651804, 2007.

[LOW 96] LOWNEY J.R., "Monte Carlo Simulation of Scanning Electron Microscope Signals for Lithographic Metrology", *Scanning*, 18, p. 301–306, 1996.

[MAC 02] MACHAVARIANI V., GARBER S., COHEN Y., "Scatterometry: interpretation by different methods of electromagnetic simulation", *Metrology*, *Inspection*, *and Process Control for Microlithography*, 16, 4689(1), p. 177–188, 2002.

[MAR 87] MARTIN Y., WICKRAMASINGHE H.K., "AFM mapping and profiling on a sub-100Å scale", *J. Appl. Phys.*, 61, p. 4723, 1987.

[MAR 94] MARTIN Y., WICKRAMASINGHE H.K., "Method for imaging sidewalls by AFM", *Appl. Phys. Lett.*, vol. 64, p. 2498–2500, 1994.

[MIN 07] MININNI L., FOUCHER J., "Advances in CD-AFM scan algorithm technology enable improved CD Metrology, Technical presentation", *Proc. SPIE Microlithography*, San Jose, USA, 25 February–2 March 2007.

[MIN 98] MINHAS B.K., COULOMBE S.A., SOHAIL S., NAQVI H., MCNEIL J.R., "Ellipsometric scatterometry for the metrology of sub-0.1 µm", *Applied Optics*, 37(22), p. 5112–5115, 1998.

[MOR 99] MORRIS V.J., KIRBY A.R., GUNNING A.P., *Atomic force microscopy for biologists*, Imperial College Press, London, second edition, 1999.

[PAQ 06] PAQUETON H., RUSTE J., "Microscopie électronique à balayage", *Techniques de l'ingénieur – techniques d'analyse*, *Imagerie*, 866, p. 1–15, 2006.

[PET 80] PETIT R., *Electromagnetic Theory of Gratings*, Springer, Berlin, December, 1980.

[PRE 92] PRESS W.H., FLANNERY B.P., TEUKOLSKY S.A., VETTERLING W.T., *Numerical Recipes in C: The Art of Scientific Computing*, Cambridge University Press, Cambridge, 1992.

[PUN 07] PUNDALEVA I., CHALYKH R., LEE J.W., CHOI S.W., HAN W., "Detailed analysis of capability and limitations of cd scatterometry measurements for 65- and 45-nm nodes", *Metrology*, *Inspection*, *and Process Control for Microlithography*, 21, 6518(1), p. 65180V, 2007.

[QUI 05] QUINTANILHA R., HAZART J., THONY P., HENRY D., "Influence of the real-life structures in optical metrology using spectroscopic scatterometry analysis", *Nano- and Micro-Metrology*, 5858(1), p. 58580C, 2005.

[RAY 04] RAYMOND C.J., LITTAU M.E., CHUPRIN A., WARD S., "Comparison of solutions to the scatterometry inverse problem", *Metrology*, *Inspection*, *and Process Control for Microlithography*, 18, 5375(1), p. 564–575, 2004.

[REI 85] REIMER L., *Scanning Electron Microscopy*, Springer Series in Optical Science, Springer Verlag, Berlin, 42, 1985.

[REI 93] REIMER L., *Image Formation in Low Voltage Scanning Electron Microscopy*, vol. TT12, 1993.

[SAR 07] SARAVANAN C.S., NIRMALGANDHI S., KRITSUN O., ACHETA A., SANDBERG R., LAFONTAINE B., LEVINSON H.J., LENSING K., DUSA M., HAUSCHILD J., PICI A., "Evaluating a scatterometry-based focus monitor technique for hyper-na lithography", *Metrology, Inspection, and Process Control for Microlithography*, 21, 6518(1), p. 651806, 2007.

[SEI 83] SEILER H., "Secondary electron emission in the scanning electron microscope", *J. Appl. Phys.*, 54, no. 11, p. R1, 1983.

[SHY 07] SHYU D.M., KU Y.S., SMITH N., "Angular scatterometry for line-width roughness measurement", *Metrology, Inspection, and Process Control for Microlithography*, 21, 6518(1), p. 65184G, 2007.

[SOU 07] SOULAN S., BESACIER M., LEVEDER T., SCHIAVONE P., "Real-time profile shape reconstruction using dynamic scatterometry", *Metrology*, *Inspection*, *and Process Control for Microlithography*, 21, 6518(1), p. 65180W, 2007.

[UKR 05] UKRAINTSEV V.A., BAUM C., ZHANG G., HALL C.L., *Proc. SPIE*, vol. 5752, p. 127, 2005.

[UKR 06] UKRAINTSEV V.A., *Proc. SPIE*, vol. 6152, p. 61521G, 2006.

[UKR 07] UKRAINTSEV V.A., TSAI M.C., LII T., JACKSON R.A., "Transition from precise to accurate critical dimension metrology", *Metrology*, *Inspection*, *and Process Control for Microlithography*, 21, 6518(1), p. 65181H, 2007.

[VIL 01] VILLARRUBIA J.S., VLADÁR A.E., LOWNEY J.R., POSTEK M.T., "Edge Determination for Polycrystalline Silicon Lines on Gate Oxide", *Proc. SPIE*, 4344, p. 147–156, 2001.

[WAS 04] WASSERMAN L., *All of statistics: A concise course in statistical inference*, Springer texts in statistics, Springer, Berlin, September, 2004.

[YEU 01] YEUNG M.S., BAROUCH E., "Electromagnetic scatterometry applied to in-situ metrology", *Metrology, Inspection, and Process Control for Microlithography*, 15, 4344(1), p. 484–495, 2001.

List of Authors

Claire AGRAFFEIL
Laboratoire des Technologies pour la Microélectronique
CEA
Grenoble
France

Karim AISSOU
Laboratoire des Technologies pour la Microélectronique
CEA
Grenoble
France

Renaud BACHELOT
University of Technology of Troyes
France

Thierry BARON
Laboratoire des Technologies pour la Microélectronique
CEA
Grenoble
France

Vincent BOUCHIAT
Institut Néel
Centre National de la Recherche Scientifique
Grenoble
France
and
University of California
Berkeley
USA

Michel BRILLOUËT
CEA-LETI-Minatec
Grenoble
France

Marianne CONSONNI
CEA-LETI-Minatec
Grenoble
France

Jörge DE SOUSA NORONHA
Ecole Supérieure d'Art et Communication (EAC)
Paris
France

Johann FOUCHER
CEA-LETI-Minatec
Grenoble
France

Gianluca GRENCI
CNR-Istituto Nazionale per la Fisica
della Materia
Basovizza
Italy

Jérôme HAZART
CEA-LETI-Minatec
Grenoble
France

Martin KOGELSCHATZ
Laboratoire des Technologies pour la
Microélectronique
CEA
Grenoble
France

Stefan LANDIS
CEA-LETI-Minatec
Grenoble
France

Benedetta MARMIROLI
Institute for Biophysics and
Nanosystems Research
Austrian Academy of Sciences
Graz
Austria

Alina PASCALE
Laboratoire des Technologies pour la
Microélectronique
CEA
Grenoble
France

Filippo ROMANATO
CNR-Istituto Nazionale per la Fisica
della Materia
Basovizza
Italy
and
Padua University
Italy

Massimo TORMEN
CNR-Istituto Nazionale per la Fisica
della Materia
Basovizza
Italy

Index

A

accuracy, 3, 35, 66, 171, 249, 251–2, 263–4, 266, 277, 280, 284, 286, 307–8, 313
adherence, 103, 107–8, 114
adhesion, 24, 101–2, 104–7, 114–5, 117, 274
adjustment, 125, 254
atomic force microscopy (AFM), 89, 137–9, 142, 170–174, 178–0, 182, 184, 186, 188–198, 200, 217–8, 220–21, 223–4, 249, 266–9, 271–7, 279–81, 285–6, 305–6, 308, 316–8
algorithm, 140, 263, 265, 297, 301, 306
aspect ratio, 4, 12, 15, 23–4, 55–6, 64–6, 68, 74, 98, 148, 172, 268, 272
average, 4, 11, 32, 33, 36, 69, 124, 140, 146, 147, 252, 254, 263, 275, 278, 305, 306, 314, 315
azobenzene, 217, 221

B

bar, 69, 126, 220–21, 224, 235

C

capillary, 90–1, 149, 152–6
cavities, 65, 91, 93, 120–2, 131, 135, 138, 145–6, 152, 154
correction, 304

D

deconvolution, 280, 306
de-embossing, 90, 93, 100–2, 107, 114–6
deformation, 101, 115, 127, 130–2, 141, 152, 155, 235
demolding, 99, 100–2, 114–8, 128, 141, 144
diffraction, 1, 4–6, 23, 28, 30, 40–4, 47–52, 55–9, 140–3, 145–6, 176, 207–8, 212, 221, 223, 286–8, 304–6, 316
distribution, 9, 17–18, 28, 30–1, 33, 35–6, 38, 44, 123–6, 130–2, 134–5, 137, 154–6, 214–5, 217, 220–2, 273, 297, 317

E

edge effect, 214–5, 217–8
elastic, 32, 34–8, 99–100, 117, 258

electron, 8– 11, 20, 24–5, 30–2, 34–40, 42–3, 63, 96, 98, 105, 107, 109, 136–7, 140, 144–5, 173, 176, 178–184, 189, 191, 193, 195, 200, 208–10, 213, 217, 249, 254–5, 258–9, 260–3, 266, 273, 286, 305, 313, 315
transistor, 184, 193, 195
ellipsometry, 290, 296, 305, 307
evanescent wave, 207, 211, 216

F

flexible, 99, 184, 232
flow, 67, 68, 70, 91, 120–2, 125, 130, 133, 138, 145, 148, 149, 152–5, 241, 305
force, 93, 102–3, 115–8, 131, 137, 142, 149–51, 154–6, 169, 171, 174, 180, 181, 184, 188–89, 217, 219, 268, 273–5, 316, 318
fracture, 115–6, 127
friction, 100–2, 108, 115, 269, 271, 274, 275

G

goniometry, 296

I

indentation, 173–4, 179, 184
interaction, 5, 6, 9, 19, 25, 32, 34–5, 102, 148, 154–5, 169–76, 180, 184, 188, 191, 219, 225, 232, 238, 258–9, 260, 267, 269, 274, 313, 315
interface, 28, 79, 100–05, 114, 119, 146, 154, 209–10, 212, 216, 250

L

library, 140, 143, 297, 301–2
local, 7, 30, 32, 44, 57, 90, 93, 123, 131, 134, 137, 140, 169–7, 180, 182–88, 190, 192–3, 197–201, 209, 213, 215, 217, 219–21, 225, 235, 237, 243, 252–4, 275, 301, 305

M

measurement noise, 302–4
metrology, 133–4, 145, 250–1, 286, 288, 303, 305, 309–10
MMFE, 140, 297

N

nano-oxidation, 190–3, 197
negative resist, 24, 57, 62, 98, 217, 220

O

optical, 3, 8, 20, 61–2, 64, 66, 77–8, 91, 93–4, 96, 134–5, 139–40, 143, 147–8, 169–171, 174, 176, 207–8, 210, 213–18, 220–25, 231, 242, 271, 273, 286–9, 291, 293, 296–8, 301, 303–6, 309
organo-metallic, 187

P

parameter, 32, 36, 45, 55, 57, 104, 144, 213, 232, 274, 290–3, 297, 301–3
PDMS, 99, 238
photon, 1, 5–6, 8–11, 14, 16–7, 25–32, 39–40, 42–3, 55, 217, 292
photosensitive resist, 212, 216–7, 222–6, 256, 261–2
plasmonic, 32, 213, 219, 222–5
point, 6, 28, 31, 32–5, 39, 41–3, 45, 47, 49, 52, 63–4, 93, 96, 105, 115, 132–4, 139–41, 143, 171, 184, 186, 191–2, 196, 198, 207, 251, 269, 273–5, 281, 284, 287, 300, 303

polarization, 36, 215, 217–2, 225, 291, 294
polymer, 33, 38, 64, 65, 72–3, 89–90, 99–100, 103, 110, 113, 120, 127, 128, 130, 137, 146, 148–9, 179–180, 217, 220–1, 231–2, 238–41
polymerization, 62, 93, 113, 217, 220, 232
positive resist, 6, 24, 57, 217
pressing, 87, 119, 121, 129, 130, 132, 139, 141, 148, 150, 152, 156
profile, 59, 65, 68, 121, 123, 147, 181, 184, 263–66, 278–9, 281, 298, 311, 313–5
proximity, 1, 3, 32, 41, 56–8, 176, 181–2, 216, 220, 225, 273, 306

Q

quantum devices, 191, 194

R

rays, 2, 3, 5, 25–6, 28, 30, 79, 287
regression, 106, 301
reproducibility, 68, 196, 251–2, 265, 280, 284, 286, 304, 307
resolution, 1, 2, 3, 5, 8, 12–15, 17, 23–4, 34, 51, 55–6, 61, 64–8, 77–8, 93, 99–100, 120, 141, 147, 155, 169, 173, 176, 178, 184, 192, 193, 199, 203, 207–8, 211, 213, 217–9, 223–6, 254, 259, 268, 275, 278, 284, 288, 296
roughness, 14, 74, 78, 113, 130, 147, 191, 192, 250–1, 253, 263, 309

S

scatterometry, 140–8, 249, 286–8, 293, 297, 303–11
sensitivity, 216–7, 221, 271, 291, 293, 302, 303
silane, 99, 111, 113
silicon, 14, 16, 19–24, 37, 62, 65, 70, 72, 75, 90, 98–9, 110–11, 131, 155, 186, 188–193, 200, 219–20, 239–40, 250, 256, 268, 271, 280, 290–2, 312, 315
silver, 212, 214, 216, 219–22
statistical, 300–4
STM, 170–1, 180, 186–88, 219, 266,
surface energy, 93, 99, 102–110, 120, 122, 148, 149, 153, 217

T

thermorepeated, 95
threshold, 29, 33, 38, 41, 132, 185, 189–190, 194, 217, 261, 263, 265, 313
topographical, 269, 275
treatment, 9, 32, 35, 37, 44, 73, 107, 113–17, 136, 186, 234, 238, 293, 305, 306

U

uncertainty, 67, 265–6, 280, 293, 302–4, 307
UV lithography, 5, 207

V

variance, 302–4
viscosity, 93, 103, 120–2, 125–8, 130, 146, 149, 150– 154, 184
volume, 28, 30, 32–3, 38–9, 44–7, 65–6, 70, 90, 93, 103, 119, 120–3, 135, 148–9, 154, 172, 187, 188, 208, 213

X

X-rays, 2, 4– 6, 8, 14, 19, 23–25, 28, 30, 31, 72, 75, 79, 96, 176